New approach for electrostatic interactions at metal/liquid interfaces and applications for the graphene/water couple.

Anton Robert

PSL
UNIVERSITÉ PARIS

THÈSE DE DOCTORAT
DE L'UNIVERSITÉ PSL

Préparée à l'École Normale Supérieure

Nouvelle approche des interactions électrostatiques aux interfaces métal/liquide et applications pour le couple graphène/eau

Soutenue par

Anton ROBERT

Le 28/09/2022

Ecole doctorale n° 388

Chimie physique et chimie analytique de Paris centre

Spécialité

Chimie Physique

Composition du jury :

Benjamin ROTENBERG DR2, Sorbonne Université	*Président*
Marie-Pierre GAIGEOT Professeur, Université d'Évry	*Rapporteure*
Nicolás LORENTE Professeur, Universidad del País Vasco	*Rapporteur*
Benoit COASNE DR2, Université Grenoble-Alpes	*Examinateur*
Hélène BERTHOUMIEUX CR, Sorbonne Université	*Invitée*
Marie-Laure BOCQUET DR2, École Normale Supérieure	*Directrice de thèse*

ENS | PSL

THÈSE DE DOCTORAT DE L'UNIVERSITÉ DE RECHERCHE PARIS SCIENCES ET LETTRES

préparée à l'École Normale Supérieure par

ANTON ROBERT

NEW APPROACH FOR ELECTROSTATIC INTERACTIONS AT METAL/LIQUID INTERFACES AND APPLICATIONS FOR THE GRAPHENE/WATER COUPLE

NOUVELLE APPROCHE DES INTERACTIONS ÉLECTROSTATIQUES
AUX INTERFACES MÉTAL/LIQUIDE
ET APPLICATIONS POUR LE COUPLE GRAPHÈNE/EAU

Dirigée par

MARIE-LAURE BOCQUET

École doctorale de Chimie Physique et de Chimie Analytique de Paris Centre (ED 388)

September 2022

À Ariane,

AVANT-PROPOS ET REMERCIEMENTS

Caminante, no hay camino, se hace camino al andar[1].

Antonio Machado

Ce travail s'est effectué à l'interface entre deux domaines de la matière condensée : une discipline qui étudie les métaux et l'autre les liquides. Je crois que mon absence de spécialité m'a été profitable, car j'ai porté le même intérêt envers les deux communautés. L'originalité de l'approche présentée dans cette thèse réside peut-être dans le mélange pragmatique d'outils d'origines diverses. Pourvu que le lecteur soit tolérant à l'usage détourné des siens. Pourvu qu'il ne se lasse pas trop vite d'instruments qu'il ne connaît peut-être pas encore. Cette thèse n'est pas une juxtaposition de travaux séparables, aucun chapitre n'est réellement hermétique. La volonté de plonger le lecteur dans un nouvel "univers", pédagogiquement d'abord, en s'appuyant ensuite sur des chapitres entiers, est assumée. Ce manuscrit est écrit en anglais afin d'être accessible à un plus grand nombre de scientifiques.

Je remercie chaleureusement ma directrice de thèse, Marie-Laure Bocquet, qui m'a mis le pied à l'étrier il y a quelques années déjà. Dès 2017, entre deux cours de chimie, je passais au pôle théorie avec mon ordinateur pour lui montrer mes calculs DFT ! Grâce à elle, j'ai beaucoup appris au fil de ces années, non seulement sur la science, mais aussi sur la recherche. Cette thèse aurait été complètement différente sans une collaboration de presque deux ans avec Nikita Kavokine et Lydéric Bocquet, à qui je suis grandement redevable. Je remercie une deuxième fois Lydéric Bocquet pour avoir permis cette thèse, en la finançant. Je tiens aussi à remercier Hélène Berthoumieux pour notre collaboration lors de cette troisième année de thèse.

Il y a d'autres personnes que j'aimerais remercier et qui ont indirectement contribué à ce travail. Je dois beaucoup à Maximilien Levesque, sa vision du travail, son goût pour le code, sa bonne humeur et sa créativité qui m'ont inspirés. Je pense aussi à Benoit Grosjean, sa patience et sa pédagogie il y a quelques années. Merci à Daniel Borgis, qui est toujours prêt à parler de liquides avec passion. Un grand merci aux professeurs que j'ai eu la chance

[1] *Marcheurs, il n'y a pas de chemin, le chemin se fait en marchant.*

d'avoir et qui m'ont fait adorer la chimie théorique : Rodolphe Vuilleumier, Damien Laage et Benjamin Rotenberg.

Un grand merci à Jules et Maxime, des amis présents[2] dans les moments difficiles. Merci à Yann pour les cours d'analyse complexe entre deux parties d'échecs et à Léa pour ses explications limpides des équations de Maxwell jusqu'au bout de la nuit. Presque trois ans de colocation entre amis scientifiques qui resteront gravés à jamais. Merci à Bertin pour ses visions sages et rafraîchissantes du monde académique. Merci à mes parents d'entretenir des visions si opposées de la science parce qu'elles nourrissent la mienne. Anjan, ton exigence de créativité alimente nos recherches et notre quotidien.

Un dernier grand merci aux membres du jury pour leurs questions durant de la soutenance et de leurs intérêts pour ce travail. Merci au président du jury pour ses corrections détaillées qui m'ont permis de corriger un certain nombre d'erreurs dispersées.

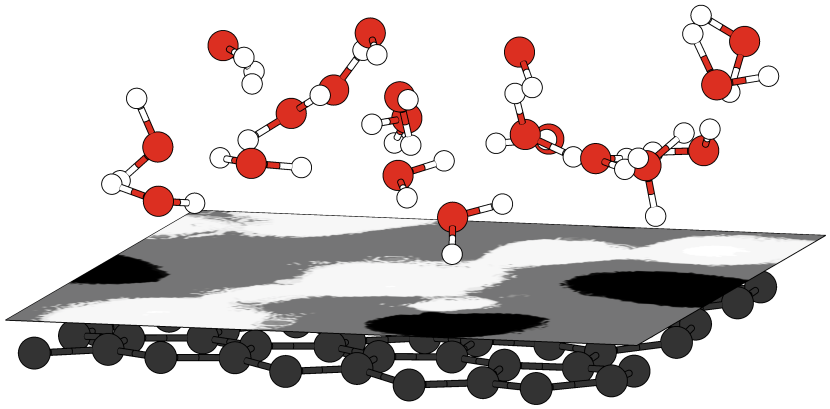

[2] On me dira qu'il est plus facile pour un ami d'être présent quand il travaille dans le même bureau.

Abstract

A theoretical framework is introduced to tackle electrostatics interactions at metal/liquid interfaces. By adopting a microscopic perspective, we displace the electrostatic problem in resolving an integral equation for the linear response function of the interfacial system. By describing the liquid's charge fluctuations and dielectric response in the framework of quantum field theory, we inherit new concepts to deal with collective interactions at the mean-field level. The precision and versatility of our approach allow us to scrutinize carbon interfaces, taking into account the specificity of their electronic band structures. This method is then used to study the mean force potential of an aqueous ion at the graphene interface, the electronic band gap of a solvated carbon nanotube, the van der Waals interactions between a metal and a liquid, and solid/liquid friction coefficients. The validity of mainstream hypothesis regarding time and length scales decoupling at metal/liquid interfaces can be systematically challenged.

CONTENTS

LIST OF ABBREVIATIONS

AIMD	ab initio molecular dynamics
BOA	Born-Oppenheimer approximation
CNT	carbon nanotube
DFT	density functional theory
FDT	fluctuation-dissipation theorem
FLG	few-layers graphene
hBN	hexagonal boron-nitride
HF	Hartree-Fock
LG	Landau-Ginzburg
LJ	Lennard-Jones
vdW	van der Waals
MD	molecular dynamics
MM	molecular mechanics
NN	nearest-neighbor
PMF	potential of mean force
SRA	specular reflection approximation
SRF	surface response function
TF	Thomas-Fermi

This thesis is motivated by a new enthusiasm for nanofluidics: studying fluids in nanochannels. This recent field, as many others before it, comes to the fore [1] because experimental measurements are nowadays technologically possible. Let us briefly dwell on those achievements to realize how extraordinary they are. Indeed, one could reasonably think that probing fluid velocities on this scale — one billionth of a meter — is unrealistic. One can even question the word "fluid": what is going out of a nanometer pipe looks much more like a "crowd" of water molecules rather than the familiar water jet from the kitchen tap (see Fig. 1a). How can we build such a small pipe? How to control what goes in there? How to detect what goes out and at which speed? We will not answer those questions in this work, but we first want to underline how amazed we are by the experimental setups and measurements that give rise to the theoretical questions we tackle — see Fig. 1b. To cite a few of those pioneers works, we refer to [2, 3, 4, 5, 6].

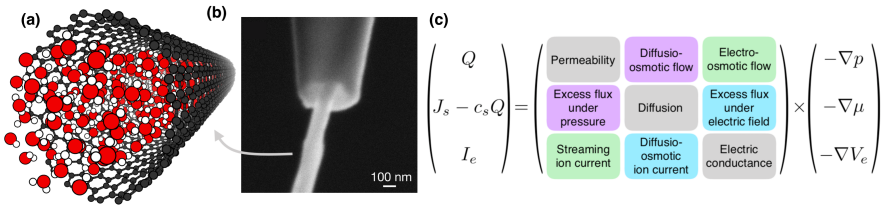

Figure 1: Nanofluidics in a nutshell. **(a)** A special pipe (a carbon nanotube or CNT) with water molecules flowing through it. **(b)** Experimental setup to measure water flow inside a CNT with a pipette. The CNT is glued on the outside to focus the water flow inside the tube. The image is taken from [6]. **(c)** Transport matrix coefficients in nanofluidics. See text for identification of driving forces and observables. The image is taken from [7].

Why is nanofluidic a field worth working in? The global need for clean and renewable energy motivates scientific research in diverse areas. Nanofluidics has made promises because phenomena generating electric currents with salt concentration gradients — like diffusio-osmosis[3] — occur in those tiny pipes. Similar exotic processes suggest some solutions for water desalination/filtration. Those applications are discussed in length in [8].

Why do liquids behave strangely in nanochannels? In nanofluidics, peculiar effects stem from the increasing surface/volume ratio for the liquid.

[3] Process in which a difference in salt concentration between two reservoirs linked by a nanometer pipe induces a net ionic current by differential ionic interaction strength with the surface of the pipe. More can be found in [7].

In fact, like with the rise of microfluidics, reducing the length scale changes the relevant physical interactions [9]. To understand this, we need to look at the transport matrix coefficient (see Fig. 1c). Without non-diagonal terms, it independently links driving forces (respectively pressure drop, chemical potential difference, electric field) to their ad hoc observables (resp. solvent flux, excess solute flux, ionic current). However, surface effects increase the contribution of the non-diagonal terms, which opens new perspectives to generate, for instance, an ionic current with a salt concentration. In order to identify those cross-terms, one needs to accurately describe the pipe/liquid interface, hence the relevance for theoretical chemists to study those systems.

The nanofluidics community now appreciates the efforts of solid-state physics in developing instruments capable of manipulating 1D or 2D materials. Graphene has undeniably the leading role among those so-called 2D vdW materials and their assemblies [10]. Interestingly, the long-awaited emergence of devices allowing reliable measurements of tiny flows can be traced back to its birth [11], around 2004. A single graphene sheet is experimentally challenging to isolate, and one usually prefers to use one of its allotropic forms to build nanofluidic devices: (single/multi-wall) carbon nanotubes (CNTs), few layers of graphene (FLG), or graphite. Note that a geometrically similar material — the hexagonal boron nitride (hBN)— is also used.

The differences between CNTs and boron-nitride nanotubes in nanofluidics illustrate the importance of the liquid/pipe or ion/pipe-specific interaction [4, 6]. However, in molecular mechanics (MM), graphene and hBN are relatively identical, and their interaction with water merely differs by the parametrization of the Lennard-Jones (LJ) potential between nuclei. More sophisticated approaches should therefore tackle this apparent oversimplification [12, 13].

Graphene and hBN more fundamentally differ in their response to an electromagnetic field. Whereas graphene is a semi-metallic material, hBN is insulating. Simulation methods are very reliable for insulating solids in their most accurate ab initio molecular dynamics (AIMD) form. A recent work dedicated to the hBN/water interface has revealed some of its secrets [14], so we will not dwell on it in this work. In contrast, there can be some doubts about the reliability of AIMD simulations in tackling metal interfaces for several reasons. Their high computational cost prevents using a simulation box larger than the typical electronic correlation length. For the same reason, it is challenging to consider the presence of ions at low concentrations. Besides the phenomenological ansatz for the exchange-correlation energy in the density functional theory (DFT) electronic calculations, the dynamics

also rely on the Born-Oppheinmer approximation (BOA). The latter can be violated for molecules at metallic interfaces because of the continuum of the electronic levels at the Fermi level [15]. In fact, in the case of graphene, water molecules are not needed for the BOA to break down [16].

In this thesis, we shall therefore focus on the graphene/water interface and try to gain analytical insights on the specificities of this couple. The goal is of course not to obtain quantitative answers, but rather to identify and estimate the contributions of so far overlooked "second-order" effects. We need a general and elastic framework that can tackle the electrostatic interactions between electrons and polar molecules at the metal/liquid interface. Surprisingly, we have found only one way to tackle this interface analytically in the literature! It is the classical continuum electrostatic approach that merely describes water by its bulk dielectric constant[4]. Therefore, this prompted us to think about electrostatics from a completely different perspective, a microscopic one. The elaboration of this versatile framework and the derivation of some critical physical observables within it may be the essential parts of this work, considering the "loophole" in the literature.

In the late '70s, many efforts were dedicated to grasping the metal/dielectric interface in the presence of ions by analytical methods. This work was partly conducted by A.A. Kornyshev and crystallized in [17] and [18]. Many insights were given, such as the crucial role of the non-local dielectric response of polar liquids near interfaces. This method is still used [19, 20] nowadays. Nevertheless, today's relatively weak interest in analytical methods to tackle those arduous systems[5] is due to the rise of computational chemistry and, most importantly, its large development in the '80s[6]. As mentioned, quantum simulations have been and still are unrivaled in gaining insights into the graphene/water interface (see e.g. [12, 22, 23, 24, 13]). However, their cost and the reduced simulation time and size constrain the system's largest and slowest collective motion of dipoles/charges.

Classical molecular dynamics or molecular mechanics (MM) have come to the rescue with semi-classical approaches to remediate those issues. Due to their intrinsic lack of metallicity, they introduce parametrized models that mimic the metal's polarization — see, e.g. [25] for graphene. A general approach [26] has received much interest. It consists in conferring to the metal's atoms a fluctuating Coulomb charge that is imposed at each time

[4] We will show in this work that the more sophisticated approach [17] that allows the dielectric to have a non-local dielectric response — the one mentioned in the next paragraph — fails for the case of water: it cannot be used! Of course, other methods could exist, but we do not know about them.

[5] "God made the bulk; surfaces were invented by the devil." — Wolfang Pauli as quoted in Growth, Dissolution, and Pattern Formation in Geosystems (1999) by Bjørn Jamtveit and Paul Meakin, p. 291

[6] See the preface of [21] for a short history about "computer experiments".

step of the simulation to maintain a constant potential at the electrode[7]. Going beyond the perfect conductor model, it can even confer an effective Thomas-Fermi (TF) type of screening to the metal [30].

Nevertheless, the specificity of metals lies within their band structure. Graphene is semi-metallic and behaves like a metal on a long wavelengths and like an insulator on shorter ones. This property seems a priori difficult to infer in a classical Hamiltonian beyond a TF model. Moreover, the optimization procedure for the atomic charges in the metal plays the same role as the BOA in AIMD. Therefore, despite those recent achievements, questions are still unanswered. It is useless to say that our role can only be limited to qualitative analytical support. We will question the implicit hypotheses in building those models. We point out that from the solid-state point of view, the graphene communities seem to have ignored the role of the dielectric environment beyond the local electrostatic case. We will see that there is room to refine the evaluation of observables such as electronic conductivities, plasmons dispersions, or electronic band gaps for solvated semi-conductors with a better description of the metal/liquid interface.

To summarize, our work elaborates a practical approach to electrodynamics at the metal/liquid interface (part i). It shall be general enough to tackle several open questions regarding "second-order" effects that are usually ignored in modeling the graphene/water interface. Therefore, in part iii, we will obtain formulas of several physical observables and study:

- the potential of mean force of an ion at the graphene/water interface
- the electronic band gap of a solvated CNT
- the metal/liquid friction and its non-adiabatic contribution at the carbon/water interface

To a less extent, we will also encounter the plasmon dispersion of solvated graphene, the dielectric response of a water slab under a static electric field, and the interfacial vdW energy at the metal/liquid interface. We compute the elementary bricks of our framework for water and graphene (and FLG) in part ii.

[7] For a detailed description of current semi-classical simulation methods, the reader is referred to [27] and to [28, 29] for more details about the constant potential method.

Part I

THE METAL/LIQUID THEORETICAL FRAMEWORK

In this first part, we lay out the basis of the theoretical framework we use throughout this thesis. In both the solid and liquid communities, interfaces are tackled from a specific point of view, usually using a trivial model for the other medium[8]. The difficulty arises from treating both media with the same rigor[9]. A common framework prevents us from making unjustified premises that are nevertheless rightfully introduced in treating the liquid or the solid separately.

As will (hopefully) become clear at the end of it, our work consists in describing the metal/liquid interface using the framework of quantum field theory The gain is attractive because it unlocks the possibility of using decades-long physical and mathematical tools. How can a quantum field describe a purely classical liquid? This part's driving question requires adopting a microscopic point of view regarding electrostatic interactions in liquids.

Being convinced that theoretical chemists could benefit from this framework, an effort has been dedicated to writing this part so that it does not require an a priori knowledge of the quantum field framework. To the cost of the mathematical rigor and completeness, we introduce Feynman diagrams because we find them to play a central role in practice. New diagrams for liquids are introduced when needed, and rules for constructing them are simplified for our work. Two chapters are included in this part. Chapter 1 introduces the physical concepts at play for the liquid and the solid. Chapter 2 gives the Hamiltonian of the interface and tackles the classical/quantum incompatibility. The "rules" summarized at the end allow us to compute the observables in part iii. For a brief recap of the standard approach to electrostatics, refer to the appendix A.1

[8] Very schematically, we consider the two communities represented by those two famous textbooks [31, 32].

[9] Interestingly, with all its limits, especially for water, the existing method[17] puts the dielectric and the metal on an equal footing.

1

PHYSICAL CONCEPTS

1.1 RESPONSE TO A PERTURBATION

1.1.1 *Response function*

We consider a thermodynamically closed system such that the term external refers to something that is not a part of the physical system under scrutiny. Under the application of a perturbating external electrostatic potential $\phi_{\text{ext}}(\mathbf{x}, t)$, it responds by generating a charge density deviation $n_{\text{ind}}(\mathbf{x}, t)$ — therefore induced by the latter. We will focus on the statistically averaged — denoted $\langle . \rangle$ — deviation produced by the system, in space-time — denoted for short by $1 \equiv (\mathbf{x}_1, t_1)$. Linear response theory relates both quantities via the response function χ — or susceptibility —, as follows:

$$\langle n_{\text{ind}}(1) \rangle = \int \mathrm{d}2 \chi(12) \phi_{\text{ext}}(2). \tag{1}$$

The total charge density of the system $n = n_0 + n_{\text{ind}}$ might not be equal to n_{ind} if, without the external perturbation, an inhomogeneity is already present in the system. In turn, the mean induced charge density creates an averaged induced electrostatic potential ϕ_{ind} that can be written

$$\langle \phi_{\text{ind}}(1) \rangle = \int \mathrm{d}2 v(12) \langle n_{\text{ind}}(2) \rangle. \tag{2}$$

Here we have used the *Green's function method* [33] to solve Poisson's equation so that the kernel is the Coulomb interaction between two particles of elementary charge (we use $e = 1$) in vacuum:

$$v(12) = \frac{1}{4\pi\epsilon_0} \frac{\delta(t_1 - t_2)}{|\mathbf{x}_1 - \mathbf{x}_2|}, \tag{3}$$

where ϵ_0 is the dielectric permittivity of the vacuum. Accordingly, we write Eq. 2 for the external potential ϕ_{ext} that arises from an external charge density n_{ext}. The statistically averaged total potential in the system is $\langle \phi_{\text{tot}} \rangle = \phi_{\text{ext}} + \langle \phi_{\text{ind}} \rangle$. Combining Eq. 1 and Eq. 2 we can write the Green's function — or the screened Coulomb potential — of the system $w(12)$ as

$$w(11') = v(11') + \iint \mathrm{d}2\mathrm{d}3 v(12) \chi(23) v(31'). \tag{4}$$

The linearity of Poisson's equation makes the introduction of w helpful because the total potential reads[1]

$$\langle \phi_{\text{tot}}(1) \rangle = \int \mathrm{d}2 w(12) n_{\text{ext}}(2). \tag{5}$$

Those last two equations directly establish the link between the averaged total potential $\langle \phi_{\text{tot}} \rangle$ in the system and χ, its two-point susceptibility. Regarding the general structure of w in Eq. 4, we see that two objects are linked by the operation $[f * g](1) = \int \mathrm{d}2 f(12) g(2)$. To prepare for future complexifications, we represent by a diagram the bare potential v and χ

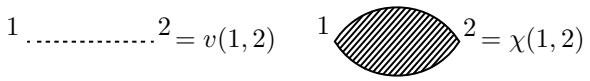

, (6)

and define their diagrammatic link by the operation $*$. Therefore, we can represent the Green's function as follows

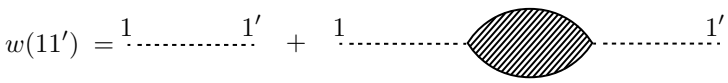

. (7)

Box 1: Eq.1 to Eq. 5 can be written by introducing the *non-local microscopic dielectric function* that relates $\langle \phi_{\text{tot}} \rangle$ and ϕ_{ext} as follows:

$$\langle \phi_{\text{tot}}(1) \rangle = \int \mathrm{d}2 \varepsilon^{-1}(12) \phi_{\text{ext}}(2). \tag{8}$$

Using $\langle \phi_{\text{tot}} \rangle = \phi_{\text{ext}} + \langle \phi_{\text{ind}} \rangle$ and Eq. 4, we obtain

$$\varepsilon^{-1}(11') = \delta(1 - 1') + \int \mathrm{d}2 v(12) \chi(21'). \tag{9}$$

1.1.2 *Mean field correction: from $\chi^{(0)}$ to χ.*

To build the response function χ of a system containing indistinguishable particles, we start from the simplest possible version and enrich the description from it. The first — drastic — physical assumption is to consider that the particles are *independent*, so we first construct the *non-interacting* response function $\chi^{(0)}$ using a microscopic model. Enriching the description of the system requires considering interparticle interactions. In this work, we use a mean-field approach. Be it for electrons in a metal [31] or in simple liquids

[1] The choice $e = 1$ makes $w(12)$ also equal to *(i)* the electrostatic potential in 1 due to a positive test charge in 2, *(ii)* the potential energy between two charges of same sign in 1 and 2.

[32], the mean-field method is a well-known renormalization scheme for homogeneous media to take into account the collective behavior of particles. It amounts to considering that independent particles respond to the external potential ϕ_{ext} plus the *mean* polarization potential $\langle \phi_{\text{pol}} \rangle = v_{\text{inter}} * \langle n_{\text{ind}} \rangle$ of the other similar particles — here v_{inter} is the interparticle potential. In other words, the mean induced charge density is given by the sum of the two contributions:

$$\langle n_{\text{ind}}(1) \rangle = \int \mathrm{d}2 \chi^{(0)}(12) \left[\phi_{\text{ext}}(2) + \int \mathrm{d}3 v_{\text{inter}}(23) \langle n_{\text{ind}}(3) \rangle \right]. \tag{10}$$

The integral equation captures the recursive nature of this interparticle renormalization scheme for the response function χ which can also be written

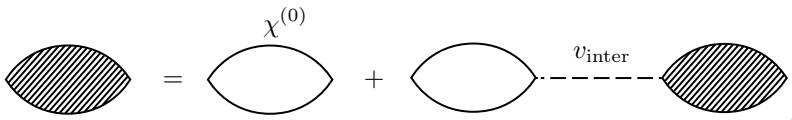

, (11)

or, for the last time in equation,

$$\chi(11') = \chi^{(0)}(11') + \iint \mathrm{d}2\mathrm{d}3 \chi^{(0)}(12) v_{\text{inter}}(23) \chi(31'). \tag{12}$$

Note that the introduction of χ is a short-cut notation for an infinite number of "convolutions" between $\chi^{(0)}$ and v_{inter}, which are the elementary bricks. Indeed, by writing the beginning of the infinite sum

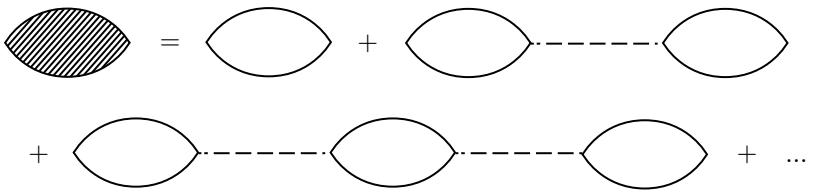

, (13)

we can observe that we have re-organized an infinite number of diagrams involving only $\chi^{(0)}$ and v_{inter}. We will say that we have *renormalized* $\chi^{(0)}$ by the interactions of the similar particles. Turning to the topographic structure of w, when the diagram depicted by χ is decomposed, it enumerates all diagrams that can be built with $\chi^{(0)}$ and v_{inter}, that start and end with a Coulomb "leg" v[2].

[2] It is like enumerating all possible ricochets on the independent particles in the system.

1.2 IMPORTANT EXAMPLES

1.2.1 *Example 1: Non-local electrostatics in dielectrics*

Here we want to find the electrostatic potential in a dielectric system, in which we have introduced a point charge. We confer to the dielectric system a spatial dispersion — we also say that the dielectric response is non-local — : the density response in one location depends on the perturbing potential in another. In contrast, continuum electrostatics considers local media, depicted solely by their dielectric constant ε_{w}. The index "w" stands for a dielectric material in the general case. We have water in mind for applications. We use Eq. 7, but we introduce a new diagram for the response function of a dielectric media χ_{w} — and leave out the other for metals (electrons to be more precise). It reads

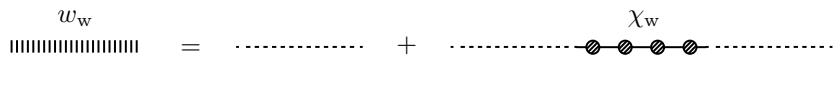

(14)

If the dielectric is homogeneous and isotropic the response function only depends on absolute distances and time differences — i.e. $\chi_{\mathrm{w}}(12) = \chi_{\mathrm{w}}(|\mathbf{x}_1 - \mathbf{x}_2|, t_1 - t_2)$. Convolutions are easier to perform as products in Fourier space: the system being translationally invariant, χ_{w} has a diagonal representation in reciprocal space[3] — $\mathbf{k}$ is the vector in the dual space. The time integration in Eq. 1 gives that the induced charge does not depend on time and that the relevant response quantity is the zero-frequency component of the spatially Fourier transformed and radially averaged response function $\chi_{\mathrm{w}}(k) = \chi_{\mathrm{w}}(k, \omega = 0)$. Using Eq. 14, we obtain

$$w_{\mathrm{w}}(k) = v(k) + v(k)\chi_{\mathrm{w}}(k)v(k) = v(k)\left[1 - \bar{\chi}_{\mathrm{w}}(k)\right] \tag{15}$$

where we have noted the Fourier transform of the Coulomb potential $v(k) = 1/\epsilon_0 k^2$ and introduced the dimensionless longitudinal susceptibility $\bar{\chi}_{\mathrm{w}}(k)$ — see Box 2.

[3] see appendix A.2 for a short recap about this crucial point.

Box 2: Whereas in the condensed matter community [31] the response function χ is used, the liquid community [32] usually deals with the dimensionless susceptibility $\bar{\chi}$. Both are linked by

$$\bar{\chi}(12) = -\int \mathrm{d}3 v(13)\chi(32). \tag{16}$$

In Fourier space, for the homogeneous, isotropic system, it reads $\chi(k) = -\epsilon_0 k^2 \bar{\chi}(k)$. The origin of such a discrepancy can be traced back to the objects under scrutiny in both research domains. For the liquid community, the standard limiting case is the dipolar fluid, and one uses the polarization field $i\mathbf{k}\cdot\mathbf{P}(\mathbf{k}) = n_{\mathrm{w}}(\mathbf{k})$ (using Eq. 263). It explains the k^2 factor in the respective correlation functions — ϵ_0 for homogeneity and minus sign so that $\bar{\chi}(k) > 0$.

The electrostatic potential $\phi_{\mathrm{tot}}(x)$ of a point charge at the origin can be written

$$\phi_{\mathrm{tot}}(x) = \int \frac{\mathrm{d}^3\mathbf{k}}{(2\pi)^3} e^{-i\mathbf{k}\mathbf{x}} w_{\mathrm{w}}(k) \tag{17}$$

$$= \int_0^{+\infty} \frac{\mathrm{d}k}{2\pi^2} k^2 j_0(kx) w_{\mathrm{w}}(k) \tag{18}$$

$$= \frac{1}{4\pi\epsilon_0 x}\left[1 - \frac{2}{\pi}\int_0^{+\infty} \mathrm{d}k \bar{\chi}_{\mathrm{w}}(k)\frac{\sin(kx)}{k}\right]. \tag{19}$$

where j_0 is the first spherical Bessel function. We can check that if $\bar{\chi}_{\mathrm{w}}(k) = 0$, we obtain the unscreened Coulomb potential $\phi_{\mathrm{tot}} = \phi_{\mathrm{ext}}$. Also, if we use the long-wavelength limit of the susceptibility, as is usually the case in continuum electrostatics, we have $\bar{\chi}(k) = \bar{\chi}(k=0) = 1 - 1/\varepsilon_{\mathrm{w}}$, and we obtain

$$\phi_{\mathrm{tot}}(x) = \frac{1}{4\pi\epsilon_0\varepsilon_{\mathrm{w}} x}, \tag{20}$$

that is the long-range Coulomb potential attenuated by the dielectric constant ε_{w}. We keep in mind that :

- the long-wavelength limit – i.e. $k \to 0$ — of non-local electrostatics gives the results of continuum electrostatics.
- for a dielectric system $\varepsilon_{\mathrm{w}}(k \to 0) = \varepsilon_{\mathrm{w}}$.
- the potential of an ion in the dielectric is attenuated by ε_{w} but remains long-range.

1.2.2 *Example 2: Thomas-Fermi screening*

In contrast to dielectrics, metals have mobile charge carriers, free electrons. The simplest Sommerfeld model of a metal assumes free and independent electrons that nevertheless respect Pauli's exclusion principle. The implicit nuclei preserve the charge neutrality. A given number of electrons, half spin-up and, half spin-down so that there is no magnetization, are included in a box of length L. The electrons cannot see each other, like in the perfect gas. Solving Schrödinger's equation

$$-\frac{\hbar^2\nabla^2}{2m}\psi_{\mathbf{k}}(\mathbf{x}) = \epsilon_{\mathbf{k}}\psi_{\mathbf{k}}(\mathbf{x}), \tag{21}$$

where m is the bare electronic mass, gives that eigenfunctions are plane waves $\psi_{\mathbf{k}}(\mathbf{x}) = e^{-i\mathbf{k}\mathbf{x}}/L^{3/2}$ that are quantized with a — labeling index — wavevector $\mathbf{k} = 2\pi/L(n\mathbf{e}_x + m\mathbf{e}_y + l\mathbf{e}_z)$ and energies $\epsilon_{\mathbf{k}} = \frac{\hbar^2k^2}{2m}$. Electrons fill up the eigenstates with the lowest kinetic energy. At zero temperature, for large L, we define the Fermi wavevector k_F such that all states with $|\mathbf{k}| < k_F$ are filled and not the others. The homogeneous density of electrons is therefore equal to

$$n_{\mathrm{e}}^0 = \frac{2}{\mathcal{V}}\sum_{\mathbf{k}}\Theta(k_F - |\mathbf{k}|) = 2\int\frac{\mathrm{d}^3\mathbf{k}}{(2\pi)^3}\Theta(k_F - |\mathbf{k}|) = \frac{k_F^3}{3\pi^2} \tag{22}$$

where Θ is the Heaviside function, and to obtain the last equality, one can refer to the details of Eq. 17. We use the index "e" for the electrons in the metal. A non-zero temperature would smear out the Fermi-Dirac distribution but is irrelevant for now. In the ground state, the chemical potential is constant all over space and indicates the energy of the highest filled electronic state. It is also called the Fermi energy because $\mu = E_F = \frac{\hbar k_F^2}{2m}$ in the absence of external potential. When a external potential is applied, the kinetic Fermi energy E_F plus the (electrostatic) potential energy ϕ_{tot} are equal to the chemical potential:

$$\mu = \frac{\hbar k_F^2}{2m} + \phi_{\mathrm{tot}}(\mathbf{x}) \tag{23}$$

The latter is constant all over space and equal to its value at infinity by continuity and the equilibrium condition. Therefore, if $\phi_{\mathrm{tot}}(\mathbf{x})$ is inhomogeneous, so is the Fermi energy, or the Fermi wavevector $k_F(\mathbf{x})$, or the electronic density $n_{\mathrm{e}}(\mathbf{x})$ according to Eq. 22. Combining Eq. 22 and Eq. 23 , we obtain

$$n_{\mathrm{e}}(\mathbf{x}) = \frac{1}{3\pi^2}\left(\frac{2m}{\hbar^2}\left[\mu - \phi_{\mathrm{tot}}(\mathbf{x})\right]\right)^{3/2} \tag{24}$$

The spatially varying Fermi wavevector is introduced in an ad hoc manner. Nevertheless, this non-linear equation illustrates the self-consistent iterations that one needs to make to solve the problem. Indeed, it is crucial to understand that ϕ_{tot} contains the externally applied potential but also the induced one that depends on n_e. We can look at the linear response using charge separation $n_{\text{ind}} = n_e - n_e^0$. Assuming that the chemical potential far from the perturbation E_F is large compared to ϕ_{tot} — that we do not know *a priori* —, that is $E_F \gg \phi_{\text{tot}}(\mathbf{x})$, we obtain

$$n_{\text{ind}}(\mathbf{x}) \simeq -\frac{3}{2}\frac{n_e^0}{E_F}\phi_{\text{tot}}(\mathbf{x}) \tag{25}$$

Finally, going to reciprocal space and using $\phi_{\text{tot}} = \phi_{\text{ind}} + \phi_{\text{ext}}$ and Eq. 2 — i.e. $\phi_{\text{ind}}(k)\epsilon_0 k^2 = n_{\text{ind}}(k)$, we can obtain an equation where $\phi_{\text{tot}}(k)$ appears on both sides, and that is solved to give

$$\phi_{\text{tot}}(k) = \frac{\phi_{\text{ext}}(k)}{\varepsilon_e(k)}\ ; \quad \varepsilon_e(k) = 1 + \frac{k_{\text{TF}}^2}{k^2}\ ; \quad k_{\text{TF}} = \left(\frac{4k_F}{\pi a_0}\right)^{1/2}\ ; \tag{26}$$

where the $a_0 = \left(m/4\pi\epsilon_0\hbar^2\right)^{-1}$ is the Bohr radius and k_{TF} the TF wavevector. We have obtained the TF dielectric function $\varepsilon_e(k)$ for the free electron gas.

Having the knowledge of the dielectric function in Eq. 26, we can obtain the corresponding response function $\chi_e(k) = -\epsilon_0 k^2\left[1 - 1/\varepsilon_e(k)\right]$ (see Box 1 and 2). We find

$$\chi_e(k) = \frac{\chi_e^{(0)}(k)}{1 - v(k)\chi_e^{(0)}(k)}, \tag{27}$$

where $\chi_e^{(0)}(k) = -\epsilon_0 k_{\text{TF}}^2$. We have met this quantity in Eq. 25 when we related the total potential to the induced charge density in the linear response approximation: $n_{\text{ind}}(k) = \chi_e^{(0)}(k)\phi_{\text{tot}}(k)$. Eq. 27 reveals the self-consistent nature of the problem:

$$\begin{aligned} n_{\text{ind}}(k) &= \chi_e^{(0)}(k)\left[\phi_{\text{ext}}(k) + \phi_{\text{ind}}(k)\right] && (28)\\ &= \left[\chi_e^{(0)}(k) + \chi_e^{(0)}(k)v(k)\chi_e(k)\right]\phi_{\text{ext}}(k) && (29)\\ &= \chi_e(k)\phi_{\text{ext}}(k) && (30) \end{aligned}$$

where we have used $\phi_{\text{ind}}(k) = v(k)n_{\text{ind}}(k) = v(k)\chi_e(k)\phi_{\text{ext}}(k)$. The last equality of Eq. 28 is nothing but Eq. 11 with $v_{\text{inter}} = v$ so that $\chi_e^{(0)}(k) = -\epsilon_0 k_{\text{TF}}^2$ is actually the non-interacting susceptibility in this case. We understand with the Sommerfeld model of free electrons, how the local character of $\chi_e^{(0)}(\mathbf{x}) = -\epsilon_0 k_{\text{TF}}^2\delta(\mathbf{x})$ is implicitly assumed by the introduction of $k_F(\mathbf{x})$ — each point in space is a small electron gas with given Fermi wavevector.

Turning to the computation of the electrostatic potential of point charge, we adopt the diagram used in Eq. 7 for metallic systems such that

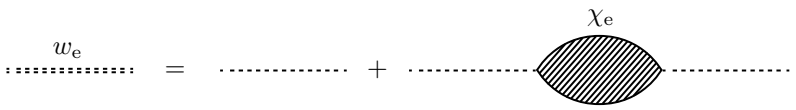

. (31)

Using Eq. 31 and Eq. 17, we can compute the total potential for the metallic system in real space when we place a charge at the origin. It reads

$$\phi_{tot}(x) = \frac{1}{4\pi\epsilon_0 x}\frac{2}{\pi}\int_0^{+\infty} dk \frac{k\sin(kr)}{k^2 + k_{TF}^2} = \frac{1}{4\pi\epsilon_0}\frac{e^{-k_{TF}x}}{x}, \tag{32}$$

where we can check that for $k_{TF} = 0$ (i.e. no electrons), we obtain $\phi_{tot}(x) = \phi_{ext}(x)$. This potential is short-range due to the exponential damping and bears the name of the Yukawa potential. It is the complete analog of the Debye screening in electrolytes. The presence of mobile charges (e.g., electrons in metals) directly impacts the screening effect, which can be traced back to the behavior of $\varepsilon_e(k)$ for $k \to 0$. We keep in mind that:

- for a homogeneous, isotropic metal: $\varepsilon_e(k \to 0) \to +\infty$.
- for a TF screening, $\varepsilon_e(k) = 1 + k_{TF}^2/k^2$.
- the potential of an ion is exponentially damped.

1.2.3 *Example 3: A semi-infinite medium*

As the last example, we now consider a semi-infinite medium (metallic or dielectric) that occupies the half-space $z < 0$ and examine the consequences of the symmetry breaking in one direction on the Green's function of the system w. Looking at the invariances and symmetries of the system, we can work in Fourier space in the plane. In cylindrical coordinates, we use $\mathbf{x} = (\mathbf{r}, z)$ and $\mathbf{k} = (\mathbf{q}, q_z)$. We look for $w(q, z, z')$. We focus on the static case and assume isotropy and homogeneity in translationally invariant interface. From Eq. 14 or Eq. 31, we obtain

$$w(q, z, z') = v(q, z, z') + \iint dz_1 dz_2 v(q, z, z_1)\chi(q, z_1, z_2)v(q, z_2, z') \tag{33}$$

where the two-dimensional Fourier transform of the Coulomb potential reads

$$v(q, z, z') = \frac{e^{-q|z-z'|}}{2\epsilon_0 q}. \tag{34}$$

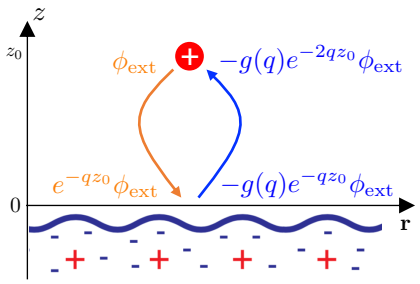

Figure 2: Schematic representation illustrating the role of the surface response function $g(q)$ – here in the case of a metallic medium. A point charge in $z > 0$ exerts an external potential ϕ_{ext} on the medium in the lower-half plane. The latter induces back a potential ϕ_{ind} on the test charge.

We ought to note several important points. First, it is crucial to note that the susceptibility appearing in Eq. 33 is the two-point response function *of the semi-infinite dielectric medium* χ. Therefore, its expression is far from obvious, and it has *a priori* no relation with the susceptibility of the bulk system. Second, because all the elements of the dielectric material are in the half-space $z < 0$, the integration in Eq. 33 is restricted to $z_1, z_2 < 0$. However, this is taken into account in the response function $\chi(q, z_1, z_2) \propto \Theta(-z_1)\Theta(-z_2)$. Finally, if we probe the dielectric material from outside, for example, if we put an external point charge *outside* the material (i.e. $z' > 0$) and we look at the potential ϕ_{tot} from outside the material ($z > 0$), then the sign of the absolute value in Eq. 34 is known, and Eq. 33 reduces to

$$w(q, z, z') = \frac{e^{-q|z-z'|}}{2\epsilon_0 q} - \frac{e^{-q(z+z')}}{2\epsilon_0 q} g(q) \qquad z, z' \geq 0, \tag{35}$$

where we have introduced a dimensionless central quantity that we call the *surface response function (SRF)*, and that reads:

$$g(q) = \frac{-1}{2\epsilon_0 q} \iint \mathrm{d}z_1 \mathrm{d}z_2 e^{q(z_1+z_2)} \chi(q, z_1, z_2). \tag{36}$$

Eq. 35 and Eq. 36 are two complementary definitions of the SRF. The former refers to the phenomenological macroscopic/electrostatic definition, whereas the latter is the link to its microscopic expression. Be it for the conducting or dielectric medium, $g(q)$ acts as a reflecting coefficient for an external potential that arises from a charge density situated outside the medium (see Fig. 2). For instance, for a perfect metal, $g_{\text{e}}(q) = 1$ and Eq. 35 gives the well-known corresponding image-charge potential for a point charge at altitude z_0, that is

$$\phi_{\text{ind}}(r = 0, z_0) = -\frac{1}{4\pi\epsilon_0} \int_0^{+\infty} \mathrm{d}q g_{\text{e}}(q) e^{-2qz_0} = \frac{-1}{4\pi\epsilon_0 (2z_0)}. \tag{37}$$

To focus on the reflection coefficient aspect of $g(q)$, we can also use Eq. 35 to write

$$\phi_{\text{ind}}(q, z = 0, \omega) = -g(q, \omega)\phi_{\text{ext}}(q, z = 0, \omega), \tag{38}$$

where we generalized our results to the dynamical case.

Box 3: We can gain valuable insights by looking at the passage from Eq. 33 to Eq. 35. As long as we look at a semi-infinite medium from the outside, Gauss's law tells us that the electrostatic potential arising from it can be considered to be the one of a charged plate situated at its surface, with the adequate two-dimensional surface charge density.

Let us find the electrostatic limit of the surface response function $g(q \to 0, \omega)$. We have seen that in the long-wavelength continuum limit, the medium in the lower half-space is local and can therefore by described by the dielectric function $\varepsilon(\omega)$. Accordingly, the electrostatic problem can now be formulated as a standard boundary condition problem. In that limit, the constitutive relation of Eq. 264 reduces to $\mathbf{D}(z, \omega) = -\epsilon_0 \varepsilon(\omega) \nabla \phi(z, \omega)$ for $z \leq 0$ — note that $\varepsilon(\omega) = 1$ for $z > 0$. What is the form of the potential ϕ in the entire space? First, the perturbating external charge density in z_0 leads to a total potential in the space $0 \leq z \leq z_0$ that can be read from Eq. 35 using $z' = z_0$. On the other hand, the potential must vanish for $z \to -\infty$ and therefore can be written as $\phi = C_0 e^{qz}/2\epsilon_0 q$ for $z \leq 0$ with C_0 a constant. The electrostatic boundary conditions [33] are the continuity of the potential and displacement field's normal component in the absence of surface charges. It leads to two equations:

$$\phi \quad \text{continuous}: \quad 1 - g(q \to 0, \omega) = C_0; \tag{39}$$

$$D_z \quad \text{continuous}: \quad 1 + g(q \to 0, \omega) = \varepsilon(\omega) C_0. \tag{40}$$

Solving for $g(q \to 0, \omega)$ gives

$$g(q \to 0, \omega) = \frac{\varepsilon(\omega) - 1}{\varepsilon(\omega) + 1}, \tag{41}$$

from which we recover the classical image charge reflection coefficient [33].

2

FORMAL DESCRIPTION

2.1 METAL AND LIQUID RESPECTIVE HAMILTONIANS

We introduce crucial notations to describe interactions between particles. We use the following functional

$$U\left[f_i, g_j\right] = (1 - \frac{\delta_{ij}}{2}) \iint \mathrm{d1d2} f_i(1) v(1,2) g_j(2) \tag{42}$$

where f_i (or g_j) is a scalar or an operator describing the element $i \in \{e, n, w, m\}$[1]. The prefactor with the Kronecker symbol prevents double counting when $i = j$[2]. We write $U_{ij} = U\left[n_i, n_j\right]$. We separate the average charge density $n_i^0 = \langle n_i \rangle$ from the charge density deviation δn_i such that $n_i = n_i^0 + \delta n_i$. Inserting in U_{ij}, it reads

$$U_{ij} = U_i^{\langle j \rangle} + (1 - \delta_{ij}) U_j^{\langle i \rangle} + \delta U_{ij} - U_{ij}^0 \tag{43}$$

where $\delta U_{ij} = U\left[\delta n_i, \delta n_j\right]$, $U_{ij}^0 = U\left[n_i^0, n_j^0\right]$ and $U_i^{\langle j \rangle} = U\left[n_i, n_j^0\right]$. U_{ij}^0 is a constant static term that we remove from now on. On the other hand, $U_i^{\langle j \rangle}$ is the one-particle mean-field potential exerted by j on i whereas δU_{ij} is a two-particle term.

2.1.1 *Metal Hamiltonian $\hat{H}_m$*

We first ignore the liquid part. We use a bosonic operator to depict the nuclear charge density of the ions in the solid $\hat{n}_n(1)$. The creation $\Psi^\dagger(1)$ and annihilation $\Psi(1)$ Fermi fields gives the electronic charge density $\hat{n}_e(1) = \Psi^\dagger(1)\Psi(1)$. We prepare the metallic slab to "welcome" a liquid on its surface. To that end, we show the different ways the polar liquid can couple to the surface: static and dynamic contributions for the nuclei and the electrons. The idea is to express the Hamiltonian of the metal $\hat{H}_m$ as a sum of two

[1] n stands for the nuclei and $m = e + n$ stands for the metal

[2] with the convention of the correct ordering for the fermion fields (creation on the left) such that $\hat{U}\left[\hat{n}_e, \hat{n}_e\right] = \frac{1}{2} \iint \mathrm{d1d2} \Psi^\dagger(1)\Psi^\dagger(2) v(1,2) \Psi(1)\Psi(2)$.

separate but effective Hamiltonians, one for electrons and one for the nuclei. The Hamiltonian of the metal $\hat{H}_\mathrm{m}$ reads

$$\hat{H}_\mathrm{m} = \hat{T}_\mathrm{e} + \hat{T}_\mathrm{n} + \hat{U}_\mathrm{ee} + \hat{U}_\mathrm{nn} + \hat{U}_\mathrm{en} \tag{44}$$

where $\hat{T}_\mathrm{i}$ is the kinetic operator (one particle term) of i. Inserting Eq. 43 in Eq. 44, we obtain

$$\hat{H}_\mathrm{m} = \hat{H}_\mathrm{e}^\mathrm{HF} + \hat{H}_\mathrm{n}^\mathrm{HF} + \delta\hat{U}_\mathrm{ee} + \delta\hat{U}_\mathrm{nn} + \delta\hat{U}_\mathrm{en}. \tag{45}$$

For the electrons, the Hartree-Fock (HF) Hamiltonian $\hat{H}_\mathrm{e}^\mathrm{HF}$ reads

$$\hat{H}_\mathrm{e}^\mathrm{HF} = \hat{H}_\mathrm{e}^{(0)} + \hat{U}_\mathrm{e}^{\langle \mathrm{e}\rangle}\ ; \qquad \hat{H}_\mathrm{e}^{(0)} = \hat{T}_\mathrm{e} + \hat{U}_\mathrm{e}^{\langle \mathrm{n}\rangle}. \tag{46}$$

$\hat{H}_\mathrm{e}^{(0)}$ is the quadratic Hamiltonian that contains the fixed lattice potential. It can be build with a tight-binding model. $\hat{U}_\mathrm{e}^{\langle \mathrm{e}\rangle}$ the Hartree term that depends on n_e^0[3]. $\hat{H}_\mathrm{n}^\mathrm{HF}$ is given by Eq. 46 after the replacement $\mathrm{e} \rightleftarrows \mathrm{n}$.

Eq. 45 does not separate the electronic and nuclei contributions because of $\delta\hat{U}_\mathrm{en}$. Doing so requires an approximation that we have not made so far. The idea is that $\delta\hat{n}_\mathrm{e}$ comes from an external perturbation which arises from $\delta\hat{n}_\mathrm{n}$. We cannot relate both instantaneously, but we know their relationship in average: it is given by linear response theory (see Eq. 1). Combining Eq. 1, Eq. 2 and replacing the average by the instantaneous deviation, we obtain

$$\delta\hat{n}_\mathrm{n}(1) = \iint \mathrm{d2d3}\chi_\mathrm{n}(12)v(23)\delta\hat{n}_\mathrm{e}(3). \tag{47}$$

Inserting Eq. 47 in $\delta\hat{U}_\mathrm{en}$ gives for

$$\delta\hat{U}_\mathrm{ee}^{(\mathrm{n})} = \delta\hat{U}_\mathrm{ee} + \frac{1}{2}\delta\hat{U}_\mathrm{en} = \frac{1}{2}\iint \delta\hat{n}_\mathrm{e}(1)w_\mathrm{n}(1,2)\delta\hat{n}_\mathrm{e}(2), \tag{48}$$

with w_n given by (see also Eq. 4)

$$w_\mathrm{n}(11') = v(11') + \iint \mathrm{d2d3}v(12)\chi_\mathrm{n}(23)v(31'). \tag{49}$$

Eq. 49 gives the Coulomb potential screened by the nuclei. We use the other half of $\delta\hat{U}_\mathrm{en}$ in Eq. 48 to write Eq. 47 with $\mathrm{e} \rightleftarrows \mathrm{n}$. Inserting Eq. 48 and its counterpart for $\mathrm{e} \rightleftarrows \mathrm{n}$ in Eq. 45 reads

$$\hat{H}_\mathrm{m} = \hat{H}_\mathrm{e}^\mathrm{HF} + \hat{H}_\mathrm{n}^\mathrm{HF} + \delta\hat{U}_\mathrm{ee}^{(\mathrm{n})} + \delta\hat{U}_\mathrm{nn}^{(\mathrm{e})}, \tag{50}$$

[3] Standard HF calculations find the solution of the Schrödinger equation self-consistently by inserting the electronic density n_e^0 — reconstructed with the wavefunctions — in $\hat{U}_\mathrm{e}^{\langle \mathrm{e}\rangle}$ at each iteration.

that is now separable. Eq. 50 is not an explicit expression because it contains a time integral (see Eq. 48). As noted in [34], an explicit Hamiltonian can be obtained by using an adiabatic approximation:

$$w_{\mathrm{n}}(12) = \int \frac{\mathrm{d}\omega}{2\pi} e^{-i\omega(t_2-t_1)} w_{\mathrm{n}}(\mathbf{x}_1, \mathbf{x}_2, \omega) \simeq w_{\mathrm{n}}(\mathbf{x}_1, \mathbf{x}_2, \omega = 0)\delta(t_1 - t_2). \quad (51)$$

In contrast to typical solid-state studies where non-adiabatic effects are at the center of the interest, our work, focusing on liquid-metal coupling, welcomes this "intra-metallic" adiabatic approximation. The result is that electrons and nuclei are decoupled, and their interplay with the liquid can be evaluated separately.

2.1.2 *Liquid Hamiltonian H_w*

We now ignore the metallic part. Considering the electronic density of the liquid's molecules is prohibitive. We model them as indiscernible classical rigid objects composed of three-point-like partial charges, and use a classical framework. We consider the classical charge density field of water n_{w}. We write H_{w} as follows:

$$H_{\mathrm{w}} = T_{\mathrm{w}} + K_{\mathrm{w}} + U_{\mathrm{ww}}, \quad (52)$$

where T_{w} is the one-point charge kinetic term and $K_{\mathrm{w}} = C_{\mathrm{w}} + U_{\mathrm{ww}}^{\mathrm{other}}$ contains a constraint term C_{w} that keeps molecules rigid and interparticle interactions $U_{\mathrm{ww}}^{\mathrm{other}}$ that are not Coulombic (e.g. short-range). The definition of $U_{\mathrm{ww}}^{\mathrm{other}}$ can be obtained by replacing v by $v_{\mathrm{w}}^{\mathrm{other}}$ in Eq. 42. Introducing $U_{\mathrm{ww}}^{\mathrm{eff}} = U_{\mathrm{ww}}^{\mathrm{other}} + U_{\mathrm{ww}}$ (i.e. $v \leftrightarrow v_{\mathrm{w}}^{\mathrm{eff}}$ in Eq. 42), we have

$$H_{\mathrm{w}} = H_{\mathrm{w}}^{(0)} + \delta U_{\mathrm{ww}}^{\mathrm{eff}} \quad (53)$$

where $H_{\mathrm{w}}^{(0)} = T_{\mathrm{w}} + C_{\mathrm{w}}$ is the *non-interacting molecular* or *ideal* part of the Hamiltonian. In the absence of an external potential we have used $n_{\mathrm{w}}^0 = 0$. We can rewrite $\delta U_{\mathrm{ww}}^{\mathrm{eff}}$ as

$$\delta U_{\mathrm{ww}}^{\mathrm{eff}} = \frac{1}{2} \iint \mathrm{d}1\mathrm{d}2 \delta n_{\mathrm{w}}(1) v_{\mathrm{w}}^{\mathrm{eff}}(12) \delta n_{\mathrm{w}}(2). \quad (54)$$

We look for an instantaneous interaction $v_{\mathrm{w}}^{\mathrm{eff}}(12) \propto \delta(t_1 - t_2)$ to build $\delta U_{\mathrm{ww}}^{\mathrm{eff}}$.

We suppose that we know how the liquid responds to perturbations. Our strategy is to express $v_{\mathrm{w}}^{\mathrm{eff}}$ with the response function of the liquid. To do so,

we assume that δn_{w} has Gaussian spatial fluctuations. We consider the static case because we look for an instantaneous interaction. H_{w} reads

$$H_{\mathrm{w}} = \frac{1}{2} \iint \mathrm{d}\mathbf{x}_1 \mathrm{d}\mathbf{x}_2 \delta n_{\mathrm{w}}(\mathbf{x}_1) M_{\mathrm{w}}(\mathbf{x}_1, \mathbf{x}_2) \delta n_{\mathrm{w}}(\mathbf{x}_2), \tag{55}$$

where M_{w} is a Gaussian kernel. To find M_{w}, we write the partition function $\mathcal{Z}_{\mathrm{w}}$ where we add a generic external potential ϕ_{ext} (a source term) to generate the moments of δn_{w}. It reads[4]

$$\mathcal{Z}_{\mathrm{w}} = \int \mathcal{D}\left[\delta n_{\mathrm{w}}\right] e^{-\beta H_{\mathrm{w}} - \beta \delta n_{\mathrm{w}} \phi_{\mathrm{ext}}} = \int \mathcal{D}\left[\delta n_{\mathrm{w}}\right] e^{-\frac{1}{2}\beta \delta n_{\mathrm{w}} M_{\mathrm{w}} \delta n_{\mathrm{w}} - \beta \delta n_{\mathrm{w}} \phi_{\mathrm{ext}}}, \tag{56}$$

where $\beta = 1/k_B T$. By functional differentiation of the partition function, we obtain

$$\langle \delta n_{\mathrm{w}}(\mathbf{x}_1) \rangle_0 = \frac{-1}{\mathcal{Z}_{\mathrm{w}}} \left. \frac{\delta \mathcal{Z}_{\mathrm{w}}}{\delta \beta \phi_{\mathrm{ext}}(\mathbf{x}_1)} \right|_{\phi_{\mathrm{ext}}=0} \tag{57}$$

where $\langle . \rangle_0$ therefore means the phase space average in absence of external potential: $\phi_{\mathrm{ext}} = 0$. We also obtain

$$\frac{\delta \langle \delta n_{\mathrm{w}}(\mathbf{x}_1) \rangle}{\delta \phi_{\mathrm{ext}}(\mathbf{x}_2)} = \frac{-1}{\mathcal{Z}_{\mathrm{w}}} \left. \frac{\delta^2 \mathcal{Z}_{\mathrm{w}}}{\delta \beta \phi_{\mathrm{ext}}(\mathbf{x}_1) \delta \phi_{\mathrm{ext}}(\mathbf{x}_2)} \right|_{\phi_{\mathrm{ext}}=0} \tag{58}$$

$$= -\beta \langle \delta n_{\mathrm{w}}(\mathbf{x}_1) \delta n_{\mathrm{w}}(\mathbf{x}_2) \rangle_0 \tag{59}$$

$$= -M_{\mathrm{w}}^{-1}(\mathbf{x}_1, \mathbf{x}_2), \tag{60}$$

where we have used a functional Gaussian integration property in the last step. In the following, we call *static structure factor* the following correlation function:

$$S_{\mathrm{w}}(\mathbf{x}_1, \mathbf{x}_2) = \langle \delta n_{\mathrm{w}}(\mathbf{x}_1) \delta n_{\mathrm{w}}(\mathbf{x}_2) \rangle_0. \tag{61}$$

Using the fluctutation-dissipation theorem [35] (FDT), we have[5] $-\beta S_{\mathrm{w}}(\mathbf{x}_1, \mathbf{x}_2) = \chi_{\mathrm{w}}(\mathbf{x}_1, \mathbf{x}_2, \omega = 0)$. Inserting in Eq. 59 and Eq. 61, we obtain $M_{\mathrm{w}} = -\chi_{\mathrm{w}}^{-1}(\omega = 0)$. Reinserting in Eq. 55 gives

$$H_{\mathrm{w}} = -\frac{1}{2} \iint \mathrm{d}\mathbf{x}_1 \mathrm{d}\mathbf{x}_2 \delta n_{\mathrm{w}}(\mathbf{x}_1) \chi_{\mathrm{w}}^{-1}(\mathbf{x}_1, \mathbf{x}_2, \omega = 0) \delta n_{\mathrm{w}}(\mathbf{x}_2). \tag{62}$$

Integrating Eq. 58, we obtain

$$\langle \delta n_{\mathrm{w}}(\mathbf{x}_1) \rangle = \int \mathrm{d}\mathbf{x}_1 \chi_{\mathrm{w}}(\mathbf{x}_1, \mathbf{x}_2, \omega = 0) \phi_{\mathrm{ext}}(\mathbf{x}_2) \tag{63}$$

and recover the results of linear response theory in Eq. 1 for a static external potential. χ_{w}^{-1} is the inverse response function of the system —

[4] We used in the exponent the notation $\int \mathrm{d}1 f(1) g(1) = fg$ and $\int \mathrm{d}1\mathrm{d}2 h(1) f(12) g(2) = hfg$.
[5] It is discussed in details in the following. One can refer to Eq. 299 for the proof.

$\int \mathrm{d}2\chi_{\mathrm{w}}^{-1}(1,2)\chi_{\mathrm{w}}(2,1') = \delta(1-1')$. Eq. 55 to Eq. 58 are also valid for the ideal part:

$$H_{\mathrm{w}}^{(0)} = -\frac{1}{2}\iint \mathrm{d}\mathbf{x}_1\mathrm{d}\mathbf{x}_2\delta n_{\mathrm{w}}(\mathbf{x}_1)\left[\chi_{\mathrm{w}}^{(0)}\right]^{-1}(\mathbf{x}_1,\mathbf{x}_2,\omega=0)\delta n_{\mathrm{w}}(\mathbf{x}_2), \tag{64}$$

We underline that χ_{w} is the response function of *the liquid slab* and $\chi_{\mathrm{w}}^{(0)}$ is the *ideal* or *non-interacting* response function of the liquid *slab*. Using $\delta U_{\mathrm{ww}}^{\mathrm{eff}} = H_{\mathrm{w}} - H_{\mathrm{w}}^{(0)}$ with Eq. 55 and Eq. 64, we obtain

$$v_{\mathrm{w}}^{\mathrm{eff}}(\mathbf{x}_1,\mathbf{x}_2) = \left[\chi_{\mathrm{w}}^{(0)}\right]^{-1}(\mathbf{x}_1,\mathbf{x}_2,\omega=0) - \chi_{\mathrm{w}}^{-1}(\mathbf{x}_1,\mathbf{x}_2,\omega=0). \tag{65}$$

By inserting Eq. 65 in the mean-field renormalization equation Eq. 12, we find that it is satisfied for $v_{\mathrm{inter}} = v_{\mathrm{w}}^{\mathrm{eff}}$ in the static case. We conclude that $v_{\mathrm{w}}^{\mathrm{eff}}$ is the charge-charge mean-field potential in the liquid. It prompts us to introduce a diagram for the response function of the liquid. We introduce a white ball-and-stick representation for $\chi_{\mathrm{w}}^{(0)}$ and χ_{w}. The mean-field equation Eq. 11, for the case of a water slab alone reads

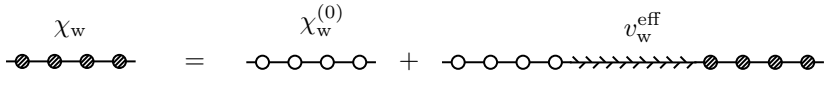

(66)

The link between our expression of H_{w} in Eq. 62 and functionals for polarization of dielectrics, can be found in appendix B.2.

2.2 QUANTUM FIELD DESCRIPTION OF THE LIQUID

2.2.1 *The quantum/classical incompatibility*

We try to assemble both Hamiltonians $\hat{H}_{\mathrm{m}}$ and H_{w}. We write $\hat{H} = \hat{H}_{\mathrm{m}} + H_{\mathrm{w}} + \hat{U}_{\mathrm{wm}}$ using $\hat{n}_{\mathrm{m}} = \hat{n}_{\mathrm{e}} + \hat{n}_{\mathrm{n}}$. Using Eq. 43, we write

$$\hat{H} = \hat{H}_{\mathrm{m}}^{\langle \mathrm{w}\rangle} + H_{\mathrm{w}}^{\langle \mathrm{m}\rangle} + \delta\hat{U}_{\mathrm{wm}}, \tag{67}$$

where $\hat{H}_{\mathrm{m}}^{\langle \mathrm{w}\rangle} = \hat{H}_{\mathrm{m}}^{\mathrm{HF}} + \hat{U}_{\mathrm{m}}^{\langle \mathrm{w}\rangle} + \delta\hat{U}_{\mathrm{ee}}^{(\mathrm{n})} + \delta\hat{U}_{\mathrm{nn}}^{(\mathrm{e})}$ and $H_{\mathrm{w}}^{\langle \mathrm{m}\rangle} = H_{\mathrm{w}} + U_{\mathrm{w}}^{\langle \mathrm{m}\rangle}$ are the Halmiltonians of both subsystems in the presence of the other. With $\hat{H}$ given by Eq. 67, we can evaluate its expectation value and, specifically, the one of $\delta\hat{U}_{\mathrm{wm}}$. Taking either the quantum or classical phase space average, we obtain $\langle\delta\hat{U}_{\mathrm{wm}}\rangle = 0$. Is there something wrong?

A way to answer is to find what we obtain by minimizing $\langle\hat{H}\rangle$ in the quantum and classical phase space alternatively. We find the minimum

average energy of the system in a self-consistent way because evaluating n_{w}^0 requires the first guess for n_{m}^0 to build ϕ_{m}^0, which in turn gives ϕ_{w}^0 to be applied to the metal and so on. However, we do not get the instantaneous energy of the system. Why are the two phase spaces incompatible? One deals with quantum operators and commutators, whereas the second only treats scalars, so they use different algebra. We scratch the surface of questions that theoretical physicists would like to answer regarding the unification of theories that works well on different scales.

What if we arbitrarily choose the quantum phase space? After all, although the classical framework cannot deal with operators, the quantum one accepts classical scalars. We would use δn_{w} as an external potential that acts on the metallic surface, but we would ignore how the liquid respond to the deviation of metallic charge $\delta\hat{n}_{\mathrm{m}}$. Note, however, the subtelty that if a static external potential (say an ion in the liquid) produces $\delta\hat{n}_{\mathrm{m}}$, the liquid would still be blind to it, unless it is incorporated back in n_{m}^0 and follows the self-consistent cycle to minimize $\langle\hat{H}\rangle$. To couple both media (and to go beyond the BOA), both media should "see" each other at once in the same framework.

Is it possible to find a common framework? It may now be clear that the two closed media can only mutually perturb each other using an electrostatic potential. The response function, well-defined in both the quantum and classical framework, processes the latter. Thus, there is no way for one medium to tell if the other needs a quantum or a classical description. Therefore, although the *computation* of the response functions is different for the metallic or liquid part, we must be able to find a common framework to treat this problem. We can take the quantum one to deal with electrons and phonons, but we need to make room for the liquid part, as discussed.

From where do we start? The key observation is that we have the dynamical equation for the metallic part (Schrödinger equation) but not for the liquid part. Indeed, so far, we have imposed the static dielectric response of the liquid thanks to the introduction of an instantaneous effective potential $v_{\mathrm{w}}^{\mathrm{eff}}$. Accordingly, we cannot yet tackle time-dependent external perturbation. The very attractive way to proceed is to generalize Eq. 65 to an arbitrary frequency. After inverse Fourier transform, it reads $v_{\mathrm{w}}^{\mathrm{eff}}(12) \overset{\text{false}}{=} \left[\chi_{\mathrm{w}}^{(0)}\right]^{-1}(12) - \chi_{\mathrm{w}}^{-1}(12)$. However, this would imply using Eq. 58 and 61 that $\chi_{\mathrm{w}}(12) \overset{\text{false}}{=} -\beta S(12)$, which we know to be false because it violates the FDT (i.e. the response function is not the structure factor). We need to find something else.

2.2.2 *A fictitious quantum operator $\hat{n}_w$*

In 1973, Martin, Siggia, and Rose (MSR) formulated classical statistical dynamics in the aspect of interacting quantum fields [36]. This was verified and used since [37, 38, 39]. The underlying complexity of the formulation and the scarce non-linearities in simple liquids might have led the liquid community to ignore such formulation. However, in our case, we describe the liquid by its charge density with Gaussian fluctuations, and the difficulties are greatly reduced. Starting from a generic Hamiltonian of a dielectric material and imposing a dissipative dynamic, we show in appendix B.3 how we can encompass this structure in the form of an out-of-equilibrium quantum field action [40, 41, 42].

We imposed the dynamics, but one can now grasp how this can be generalized to an arbitrarily complex Gaussian dynamics. The key aspect of the derivation is introducing the auxiliary charge density field, as revealed in [36]. The origin of such doubling to mimic quantum field theory can be understood by the lack of commutators and anticommutators in the classical paradigm. They contain information on the response to external perturbations and the amplitude of the fluctuations when considered observables. Also, time ordering appears naturally in all possible correlation functions one can build using them. On the contrary, the classical formulation sweeps up those albeit physical subtleties, and the linear response is given by the Poisson bracket [43], a more complicated formulation of response functions in a way. From now on, response and fluctuation amplitudes are simple correlation functions of the real n_w and auxiliary $\tilde{n}_w$ fields.

Why do past and future distinguished in a non-equilibrium situation? Perturbation theory needs a reference state to compute observables. It is usually the one where the perturbation is turned off. In classical or quantum linear response theory *at equilibrium*, the interactions are switched on and off adiabatically to recover the same initial and final state for $t \to -\infty$ and $t \to +\infty$. This assumption is challenged in a non-equilibrium situation. For instance, for two media in relative motion, if one happens to be centered in $\mathbf{x}(t) = \mathbf{v}t$, it is not at the same place for $t \to -\infty$ and $t \to +\infty$ and the final state differs from the initial one. This subtlety requires to propagate the wavefunctions forward and back in time to reach the same initial and final state. The doubling of the fields stems from this doubling of forward and backward propagation. The reader can refer to [42] for the details.

The observation that results from this derivation is that the central quantities appearing in the partition function are the three response functions: retarded, advanced, and Keldysh. In this framework, a field, be it an operator

or a scalar, is solely represented by its response functions. In return, it means that we can introduce a fictitious bosonic quantum operator $\hat{n}_{\mathrm{w}}$ for the charge density of point charges in the liquid. Its response functions in the quantum framework are defined by the classical ones as follows:

$$\chi^{\mathrm{R}}_{\mathrm{w}}(12) = -\frac{i}{\hbar}\Theta(t_1 - t_2)\left\langle[\hat{n}_{\mathrm{w}}(1)\hat{n}_{\mathrm{w}}(2)]\right\rangle = -\frac{i}{\hbar}\langle n_{\mathrm{w}}(1)\tilde{n}_{\mathrm{w}}(2)\rangle \tag{68}$$

$$\chi^{\mathrm{A}}_{\mathrm{w}}(12) = -\frac{i}{\hbar}\Theta(t_2 - t_1)\left\langle[\hat{n}_{\mathrm{w}}(2)\hat{n}_{\mathrm{w}}(1)]\right\rangle = -\frac{i}{\hbar}\langle \tilde{n}_{\mathrm{w}}(1)n_{\mathrm{w}}(2)\rangle \tag{69}$$

$$\chi^{\mathrm{K}}_{\mathrm{w}}(12) = -\frac{i}{\hbar}\left\langle\{\hat{n}_{\mathrm{w}}(1)\hat{n}_{\mathrm{w}}(2)\}\right\rangle = -\frac{2i}{\hbar}\langle n_{\mathrm{w}}(1)n_{\mathrm{w}}(2)\rangle \tag{70}$$

Therefore, *as long as the classical polar fluid has Gaussian fluctuations, we shall describe it in quantum field theory by a fictitious bosonic operator $\hat{n}_w$ with prescribed response functions.* For a classical system, $\chi^{\mathrm{A}}(12) = \chi^{\mathrm{R}}(21)$ is implicit. This is not case for the quantum correlation function because operators do not commute. To keep the anticommutator's structure of the Keldysh correlation function, the structure factor is multiplied by two: $\chi^{\mathrm{K}}_{\mathrm{w}}(12) = -\frac{2i}{\hbar}S_{\mathrm{w}}(12)$[6]. For the homogeneous, isotropic and infinite system, at equilibrium, the FDT is now given by

$$\chi^{\mathrm{R}}(k,\omega) - \chi^{\mathrm{A}}(k,\omega) = \tanh\left(\frac{\hbar\omega}{2k_BT}\right)\chi^{\mathrm{K}}(k,\omega) \tag{71}$$

from which we recover $\mathrm{Im}\chi(k,\omega) = -\frac{\omega}{2k_BT}S(k,\omega)$ in the classical limit of the FDT — i.e. $\hbar \to 0$. Recall that the response function we have encountered so far is $\chi^{\mathrm{R}} = \chi$ — as obtained in appendix B.3. The consequence of Eq. 71 is that, at equilibrium, the three response functions are linked and that the knowledge of χ^{R} — note that $\chi^{\mathrm{A}}(\omega)^* = \chi^{\mathrm{R}}(\omega)$ — is enough to describe the entire system. For future reference, following [44], we shall also rotate by $\pi/4$ the matrix that gathers the response functions. It reads[7]

$$\mathcal{X} = L\mathcal{X}_{-\pi/4}L^\dagger = \begin{pmatrix} \chi^{\mathrm{R}} & \chi^{\mathrm{K}} \\ 0 & \chi^{\mathrm{A}} \end{pmatrix}. \tag{72}$$

This simple operation makes the diagrams very useful for an out-of-equilibrium situation too. Indeed, at the beginning of this part, we defined the diagrammatic link between scalar functions f and g to be $[f * g](1) = \int \mathrm{d}2 f(12)g(2)$, at equilibrium (see Eq. 7). For an out-of-equilibrium situation, f and g can be matrices, say $\mathcal{F}$ and $\mathcal{G}$ (such as defined in Eq. 72). We extend this definition by stating that the diagrammatic link requires a matrix multiplication in

[6] assuming $n^0_{\mathrm{w}} = 0$.

[7] We use $L = \frac{1}{\sqrt{2}}\begin{pmatrix} 1 & -1 \\ 1 & 1 \end{pmatrix}$ and $\mathcal{X}_{-\pi/4}$ is defined in appendix B.3.

this matrix space. For instance, $[\mathcal{F} * \mathcal{G}](1) = \int \mathrm{d}2\mathcal{F}(12) \cdot \mathcal{G}(2)$ has a matrix structure with

$$\begin{aligned}[\mathcal{F} * \mathcal{G}]^{\mathrm{R/A}}(1) &= \int \mathrm{d}2 f^{\mathrm{R/A}}(12) g^{\mathrm{R/A}}(2) \\ [\mathcal{F} * \mathcal{G}]^{\mathrm{K}}(1) &= \int \mathrm{d}2 \left(f^{\mathrm{R}}(12) g^{\mathrm{K}}(2) + f^{\mathrm{K}}(12) g^{\mathrm{A}}(2) \right). \end{aligned} \tag{73}$$

We refer to [42] for the proof of this statement. We can check from Eq. 73 that if $\mathcal{F}$ and $\mathcal{G}$ follow the FDT, then $\mathcal{F} * \mathcal{G}$ does too. We keep in mind that an element i can be represented by its response function $\mathcal{X}_\mathrm{i}$ and that, at equilibrium, the matrix structure $\mathcal{X}_\mathrm{i}$ can be reduced to the scalar $\chi_\mathrm{i} = \chi_\mathrm{i}^\mathrm{R}$ function.

2.3 OUR FRAMEWORK

2.3.1 *Vacuum gap*

In this section, we discuss the microscopic physical/chemical details of the metal/liquid interface. If the frontiers orbitals of the two media are energetically separated, the effective electron-electron interactions between liquid molecules and metal's electrons are merely governed by the Pauli exclusion principle. This short-range repulsion force prevents electronic clouds from overlapping. Fig. 3a shows the drastic decrease of the plane-averaged electronic density at the interface between the graphene and water — for one snapshot taken randomly at equilibrium from an ab initio molecular dynamics (AIMD)[8]. It prompts us to model the interface as two separated closed systems, thus neglecting charge transfer[9]. Quantum chemistry calculations, showing no band mixing when a single water molecule is adsorbed on graphene, support this hypothesis [45, 23].

We model the drastic decrease in electronic density between the two media by a vacuum gap of thickness $d \sim 1$Å (see inset of Fig. 3a). If we describe both media so well that we recover the exact shape of the charge densities that vanish on an impenetrable plane, we will use $d = 0$ Å. Otherwise, if we resort to a simplified version of the charge density profiles, we will adjust the thickness $d > 0$ to model this effective vacuum gap (see Fig. 3b). From an electrostatic perspective, this gap model the low dielectric region between both media due to the absence of charges. The consideration of this impenetrable plane is crucial in our microscopic description of the

[8] see methods in appendix B.1

[9] This hypothesis may need to be challenged depending on the nature of the metal/liquid interface.

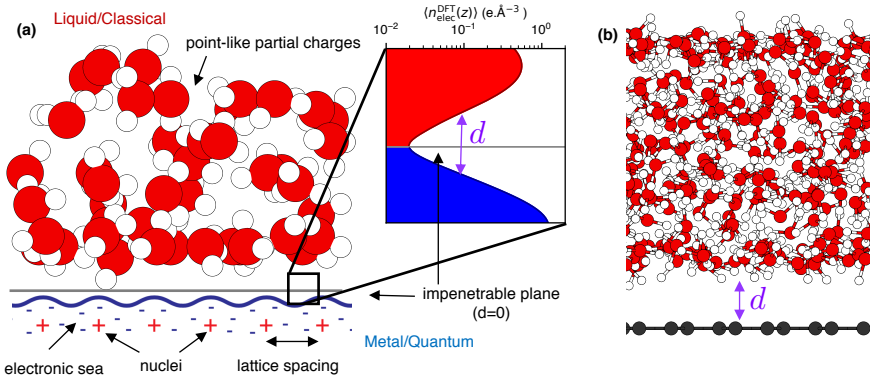

Figure 3: Schematic drawing of the metal/liquid interface. **(a)** From a quantum perspective, the zoom shows the electronic density near the interface between graphene and water. It is obtained with a static DFT calculation on a snapshot taken randomly at equilibrium. We fix an altitude for the impenetrable plane ($d = 0$). **(b)** From a classical or practical modeling perspective, a vacuum gap $d > 0$ is introduced. The image is a snapshot from an interfacial MM simulation.

dielectric. A liquid molecule should never not be cut in two by this plane[10] — see more details in Appendix B.2.

Our description is limited to scales larger than the lattice spacing near the interface. From a purely practical point of view, due to the discrete lattice structure of the solid, one cannot describe small scales without introducing specificities due to lattices. It means adding local-field effects that burden the mathematical description. The rigorous criteria on in-plane wavevectors would be $q \ll 2\pi/a$, with a the lattice spacing. The introduction of the vacuum gap d relaxes this restriction because it cuts off the electrostatic interactions between the solid and the liquid at wavevectors $q \simeq 1/d$.

2.3.2 *Hamiltonian of the interface*

Turning back to the Hamiltonian in Eq. 67, we now replace $n_{\rm w}$ by $\hat{n}_{\rm w}$ and rearrange the terms to prepare many-body perturbation theory. The Hamiltonian of the system $\hat{H} = \hat{H}_0 + \hat{H}_{\rm int}$ can always be decomposed in a quadratic part $\hat{H}_0$ and and interaction part $\hat{H}_{\rm int}$ such that we will note $\langle \mathcal{O} \rangle = {\rm Tr}(e^{-\beta \hat{H}} \mathcal{O})$ the expectation value of an operator $\mathcal{O}$ and $\langle . \rangle_0 = {\rm Tr}(e^{-\beta \hat{H}_0} .)$.

We do not to study the role of nuclei (phonons), because they are *a priori* well-descibed by AIMD or MM. We left the study of their non-negligeable role for future work and merely consider the frozen lattice. With $\delta n_{\rm n} = 0$, we obtain $\chi_{\rm n} = 0$ and $w_{\rm n} = v$. Using Eq. 67, we obtain $\hat{H}_0 = \hat{H}_{0{\rm e}}^{\langle {\rm w} \rangle} + \hat{H}_{0{\rm w}}^{\langle {\rm m} \rangle}$, with

$$\hat{H}_{0{\rm e}}^{\langle {\rm w} \rangle} = \hat{T}_{\rm e} + \hat{U}_{\rm e}^{\langle {\rm n} \rangle} + \hat{U}_{\rm e}^{\langle {\rm w} \rangle} \qquad \hat{H}_{0{\rm w}}^{\langle {\rm m} \rangle} = \hat{H}_{\rm w}^{(0)} + \hat{U}_{\rm w}^{\langle {\rm m} \rangle}. \tag{74}$$

[10] In a bulk MD simulation, periodic boundary conditions lead to surface charges at the edge of a simulation box because some molecules are cut in two at each time step. Here, we put a hard wall at a some altitude. We call it the impenetrable plane because it acts also on the electrons.

We underline the presence of $\hat{U}_e^{\langle w \rangle}$ and $\hat{U}_w^{\langle m \rangle}$ in the quadratic Hamiltonians. They point to the necessity to make recursive static calculations to obtain n_w^0 and n_e^0. The non quadratric terms are gathered in $\hat{H}_{int}$ and read:

$$\hat{H}_{int} = \hat{U}_e^{\langle e \rangle} + \delta\hat{U}_{ee} + \delta\hat{U}_{ww}^{eff} + \delta\hat{U}_{we}. \tag{75}$$

$\hat{U}_e^{\langle e \rangle}$ is the one-particle Hartree term that requires self-energy calculations to evaluate the exchange-correlation contribution (see chapter 7). The remaining two-particles operators have been clearly identified.

2.3.3 *Some practical rules*

In this part i, we gathered the physical concepts and the mathematical tools to tackle the electrostatic interactions at interfaces following standard diagrammatics. In a nutshell, our approach hijacks the electron-phonon problem in quantum field theory to address metal/liquid interfaces.

We have laid out a systematic way of addressing the problem that we shall adopt and summarize it here, for two elements, "i" and "j" — that can be electrons (e) or liquid molecules (w). Chapter 2 prompts us to:

- Minimize self-consistently $\hat{H}_{0i}^{\langle j \rangle}$ and $\hat{H}_{0j}^{\langle i \rangle}$ and obtain n_i^0 and n_j^0.
- Fill the matrices $\mathcal{X}_i^{(0)}$ and $\mathcal{X}_j^{(0)}$ with the adequate response functions computed with respect to $\hat{H}_{0i}^{\langle j \rangle}$ and $\hat{H}_{0j}^{\langle i \rangle}$. Only $\chi_{i/j} = \chi_{i/j}^R$ is needed at equilibrium.

This work will be done in the next part ii for water and graphene/few-layers graphene. We now state how to assemble the response functions to find practical observables. In chapter 1, we have guessed that

- For a response function $\mathcal{X}_{ij} \equiv [\![\hat{n}_i \hat{n}_j]\!]$[11]: draw all possible *linked* diagrams with $\mathcal{X}_i^{(0)}$ and $\mathcal{X}_j^{(0)}$ that start with $\mathcal{X}_i^{(0)}$ and end with $\mathcal{X}_j^{(0)}$. The nature of links are given by the potential between "i" and "j" in $\hat{H}_{int}$.
- For the screened Coulomb potential w: draw all possible *linked* diagrams with $\mathcal{X}_i^{(0)}$ and $\mathcal{X}_j^{(0)}$ that start and end with a Coulomb leg v. The nature of links are given by the potential between "i" and "j" in $\hat{H}_{int}$.

To present the results in a physically transparent way:

- Organize the diagrams to make *renormalized* response functions appear — see e.g. Eq. 114

[11] a short notation for the Keldysh matrix such as the one of Eq. 72. If i=j this is $\mathcal{X}_i$

- Write down the equation by reading the diagrams; a link is defined by the operation $*$.

Several observables are derived in part iii. For now, we build the response functions of water and graphene/FLG.

Part II

MODELING WATER AND GRAPHENE

In this part, we aim to construct the response function of water and graphene — and few-layers graphene (FLG) — at interfaces. We look for the retarded response function $\chi(q, z, z', \omega) = \chi^{\mathrm{R}}(q, z, z', \omega)$. Regarding water, we introduce two original approaches that can be generalized for other dielectric media. We first obtain the dynamic SRF $g_{\mathrm{w}}(q, \omega)$ by carrying MD simulations. We then construct a microscopic model for the static response function of a water slab $\chi_{\mathrm{w}}(q, z, z')$. For FLG, we progress from a tight-binding (TB) model exploring the advantages of Wannier functions. We follow a strategy developed during the rising era of computers [46] to obtain the complete response function $\chi_{\mathrm{e}}(q, z, z', \omega)$ of FLG. We restrain, in this case, our discussion to the SRF $g_{\mathrm{e}}(q, \omega)$.

3

INSIGHTS FROM MM SIMULATIONS

All simulations were carried out using the LAMMPS software [47]. We used the SPC/E water model [48] with the SHAKE algorithm [49, 50]. The simulations were carried out in the canonical (NVT) ensemble, with a stochastic CSVR thermostat [51] with time constant 1 ps maintaining a temperature $T = 298.15$ K. We used a timestep of 2 fs, and atomic positions were written out every 4 fs. Electrostatic interactions were calculated with a particle-mesh Ewald summation with a Coulomb cutoff of 1.4 nm.

3.1 BULK SIMULATION

3.1.1 *Methods*

The bulk simulation uses $N = 8000$ water molecules. The volume of the simulation box is adjusted in the NPT ensemble to yield a mass density $\rho = 0.99715\ \mathrm{g \cdot cm^{-3}}$. The resulting volume is $\mathcal{V} = (64.145)^3 \text{Å}^3$. The simulation is equilibrated in the NVT ensemble for 200 ps, and the subsequent 20 ns are used for analysis.

The simulation is split into $N_\mathrm{s} = 20$ pieces of length $\Delta t = 1$ns, and the results obtained from each of the pieces are averaged to obtain the final result. The accessible frequencies are thus from 1 GHz to 62.5 THz. At every sampled time t, we compute the Fourier-transformed water charge density $n_\mathrm{w}(\mathbf{k}, t) = \sum_i c_i e^{-i\mathbf{k}\mathbf{x}_i(t)}$, with the index i running over all the charged sites of the SPC/E water molecules, and c_i the corresponding partial charge. We define the dynamic charge structure factor according to

$$S_\mathrm{w}(\mathbf{k}, \omega) = \frac{1}{\mathcal{V}} \int_{-\infty}^{+\infty} \mathrm{d}t \langle n_\mathrm{w}(\mathbf{k}, t) n_\mathrm{w}(-\mathbf{k}, 0) \rangle e^{-i\omega t}, \tag{76}$$

where $\mathcal{V}$ is the volume of the simulation box. Then, the classical FDT gives the susceptibility $\bar{\chi}$ in the classical limit[1]:

$$\mathrm{Im}\,\bar{\chi}_{\mathrm{w}}(\mathbf{k},\omega) = \frac{1}{\epsilon_0 k^2}\frac{\omega}{2k_{\mathrm{B}}T}S_{\mathrm{w}}(\mathbf{k},\omega). \tag{77}$$

The susceptibility is related to the dielectric permittivity according to $\bar{\chi}_{\mathrm{w}}(\mathbf{k},\omega) = 1 - 1/\varepsilon_{\mathrm{w}}(\mathbf{k},\omega)$. We therefore require also the real part of the susceptibility, which can be determined through a Kramers-Krönig relation (see Eq. 298) that reads

$$\mathrm{Re}\bar{\chi}_{\mathrm{w}}(\mathbf{k},\omega) = \mathcal{P}\int_{-\infty}^{+\infty}\frac{\mathrm{d}\omega'}{\pi}\frac{\mathrm{Im}\bar{\chi}_{\mathrm{w}}(\mathbf{k},\omega')}{\omega'-\omega}, \tag{78}$$

where $\mathcal{P}$ indicates that the principal part of the integral is taken. In practice, the structure factor in Eq. 76 is computed from the simulation data by making use of the Wiener-Khinchin theorem. The resulting spectra is convoluted with a Gaussian filter of half-width 50 GHz. This allows for some smoothing of the spectra, while not affecting their low-energy region, since the spectra are constant below 200 GHz. Then, spherical averaging is performed over the quantity $|\delta n_{\mathrm{w}}(\mathbf{k},\omega)|^2/k^2$. This gives

$$\mathrm{Im}\bar{\chi}_{\mathrm{w}}(k,\omega) = \frac{1}{\epsilon_0\mathcal{V}}\frac{\omega}{2k_BT}\frac{1}{\Delta t N_{\mathrm{samples}}}\sum_{\substack{\mathbf{k}'\\ k\le|\mathbf{k}'|<k+dk}}^{N_{\mathrm{samples}}}\frac{|\delta n_{\mathrm{w}}(\mathbf{k}',\omega)|^2}{|\mathbf{k}'|^2}. \tag{79}$$

Warning: the definition and relevance of $\bar{\chi}^{\infty}_{w}(q)$ becomes clear only in part iii. One can skip the following paragraph if read for the first time. The results of Fig. 21a show the computation of the integral in Eq. 141. We show how it can be computed using MD simulations. The idea is to realize that $\bar{\chi}^{\infty}_{\mathrm{w}}(q)$ can be expressed as follows:

$$\bar{\chi}^{\infty}_{\mathrm{w}}(q) = \frac{-1}{2\epsilon_0 q}\iint_{-\infty}^{+\infty}\mathrm{d}z_1\mathrm{d}z_2\chi^{\infty}_{\mathrm{w}}(q,z_1,z_2)e^{-q(|z_1|+|z_2|)}. \tag{80}$$

Following the FDT, we compute $\bar{\chi}^{\infty}_{\mathrm{w}}(q) = -\beta S^{\infty}_{\mathrm{w}}(q)$, in the bulk simulation, where $S^{\infty}_{\mathrm{w}}(q) = \frac{1}{\mathcal{A}}\left\langle|n^{\infty}_{\mathrm{w}}(\mathbf{q})|^2\right\rangle$. Here, $n^{\infty}_{\mathrm{w}}(\mathbf{q}) = \sum_i c_i e^{-i\mathbf{q}\mathbf{r}_i}e^{-q|z_i|}$ according to Eq 80. The origin of the vertical axis is unimportant due to the periodic boundary conditions.

[1] The discussion whether it is technically appropriate for water that has modes with frequecies larger than $k_BT/\hbar$ can be found in [52]. In fact, using the quantum FDT would require to dissymetrize the structure factor that is time-reversible $S_{\mathrm{w}}(\mathbf{k},\omega) = S_{\mathrm{w}}(\mathbf{k},-\omega)$ by definition of the use of MD. We ignore this correction and fully assume the "classical" limits of MM. We can expect the contribution from the high frequencies peaks to be slightly overestimated by a factor of $(\beta\hbar\omega/2)/\tanh(\beta\hbar\omega/2)$.

3.1.2 *Results*

The dispersion for the SPC/E water model is known [52], and we only report the long-wavelength limit of the relevant response functions in Fig. 4. Regarding the imaginary parts of $\bar{\chi}_{\mathrm{w}}(\omega)$ and $\varepsilon_{\mathrm{w}}(\omega)$ (respectively blue and green in Fig. 4a), they both exhibit in the low-frequency region $\omega < k_B T/\hbar$ a Debye relaxation peak. Despite historical controversies [53], Debye relaxation in water involves translational and rotational modes of single molecules and collective long-range dipole-dipole interactions. For a relaxation timescale of τ_{D} in $\varepsilon_{\mathrm{w}}(\omega)$, the one of $\bar{\chi}_{\mathrm{w}}(\omega)$ is roughly $\varepsilon_{\mathrm{w}} = 71$ — the dielectric constant of SPC/E water – times shorter. Indeed, using $\varepsilon_{\mathrm{w}}(\omega) = 1 + \frac{\varepsilon_{\mathrm{w}}-1}{1-i\omega\tau_{\mathrm{D}}} = \frac{\varepsilon_{\mathrm{w}}-i\omega\tau_{\mathrm{D}}}{1-i\omega\tau_{\mathrm{D}}}$, we see that the imaginary pole of $\varepsilon_{\mathrm{w}}(\omega)$ is at $1/\tau_{\mathrm{D}}$ and the one of $1/\varepsilon_{\mathrm{w}}(\omega)$ is at $\varepsilon_{\mathrm{w}}/\tau_{\mathrm{D}}$. At interfaces, a relevant response function is the long-wavelength limit of the SRF of the semi-infinite water medium, that is $g_{\mathrm{w}}(\omega)$. Using the same Debye model, we find that the imaginary pole is at $(\varepsilon_{\mathrm{w}}+1)/2\tau_{\mathrm{D}}$. This is confirmed by Fig. 4a — see orange curve.

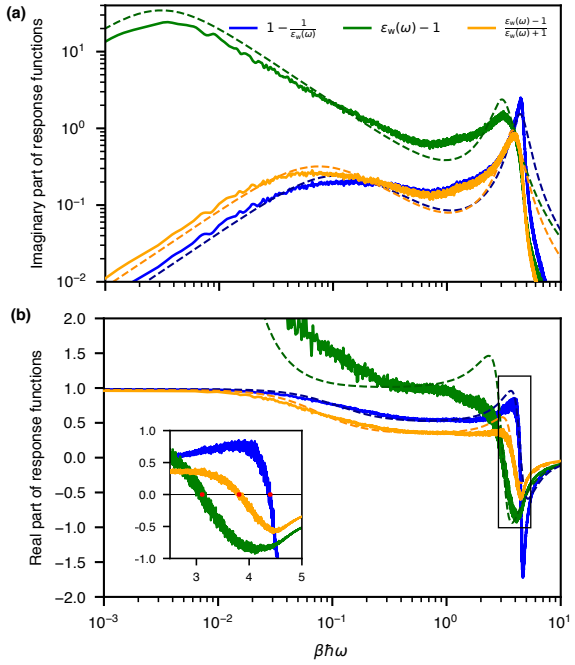

Figure 4: Dynamical response functions of water (SPC/E) in the long-wavelength limit. The dashed lines stems form the model introduced in Eq. 81. Imaginary **(a)** and real part **(b)** (and zoom in the inset). We use $\bar{\chi}_{\mathrm{w}}(\omega) = \bar{\chi}_{\mathrm{w}}(k \to 0, \omega) = 1 - 1/\varepsilon_{\mathrm{w}}(\omega)$ and $g_{\mathrm{w}}(\omega) = g_{\mathrm{w}}(q \to 0, \omega) = \frac{\varepsilon_{\mathrm{w}}(\omega)-1}{\varepsilon_{\mathrm{w}}(\omega)+1}$.

In the high frequency region, we find that $\bar{\chi}_{\mathrm{w}}(\omega)$ and $\varepsilon_{\mathrm{w}}(\omega)$ also exhibit a resonnance. The resonnant frequencies — we note ω_{T} the one of $\varepsilon_{\mathrm{w}}(\omega)$ ("T" for transverse) and ω_{L} for the one of $\bar{\chi}_{\mathrm{w}}(\omega)$ ("L" for longitudinal) — are close, but not exactly the same. It is an important detail of water dynamics

because the difference in the transverse and longitudinal resonances, called the LO-TO splitting, is a characteristic of polar solids [54]. We prefer a more continuous interpretation of the solid/liquid transition that do not resort to solid-state tools. The relatively low ($\gamma < \omega_T/2$) damping coefficient γ of the oscillator at frequency ω_T confers to the libration peak of water a relatively long (few oscillations before being damped) lifetime. It is a phonon-like characteristic, usually imposed by the crystal lattice in solids ($\gamma \to 0$). In water, this originates from the cage-like structure of the tetrahedric hydrogen bond structure.

Using a damped harmonic oscillator model is not possible to account for the observed ratio of $\omega_L$of ω_T because the crucial Debye peak, that is responsible for the high dielectric constant of water, cannot be ignored. However, using a reformulated expression [55] of the dielectric function $\varepsilon_w(\omega) = \frac{\omega_L^2-\omega^2-i0^+\omega}{\omega_T^2-\omega^2-i0^+\omega}$ of a damped harmonic oscillator, we can infer ω_L using our data and check the consistency with the pole obtained at the surface. After some straighforward algebra, we expect the pole of $g_w(\omega)$ at $\omega_S = \sqrt{\frac{\omega_L^2+\omega_T^2}{2}}$. To insert quantitative values, we refer to the real part of the response functions in Fig. 4b. The maxima of the imaginary parts are the zero of the real parts from which we can read $\beta\hbar\omega_T = 3.11$ and $\beta\hbar\omega_L = 4.4$ (see the two extreme red dots in the inset of Fig. 4b). We obtain $\beta\hbar\omega_S = 3.81$ that we report by another red dot (the middle one) in the inset of Fig. 4b. It quantitatively matches the intersection of the orange curve with the horizontal axis and attests to our model's relevance.

Those two accurate but separate models tackling the low and high-frequency regions prompt us to introduce a common one. We find a compact expression with the three parameters γ, ω_T, and τ_D (see Table 1) that can reproduce nearly quantitatively all spectra. It reads:

$$\varepsilon_w(\omega) = 1 + \frac{\varepsilon_w - 2}{1 - i\omega\tau_D} + \frac{\omega_T^2}{\omega_T^2 - \omega^2 - i\gamma\omega}. \tag{81}$$

We report the model with dashed lines in Fig. 4, for the three response functions. The region near $\beta\hbar\omega \simeq 1$ is the less accurately described, but this is also the case in MM due to the use of a non-polarizable force field [54].

	$1/\tau_D$	ω_T	γ
$k_BT/\hbar$	3.11×10^{-3}	3.11	1.36

Table 1: Parameters of the water dielectric function of SPC/E water $\varepsilon_w(\omega)$.

3.2 INTERFACE SIMULATIONS

3.2.1 *Methods*

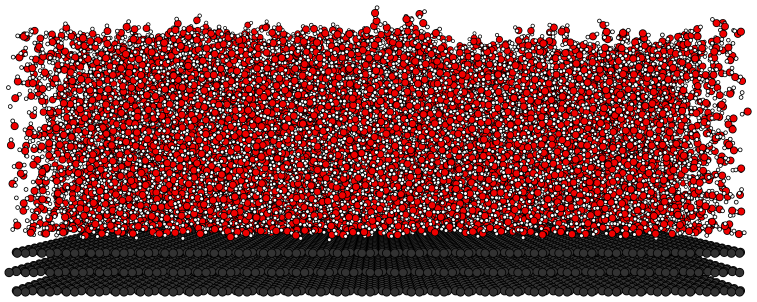

Figure 5: Snapshots of the interface simulation. The surface area is 128.316 × 123.490 Å^2 and the number of water molecules is $N = 20200$.

The interface simulation is carried out with $N = 20200$ water molecules. The solid surface consists of three graphene layers (with ABA stacking), with surface area 128.316 × 123.490 Å^2, and the simulation box height was 6.5 nm. The positions of the carbon atoms are frozen. The direction normal to the surface was aperiodic, and spurious slab-slab interactions are removed. A reflective wall is placed close to the top edge of the box to prevent gaseous water molecules from crossing the top boundary. We use two sets of Lennard-Jones (LJ) parameters for the water-carbon interaction, to which we refer to as "Werder" and "Aluru", listed in Table 2. We exhibit the results for the Aluru force field because it is based on first-principle calculations. The simulation is equilibrated in the NVT ensemble for 200 ps, and the subsequent 6 ns are used for analysis.

Name	ϵ_{CO} (kcal/mol)	σ_{CO} (Å)	ϵ_{CH} (kcal/mol)	σ_{CH} (Å)
Werder [56]	0.0937	3.19	-	-
Aluru [57]	0.0850	3.436	0.0383	2.69

Table 2: Lennard-Jones force-field parameters for the carbon-water interaction.

The simulation is split into $N_s = 60$ pieces of length $\Delta t = 0.1$ ns, and the results from each of the pieces are then averaged. The accessible frequencies

are from 10 GHz to 62.5 THz. At every sampled time t, we computed the Fourier-Laplace transform of the water charge density

$$n_{\mathrm{w}}^{\mathrm{s}}(\mathbf{q},t) = \sum_i c_i e^{-i\mathbf{q}\mathbf{r}_i(t)} e^{-qz_i}, \tag{82}$$

with the index i running over all the charged sites of the SPC/E water molecules, and c_i the corresponding charge. According to Eq. 36, the dynamic surface charge structure factor reads

$$S_{\mathrm{w}}^{\mathrm{s}}(\mathbf{q},\omega) = \frac{1}{\mathcal{A}} \int_{-\infty}^{+\infty} \mathrm{d}t \langle \delta n_{\mathrm{w}}^{\mathrm{s}}(\mathbf{q},t) \delta n_{\mathrm{w}}^{\mathrm{s}}(-\mathbf{q},0) \rangle e^{-i\omega t}, \tag{83}$$

with $\mathcal{A}$ the surface area, and $\delta n_{\mathrm{w}}^{\mathrm{s}} = n_{\mathrm{w}}^{\mathrm{s}} - \langle n_{\mathrm{w}}^{\mathrm{s}} \rangle$. Note that including $\langle n_{\mathrm{w}}^{\mathrm{s}} \rangle$ does not change the computed quantity. We then obtain the imaginary part of the SRF with the classical FDT:

$$\mathrm{Im} g_{\mathrm{w}}(\mathbf{q},\omega) = \frac{1}{2\epsilon_0 q} \frac{\omega}{2k_{\mathrm{B}}T} S_{\mathrm{w}}^{\mathrm{s}}(\mathbf{q},\omega), \tag{84}$$

In practice, the structure factor in Eq. (83) is computed from the simulation data by making use of the Wiener-Khinchin theorem. The resulting spectra are convoluted with a Gaussian filter of half-width 50 GHz. Then, radial averaging is performed over the quantity $|n_{\mathrm{w}}^{\mathrm{s}}(\mathbf{q},\omega)|^2/q$.

3.2.2 *Results for ϕ_w^0*

The mean charge density profile $n_{\mathrm{w}}^0(z) = n_{\mathrm{w}}^0(q \to 0, z)$ is computed to obtain $\phi_{\mathrm{w}}^0(z)$. Recall that we need to include it in $\hat{H}_{\mathrm{e}}^{(0)}$ — to find graphene's electronic states. By successive integrations of Poisson's equation in one dimension, we get:

$$\phi_{\mathrm{w}}^0(z) = -\epsilon_0^{-1} \int_0^z \mathrm{d}z_1 \int_0^{z_1} \mathrm{d}z_2 n_{\mathrm{w}}^0(z_2). \tag{85}$$

Also, note that the normal polarization density reads $P_\perp^0(z) = -\int_0^z \mathrm{d}z' n_{\mathrm{w}}^0(z')$. The results are shown in Fig. 6. Due to the mean charge density's inhomogeneity (see Fig. 6a), $\phi_{\mathrm{w}}^0(z) \neq 0$. The mean static electric field in Fig. 6b reaches ± 1 V. nm^{-1} near the surface, which agrees with the value experimentally probed for water above graphene, using electrostatic force microscopy [58]. Fig. 6c gives several essential insights into $\phi_{\mathrm{w}}^0(z)$.

First, $\phi_{\mathrm{w}}^0(z) = 0$ for z outside the water medium. It stems from the charge neutrality of water. Indeed, the dipole layering of water can be schematically modeled by three or four infinite charged plates whose surface

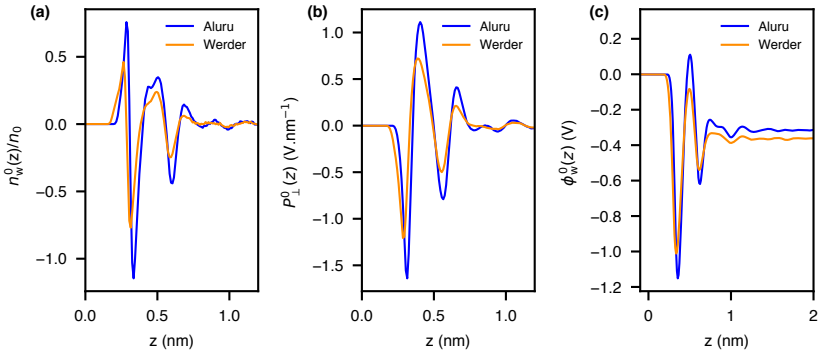

Figure 6: Mean charge density **(a)**, polarization **(b)** and electrostatic potential **(c)** at graphene-water interface for the SPC/E model.

charge adds up to zero. The electric field and electrostatic potential seen outside this charged plate system is zero using Gauss's law. Therefore, while $n_w^0 \neq 0$ is due to $\hat{U}_w^{\langle m \rangle} \neq 0$ because of the LJ interactions, we can write $\hat{U}_e^{\langle w \rangle} = 0$. Equivalently, graphene cannot be doped (a shift in the free charge concentration) by the mere presence of unsalted water. Finally, we conclude that the recursive static calculations required by Eq. 74 can be restricted to the first step: n_m^0 gives ϕ_m^0, which gives n_w^0.

Second, the value of $\phi_w^0(z \to \infty) = -0.3\text{V}$ and minimum $\min_z \phi_w^0 \simeq -1\text{V}$ (Aluru) puts into perspective the hypothesis in [59] asserting that the water makes graphene metallic. The authors support that the nearly free electron band at the Γ point of graphene's Brillouin zone is pushed down to the Fermi level, assuming $\phi_w^0(z \to \infty) = -9\text{V}$. Our results show that it seems largely overestimated at room temperature. We can neglect the σ band of graphene at the Γ point and reaffirm the validity of the closed system hypothesis. For lower temperature, an ice-like structure of oriented dipoles could however produce this high potential [45].

Last, $\phi_w^0(z)$ is the electrostatic potential felt by a point charge at the interface if the relatively homogeneous water structure is not disturbed. It is not a realistic point of view because water rearranges around an ion and therefore does not apply $\phi_w^0(z)$. In fact, we need to consider the electrostatic potential at the center of a LJ cavity. It has been computed here [60], for graphene. The mean average potential variations are of the order of the thermal energy with the distance to the surface due to the compensating orientations of the water molecules surrounding the ion. To a first approximation, it can be neglected. However, it is a source of charge asymmetry (anion/cation) at the interface.

3.2.3 *Results for $g_w(q)$*

In this paragraph, we aim to identify the static SRF of water — i.e. $g_{\mathrm{w}}(q)$ — at the graphene interface. The computation of $S^{\mathrm{s}}_{\mathrm{w}}$ depends on the origin along the vertical axis, which we take to be the one of the top graphene layer.

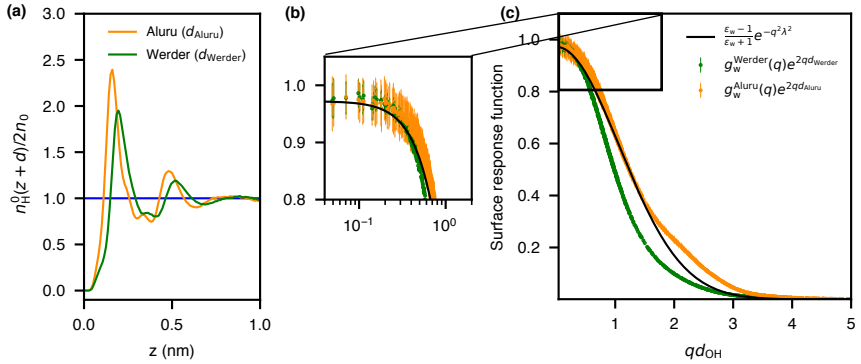

Figure 7: Surface response function $g_{\mathrm{w}}(q)$ of water. **(a)** Comparison of the hydrogen density profile along the graphene/water interface for the Werder (green) and Aluru (orange) force field. **(b)** Obtention of $d_{\mathrm{Werder}} = 1.3$Å and $d_{\mathrm{Aluru}} = 1.74$Å by considering the fastest convergence of $g_{\mathrm{w}}(q)$ for $q \to 0$. **(c)** Gaussian fit of the $g_{\mathrm{w}}(q)$ at graphene interface ($\lambda = 0.35$Å).

We compute $g_{\mathrm{w}}^{\mathrm{Werder}}(q)$ and $g_{\mathrm{w}}^{\mathrm{Aluru}}(q)$ for the two different force fields and show the results in Fig. 7. To compare both quantities, we put them on an equal footing regarding the actual microscopic vacuum gap thickness d. We set the difference $d_{\mathrm{Aluru}} - d_{\mathrm{Werder}} = 0.44$Å by equating $g_{\mathrm{w}}^{\mathrm{Werder}}(q)e^{2qd_{\mathrm{Werder}}}$ and $g_{\mathrm{w}}^{\mathrm{Aluru}}(q)e^{2qd_{\mathrm{Aluru}}}$ in the long-wavelength limit $q \to 0$. It makes the charge (or hydrogen) distribution for both force fields to start at the same altitude, as shown in Fig. 7a. To visualize and model both quantities, we also set the absolute value d_{Werder} by imposing the fastest convergence of $g_{\mathrm{w}}(q)$ with $q \to 0$. This imposes a horizontal asymptote in $q = 0$ (see Fig. 7b). We obtain $d_{\mathrm{Werder}} = 1.3$Å. To model those results, taking into both force fields, we use a simple Gaussian model:

$$g_{\mathrm{w}}(q)e^{2qd} = \frac{\varepsilon_{\mathrm{w}} - 1}{\varepsilon_{\mathrm{w}} + 1} e^{-q^2\lambda^2}. \tag{86}$$

The value of d is interface-dependent and defines the thickness of the vacuum gap. As a reference, we keep in mind $d = \frac{d_{\mathrm{Werder}} + d_{\mathrm{Aluru}}}{2} = 1.52$Å. We use $\lambda^{-1} = q_{\mathrm{w}} = 2.86\text{Å}^{-1}$. The fit is shown in Fig. 7c.

3.2.4 *Results for $g_w(q, \omega)$*

To fully characterize the SRF, we turn to the dynamics. To avoid differences between the SRF that arise from static considerations, we focus on the

renormalized quantity $g_w(q,\omega)/g_w(q)$. The long-wavelength limit[2] of this quantity can be checked using three different ways: two different force fields (for the interfacial simulations) and one bulk simulation (using the orange curve in Fig. 4). The results are shown in Fig. 8a.

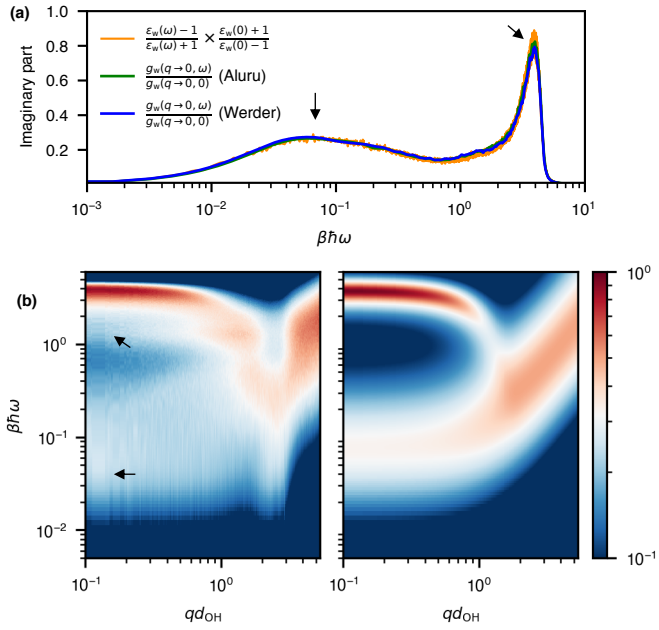

Figure 8: Imaginary part of the dynamical SRF $g_w(q,\omega)/g_w(q)$. **(a)** Long-wavelength limit for two force fields model and theoretical prediction. **(b)** 2D map showing the frequency-resolved dispersion of the surface response. The left panel is the simulation data for the Aluru force field and the right one is the proposed model. Black arrows relate the two peaks in **(a)** and **(b)**.

Remarkably, we find that the dynamical SRF for the Aluru and Werder force fields overlap with the theoretical prediction: the specificity of the static surface potential disappears. It prompts us to build a dynamical model starting from the dielectric function model in Eq. 81. The dispersion relation obtained in the simulation is given in Fig. 8b (left panel). We schematically gather the negative dispersion of the high-frequency peak from those data, its increasing damping, and its decreasing contribution to the total spectra. At the same time, the low-frequency Debye peak disperses positively, and its relative contribution to the dynamics increases. It roughly happens on the length scale $qd_{OH} \simeq 1$. We suggest to model the dielectric function as follows

$$\varepsilon_w(q,\omega) = 1 + \frac{\varepsilon_w - 1 - e^{-q^2 d_{OH}^2/2}}{1 - i\omega\tau_D(q)} + \frac{\omega_T^2(q) e^{-q^2 d_{OH}^2/2}}{\omega_T^2(q) - \omega^2 - i\gamma(q)\omega}, \tag{87}$$

with the parameters dispersion given in Table 3.

[2] For interfacial simulations, the smallest accessible wavevector is $q_{min} = 2\pi/\max(L_x, L_y) = 0.049\text{Å}^{-1}$.

	$1/\tau_D(q)$	$\omega_T(q)$	$\gamma(q)$
Dispersion	$\tau_D^{-1}(1+\frac{q^2d_{OH}^2}{2})$	$\omega_T e^{-q^2d_{OH}^2/2}$	$\gamma(1+\frac{q^2d_{OH}^2}{2})$

Table 3: Dispersive relation for the parameters of the waterr dielectric function.

The characteristic length scale d_{OH} can be understood as the transition between collective and individual dynamics. The libration peak describes a collective "phonon-like" fast oscillation mode that requires several water molecules. Therefore, it disappears for sub-molecular wavelength — i.e. $q > 1/d_{OH}$. In contrast, the Debye peak has a collective and individual molecular contribution. For $q > 1/d_{OH}$, the collective, slow ($\omega\tau_D \sim 1$) ones are filtered out, and the fast unimolecular ones dominate.

Eq. 87 gives Eq. 81 for $q \to 0$. Also the limits $\varepsilon_w(q \to 0, \omega) = \varepsilon_w(\omega)$ and $\varepsilon_w(\omega \to 0) = \varepsilon_w$ are ensured. However, we underline that Eq. 87 *does not* model the bulk dielectric function $\varepsilon_w(k, \omega)$[3]. Our work finally produces a general model for the SRF of water that reads

$$g_w(q,\omega)e^{2qd} = \frac{\varepsilon_w(q,\omega)-1}{\varepsilon_w(q,\omega)+1}e^{-q^2\lambda^2}. \tag{88}$$

The right panel of Fig. 8b shows that the dynamical modeling captures the simulation's essential features using the Aluru force field parameters (left panel). The Werder force field dynamics are very similar (not shown).

We have carried out slab simulations to find if those results would change for water under finite confinement. We find that as long as the size of the water slab is larger than 1 nm, the results are identical. The results are reported in appendix C. As long as the size of the water slab is larger than 1 nm, the results are identical.

[3] One can easily check that $\forall q,\ \varepsilon_w(q, \omega = 0) = \varepsilon_w$.

4

MICROSCOPIC WATER MODEL

4.1 WATER MODEL

In this part, we build a versatile microscopic model for water. It relies on the construction of the non-interacting response function $\chi_w^{(0)}$ and the effective potential between molecules v_w^{eff} (see Eq. 65). We scrutinize the bulk medium before tackling the water slab.

4.1.1 *Water bulk*

Herein, we build the response function χ_w of an homogeneous, isotropic, bulk water medium. Using Eq. 66, the effective charge-charge electrostatic potential in bulk water $v_{\text{inter}} = v_w^{\text{eff}}$ can be written

$$v_w^{\text{eff}}(k) = \frac{1}{\chi_w^{(0)}(k)} - \frac{1}{\chi_w(k)}, \tag{89}$$

The FDT gives $\chi_w^{(0)}(k) = -\beta S_w^{(0)}(k)$ where $\beta = 1/k_B T$ and $S_w^{(0)}(k)$ is the single-molecule – or "self" – charge structure factor, and $\chi_w(k) = -\beta S_w(k)$, $S_w(k)$ the charge structure factor of the liquid. Here, we apply this framework to the widely-used 3 point-charge model of water, SPC/E [48]. The analytical expression of $S_w^{(0)}(k)$ is given in Eq. 310. The second term can be computed in MM — e.g. the result of [61] computing the polarization response function $\bar{\chi}_w(k) = -\chi_w(k)/\epsilon_0 k^2$ that is reported in Fig. 9. The sharp peak of $\bar{\chi}_w(k)$ centered at $k \simeq 3$Å illustrates the nonlocal and over-screening properties[1] of water [63]. From the numerical knowledge of $v_w^{\text{eff}}(k)$ using Eq. 89, we suggest an ansatz.

We work with $1/\varepsilon_w^{\text{eff}}(k) = v_w^{\text{eff}}(k)/v(k)$. First, the long-wavelength limit of $\varepsilon_w^{\text{eff}}(k)$ can be expressed analytically as shown in appendix D.2. We obtain

[1] A system's screening ability is its faculty to moderate the external force it undergoes. In order to damp the external electric field of, say, a point charge in an infinite homogenous medium, the induced charge density must generally be of opposite sign closed to the test charge. Thus, it is usually the case that the total electric field ϕ_{tot} is smaller than ϕ_{ext}. However, there is no physical reason why the system cannot locally overreact to the original perturbation. In other words, it is also possible that the electric potential induced in the system is locally larger than the external one. For example, in the case of a homogenous isotropic system that can be described with dielectric function $\varepsilon(k)$ (here in Fourier space) , the total potential reads $\phi_{\text{tot}}(k) = \phi_{\text{ext}}(k)/\varepsilon(k)$ and the stability criteria – see e.g. [62]– reads $\varepsilon(k) > 1$ or $\varepsilon(k) < 0$. It means that the external potential cannot be plainly amplified (i.e. with the same sign), but that some wavelengths can be overscreened (i.e. $\varepsilon(k) < 0$ or $\bar{\chi}(k) > 1$).

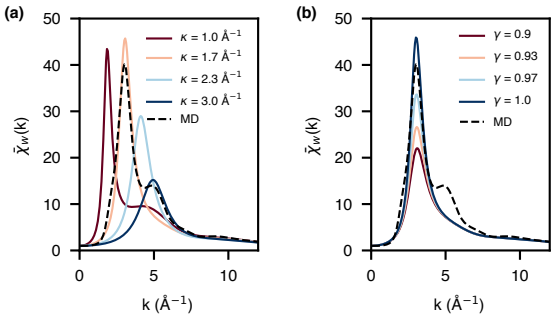

Figure 9: Susceptiblity of SPC/E water obtained with MD [61] and with the theoretical model for **(a)** varying κ with $\gamma = 0.99$ and **(b)** varying γ with $\kappa = 1.65\text{Å}^{-1}$. We show the dimensionless quantities $\bar{\chi}_w(k) = -\chi_w(k)/\epsilon_0 k^2$.

$\varepsilon_w^{\text{eff}}(k \to 0) = \varepsilon_w^{\text{eff}} \simeq 1.04$ (for SPC/E water). For the remaining wavelengths, and with the help of the MD results shown in Fig. 9, we suggest the following ansatz:

$$\frac{\varepsilon_w^{\text{eff}}}{\varepsilon_w^{\text{eff}}(k)} = 1 - \frac{k^2}{k^2+\kappa^2} - \gamma \frac{k^2}{\kappa^2} \frac{e^{-k^2/2\kappa^2}}{\sqrt{2\pi}}, \tag{90}$$

with the inverse screening length κ and the prefactor γ as parameters. The values of (κ, γ) are adjusted to reproduce the position and the amplitude of the over-screening peak of $\bar{\chi}_w$. The effect of those parameters on $\bar{\chi}_w(k)$ is shown in Fig. 9. The experimental spectra [63] shows a less intensive peak that can be easily fitted by tuning down γ. The second peak of $\bar{\chi}_w(k)$ around $k \simeq 5\text{Å}^{-1}$can also be included to refine the model, but we expect no important change on the long-range collective dielectric response of water. The ansatz ensures $\chi_w(k) \to \chi_w^{(0)}(k)$ for $k \to \infty$. We have found that $\kappa = 1.65\text{Å}$ and $\gamma = 0.99$ can reproduce the spectra of SPC/E water. We plot the polarization response function derived from our framework, $1/\bar{\chi}_w(k) = 1/\varepsilon_w^{\text{eff}}(k) + 1/\bar{\chi}_w^{(0)}(k)$ (orange curve, Fig.10a) and compare it to MD results for validation. It shows that this model captures nicely the dielectric properties of bulk water. The expression of v_w^{eff} in real space is given in Eq. 315.

4.1.2 *Water slab*

We turn to the dielectric response of a water slab confined between two infinite flat interfaces located in $z = 0$ and $z = L$ respectively (see the sketch

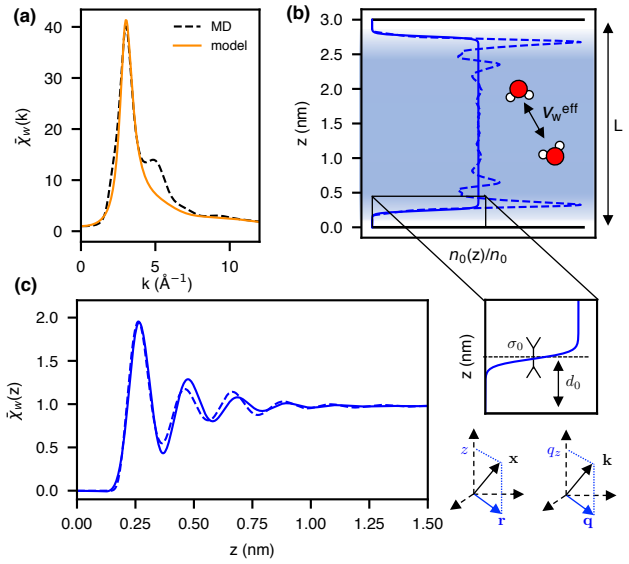

Figure 10: Dielectric response functions of water. **(a)** Susceptiblity of SPC/E water obtained with MD Jeanmairet *et al.* [61] and with the theoretical model for ($\epsilon_w^{eff} \simeq 1.04$, $\kappa = 1.65$Å^{-1}, $\gamma = 0.99$) . We show the dimensionless quantities $\tilde{\chi}_w(k) = -\chi_w(k)/\epsilon_0 k^2$. **(b)** Schematic drawing of the water slab and of the two considered molecular density profiles $n_0(z)$ for $L = 3$nm. The inset shows the two parameters of the smoothed step function model for $n_0(z)$: the vacuum distance (d_0) and the width (σ_0). **(c)** Local dielectric susceptibility $\tilde{\chi}_w(z)$ of the slab $P_z = \tilde{\chi}_w(z) D_z$ corresponding to the molecular profile $n_0(z)$, we use $\sigma_0 = .3$Å.

in Fig. 10b). Assuming equiprobable orientation of water molecules in the slab, we show in appendix D.3 that we can write

$$\chi_w^{(0)}(q, z, z') \simeq -\beta \frac{\sqrt{n_0(z) n_0(z')}}{n_0} S_w^{(0)}(q, |z - z'|) \tag{91}$$

where $S_w^{(0)}(q, |z - z'|) = \int \frac{dq_z}{2\pi} e^{iq_z|z-z'|} S_w^{(0)}(k)$ and $n_0(z)$ is the molecular density profile that converges to bulk density n_0 in the middle of the channel (see Fig. 10b). We assume that water molecules interact in the slab between themselves as they would in the bulk, so the slab-geometry effective potential $v_w^{eff}(q, |z - z'|)$ can be obtained by Fourier transforming Eq. 90 (see Eq. 317 in appendix D.2).

Obtaining $\chi_w(q, z, z')$ requires to solve the mean-field intergral equation in Eq. 66. We resort to matrix multiplications — now, and for all subsequent computations — in the discretized space along z and z'. The $(i, j)^{th}$ element of the matrix $M[z_i, z'_j]$ is given by the function $m(q, z_i, z'_j)$. The solution of Eq. 66 reads

$$X_w = (1 - X_w^{(0)} V_w^{eff} [dz]^2)^{-1} X_w^{(0)} \tag{92}$$

where $dz = 0.02$Å is the converged grid spacing and where a matrix of size $\lfloor L/dz \rfloor^2$ has been inversed. We rely on the condition that an homo-

geneous external potential cannot induce a charge density disturbance (i.e. $\int \mathrm{d}z' \chi_{\mathrm{w}}^{(0)}(z,z') = 0$) to fill the matrix $X_{\mathrm{w}}^{(0)}$. This can be checked in bulk and imposed at altitudes close to the molecular density depletion. Therefore, in order to obtain the entire matrix $X_{\mathrm{w}}^{(0)}$ and avoid numerical integration errors due to the Dirac delta functions, we fill the non-diagonal entries of $X_{\mathrm{w}}^{(0)}$ according to $\chi_{\mathrm{w}}^{(0)}(q,z,z') = -\beta S_{\mathrm{w}}^{(0)}(q,z,z')$ and impose that all lines and columns sum to 0 to fill the diagonal.

4.2 TWO APPLICATIONS

4.2.1 *Local susceptibility at interfaces*

Theory

As an intermediate check to validate our approach, we derive the local dielectric susceptibility $\bar{\chi}_{\mathrm{w}}(z)$, relating the response polarization field $P_z(z)$ to a constant excitation $\mathbf{D} = D_z \mathbf{e}_z$.

Within the standard approach of electrostatics, using Eq. 264 for a constant $\mathbf{D}$, gives $\mathbf{E}(z) = \epsilon_0 \underline{\varepsilon}(z) \cdot \mathbf{D}$, where $\underline{\varepsilon}$ is the dielectric tensor. At a translationally invariant interface, $\underline{\varepsilon}$ is diagonal [64][2]. Therefore, we obtain

$$E_z(z) = \varepsilon_{\perp}^{-1}(z) \frac{D_z}{\epsilon_0}. \tag{94}$$

Using $\epsilon_0 E_z(z) = D_z - P_z(z)$, we find the local susceptibility $\bar{\chi}_{\mathrm{w}}(z) = 1 - \varepsilon_{\perp}^{-1}(z)$ with $P_z(z) = \bar{\chi}_{\mathrm{w}}(z) D_z$.

On the other hand, we microscopically construct the external electric field. We place two infinite plates of opposite surface charge that sandwich from very far the system under scrutiny. The system of finite size experiences $\phi_{\mathrm{ext}}(z) = -\frac{D_z}{\epsilon_0}(z - \frac{L}{2})$ plus a constant that we set to zero. The electric field in the system reads $E_z(z) = -\frac{\mathrm{d}}{\mathrm{d}z}\phi_{\mathrm{tot}}(z)$. Using Eq. 8, ϕ_{tot} and ϕ_{ext} are linked as follows[3]:

$$\phi_{\mathrm{tot}}(z) = \int_0^L \varepsilon_{\mathrm{w}}^{-1}(q \to 0, z, z') \phi_{\mathrm{ext}}(z') \mathrm{d}z'. \tag{96}$$

[2] It reads

$$\underline{\varepsilon}(z) = \begin{pmatrix} \varepsilon_{\parallel}(z) & 0 & 0 \\ 0 & \varepsilon_{\parallel}(z) & 0 \\ 0 & 0 & \varepsilon_{\perp}(z) \end{pmatrix}. \tag{93}$$

[3] From Eq. 9, recall that

$$\varepsilon_{\mathrm{w}}^{-1}(q,z,z') = \delta(z-z') + \int \mathrm{d}z_1 v(q,z,z_1) \chi_{\mathrm{w}}(q,z_1,z'). \tag{95}$$

We now link $\varepsilon_{\mathrm{w}}^{-1}(q,z,z')$ to $\varepsilon_{\perp}^{-1}(z)$. We differentiate Eq. 96, use Eq. 94 and all formulas in the preceeding paragraph to obtain

$$\varepsilon_{\perp}^{-1}(z) = \frac{\mathrm{d}}{\mathrm{d}z}\left[\int_0^L \mathrm{d}z' \varepsilon_{\mathrm{w}}^{-1}(q\to 0,z,z')\left(z'-\frac{L}{2}\right)\right], \tag{97}$$

and therefore $\bar{\chi}_{\mathrm{w}}(z)$.

Results

The slab molecular density profile $n_0(z)$ is an input of the model (see Eq. 91) and we first consider a generic smoothed step function model:

$$n_0(z) = \frac{n_0}{4}\left[\tanh(\frac{z-d_0}{\sigma_0})+1\right]\left[\tanh(\frac{L-z-d_0}{\sigma_0})+1\right]. \tag{98}$$

It captures the vacuum layer between the fluid and the surface (encoded by d_0) and the width (σ_0) of the fluid interface (inset of Fig. 10b). We have converged $L\to\infty$ and used $L = 3$nm. In agreement with previous results [32], the susceptibility calculated in this framework and plotted in Fig. 10c presents an alternation of overresponding ($\bar{\chi}_{\mathrm{w}}(z) > \chi_b$) and underresponding ($\bar{\chi}_{\mathrm{w}}(z) < \chi_b$) layers before reaching its bulk value $\chi_b = 1-1/\varepsilon_{\mathrm{w}}$ for $z > 1.25$ nm.

The effect of the smoothness parameter is shown in Fig. 11a. We observe that steeper the density profile is, the sharper $\bar{\chi}_{\mathrm{w}}(z)$ near the surface. The agreement with the Landau-Ginzburg model introduced in [65] is excellent for $\sigma_0 = 0.2$Å. Refining $n_0(z)$ by extracting the hydrogen density from the MD simulations (see Fig. 10b, where we use the Werder force field hydrogen profile) induces minor modifications in $\bar{\chi}_{\mathrm{w}}(z)$ (dotted line in Fig. 10c). For future references, we will use the first density model and fix $\sigma_0 = 0.3$Å (see also appendix D.4 and [65]).

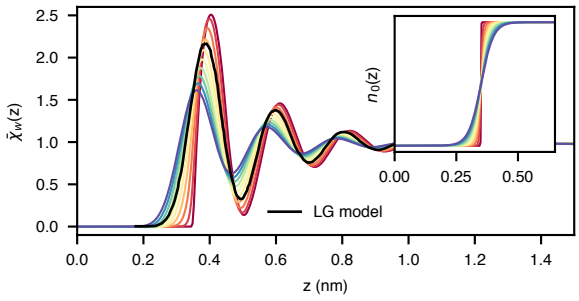

Figure 11: **(a)** Local dielectric susceptibility of the slab $P_z = \bar{\chi}_{\mathrm{w}}(z)D_z$ computed from the non-local response function $\chi_{\mathrm{w}}(q,z,z')$ with varying smoothness of the step function σ_0 and compared with Landau-Ginzburg model of Ref. [65].

4.2.2 *On the effective dielectric constant*

Theory

In the recent literature [65, 66, 67], we have found some recent interest in the effective dielectric constant ε_{eff} of a L nm thick water slab. In the following, by resolving the electrostatic potential $\phi_{\text{tot}}(z)$, we show that it is poorly defined from a microscopic perspective.

The effective dielectric constant relates the potential difference between the two ends of the water slab as follows

$$\frac{1}{\varepsilon_{\text{eff}}} = \frac{1}{L}\int_0^L \mathrm{d}z \varepsilon_{\perp}^{-1}(z) = \frac{\epsilon_0\left[\phi_{\text{tot}}(L) - \phi_{\text{tot}}(0)\right]}{-D_z L}. \tag{99}$$

We have used Eq. 97 for the last step. ϕ_{tot} is actually simpler to compute in our framework because it does not require the numerical gradient. From Eq. 96 obtain

$$\frac{\epsilon_0\phi_{\text{tot}}(z)}{-D_z} = \int_0^L \varepsilon_{\text{w}}^{-1}(q\to 0, z, z')\left(z' - \frac{L}{2}\right)\mathrm{d}z'. \tag{100}$$

Results

We show $\phi_{\text{tot}}(z)$ in Fig. 12a for a slab of $L = 4$nm. We have used a large value $d_0 = 5$Å to observe the potential at the borders of the water slab, situated in d_0 and $L - d_0$ — see also black lines in Fig. 12a. As expected, we find a slope of 1 in vacuum and $1/\varepsilon_{\text{w}}$ in the bulk region — see orange triangles. The non-monotonic variation of the potential is due to the non-local properties of water at the interface, as previously noted in Fig. 10.

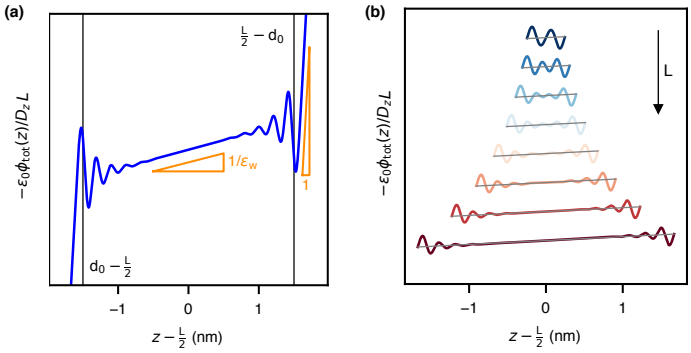

Figure 12: Electrostatic potential $\phi_{\text{tot}}(z)$ for **(a)** $L = 4$nm and $d_0 = 5$Å to see the potential in vacuum **(b)** with $d_0 = 0.88$Å and varying size L to make $\varepsilon_{\text{eff}} = \varepsilon_{\text{w}}\ \forall\ L$. We use $\mathrm{d}z = 0.005$. The orange triangle is a guide for the eye, to understand the slopes.

We compute Eq. 99 as the difference between two extreme points. However, what are the two extreme points? According to Eq. 99, we should use

$z = 0$ and $z = L$. In this case, the results would highly depend on d_0 because the slope in the vaccum is ε_w times higher than in bulk. A more intuitive choice is to take the two points that delimitate the water slab: $z = d_0$ and $z = L - d_0$[4]. It turns out that it makes ε_{eff} negative — see intersection of the dark and blue curve in Fig. 12a —, layers of water dipoles overscreen the external potential. As L grows, ε_{eff} retrieve a positive sign and converges to ε_w for $L \to \infty$. Without any specific definition of d_0, ε_{eff} can take any value (see Fig. 12b for $\varepsilon_{\text{eff}} = \varepsilon_w$, $\forall\ L$). In a real experiment that probes ε_{eff}, water is contained in a slit made of another material such that a vacuum gap does exist.

To understand the effect of d_0, we first extract a d_0-independent result. From Eq. 100, we express analytically the $q \to 0$ limit. After some straightforwards steps[5] we obtain the result in agreement with [64]. Introducing $1/\varepsilon_{\text{eff}} = 1 - \chi_{\text{eff}}$, we obtain

$$\chi_{\text{eff}} = \frac{-1}{\epsilon_0 L} \int\int \mathrm{d}z_1 \mathrm{d}z_2 \left(z_1 - \frac{L}{2}\right) \chi_w(q = 0, z_1, z_2) \left(z_2 - \frac{L}{2}\right) \tag{101}$$

$$= -\frac{\beta}{\epsilon_0} \left[\langle P_\perp^2 \rangle_0 - \langle P_\perp \rangle_0^2\right]. \tag{102}$$

The polarization of the slab in the perpendicular direction reads $P_\perp = \int \mathrm{d}z \left(z - \frac{L}{2}\right) n_w(z)$. We use $\sigma_0 \to 0$ (heaviside step function in Eq. 98) and compute χ_{eff} following Eq. 101 for increasing L. The results are given in Fig. 13a. χ_{eff} decreases with L and converges to $\chi_{\text{eff}} \to 1 - 1/\varepsilon_w$ for $L \to \infty$. The overscreening transition ($\chi_{\text{eff}} > 1$) occurs at $L \simeq 7$nm. As discussed, it gives $\varepsilon_{\text{eff}} < 0$ for small slabs if the vacuum gap d_0 is ignored.

A dielectrically dead water layer at interfaces ($\varepsilon_w^{\text{surf}} = 2.1$ on a distance of 0.7 nm) has been postulated to understand an anomalous dielectric constant of water in nanometric channels [66]. According to our results, this explanation could be misleading as it does not account for the oscillating potential in Fig. 13a, which is not linear with a slope of $1/\varepsilon_w^{\text{surf}}$.

Nevertheless, let us assume a continuous slope of $1/\varepsilon_w$ in the entire slab (local continuous media). The effect of the vacuum gap d_0 gives with a simple capacitor model:

$$\frac{1}{\varepsilon_{\text{eff}}} = \frac{2d_0}{L} + \frac{L - 2d_0}{L\varepsilon_w}. \tag{103}$$

[4] Of course, replacing L by $L - 2d_0$ in the denominator of Eq.99.

[5] make a $\sinh(q\,[z_1 - L/2])$ appear using the difference $\phi(L) - \phi(0)$ and the use the limit $q \to 0$.

The result for $\varepsilon_{\text{eff}}(L)$ is shown in Fig. 13b with the experimental data of [66]. The simple model fits the measurements reasonably well. However, the overall trend is solely due to the vaccum gap d_0.

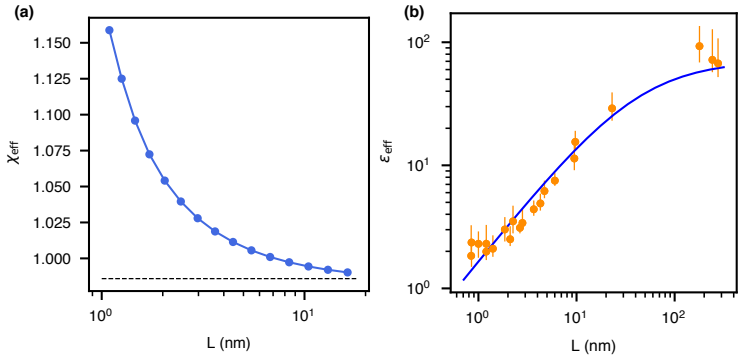

Figure 13: Evolution of dielectric properties of water with L. **(a)** Computation of χ_{eff} using Eq. 101. No dependency on d in this case and we use a heaviside step function ($\sigma_0 \to 0$) for the molecular profile **(b)** Experimental data [66] and capacitor model with a vacuum gap of $d_0 = 3$Å and constant dielectric constant of SPC/E water $\varepsilon_{\text{w}} = 71$.

In short, in our microscopic formalism, ε_{eff} highly depends on the vacuum gap d_0. It can be positive, negative, infinite or equal to ε_{w} and increase/decrease/be constant with L. It is a poor observable from a microscopic perspective. We also argue that its use might be misleading in grasping the non-local behavior of water at interfaces.

5

FEW-LAYERS GRAPHENE MODEL

5.1 RPA RESPONSE FUNCTION

5.1.1 *Wannier functions*

Warning: in this chapter, $\mathbf{k}$ *is a two-dimensional wavevector.*

In this part, we consider a metallic slab in the lower half-space $z < 0$, at temperature T. We aim to compute its response function χ_e and its SRF g_e with a tight-binding (TB) model. The interface is translationally invariant, and electronic states are labeled with a continuous two-dimensional wavevector $\mathbf{k}$ belonging to the Brillouin zone. We neglect the corrugation due to the lattice and therefore ignore local-field effects as discussed in 2.3.1. Two electrons with opposite spin can occupy a state labeled with a band index ν. The Fermi field reads $\Psi(\mathbf{x}) = \sum_{\nu\mathbf{k}} \psi_{\nu\mathbf{k}}(\mathbf{x})\hat{c}_{\nu\mathbf{k}}$ where $\psi_{\nu\mathbf{k}}(\mathbf{x})$ is the wavefunction of the electron in state $(\nu\mathbf{k})$ and $\hat{c}_{\nu\mathbf{k}}$ is the fermionic annihilation operator. The electronic density operator reads $\hat{n}_e(\mathbf{x}) = \Psi^\dagger(\mathbf{x})\Psi(\mathbf{x})$, with $\mathbf{x} = (\mathbf{r}, z)$. The quadratic hamiltonian reads $\hat{H}_e^{(0)} = \sum_{\nu\mathbf{k}} \epsilon_{\nu\mathbf{k}}\hat{c}^\dagger_{\nu\mathbf{k}}\hat{c}_{\nu\mathbf{k}}$. The wavefunctions are decomposed on Wannier functions:

$$\psi_{\nu\mathbf{k}}(\mathbf{x}) = \frac{1}{\sqrt{N_p}} \sum_{\kappa p} e^{-i\mathbf{k}\mathbf{R}_p} d^\kappa_{\nu\mathbf{k}} \phi(\mathbf{r} - \boldsymbol{\tau}_{\kappa p}, z - z_\kappa), \tag{104}$$

where κ labels the atomic sites at position $\boldsymbol{\tau}_\kappa$ in the two-dimensional unit cell of the material, p labels the N_p cells at position $\mathbf{R}_p$ in the plane, and $\boldsymbol{\tau}_{p\kappa} = \mathbf{R}_p + \boldsymbol{\tau}_\kappa$. We consider one electron per atomic orbtital ϕ that have the same form. We neglect the overlap integral between two neighboring atomic site. The normalization of wavefunction $\int \mathrm{d}\mathbf{x}|\psi_{\nu\mathbf{k}}(\mathbf{x})|^2 = 1$ therefore requires $\sum_\kappa |d^\kappa_{\nu\mathbf{k}}|^2 = 1$. The coefficients $d^\kappa_{\nu\mathbf{k}}$ and the eigenenergies $\epsilon_{\nu\mathbf{k}}$ solve the Schrödinger equation $\hat{H}_e^{(0)}|\psi_{\nu\mathbf{k}}\rangle = \epsilon_{\nu\mathbf{k}}|\psi_{\nu\mathbf{k}}\rangle$. Note that the number of sites in the unit cell, N_κ, increases when the medium grows in the direction normal to the surface. The Fourier-transform of the electronic density operator reads

$$\hat{n}_e(\mathbf{q}, z) = \sum_{\nu\mu\mathbf{k}} \lambda^{\mu\nu}_{\mathbf{k}+\mathbf{q}\mathbf{k}}(z)\hat{c}^\dagger_{\mu\mathbf{k}+\mathbf{q}}\hat{c}_{\nu\mathbf{k}}. \tag{105}$$

To obtain Eq. 105, we have used the crystal momentum conservation as detailed in appendix E.1. The coefficient $\lambda^{\mu\nu}_{\mathbf{k}+\mathbf{qk}}(z)$ is given by

$$\lambda^{\mu\nu}_{\mathbf{k}+\mathbf{qk}}(z) = \langle \psi_{\mu\mathbf{k}+\mathbf{q}} | e^{-i\mathbf{qr}} | \psi_{\nu\mathbf{k}} \rangle(z) \tag{106}$$

$$= \int \mathrm{d}\mathbf{r} \psi^*_{\mu\mathbf{k}+\mathbf{q}}(\mathbf{x}) \psi_{\nu\mathbf{k}}(\mathbf{x}) e^{-i\mathbf{qr}}$$

$$\overset{\text{Eq.104}}{=} \sum_{\kappa} u_{\mathbf{q}}(z,\kappa) (d^{\kappa}_{\mu\mathbf{k}+\mathbf{q}})^* d^{\kappa}_{\nu\mathbf{k}} \tag{107}$$

where the last line is obtained after insertion of Eq. 104. (see also appendix E.1). The in-plane Fourier transform of the electronic density on site κ, that reads

$$u_{\mathbf{q}}(z,\kappa) = u_{\mathbf{q}}(z + z_\kappa, 0) e^{+i\mathbf{q}\cdot\boldsymbol{\tau}_\kappa} \qquad u_{\mathbf{q}}(z,0) = \int \mathrm{d}\mathbf{r} e^{-i\mathbf{qr}} |\phi(\mathbf{r},z)|^2. \tag{108}$$

5.1.2 *Non-interacting response function* $\chi^{(0)}_e$

Using Eq. 68, we obtain after Fourier transformation:

$$\chi^{(0)}_{\mathrm{e}}(\mathbf{q},z,z',t) = -\frac{i}{\hbar}\frac{\Theta(t)}{\mathcal{A}} \left\langle \left[\hat{n}_{\mathrm{e}}(\mathbf{q},z,t), \hat{n}_{\mathrm{e}}(-\mathbf{q},z',0) \right] \right\rangle_0 \tag{109}$$

where $[.,.]$ is the anticommutator, Θ the Heaviside function. We use Matsubara's framework [31] to compute $\chi^{(0)}_{\mathrm{e}}$ at $T = 0$ K. Those steps are detailed in appendix E.2. We find

$$\chi^{(0)}_{\mathrm{e}}(\mathbf{q},z,z',i\Omega_m) = \frac{k_B T}{\mathcal{A}} \sum_{\nu\mu\mathbf{k}} \sum_{ik_n} \lambda^{\mu\nu}_{\mathbf{k}+\mathbf{qk}}(z) \mathcal{G}^{(0)}_{\nu}(\mathbf{k}, ik_n) ... \tag{110}$$

$$... \mathcal{G}^{(0)}_{\mu}(\mathbf{k}+\mathbf{q}, ik_n + i\Omega_m) \lambda^{\nu\mu}_{\mathbf{kk}+\mathbf{q}}(z'),$$

that we now detail. First, $\chi^{(0)}_{\mathrm{e}}(\mathbf{q},z,z',i\Omega_m)$ is linked to the Fourier transform of $\chi^{(0)}_{\mathrm{e}}(\mathbf{q},z,z',\omega)$ by analytic continuation along the real axis $i\Omega_m \to \omega + i\eta$ with $\eta = 0^+$. Second, $\mathcal{G}^{(0)}_{\nu}(\mathbf{k}, ik_n) = (ik_n - \epsilon_{\nu\mathbf{k}})^{-1}$ is the Matsubara single–particle Green's function. Third, the summation is over fermionic Matsubara frequencies $k_n = \pi(2n+1)k_B T/\hbar$.

We open a parenthesis to appreciate how Feynman diagrammatics, adapted to the Matsubara formalism, saves us a lot of tedious work to obtain Eq. 110. We first define two symbols: *(i)* the line diagram as the single-particle

Green's function propagator, *(ii)* the Coulomb vertex $\lambda^{\mu\nu}_{\mathbf{k}+\mathbf{q}\mathbf{k}}(z)$ of Eq. 106 that couples two eigenstates due to the Coulomb interaction. It reads

$\mathcal{G}^{(0)}_{\nu}(\mathbf{k}, ik_n) =$ $\lambda^{\mu\nu}_{\mathbf{k}+\mathbf{q}\mathbf{k}}(z) =$ 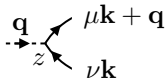 , (111)

from which we can represent the non-interacting response function $\chi^{(0)}_{\mathrm{e}}$ from Eq. 110 as follows

$\chi^{(0)}_{\mathrm{e}}(\mathbf{q}, z, z', i\Omega_m) =$ 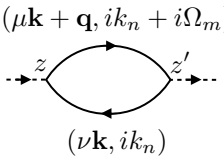 . (112)

Note that *(i)* there is a conservation of momentum and energy at each vertex, and *(ii)* the dummy indices are summed up — that we will use again. All terms appearing in the diagrams are multiplied as shown in Eq. 110.

Using standard Matsubara summations [31], we simplify Eq. 110. By taking the analytic continuation on the real axis $i\Omega_m \to \omega + i\eta$, we obtain

$$\chi^{(0)}_{\mathrm{e}}(\mathbf{q}, z, z', \omega) = \frac{-g_s}{\mathcal{A}} \sum_{\nu\mu\mathbf{k}} \lambda^{\mu\nu}_{\mathbf{k}+\mathbf{q}\mathbf{k}}(z) \frac{n_F(\epsilon_{\mu\mathbf{k}+\mathbf{q}}) - n_F(\epsilon_{\nu\mathbf{k}})}{\omega + i\eta - (\epsilon_{\mu\mathbf{k}+\mathbf{q}} - \epsilon_{\nu\mathbf{k}})} \lambda^{\nu\mu}_{\mathbf{k}\mathbf{k}+\mathbf{q}}(z'), \tag{113}$$

where the factor $g_s = 2$ comes from the spin degeneracy and n_F is the Fermi-Dirac distribution function.

Eq. 113 has to be distinguished from the formula usually found in the literature. The wavevectors $\mathbf{k}$ and $\mathbf{q}$ lie in the plane. The number of bands increases as the material becomes thicker in the vertical direction. In the limit of an infinite medium in this direction, we would label the bands differently, using $\nu = k_z$ and $\mu = k_z + q_z$. Conservation of momentum in this direction would then impose $q'_z = -q_z$, and the textbook bubble diagram would be obtained.

5.1.3 *RPA equation*

We now use Eq. 11 to renormalize $\chi^{(0)}_{\mathrm{e}}$ by the interparticle effective potential v_{inter}. A special case of mean-field renormalization is the random phase approximation (RPA) [68]. It is equivalent to identifying the interparticle

mean-field potential with the direct potential — e.g. $v_{\text{inter}} = v$. We confer the *hatched* diagram to the RPA response function for electrons (χ_e) that reads

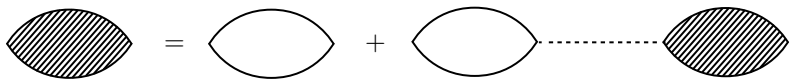

. (114)

To solve Eq. 114, we proceed by matrix inversion. Again, using the matrix notations — i.e. $M[z,z'] = m(\mathbf{q},z,z',\omega)$ — we find

$$X_e = (I - X_e^{(0)} V dz^2)^{-1} X_e^{(0)}. \tag{115}$$

However, in contrast to the dielectric case, computing $\chi_e^{(0)}(\mathbf{q},z,z',\omega)$ with the help of Eq. 113 is not numerically straightforward. The grid in (z,z') requires at least $\lfloor Nc/2dz \rfloor^2$ evaluations of Eq. 113, where $Nc/2$ is about slab height and dz the grid spacing. Consequently, we change the basis set and take advantage of Wannier functions as suggested for the bulk case in [46]. It was also suggested for the case of a finite slab [69], but never applied for carbon materials to our knowledge.

5.1.4 *Basis change*

Herein, we change the (z,z') grid to the local atomic sites (κ,κ') basis. Inserting Eq. 107 in Eq. 113, we obtain that $X_e^{(0)} = U_{\mathbf{q}} \tilde{X}_e^{(0)} U_{\mathbf{q}}^\dagger$ where

$$\tilde{\chi}_e^{(0)}(\mathbf{q},\kappa,\kappa',\omega) = \frac{-g_s}{\mathcal{A}} \sum_{\nu\mu\mathbf{k}} (d^\kappa_{\mu\mathbf{k}+\mathbf{q}})^* d^\kappa_{\nu\mathbf{k}} \frac{n_F(\epsilon_{\mu\mathbf{k}+\mathbf{q}}) - n_F(\epsilon_{\nu\mathbf{k}})}{\omega + i\eta - (\epsilon_{\mu\mathbf{k}+\mathbf{q}} - \epsilon_{\nu\mathbf{k}})} d^{\kappa'}_{\mu\mathbf{k}+\mathbf{q}} (d^{\kappa'}_{\nu\mathbf{k}})^*. \tag{116}$$

Inserting $X_e^{(0)} = U_{\mathbf{q}} \tilde{X}_e^{(0)} U_{\mathbf{q}}^\dagger$ in Eq. 115, we find that $X_e = U_{\mathbf{q}} \tilde{X}_e U_{\mathbf{q}}^\dagger$ with

$$\tilde{X}_e = (I - \tilde{X}_e^{(0)} \tilde{V}_e)^{-1} \tilde{X}_e^{(0)}. \tag{117}$$

Here we have introduced the site-site interaction matrix $\tilde{V}_e = U_{\mathbf{q}}^\dagger V U_{\mathbf{q}}$ that reads

$$\tilde{v}_e(\mathbf{q},\kappa,\kappa') = \frac{1}{2\epsilon_0 q} \iint dz dz' u^*_{\mathbf{q}}(z,\kappa) e^{-q|z-z'|} u_{\mathbf{q}}(z,\kappa'). \tag{118}$$

We have expressed the RPA equation Eq. 114, in the basis of local atomic sites. If N_κ is the number of sites in the two-dimensional unit cell, then we have to compute N_κ^2 times Eq. 116. In order to compute the SRF, we use that $X_e = U_{\mathbf{q}} \tilde{X}_e U_{\mathbf{q}}^\dagger$, Eq. 36 and Eq 108. It reads

$$g(\mathbf{q},\omega) = \left|u^{\mathrm{s}}_{\mathbf{q}}\right|^2 \sum_{\kappa\kappa'} \tilde{\chi}_{\mathrm{e}}(\mathbf{q},\kappa,\kappa',\omega) e^{+i\mathbf{q}\cdot(\boldsymbol{\tau}_\kappa - \boldsymbol{\tau}_{\kappa'}) - q(z_\kappa + z_{\kappa'})} \tag{119}$$

where $u^{\mathrm{s}}_{\mathbf{q}} = \int \mathrm{d}z e^{qz} u_{\mathbf{q}}(z,0) = \int \mathrm{d}\mathbf{x} e^{-i\mathbf{q}\mathbf{r}} e^{qz} |\phi(\mathbf{x})|^2$.

5.2 TIGHT-BINDING MODELS

5.2.1 *Graphene*

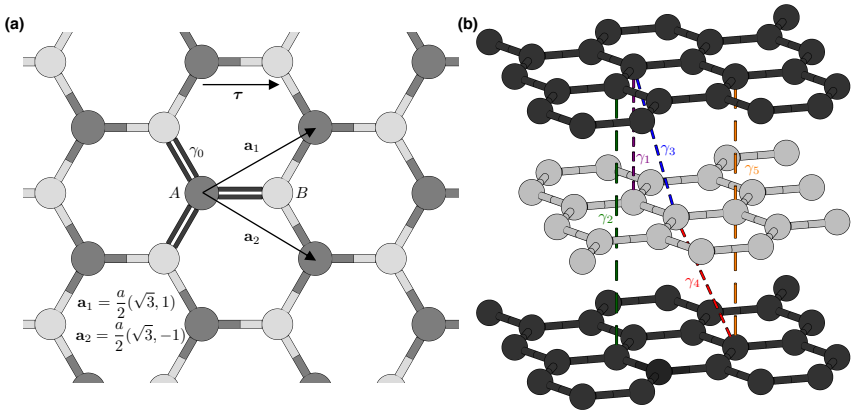

Figure 14: Tight-binding model for graphene and few-layers graphene. **(a)** Lattice vectors $(\mathbf{a}_1, \mathbf{a}_2)$ of graphene with two sites (A, B) per unit cell that are linked by the vector $\boldsymbol{\tau}$. The chemical bonds are highlighted and defined by the vectors $\boldsymbol{\tau}$, $\boldsymbol{\tau} - \mathbf{a}_1, \boldsymbol{\tau} - \mathbf{a}_2$. The covalent bond strength $\gamma_0 = \langle \phi_{B,0} | \hat{H}^{(0)}_{\mathrm{e}} | \phi_{A,0} \rangle$ is represented. (**b**) Other coupling parameters between different sites in the SWMC [70] TB model.

For the tight-binding model of graphene [71], the lattice vectors (see Fig. 14a) read $\mathbf{a}_1 = \frac{a}{2}(\sqrt{3}, 1)$ and $\mathbf{a}_2 = \frac{a}{2}(\sqrt{3}, -1)$ in real space and $\mathbf{b}_1 = \frac{2\pi}{\sqrt{3}a}(1, \sqrt{3})$ and $\mathbf{b}_2 = \frac{2\pi}{\sqrt{3}a}(1, -\sqrt{3})$ in reciprocal space. Here, $a = \sqrt{3} d_{\mathrm{cc}}$ with $d_{\mathrm{cc}} = 1.42$Å the carbon-carbon distance. There are two carbon atoms in the unit cell such that the first one (site A) is placed at the origin and the second (site B) at a vector $\boldsymbol{\tau} = (\mathbf{a}_1 + \mathbf{a}_2)/3$ from it. The Hamiltonian is limited to nearest-neighbor (NN) interactions. It reads

$$\hat{H}^{(0)}_{\mathrm{e}} = -\gamma_0 \sum_{\kappa} \sum_{\kappa' p' \in \mathrm{NN}(\kappa)} |\phi_{\kappa,0}\rangle \langle \phi_{\kappa',p'}|,$$

where $|\phi_{\kappa,p}\rangle = |\phi(\mathbf{r} - \boldsymbol{\tau}_{\kappa p}, z - z_\kappa)\rangle$ and γ_0 is the NN covalent bond strength. We project Schrödinger's equation $\hat{H}^{(0)}_{\mathrm{e}} |\psi_{\nu\mathbf{k}}\rangle = \epsilon_{\nu\mathbf{k}} |\psi_{\nu\mathbf{k}}\rangle$ on $|\phi_{A,0}\rangle$ and $|\phi_{B,0}\rangle$

— where $|\psi_{\nu\mathbf{k}}\rangle$ is defined in Eq. 104 — to obtain the coefficients $d^{\kappa}_{\nu\mathbf{k}}$ for $\kappa = A, B$. We obtain, with $f(\mathbf{k}) = 1 + e^{-i\mathbf{k}\mathbf{a}_1} + e^{-i\mathbf{k}\mathbf{a}_2}$,

$$\begin{cases} -\gamma_0 f(\mathbf{k}) d^B_{\nu\mathbf{k}} = \epsilon_{\nu\mathbf{k}} d^A_{\nu\mathbf{k}} \\ -\gamma_0 f^*(\mathbf{k}) d^A_{\nu\mathbf{k}} = \epsilon_{\nu\mathbf{k}} d^B_{\nu\mathbf{k}} \end{cases} . \tag{120}$$

With $\theta_{\mathbf{k}} = \arg f(\mathbf{k})$, Eq. 120 gives $d^B_{\nu\mathbf{k}} = \pm e^{-i\theta_{\mathbf{k}}} d^A_{\nu\mathbf{k}}$. Moreover, the normalization condition for the wavefunction leads to $d^A_{\nu\mathbf{k}} = 1/\sqrt{2}$. Therefore, we label the two energy bands with the index $\nu = \pm 1$ and write $d^B_{\nu\mathbf{k}} = \nu e^{-i\theta_{\mathbf{k}}} d^A_{\nu\mathbf{k}}$. The wavefunction reads

$$\psi_{\nu\mathbf{k}}(\mathbf{x}) = \frac{1}{\sqrt{N_p}} \sum_{\kappa p} e^{i\mathbf{k}\mathbf{R}_p} \left(\phi(\mathbf{r} - \mathbf{R}_p, z) + \nu e^{-i\theta_{\mathbf{k}}} \phi(\mathbf{r} - \boldsymbol{\tau} - \mathbf{R}_p, z) \right) , \tag{121}$$

where $\phi(\mathbf{x}) = \frac{k_c^{5/2} z}{\sqrt{32\pi}} e^{-\frac{k_c |\mathbf{x}|}{2}}$ is the p_z carbon orbital with $k_c = 3.18/a_0$ [72] — a_0 is the Bohr radius.

Having obtained the coefficients $d^{\kappa}_{\nu\mathbf{k}}$, we reinsert them in Eq. 120 to find the eigenenergies $\epsilon_{\nu\mathbf{k}} = \nu\gamma_0 |f(\mathbf{k})|$. Filling the bands of graphene with the two available electrons means that the $\nu = -1$ band is occupied but not the $\nu = +1$, at $T = 0$ K. The Fermi level, in an undoped situation, is therefore at the top of the valence band. This is also the bottom of the conduction band (where $|f(\mathbf{k})| = 0$). This condition is fulfilled in two special points $\mathbf{K} = (\mathbf{b}_1 - \mathbf{b}_2)/3$ and $\mathbf{K}'$. Ignoring the differences between the two valleys, we scrutinize the energy bands near $\mathbf{K}$, for $\mathbf{k} = \mathbf{K} + \delta\mathbf{k}$.

After some straightforward algebra, we find $|f(\mathbf{k})| \simeq \sqrt{3} a |\delta\mathbf{k}|/2$ for $|\delta\mathbf{k}| \ll |\mathbf{K}|$. This conical behavior of the energy bands is responsible for the semimetallic properties of graphene. Reducing the tight-binding model to the linear behavior near the independent $\mathbf{K}$ and $\mathbf{K}'$ points is called the Dirac approximation. This approximation is excellent for computing the response function of graphene χ_e, even at large wavevector — i.e., for $|\mathbf{q}| \sim 1/a$ [73]. Therefore, in the following, we introduce the Fermi velocity $v_F = \sqrt{3} a \gamma_0 / 2\hbar$ and write the eigenstates[1]

$$\epsilon_{\nu\mathbf{k}} \simeq \nu \hbar v_F |\mathbf{k} - \mathbf{K}| \quad \text{for} \quad |\mathbf{k} - \mathbf{K}| \ll 1/a. \tag{122}$$

We now search for the Coulomb potential coupling matrix element between different electronic states. It is defined in Eq. 105 and Eq. 106 and reads $\lambda^{\nu\mu}_{\mathbf{k}\mathbf{k}+\mathbf{q}}(z) = \frac{U_0(z)}{2} \left(1 + \nu\mu e^{-i(\theta_{\mathbf{k}+\mathbf{q}} - \theta_{\mathbf{k}})} \right)$ with $U_0(z) \simeq \frac{k_c^3 z^2}{16} \left(1 + k_c |z| \right) e^{-k_c |z|}$ that is valid for $q \ll k_c$. In this work, we may invoke the argument of the small spatial extent of the carbon p_z orbital — i.e. $k_c a_0 = 3.18$ — to make

[1] It is also valid near $\mathbf{K}'$.

the 2D approximation using $\int_{-\infty}^{+\infty} \mathrm{d}z U_0(z) = 1$ or even $U_0(z) \simeq \delta(z)$. In those cases, we may use $\lambda^{\nu\mu}_{\mathbf{k}\mathbf{k}+\mathbf{q}} = \int \mathrm{d}z \lambda^{\nu\mu}_{\mathbf{k}\mathbf{k}+\mathbf{q}}(z)$ such as the coupling matrix element squared reads

$$|\lambda^{\nu\mu}_{\mathbf{k}\mathbf{k}+\mathbf{q}}|^2 = \frac{1}{2}\left(1 + \nu\mu \frac{\mathbf{k}\cdot(\mathbf{k}+\mathbf{q})}{|\mathbf{k}||\mathbf{k}+\mathbf{q}|}\right). \tag{123}$$

5.2.2 *FLG*

We use the Slonzcewski-Weiss-McClure (SWMC) model [70] to describe few-layers graphene (FLG). Graphene layers, arranged in the Bernal stacking (ABAB..), are separated by a distance $c/2 = 3.35$Å (see Fig. 14b). In the limit of $N \to \infty$, it is graphite. The interaction between sites is truncated at the first NN within the same layer and second NN between layers. The unit cell contains 4 atoms situated at $\boldsymbol{\tau}_0 = \mathbf{0}, \boldsymbol{\tau}_1 = \boldsymbol{\tau}, \boldsymbol{\tau}_2 = -\frac{c}{2}\mathbf{e}_z, \boldsymbol{\tau}_3 = -\boldsymbol{\tau} - \frac{c}{2}\mathbf{e}_z$. The primitive pattern includes three graphene layers (ABA) — we thus use $\boldsymbol{\tau}_4 = -c\mathbf{e}_z$ and $\boldsymbol{\tau}_5 = \boldsymbol{\tau} - c\mathbf{e}_z$. The interaction parameters γ_i are indicated in Figure 14, and their values are given in Table 4.

TB paramaters	γ_0	γ_1	γ_2	γ_3	γ_4	γ_5	Δ
eV	3.16	0.39	−0.02	0.315	0.044	0.038	−0.008

Table 4: Tight-binding paramerters for the SWMC model of FLG [70].

The Hamiltonian, whose eigenvalues and eigenvectors are given by $\hat{H}^{(0)}_{\mathrm{e}}|\psi_{\nu\mathbf{k}}\rangle = \epsilon_{\nu\mathbf{k}}|\psi_{\nu\mathbf{k}}\rangle$, is written in a matrix form. The primitive pattern reads

$$\hat{H}^{(0)}_{\mathrm{e}}(\mathbf{k}) = \begin{pmatrix} \Delta & f(\mathbf{k})\gamma_0 & \gamma_1 & f^*(\mathbf{k})\gamma_4 & \gamma_5 & 0 \\ f^*(\mathbf{k})\gamma_0 & 0 & f^*(\mathbf{k})\gamma_4 & f(\mathbf{k})\gamma_3 & 0 & \gamma_2 \\ \gamma_1 & f(\mathbf{k})\gamma_4 & \Delta & f^*(\mathbf{k})\gamma_0 & \gamma_1 & f(\mathbf{k})\gamma_4 \\ f(\mathbf{k})\gamma_4 & f^*(\mathbf{k})\gamma_3 & f(\mathbf{k})\gamma_0 & 0 & f(\mathbf{k})\gamma_4 & f^*(\mathbf{k})\gamma_3 \\ \gamma_5 & 0 & \gamma_1 & f^*(\mathbf{k})\gamma_4 & \Delta & f(\mathbf{k})\gamma_0 \\ 0 & \gamma_2 & f^*(\mathbf{k})\gamma_4 & f(\mathbf{k})\gamma_3 & f^*(\mathbf{k})\gamma_0 & 0 \end{pmatrix} \tag{124}$$

and $|\psi_{\nu\mathbf{k}}\rangle = \left(d^0_{\nu\mathbf{k}}, d^1_{\nu\mathbf{k}}, ..., d^{2N}_{\nu\mathbf{k}}\right)$. It contains $N_\kappa = 2N$ lines and rows with N the number of graphene layers. The band label index ν runs from 1 to $2N$. The eigenenergies for an increasing number of layers are given in Fig. 15. For graphene, Eq. 122 is verified and for $N > 1$, the angular dependency $\theta_{\mathbf{k}}$ can longer be ignored, and analytical results cannot be obtained even near the **K** point.

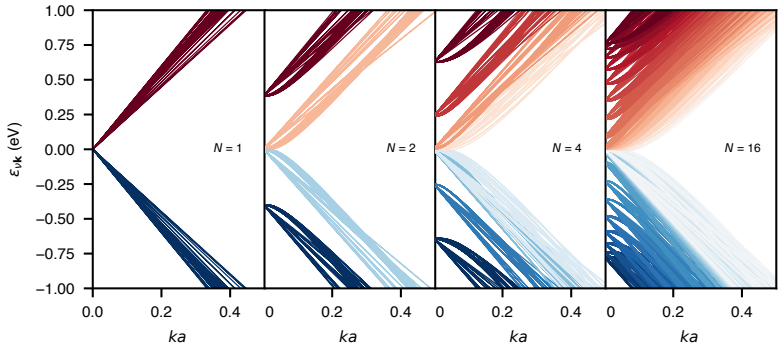

Figure 15: Evolution of the band structure near the **K** point for FLG. The number of graphene layers N are stacked in the Bernal configuration (ABA...). For each band, we represent $N_{\theta_\mathbf{k}} = 20$ angles for the same norm of $k = |\mathbf{k}|$.

Given a wavevector $\mathbf{q}$, we diagonolize $\hat{H}_\mathrm{e}^{(0)}$ for every couple $(\mathbf{k}, \mathbf{k}+\mathbf{q})$ to obtain the eigenenergies and eigenvectors required to calculate $\tilde{\chi}_\mathrm{e}^{(0)}$ in Eq. 116. We compute

$$\tilde{\chi}_\mathrm{e}^{(0)}(\kappa,\kappa') = -g_s g_v \int_0^{k_\mathrm{max}} \frac{\mathrm{d}k}{2\pi} k \int_0^{2\pi} \frac{\mathrm{d}\theta_\mathbf{k}}{2\pi} \sum_{\nu\mu} .... \tag{125}$$
$$...(d^\kappa_{\mu\mathbf{k}+\mathbf{q}})^* d^\kappa_{\nu\mathbf{k}} \frac{n_F(\epsilon_{\mu\mathbf{k}+\mathbf{q}}) - n_F(\epsilon_{\nu\mathbf{k}})}{\omega + i\eta - (\epsilon_{\mu\mathbf{k}+\mathbf{q}} - \epsilon_{\nu\mathbf{k}})} d^{\kappa'}_{\mu\mathbf{k}+\mathbf{q}} (d^{\kappa'}_{\nu\mathbf{k}})^*,$$

where and $g_s = g_v = 2$ is the spin and valley degeneracy. Note that the coefficients $d^\kappa_{\nu\mathbf{k}}$ are orthonormalized. Regarding the U matrix, we shall focus on small wavevectors where $q|\boldsymbol{\tau}| \ll 2\pi$ and use the approximation $U_0(z) \simeq \delta(z)$. Therefore, with $z_\kappa = \frac{c}{2}\lfloor \kappa/2 \rfloor$ we read $\tilde{v}_\mathrm{e}(\kappa,\kappa') = \frac{1}{4\pi\epsilon_0}\frac{2\pi}{q} e^{-q|z_\kappa - z_{\kappa'}|}$. The SRF — that does not depend on the angle of $\mathbf{q}$ — reads, using Eq. 119, $g_\mathrm{e}(q,\omega) = \sum_{\kappa\kappa'} \tilde{\chi}_\mathrm{e}(\kappa,\kappa') e^{-q(z_{\kappa'}+z_\kappa)}$.

5.3 RESULTS

5.3.1 *Numerical details*

We use $\mathrm{d}k = 10^{-3}/a$ and $k_\mathrm{max} = 1/a$. The angular grid is composed of $N_{\theta_\mathbf{k}} = 20$ angles. We fix $\eta = 5$meV. If analytic expressions are invoked [74, 75], they are obtained in the $T = 0$ K limit. We verified that our code reproduces the analytical results of graphene in this limit [74] and focus on room temperature $T = 300$ K.

5.3.2 *Graphene*

In this section, we qualitatively discuss the electronic properties of graphene ($N = 1$) with the help of Fig. 16.

Fig. 16a shows $g_e(q)$ for intrinsic graphene at $T = 0$ K and $T = 300$ K, along with three curves of extrinsic graphene ($E_F \neq 0$) at $T = 0$ K. The constant black dashed curve shows that intrinsic graphene at $T = 0$ K acts like a dielectric, that is $g_e(q) = 1 - 1/\varepsilon_e$ with ε_e the dielectric constant of the material. Indeed, there is no free electrons for $E_F = 0$ and $T = 0$K (see Fig. 15 for $N = 1$).

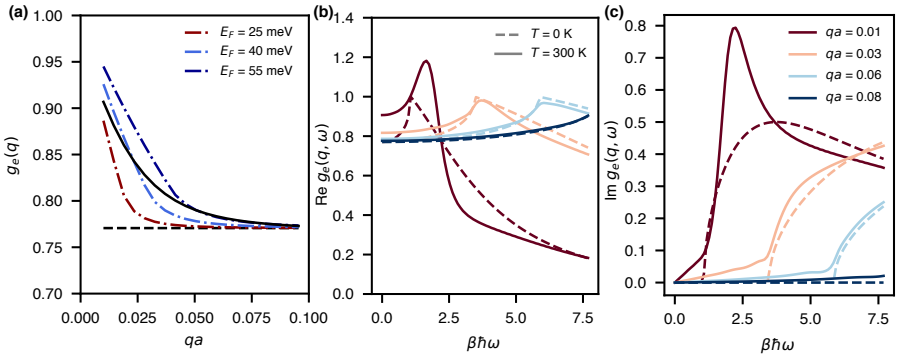

Figure 16: Surface response function (SRF) of graphene $g_e(q,\omega)$. **(a)** Static SRF $g_e(q) = g_e(q,\omega = 0)$ of intrinsic graphene at $T = 0$K (black dashed curved), at $T = 300$K (black curve) and for various doping level E_F at $T = 0$K (dashed dotted curve). Evolution of the **(b)** real and **(c)** imaginary part of $g_e(q,\omega)$ with wavevector and temperature.

For $T = 300$ K, mobile charge carriers are present at the Fermi level due to thermal smearing. Fig. 16a shows that graphene has a metallic behavior — i.e., $g_e(q) \to 1$ for $q \to 0$ — at this temperature. Can we define an effective Fermi surface area at $T = 0$ K, that relates the properties of room temperature graphene? Fig. 16a shows $g_e(q)$ for extrinsic graphene with varying $E_F = \hbar v_F k_F$. We find that $E_F \simeq k_B T \simeq 25$ meV at $T = 0$ K roughly mimics an effective electron concentration at $T = 300$ K for $E_F = 0$. We could therefore benefit from an analytical formula at $T = 0$ K.

Using the small spatial extent of the p_z orbitals of graphene, we use the 2D approximation for graphene:

$$\chi_e^{(0)}(q,z,z') \simeq \delta(z)\delta(z)\int \mathrm{d}z \int \mathrm{d}z \chi_e^{(0)}(q,z,z') = \delta(z)\delta(z)\chi_e^{(0)}(q). \quad (126)$$

Using Eq. 126 and Eq. 113, an analytical formula exists for $\chi_e^{(0)}(q,\omega)$ [74], at $T = 0$ K. We provide the expression of $\chi_e^{(0)}(q)$ in Eq. 345. Solving Eq. 114 and using Eq. 36, we obtain

$$g_e(q,\omega) \overset{2D}{=} \frac{-\chi_e^{(0)}(q,\omega)/2\epsilon_0 q}{1-\chi_e^{(0)}(q,\omega)/2\epsilon_0 q} = 1 - \frac{1}{\varepsilon_e(q,\omega)}, \tag{127}$$

Introducing the TF wavevector $q_{TF} = g_s g_v k_F/4\pi\epsilon_0\hbar v_F$, and inserting Eq. 345 in Eq. 127, we obtain

$$g_e(q < 2k_F) = \frac{q_{TF}}{q+q_{TF}} \qquad g_e(q \gtrsim q_{TF}) = 1 - \frac{1}{\varepsilon_e} \tag{128}$$

with $\varepsilon_e \simeq 1 + g_s g_v/32\epsilon_0\hbar v_F \simeq 4.4$. The form of $g_e(q < 2k_F)$ is similar to the one of a 2D TF metal — with $\varepsilon_e(q) = 1 + \frac{q_{TF}}{q}$ [76]. For $E_F = k_B T$, we can keep in mind

$$q_{TF} a \simeq 0.08 \tag{129}$$

with $a = 2.46$Å. Eq. 128 shows the peculiar semi-metallic properties of graphene. Depending on the external perturbation's wavelength, it acts as a metal or as an insulator. It is difficult to translate this behavior in real space. This behavior can be traced back to the presence of the Dirac cones in the zero-gap band structure of graphene[2].

Turning to Fig. 16b, we scrutinize the dynamical SRF of graphene in the low-frequency region $0 < \hbar\omega < 200$meV. Fig. 16b and Fig. 16c show that $g_e(q,\omega) \simeq g_e(q)$ for $\omega < v_F q$. In fact, at $T = 0$ K, only interband transitions can cancel out the denominator in Eq. 125 — for $\hbar\omega = \epsilon_{+\mathbf{k}+\mathbf{q}} - \epsilon_{-\mathbf{k}} \geq v_F q$. At room temperature, this strict condition is relaxed and dissipation occurs even at low frequencies so that $\mathrm{Im} g_e(q,\omega) \propto \omega$ with varying proportionality coefficient that monotically decreases with increasing q.

5.3.3 *FLG*

Turning to the electronic properties of FLG with Fig. 18, we focus on discussing the qualitative evolution of the SRF with N. Fig. 18 shows the static SRF for $N = 2$ to $N = 4$, which quickly converges. Fig. 18 also shows *(i)* the SRF of intrinsic graphene at $T = 0$ K with a dashed black line, and *(ii)* the analytical SRF of bilayer graphene (BLG) [75] with a gray dashed line.

[2] We note in passing that a recent study [77] has studied the water-graphene interface using the perfect-metal or "mirror" approximation for graphene — i.e., $g_e(q) = 1$. The approximation seems drastic by looking at Eq. 128.

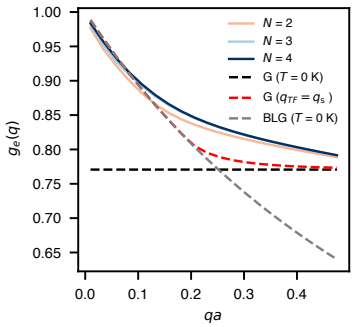

Figure 17: Static SRF of FLG. The curves are shown for $N = 2, 3, 4$ and superimposes with the latter for $N \geq 4$. The black (red) dashed line is the analytical model for graphene [74] using $E_F = 0$ and $E_F = (\hbar v_F)^2 m \log 4$. The grey dashed line is the BLG model [78], $g_e(q) = \frac{q_s}{q+q_s}$.

The latter model considers a 2D material with two parabolic bands — i.e., $\epsilon_{vk} = v\hbar^2 k^2/2m^*$ where $m^* = \gamma_1/2v_F^2$. Within this model, the SRF reads

$$g_e^{\mathrm{BLG}}(q) = \frac{q_s}{q_s + q}, \tag{130}$$

with $q_s = 4m^* \log 4/4\pi\epsilon_0$, and is shown with a gray dashed line in Fig. 17[3]. We keep in mind:

$$q_s a \simeq 0.8. \tag{131}$$

The BLG model captures $g_e(q)$ for $N \geq 2$ and $q \to 0$. However, this result is different from the one of graphene, even at room temperature (see Fig. 16a). The striking difference between graphene and FLG for $q \to 0$ can be understood by comparing Eq. 129 and Eq. 131 — i.e., $q_s/q_{\mathrm{TF}} \simeq 10$. The limit $q \to \infty$ for the SRF $g_e(q)$ of FLG has to be the one of graphene ($N = 1$) because the RPA correction vanishes, and only the immediate vicinity of the surface matters. The BLG model does not capture this crucial limit. However, Fig. 17 shows that the SRF for $N \geq 4$ converges to $g_e(q) = 1 - 1/\varepsilon_e$ of graphene. Therefore, to describe the static SRF of FLG shown in Fig. 17, we suggest to use an effectively doped graphene layer, with $q_{\mathrm{TF}} = q_s$ at $T = 0$ K[4]. It ensures the correct limit for $q \to 0$ and $q \to +\infty$ — see red dashed line in Fig. 17.

Turning to the dynamical SRF of FLG, the complexity of eigenenergies in Fig. 15 prevents us from gaining valuable analytical insights. Fig. 18a and Fig. 18b warn us against naive arguments regarding the number of available states in the low-energy region and the intensity of $\mathrm{Im} g_e(q, \omega)$. Fig.

[3] It is therefore equivalent to the 2D TF metal with $q_{\mathrm{TF}} = q_s$.
[4] It corresponds to an effective doping level of $E_F^{\mathrm{eff}} = 0.27$ eV.

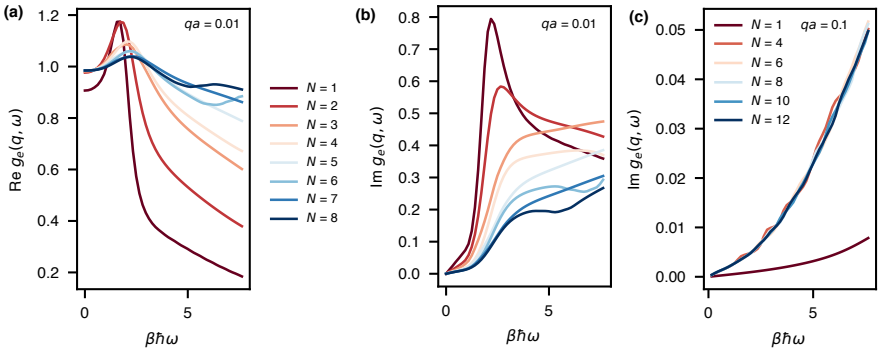

Figure 18: Surface response function $g_e(q,\omega)$ of FLG from $N = 1$ (graphene) to $N = 8$. Evolution of the **(a)** real and **(b)** imaginary part of $g_e(q,\omega)$ with the number of layers for $qa = 0.01$ at $T = 300$K. **(c)** Im$g_e(q,\omega)$ for $qa = 0.1$ and increasing number of layers.

18c shows the convergence with N, for $qa = 0.1$. We will therefore use raw numerical values if we use the dynamical SRF of FLG.

Part III

PREDICTION OF PHYSICAL OBSERVABLES

6

IONIC POTENTIAL OF MEAN FORCE AT INTERFACES

The presence of charges in a wet nanometric channel constituted of graphene sheets leads to exotic ionic behaviors [4, 79, 80, 81]. They are at the cornerstone of energy storage applications [82] and blue energy harvesting [8]. Although experimental data [83, 84] regarding specific graphene-ion interactions in water are still few, the limits of MM to describe those interfaces have been established [85], and the need to describe the system with the same rigor as metal/liquid interfaces [27] has been acknowledged. State-of-the-art quantum calculations combined with solvation codes [86, 87, 88] and even fully explicit AIMD methods [22, 24] have been carried out very recently, but their computational cost remains prohibitive for systematic investigations. On the other hand, although recent semi-classical numerical studies – mimicking the behavior of electrons classically — have described graphene using a perfect metal [77], a TF [30, 89], and an all-atomistic polarizable force field [85, 90] model, they still ignore the peculiar semimetallic band structure of graphene and resort to ad hoc surface polarization models. Lastly, analytical approaches such as continuum electrostatics [33, 60] evaluate the well-known attractive "image-charge" electrostatic potential in a dielectric medium. Spatial correlations of both the fluid and the metal can a priori be included [17, 18, 19, 80] to investigate microscopic effects. However, in our view, this method[1] has not widely been used because of three reasons:

- It uses the phenomenological "specular reflection approximation" (SRA) that lacks physical grounds.
- The self-consistent electrostatic problem is not addressed — i.e. liquid does not "see" the metal and vice-versa.
- It cannot be used for some media, such as water — i.e., the potential diverges.

To our knowledge, the last limit has not been pointed out in the literature. We first prove this statement. Then, we suggest a new method to find the potential of an ion at a metal/dielectric interface by deriving a Hedin's-like equation thanks to our work in part i. We apply this method to find the

[1] Other approximations were initially suggested [91], but they consist of cruder approximations that are not satisfactory from a conceptual point of view (such as the dielectric response of a slab identical to the one of the bulk medium). It also appears that only the SRA has traveled "through the ages" [19, 80].

PMF of ions in a nanometric channel made of two graphene sheets filled with water and finally conclude on the limits of the TF model to describe graphene.

6.1 LIMITS OF EXISTING APPROACHES

6.1.1 *The specular reflection approximation (SRA)*

The SRA was first introduced to address the anomalous skin effects on metallic surfaces [92]. The idea is to express the non-local dielectric tensor of the semi-infinite medium in terms of the same quantity for the infinite medium. It gives up on the possibility of changing the response function of, e.g., the liquid, depending on the nature of the solid. It also considers that the medium terminates abruptly at the interface in $z = 0$. In the standard approch, the constitutive relation (Eq. 264) is fed with the specific dielectric tensor $\underline{\varepsilon}$ shown in Eq. 93. Let us consider a single semi-infinite medium in the lower half-space. The dielectric tensor reads:

$$\begin{aligned} \varepsilon_{\perp}(\mathbf{r}, z_1, z_2) &= \varepsilon_{\perp}(\mathbf{r}, |z_1 - z_2|) - \varepsilon_{\perp}(\mathbf{r}, z_1 + z_2) \\ \varepsilon_{\parallel}(\mathbf{r}, z_1, z_2) &= \varepsilon_{\parallel}(\mathbf{r}, |z_1 - z_2|) + \varepsilon_{\parallel}(\mathbf{r}, z_1 + z_2) \end{aligned} \tag{132}$$

for $z_1, z_2 \leq 0$, where $\perp$ stands for the direction normal to the interface. Here the dielectric function on the right-hand side is the bulk one. Eq. 132 is not physically transparent because it is a phenomenological ansatz. Nevertheless, it has the advantage of being correct in the long-wavelength limit [93] and the electrostatic problem can be solved using the cosine convolution theorem with the appropriate boundary conditions [17].

In the following, we solve the electrostatic problem under the SRA, using Green's functions. We do not resort to Eq. 132, but obtain identical results. We believe our original approach is physically more transparent, facilitating the understanding of the SRA's limits.

6.1.2 *The Green's function of the semi-infinite medium*

We look for the Green's function w of a generic semi-infinite medium situated in the lower half-space $z \leq 0$, such as the one defined in Eq. 33. The medium terminates abruptly in $z = 0$, the upper-half space is a vacuum. For a point charge in the medium, $z' \leq 0$, the electrostatic potential seen from outside in $z \geq 0$ can be written[2]

[2] We omit the index q is this section.

$$w(z,z') = e^{-qz} w(0,z') \quad z \geq 0, z' \leq 0. \tag{133}$$

Identically, in the opposite case of a point charge outside the medium, we have

$$w(z,z') = w(z,0) e^{-qz'} \quad z \leq 0, z' \geq 0, \tag{134}$$

which is also obtained considering the symmetry $w(z,z') = w(z',z)$ of the Green's function [33]. The case $z,z' \geq 0$ is given in Eq. 35. It reads

$$g(q) = -\frac{\Delta w(0,0)}{v(0,0)} \tag{135}$$

with $\Delta w = w - v$. By continuity of w, Eq. 133, Eq. 134, and Eq. 135 are obtained once the case $z,z' \leq 0$ is dealt with. We now tackle this case.

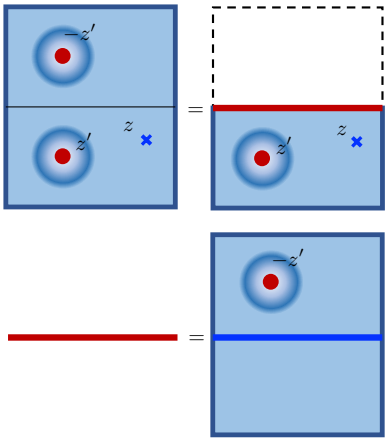

Figure 19: Illustration of the physical assumptions underlying the SRA. The corresponding equations for the first line are Eq. 136 (left) and Eq. 137 (right). External sources are in red and the zone at which the electrostatic potential is evaluated are in bright blue.

The gist of the idea is presented with the help of Fig. 19. We consider an infinite water medium with two test charges symmetrically placed in z' and $-z'$ for a fictitious interface in $z = 0$. The system can also be considered as two semi-infinite media in contact. We introduce the Green's function of the infinite system $w^\infty(z,z') = w^\infty(|z - z'|)$ that we consider to be known. We express the electrostatic potential $\phi(z)$ stemming from the two charges in a point $z \leq 0$, using two different ways. The simplest way is to use the linearity of Poisson's equation and superpose the external perturbations (see Fig 19 upper-left cartoon), that is

$$\phi(z) = w^\infty(z,z') + w^\infty(z,-z'). \tag{136}$$

The second way consists in adopting the two semi-infinite media picture. We focus on the one in the lower half-space because we are looking for its Green's function — that is $w(z,z')$ for $z,z' \leq 0$. First, we separate the screening contribution of the lower semi-infinite medium to the point charge in z' from the remaining contribution, that is $\phi(z) = w(z,z') + ...$ What is missing?

Using Eq. 134 and the insights in Box 3, we can consider that the lower-half medium reacts to a surface charge density applied by the upper-half medium, that is $\phi(z) = w(z,z') + w(z,0) \times$ surface charge. From which external source does this surface charge exists? It is from the charge in $-z'$ that is screened *by the infinite medium* (see second line of Fig. 19) — and not only the upper-half one. Therefore, (see also Fig 19 second cartoon), we read

$$\phi(z) = w(z,z') + w(z,0)\frac{w^\infty(0,-z')}{v(0,0)}. \tag{137}$$

We divided by the bare Coulomb potential to obtain the surface charge instead of the screened potential at the interface. Equating Eq. 136 and Eq. 137 and evaluating in $z' = 0$ allows to solve the equation for $w(z,0)$. Reinjecting into Eq. 137 and equating once again gives

$$w(z,z') = w^\infty(z,z') + w^\infty(z,-z') - \frac{2w^\infty(z,0)w^\infty(0,-z')}{v(0,0)+w^\infty(0,0)} \qquad z,z' \leq 0 \tag{138}$$

which is the main result of this paragraph. Eq. 138 is obtained in [17] if one solves the (difficult) non-local electrostatic problem, using the dielectric tensor given in Eq. 132. Our approach reveals the implicit physical assumptions that are made using Eq. 132 and sheds light upon this approach.

6.1.3 *Limits of the SRA*

Opening the black box in Eq. 132 also helps to understand why it does not work for a case of study, water. First, we precise the expression of w^∞. It is obtained with Eq. 33, replacing the response function of the semi-infinite medium $\chi(z,z')$ by the one of the infinite medium $\chi^\infty(|z-z'|)$. It gives,

$$w^\infty(z,z') = v(z,z') + \int_{-\infty}^{+\infty} \frac{dq_z}{2\pi} v(k)\chi(k)v(k)e^{-iq_z(z-z')} \tag{139}$$

$$= v(z,z') - v(0,0)\bar{\chi}^\infty(q,|z-z'|) \tag{140}$$

with

$$\bar{\chi}^{\infty}(q,z) = \frac{2}{\pi}\int_0^{+\infty} \frac{\mathrm{d}q_z q \bar{\chi}(k)}{q^2+q_z^2}\cos(q_z z). \tag{141}$$

For completeness, we give the expression of the SRF in Eq. 35 that reads

$$g(q) = \frac{\bar{\chi}^{\infty}(q)}{2-\bar{\chi}^{\infty}(q)}, \tag{142}$$

where $\bar{\chi}^{\infty}(q) = \bar{\chi}^{\infty}(q, z=0)$. Using Eq. 138, we find that

$$\text{SRA can be used} \Leftrightarrow \forall\, q, \bar{\chi}^{\infty}(q) < 2 \tag{143}$$

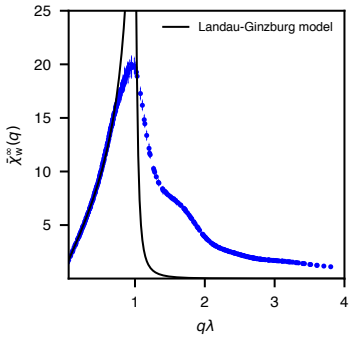

Figure 20: Computation of $\bar{\chi}^{\infty}(q)$ for SPC/E water. For $z = 0$, Eq. 141 is transformed into Eq. 80 and computed for SPC/E water direclty from an MD simulation as a correlation function (see details in 3.1.1). The condition $\forall\, q, \bar{\chi}^{\infty}_{w}(q,0) < 2$ is not met. We add the specific LG fit with $(\alpha, \lambda) = (0.9989, 0.35\text{Å})$.

How to test Eq. 143? The integral in Eq. 141 does not behave nicely for $q \to 0$; numerical integration starting from a model of $\bar{\chi}(k)$ is adventurous. We find that $\bar{\chi}^{\infty}(q)$ can be expressed as a correlation function and directly computed in a MM simulation of bulk SPC/E water molecules. The correlation function and the numerical details are given in 3.1.1 and specifically in Eq. 80 which is obtained from Eq. 141. The results are reported in Fig. 20. We observe that $\bar{\chi}^{\infty}_{w}(q) > 2$ for a large range of wavevectors: the SRA cannot be used for SPC/E water. Using the experimental spectra [63] for $\bar{\chi}(k)$ as input of Eq. 141 leads to the same conclusion.

What is the reason for that? From Eq. 141, we find that $\bar{\chi}(k)$ needs to be larger than 2 for a "large" range of wavevectors. This means that the bulk medium is able to largely over-screen an external response on large range of wavevectors. We can write

$$\forall\, k, \bar{\chi}(k) < 2 \Rightarrow \text{SRA can be used.} \tag{144}$$

Eq. 144 means that the overscreening condition (i.e. $\bar{\chi}(k) > 1$) is not sufficient to prevent the use of the SRA. This divergence can be traced back to the

self-consistent Eq 137. When the ions in z' and $-z'$ come close the interface $z' \to 0$, Eq. 136 states that the potential on the infinite system is the one of a point charge with a partial charge multiplied by 2 — i.e. $\phi(z) = 2w^{\infty}(z, 0)$ —, regardless of the value of $\bar{\chi}^{\infty}(q)$. In contrast, Eq. 137 states that it is zero if $\bar{\chi}^{\infty}(q) = 2$ because we subsequently consider the overscreening of the two semi-infinite media.

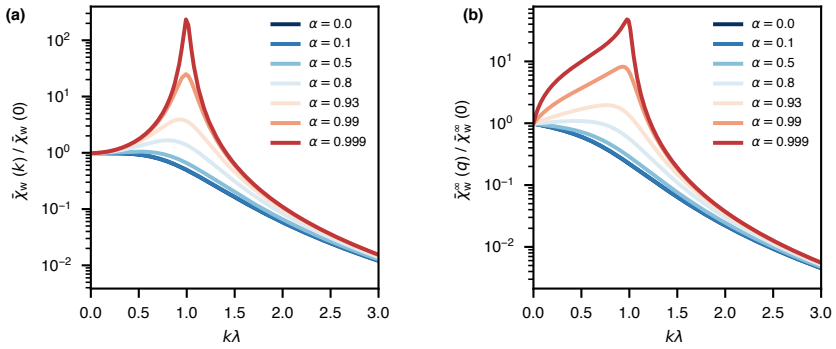

Figure 21: Limits of the specular reflection approximation. **(a)** (**b**) Bulk Landau-Ginzburg susceptibility $\bar{\chi}_{\mathrm{w}}(k)$ for various α. (**b**) Landau-Ginzburg susceptibility $\bar{\chi}^{\infty}_{\mathrm{w}}(q)$ for various α. Note that $\bar{\chi}_{\mathrm{w}}(0) = \bar{\chi}^{\infty}_{\mathrm{w}}(0) = 1 - 1/\varepsilon_{\mathrm{w}}$ with $\varepsilon_{\mathrm{w}} = 71$.

To find a versatile result regarding the limits of the SRA, we adopt a Landau-Ginzburg model [94] to build $\bar{\chi}(k)$ for a dielectric medium and compute Eq. 141 analytically. We use a model that encompasses overscreening [65]. The susceptibility reads[3]:

$$\frac{\bar{\chi}_{\mathrm{w}}(k)}{\bar{\chi}_{\mathrm{w}}(0)} = \frac{1}{1 - 2\alpha^2\lambda^2k^2 + \lambda^4k^4}. \tag{145}$$

The characteristic length λ gives the position of the maximum of $\bar{\chi}(k)$ and $\alpha < 1$ gives the intensity of the peak (see Fig 21a). Eq. 145 only depends on λk so that we can find a condition for the SRA's validity independent of λ.

We express the condition in Eq. 143 as a condition on α. Inserting Eq. 145 in Eq. 141, we compute the integral analytically in Appendix F.1. The result for $\bar{\chi}^{\infty}(q)$ is provided in Eq. 348 and shown Fig. 21b. To linear order in q, we find

$$\frac{\bar{\chi}^{\infty}_{\mathrm{w}}(q)}{\bar{\chi}^{\infty}_{\mathrm{w}}(0)} = 1 + \frac{\lambda q}{2\sqrt{1-\alpha}} + \mathcal{O}(\lambda^2 q^2). \tag{146}$$

We need $1 - \alpha \ll 1$ to make $\bar{\chi}^{\infty}(q) > 2$. Using Fig. 21, we find

$$\text{SRA can be used} \Leftrightarrow \alpha \lesssim 0.93. \tag{147}$$

[3] The LG Hamiltonian of the microscopic polarization reads: $H[\mathbf{P}] = \frac{1}{2\varepsilon_0}\int \mathrm{d}\mathbf{x}\left[r\mathbf{P}^2 - K^2(\nabla\cdot\mathbf{P})^2 + p^4(\nabla(\nabla\cdot\mathbf{P}))^2\right]$. We have used $\alpha = \frac{K}{\sqrt{2}p}\bar{\chi}_{\mathrm{w}}^{1/4}(0)$ and $\lambda = p\bar{\chi}_{\mathrm{w}}^{1/4}(0)$ and $\bar{\chi}_{\mathrm{w}}(0) = 1/(1+r)$.

For water, the result of $\bar{\chi}_{\mathrm{w}}^{\infty}(q)$ computed in MM is fitted with the two-parameters LG model (see Eq. 145). We find an excellent agreement for $\alpha = 0.9989$ and $\lambda^{-1} = q_{\mathrm{w}} = 2.86\text{Å}^{-1}$ as long as $q\lambda < 1$ (see Fig. 7c).

Having established the limits of the SRA, we now overcome them using the tools developped in part i.

6.2 SELF-CONSISTENT HEDIN'S-LIKE EQUATIONS

Hedin proposed [95] an approach to tackle the electron-phonon problem by obtaining a well-known set of self-consistent equations. We have seen in part i how to represent a classical polar liquid by a bosonic operator in the quantum field framework. Therefore, we obtain the same equations for the metal/liquid interface problem. We focus on the screened potential w in the following. We ignore some corrections that are present in Hedin's framework (self-energy and vertex corrections) for simplicity, but they can be incorporated as well (see e.g., chapter 7). A rigorous mathematical derivation can be found in the original article [95] or more recently in [96].

We follow the rules fixed in 2.3.3 for enumerating diagrams. In practice, our approach consists of writing diagrams by hand and finding ways to express them in a compact form. The physical relevant insights only come a posteriori. The automaticity of the approach is a significant advantage of the diagrammatic approach. We do not detail the steps in obtaining Eq. 149 as they result from systematic computations using the rules in 2.3.3. Note that adding phonons can be done easily following the same scheme[4].

6.2.1 *Green's function at interfaces*

There are two convenient ways of organizing diagrams when treating electrons and liquid molecules. Here, we chose to separate the contribution of the liquid because it will be relevant to understand the different contributions to a PMF[5].

The Green's function of the liquid slab w_{w} is given in Eq. 14. The response function of electrons $\chi_{\mathrm{e}}^{(0)}$ can now be renormalized at the mean field level — see Eq. 11. However, the electrons now interact via the Coulomb potential

[4] For n elements, it adds up in enumerating all paths on a complete looped graph with n vertices. Surprisingly, we did not find this remark in the literature, maybe because those graphs represent complex equations making the cases $n \geq 3$ already too complicated if we think about the physical aspect. However, encompassing an entire graph in the form of Eq.149, that is in terms of its "renormalized" vertices, could be very convenient for some fields outside many-particle physics... work in progress.

[5] We use the other "smart" way of organizing the diagrams in the next chapter.

screened by water so that $v_{\text{inter}} = w_{\text{w}}$. This means that we need to introduce the *in situ* response function of electrons $\chi_{\text{e}}^{(\text{w})}$ that reads

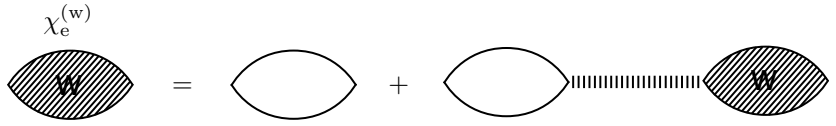

(148)

All diagrams starting and ending with the Coulomb "leg" v are contained by expressing w as follows

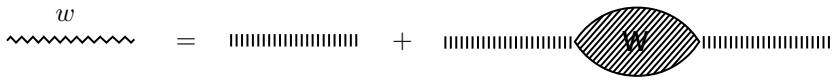

(149)

.

6.2.2 *Special case of the slit geometry*

Until now, our work does not depend on geometry. If the system has one interface, Eq. 149 can be written in terms of the well-identified response function $\chi_{\text{e}}^{(\text{w})}$. In contrast, when two interfaces are present, $\chi_{\text{e}}^{(\text{w})}$ is the response function for the whole electronic part, the two metals with a channel filled with the liquid in between. We understand it is a poor choice because computing the response function of "two metallic plates separated by a water slab of length L" is tedious. It is simpler to decompose it in terms of the non-interacting response function of the two metals, taken separately with some adequate renormalizations.

Naively, we would like to split the electronic response into two parts, one for the electrons at the bottom $\downarrow$ of the channel and one for the electrons at the top $\uparrow$ that is

, (150)

where the diagrams on the right-hand side are the renormalized response functions for the metal in $z \leq 0$ (bottom, $\downarrow$) and at $z \geq L$ (top, $\uparrow$). The diagram on the left-hand side is our first guess. The correct result is not that simple because we neglected cross-correlations. Indeed, according to the aforementioned rules, we miss some diagrams in w and need to combine top and bottom response functions in all possible ways. We can separate all

combinations into four categories depending on their first and last diagram (↑↑,↑↓, ↓↑, ↓↓). The task is easier if we introduce the cross-correlation response function

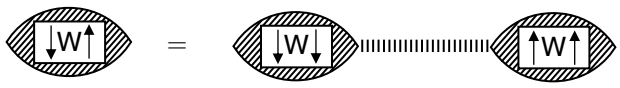

, (151)

and its mean-field renormalized analogue

. (152)

This gives the first two independent integral equations (Eq. 152 can also be written for ↑↓) and the remaining two read

, (153)

— and the same for ↑↑. Assembling the four categories gives the response function that we look for and

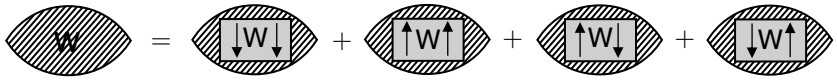

. (154)

It can be checked that if $L \to \infty$, the cross-susceptibilities are 0 and our guess is correct — i.e., Eq. 154 and Eq. 150 are equal.

6.3 COUPLED INTERACTIONS AT IONIC GRAPHENE/WATER INTERFACE

In this section, we use the results of section 6.2, the microscopic water model developed in chapter 4, and the graphene SRF obtained in chapter 5, to study the PMF of an ion in a nanometric slab of water — of length L — confined between two graphene sheets.

6.3.1 *Potential of mean force (PMF)*

The Coulomb free energy of the interfacial graphene/water system, when a spherical test charge $n_{\text{ext}}(\mathbf{x}) = \pm\delta(b - |\mathbf{x} - z_0\mathbf{e}_z|)/4\pi b^2$ of radius b is placed in the channel reads[33]

$$F(z_0) = \frac{1}{2}\iint \mathrm{d}\mathbf{x}\mathrm{d}\mathbf{x}' n_{\text{ext}}(\mathbf{x})\Delta w(\mathbf{x},\mathbf{x}')n_{\text{ext}}(\mathbf{x}'), \tag{155}$$

where $\Delta w = w - v$ and w is the Green's function of the interfacial system. We define the PMF as $\Delta F(z) = F(z) - F(L/2)$. To gain insights into the water and electronic contributions to the PMF, we can further decompose the free energy contribution into two terms: $F = F_{\text{e}} + F_{\text{w}}$, where F_{w} solely contains the contribution of water as in an air/water interface replacing w by w_{w} in Eq. 155.

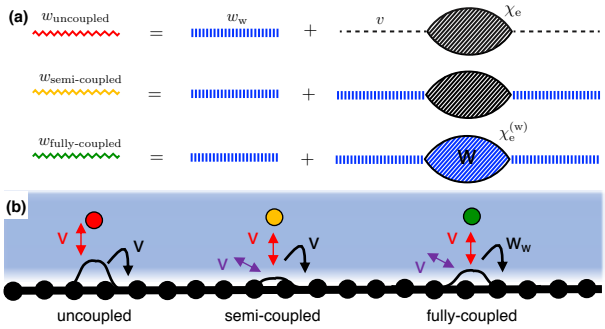

Figure 22: **(a)** Computed Feynman diagrams included in the Green's functions for various approximations. The colors of w match the one of curves in Fig. 23. The dashed line represents the Coulomb potential. The hatched bubble diagram depicts χ_{e}. **(b)** Schematic illustration of the screening in the different cases (see text for interpretation).

We gradually introduce coupled interactions in three steps labeled uncoupled, semi-coupled and fully-coupled to build w from the knowledge of χ_{e} and χ_{w}. Fig. 22 reports the computed Feynman diagrams and the sketched coupling scenarios. First, we consider the uncoupled case, where water and graphene are blind to each other such that w is separable:

$$w_{\text{uncoupled}} = w_{\text{w}} + v * \chi_{\text{e}} * v. \tag{156}$$

Second, we consider the semi-coupled scenario where the polarization charge on the graphene surface results from the potential exerted by the ion and surrounding water molecules. It is the sum of the bare ionic potential and

the one induced by the solvating structure of dipoles, that is, the screened potential that is obtained by the water slab Green's function w_{w} and therefore

$$w_{\text{semi-coupled}} = w_{\mathrm{w}} + w_{\mathrm{w}} * \chi_{\mathrm{e}} * w_{\mathrm{w}}. \tag{157}$$

It is equivalent to an interfacial semi-classical simulation adding a self-consistent optimization of the surface polarization at each time step, taking into account fixed — and equal to their values in the vacuum — site-site interactions of the atomistic model of the metal. Finally, the last fully-coupled case unveils the presence of the polar liquid for electrons of the solid. At the mean-field level, electron-electron interactions are effectively modified due to the presence of water. We introduce the in situ response function of the metal $\chi_{\mathrm{e}}^{(\mathrm{w})}$, which is built from Eq. 11 with $v_{\text{inter}} = w_{\mathrm{w}}$. The most refined Green's function systems therefore reads

$$w_{\text{fully-coupled}} = w_{\mathrm{w}} + w_{\mathrm{w}} * \chi_{\mathrm{e}}^{(\mathrm{w})} * w_{\mathrm{w}}. \tag{158}$$

With the different w expressions for the uncoupled, semi-coupled and fully-coupled cases respectively, three different PMFs can be computed using Eq. 155. Note that the double integration of Eq. 155 is made in Fourier space and by matrix multiplication[6]. The $(i,j)^{\text{th}}$ element of the matrix $M[z_i, z'_j]$ is given by the function $m(q, z_i, z'_j)$. We obtain $w_{\mathrm{w}} = v + v\chi_{\mathrm{w}}v$ in a matrix form, as detailed in chapter 4. For the smoothed step function model of $n_0(z)$, we use $\sigma_0 = 0.3$Å and $d_0 = 1.3$Å$(= d_{\text{Werder}})$, as discussed in 4.2.1. For graphene (see chapter 5), we use the 2D approximation — see Eq. 126— and the analytic form of $\chi_{\mathrm{e}}^{(0)}$ at $T = 0$ K — see Eq. 345 — with an effective Fermi level of $E_F = 25$ meV to take into account temperature. We find a negligible impact of E_F on the PMF. Refinements due to long-range graphene-graphene interactions are detailed in appendix F.2. We converge the PMFs for $L \to +\infty$ and use $L = 6$nm.

6.3.2 *Comparison with AIMD simulations*

Fig. 23a displays the resulting different computed profiles for ΔF for one single positive charge of radius $b = 2$ Å, together with a reference curve computed recently from an AIMD study for K^+ solvated in a 2nm thick water slab on graphene [24]. For sake of comparison, we shift the ab initio

[6] Using $N_{\text{ext}}[z] = J_0(q\sqrt{b^2 + (z - z_0)^2})/2b$ with J_0 being the zeroth order Bessel function, we compute $F(z_0) = \frac{1}{2}\int_0^{+\infty} \frac{\mathrm{d}q}{2\pi} q \left[N_{\text{ext}}^{\dagger}(W - V)N_{\text{ext}}\right](q)$, for the three Green's functions, in log-log space using $q = e^y E_F/v_F$, $y \in [-1, 8]$ and $N_y = 100$ for convergence. Note that $V[z, z'] = e^{-q|z-z'|}/2\epsilon_0 q$.

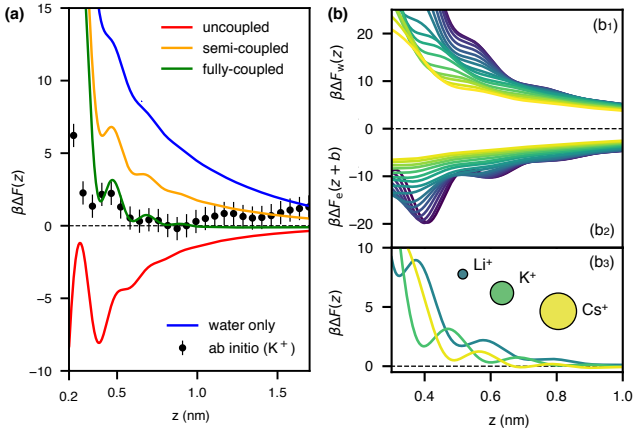

Figure 23: **(a)** PMF of K^+ at the graphene-water interface. We model K^+ by a sphere a radius $b = 2$Å and compare our results with ab initio simulation results [24]. The right side of the ab initio data depicts the part of the PMF that is repulsive for K^+ due to the presence of the hidden air interface at $z \simeq 1.8$ nm [97]. **(b)** Detailed contributions to the PMF from water (b_1) and from graphene (b_2) with varying ionic radius. The ionic center is placed at increasing altitude $\mathbf{x} = (0, 0, z + b)$ for increasing radius. (b_3) Comparative PMF for three alkali ions. The PMF for Li^+ (resp. Cs^+) is obtained using $b = 1$Å (resp. $b = 3$Å).

PMF such that it is vanishing in the middle of the water slab, for z around 1 nm (black dots, Fig. 23a). The water contribution ΔF_w shows the expected repulsive behaviour of the ion at an air/interface (blue curve, Fig. 23a).

Concerning the graphene/water interface, the uncoupled PMF profile (red curve, Fig. 23a) is strongly attractive and presents oscillations with small amplitudes near the surface stemming from the non-local dielectric response of water that is crucial at interfaces.

Indeed, by taking the long-wavelength limit for the description of water henceforth solely described by its dielectric constant ε_w, we can confirm the large magnitude of the error on the PMF near the surface. For an infinite channel height $L \to \infty$, we have

$$w_w(q, z = 0, z = 0) = \frac{1 - g_w(q)}{2\epsilon_0 q}, \tag{159}$$

where $g_w(q)$ is the SRF of water as defined in Eq. 36. Taking the long-wavelenght limit for $g_w(q)$ (see Eq. 41), we obtain that Eq. 159 is the Coulomb potential attenuated by a factor $\varepsilon_w^* = (\varepsilon_w + 1)/2$. Moreover, using Eq. 158, we obtain

$$w(q, z, z') = w_w(q, z, z') + w_w(q, z, 0)\chi_e^{(w)}(q)w_w(q, 0, z'). \tag{160}$$

Close to the surface, for $z \simeq z' \simeq 0$, if we take the long-wavelength limit according of Eq. 159, the second electronic term on the r.h.s. of Eq. 160 is reduced by a factor a roughly $(\varepsilon_w^*)^2 \simeq 1600$, as first noticed in [18].

The uncoupled PMF deviates a lot from the ab initio plot. Interestingly, this strong difference quantifies the large error which is made in MM simulations when the same pairwise ion-carbon potential is used in vacuum and in water [85].

Moving to the semi-coupled PMF profile (orange curve, Fig. 23a), its energy position is shifted to positive values fingerprinting a long-range repulsion and a net reduction of the graphene-ion interaction due to surrounding water molecules. This effect has been already observed in semi-classical simulations [77, 85, 98] using ad hoc surface polarization models. The ionic potential attenuation due to water molecules, evaluated by detailing the electronic contribution in appendix F.3, is in very good agreement with the results of [85].

Finally, the fully-coupled PMF curve (green curve in Fig. 23a) reveals a re-amplification of the wall-ion attraction by several thermal energy units and matches almost quantitatively the ab initio PMF. It is the key finding of our approach. The nice agreement suggests that our semi-analytical approach incorporating electrostatics in a self-consistent way can reproduce some key features of the state-of-art reference PMF like the position and amplitude of the three local minima. The origin of the oscillations will be associated later with the hydration shells of the cation.

To qualitatively rationalize the stabilizing effect in the fully-coupled case, we first need to picture a metallic sheet with independent electrons — responding with $\chi_e^{(0)}$. The unphysical absence of repulsive interaction between charge carriers makes them accumulate to one point to screen the ionic potential. Thanks to electron-electron interactions, a finite polarization charge can accumulate on the surface, as shown by the uncoupled case cartoon in Fig. 22b. Water molecules screen the ionic potential and reduce the polarization charge (semi-coupled case Fig. 22b). However, in the last fully-coupled case, water's presence effectively reduces electron-electron interactions — by roughly a factor of ε_w^* for far apart electrons, as shown in Eq. 159. As a result, the polarization charge gets re-amplified, and so does the surface-ion screened potential.

6.3.3 *Alkali series*

We now investigate the variations of the PMF with the ionic radius b. We first explore a vast continuous range of radii to qualitatively understand its role

on water ΔF_w and surface ΔF_e contributions to the PMF. Then, considering that $b = 2$ Å accurately describes K^+, we highlight the adsorption profiles of a smaller and a larger cation, that is for Li^+ using $b = 1$ Å and Cs^+ using $b = 3$ Å. Fig. 23b_1 shows that water repels more strongly smaller ions from the interface. It can be understood by considering the hydrated radius of the cations that is inversely proportional to the ionic radius [99]. Coming from the bulk, $Li^+$is the first to break its solvation shell. Fig. 23b_2 compares the non-monotonic surface contribution ΔF_e for the series of ions, which center is shifted so that the available space for water molecules between ion and surface is equal for each ion. We link the increasing attraction for smaller radii to the ordering degree of the hydration shells. In the limit of poorly structured hydration shells – e.g. for Cs^+– we find the monotonic surface-ion potential of an attenuated charge in a vacuum. The opposite limit is a point charge with three highly ordered hydration shells. It gives rise to three special places where ice-like water, with low permittivity, is practically transparent to the potential stemming from the polarization charge on the graphene surface. Summing both contributions in Fig. 23b_3 for three cations in the alkali series leads to complex profiles that cannot be easily rationalized. However, we observe that for increasing radius, the three local minima are stabilized and shifted away from the surface, which is in agreement with capacitance experiments [84] and recent quantum simulations [87].

6.3.4 *On the Thomas-Fermi modeling of graphene*

The change of the surface's screening properties in the dielectric medium has been systematically ignored in previous analytical studies because they did not tackle the microscopic problem. For the case of graphene, we have shown that it is a crucial phenomenon captured thanks to considering a relatively accurate description of the collective properties of electrons and water. It raises the question of whether the electronic/dipolar coupling at the graphene/water interface can be captured with a metal/water — and not semi-metal/water — modeling of the interface. To answer this question, we model graphene as a two-dimensional TF metal and try to obtain similar PMFs.

Gaining insights analytically to grasp the eventual differences between the metallic and semi-metallic structures, we introduce the fictitious system that describes a point charge $b \to 0$ in a vacuum ($L \to \infty$) above the "fictitiously solvated" graphene sheet. It amounts to considering the system described by the Green's function $w_{\text{fictitious}} = v + v * \chi_e^{(w)} * v$. We denote by $\Delta F_e^{(\text{fic})}$ the

surface contribution to the PMF of the fictitious system, and using Eq. 160 we obtain

$$\Delta F_{\mathrm{e}}^{(\mathrm{fic})}(z_0) = -\frac{1}{4\pi\epsilon_0}\int_0^{+\infty} \mathrm{d}q g_{\mathrm{e}}^{(\mathrm{w})}(q) e^{-2qz_0}, \tag{161}$$

where $g_{\mathrm{e}}^{(\mathrm{w})}(q) = -\chi_{\mathrm{e}}^{(\mathrm{w})}(q)/2q\epsilon_0$. $\Delta F_{\mathrm{e}}^{(\mathrm{vac})}$ is the similar quantity for the analog real system that considers an unsolvated graphene sheet — i.e., g_{e} instead of $g_{\mathrm{e}}^{(\mathrm{w})}$ in Eq. 161. We have introduced the SRF of the metallic medium $g_{\mathrm{e}}(q)$, its renormalized analog[7]

$$g_{\mathrm{e}}^{(\mathrm{w})}(q) = \frac{g_{\mathrm{e}}(q)}{1 - g_{\mathrm{w}}(q) g_{\mathrm{e}}(q)}, \tag{162}$$

and therefore the one of the polar liquid $g_{\mathrm{w}}(q)$ — see Eq. 86 with $d = d_0$. Eq. 161 reveals that $|\Delta F_{\mathrm{e}}^{(\mathrm{fic})}| > |\Delta F_{\mathrm{e}}^{(\mathrm{vac})}|$ because the denominator of Eq. 162 can be expressed as an infinite sum of contributions that adds to $\Delta F_{\mathrm{e}}^{(\mathrm{vac})}$. Those successive powers of $g_{\mathrm{w}}(q) g_{\mathrm{e}}(q)$ corresponds to an infinite number of convolutions between response functions of the liquid and graphene and therefore depends on the (semi-)metal/liquid couple. It can be understood as a mutual screening process: the polarization charge on the surface is screened by water molecules so the former is magnified and the latter readapt, etc.

The difference between the SRF of graphene (Eq. 127) and the one of a 2D TF metal — i.e., $g_{\mathrm{e}}(q) = q_{\mathrm{TF}}/(q + q_{\mathrm{TF}})$ — such as BLG, have been detailed in chapter 5. We compare those two cases in the following (respectively denoted G and TF). However, we use two values for q_{TF}. The case TF(G) uses q_{TF} from Eq. 129 and the case TF(BLG) uses $q_{\mathrm{TF}} = q_{\mathrm{s}}$ from Eq. 131.

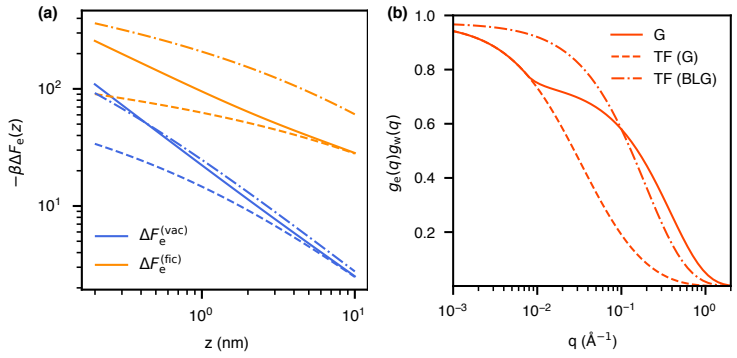

Figure 24: Role of the surface polarization model of graphene on the ionic PMF. (**a**) PMF for G (plain lines), TF(G) (dashed lines) and TF(BLG) (dashed dotted lines). The ion is in a vacuum (blue) and in the fictitious system (orange) **(b)** Product of SRFs $g_{\mathrm{e}}(q) g_{\mathrm{w}}(q)$.

[7] It can be obtained with Eq. 148 for a 2D metal. In fact this is valid for a 3D metal as well (see next chapter).

Fig. 24a shows $\Delta F_e^{(fic)}$ and $\Delta F_e^{(vac)}$ for the three cases. Unsurprisingly, we find that even in the vacuum, TF(G) does not correctly describe ion adsorption. However, a routine procedure of semi-classical simulations is first to fit parameters for the ion-metal potential in vacuum against results from quantum calculations. Here, this amounts to considering the TF(BLG) case in Fig. 24a, where we have tuned $q_{TF} = q_s$ to reproduce the amplitude of the graphene-ion interaction in a vacuum near the surface. Turning to the fictitious system, Fig. 24a shows that $\Delta F_e^{(fic)}$ is largely overestimated. We conclude that describing the ion-graphene potential near the surface both in a vacuum and in water using the same TF model is impossible.

We trace back this observation in the quantity $g_w(q)g_e(q)$, that Eq. 161 and Eq. 162 prompt us to scrutinize. Fig. 24b shows this product for the three models. It points to the fact as long as $2q_{TF}d_0 < 1$, a metal will mainly "see" the polar liquid's macroscopic dielectric constant ε_w. For graphene, in addition, the intermedium distance d gets imprinted in the solvated SRF $g_e^{(w)}(q)$, albeit the length scale decoupling $2q_{TF}d \ll 1$. It can be traced back to the semi-metallicity of graphene, more precisely to the presence of the Dirac cones in the zero-gap band structure of graphene. As a result, the dielectric response of graphene cannot be easily isolated from its aqueous environment, and the amplification of the surface-ion potential due to the presence of water cannot be quantitatively evaluated using a metallic model for graphene.

Conclusion

After highlighting the limits of current approaches, we built a self-consistent theoretical framework that permits us to investigate ionic adsorption analytically at the graphene/water interface. By including graphene's peculiar semi-metallic band structure, building a microscopic model for interfacial water, and considering the mutual screening of the two materials, we obtained results that are in excellent agreement with expensive quantum free energy perturbation methods at a negligible computational cost.

Our PMF predictions for the alkali series agree with experimental observations and permit us to distinguish the liquid water and graphene surface contributions. Beyond the particular case of graphene, our study shows that the attenuation of electron-electron interactions by the surrounding dielectric medium plays an essential role in the adsorption of ions at the metallic interfaces. It suggests that local models of surface polarization miss some critical physical ingredients.

For the particular case of graphene and water, the vacuum gap thickness d changes the screening properties of graphene in constrat to a typical metal with wavevector $2q_{\mathrm{TF}}d < 1$. This phenomenon can only be correctly apprehended if the semi-metallic properties of graphene are included, at least by considering its band structure at the RPA level. We find impossible to model graphene with a TF model that is valid both in water and vacuum.

7

BAND GAP OF WATER-FILLED CARBON NANOTUBES

CNTs are promising materials for numerous applications ranging from microelectronics [100, 101] to optical sensors [102] and solar cells [103]. Most of these potentials can be traced back to the electronic properties [71] of CNTs. Experimental and theoretical works are abundant because CNTs are affordable and composed of carbon atoms only. As a key example, theoretical predictions [104, 105] in the field of exciton photophysics [106] need an accurate description of electron-electron interactions to correctly evaluate the binding energies of these quasiparticles, measured in Raman spectroscopy or fluorescence experiments [107, 108].

The strength of the interaction between charge carriers is crucial because it defines the band-gap of the semiconducting CNT. To compute the band gap value defined by a TB model of graphene combined with a zone-folding approximation, the exchange and correlation electronic energy are estimated via many-body calculations: the so-called GW scheme. In those carbon structures, band-gap variations by a factor as significant as 200% are expected [104] and observed [109], so they are, in fact, crucial.

In most applications, the dielectric environment of semiconducting CNTs is not a vacuum. Its band-gap varies because the liquid or substrate additionally screens the Coulomb interaction between electrons. There has been experimental evidences [110, 111, 112, 113] of the excitonic binding energy redshift and theoretical explanation for the latter [114, 115, 116]. Nevertheless, state-of-the-art models [117] that fit experimental data [118] require the introduction of an effective dielectric constant that depends on a prefactor, the radius of the CNT, the exciton radius and three fitted exponents. It leaves room for improvement, but the difficulty arises from the fact that only exciton binding energies are easily accessible and do not depend only on the electronic band gap. In a pioneer work, Ando [115] calls for a more elaborated model:

> "the sensitive dependence of the environment effect [...] makes the dielectric continuum model marginally valid and may necessitate more elaborate calculations explicitly including microscopic structure of surrounding materials."

We have developed a framework that includes the non-local behavior of the liquid. Therefore, we focus on the crucial first step in evaluating excitons

binding energies in the following: we express the band gap of a CNT immersed in a liquid. It paves the way towards the precise evaluation of band gaps, using adequate evaluation of SRFs. More generally, this work gives an enriched description of surrounding liquids in solid-state condensed-matter studies.

7.1 GW APPROXIMATION AND BAND GAP OF CNTS

7.1.1 *GW approximation*

The single-particle Green's function G follows the Dyson equation that reads

, (163)

where $G^{(0)}$ is the non-interacting Green's function. Hedin [119] has given a self-consistent expression of the self-energy as a functional the Green's function $\Sigma[G]$. However, in practice, a common approach is using the GW approximation. It is known [120, 121] that the most straightforward $G^{(0)}w$ approximation better evaluates the bang gap. In the following we therefore compute

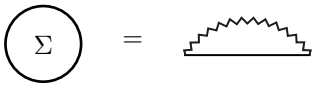

. (164)

Note that the bended line is nothing but the screened potential w, as defined in Eq. 149.

7.1.2 *From graphene to CNTs*

We first obtain Σ for graphene in the Matsubara framework (see appendix G). Then, we make the zone-folding approximation (see appendix G.2) and consider a CNT as a rolled graphene ribbon. We ignore the local curvature of the carbon-carbon bonds. It is a very good approximation for CNTs with

radii $R \geq 2$ nm [71]. We change our spatial notations (see appendix G.2). In cylindrical coordinates, $\mathbf{x} = (\rho, \varphi, z)$, The Fourier transform reads

$$f(\rho,\zeta) = \int_0^L \int_0^{2\pi} \mathrm{d}\varphi \mathrm{d}y f(\mathbf{x}) e^{-i(\varphi l/R + pz)};\ f(\mathbf{x}) = \frac{1}{2\pi L} \sum_{l,p} f(\rho,l,p) e^{+i(\varphi l/R+pz)} \tag{165}$$

where $\zeta = (l,p)$ refers to a wavevector that has continuous component p along the translational vector $\mathbf{T}$ of the CNT — aligned with the CNT axis of length L — and a component l/R along with the chiral vector $\mathbf{C}$ with $|\mathbf{C}| = 2\pi R$ — with l being an integer. The wavefunctions $\psi_{\nu\zeta}(\mathbf{x})$ of the CNT have eigenenergies $\epsilon_{\nu\zeta} = \nu\hbar v_F \sqrt{\kappa^2(l) + p^2}$ with $\nu = \pm 1$, $\kappa(l) = (\sigma/3 + l)/R$ and $\sigma = \pm 1$ for semiconducting CNTs (see Fig. 25a).

Green's functions in Matsubara's framework follow the Dyson equation

$$\frac{1}{\mathcal{G}_\nu(\zeta, ik_n)} = \frac{1}{\mathcal{G}_\nu^{(0)}(\zeta, ik_n)} - \Sigma_\nu(\zeta, ik_n) \tag{166}$$

with $1/\mathcal{G}_\nu^{(0)}(\zeta, ik_n) = ik_n - \epsilon_{\nu\zeta}$ and where $k_n = \pi(2n+1)k_B T/\hbar$ are fermionic frequencies. The RPA self-energy in the $G^{(0)}w$ approximation (see also [104, 114, 115]) and at temperature $T = 1/\beta k_B$ reads

$$\Sigma_\nu(\zeta_0, ik_n) = \frac{-k_B T}{2\pi L_y} \sum_{\mu\zeta} \sum_{i\Omega_m} |\lambda^{\nu\mu}_{\zeta_0,\zeta_0+\zeta}|^2 \mathcal{G}_\mu^{(0)}(\zeta_0+\zeta, ik_n + i\Omega_m) w(\zeta, i\Omega_m), \tag{167}$$

where $w(\zeta, i\Omega_m) = w(\rho = R, \rho' = R, \zeta, i\Omega_m)$ is the Fourier–transformed screened Coulomb potential on the cylinder[1]. It is given by

$$w(\zeta, i\Omega_m) = \int_{-\infty}^{+\infty} \mathrm{d}\omega \frac{\mathrm{Im} w(\zeta,\omega)}{\omega - i\Omega_m}. \tag{168}$$

7.1.3 *Electronic band gap*

Σ_ν contains a static exchange and a dynamical correlation term: $\Sigma_\nu(ik_n) = \Sigma_\nu^{\mathrm{X}} + \Sigma_\nu^{\mathrm{C}}(ik_n)$. We use v instead $w(ik_n)$ in Eq. 167 to obtain Σ_ν^{X}. The correlation term is also split $\Sigma_\nu^{\mathrm{C}}(ik_n) = \Sigma_\nu^{\mathrm{C(static)}} + \Sigma_\nu^{\mathrm{C(dyn)}}(ik_n)$. We use Δw instead of $w(ik_n)$ in Eq. 167 to obtain $\Sigma_\nu^{\mathrm{C(static)}}$. According to [114], gathering all static terms is enough to correctly evaluate the band gap. However, Ando *a priori* excluded the fluid dynamics. It raises the question of whether non-adiabatic

[1] Note that $\lambda^{\nu\mu}_{\zeta_0,\zeta_0+\zeta} = \int \mathrm{d}\mathbf{x} \psi^*_{\nu\zeta_0}(\mathbf{x}) \psi_{\mu\zeta_0+\zeta}(\mathbf{x}) e^{-i(py+l\varphi/R)}$ in analogy to Eq. 106. We have used the equivalent of the 2D approximation for the CNT (see appendix G.2).

effects affect the electronic band gap of CNTs. One needs to compute all terms to answer. After the Matsubara summation in Eq. 167, we obtain

$$\Sigma_\nu(\zeta_0, E) = \frac{-1}{2\pi L_y} \sum_{\mu\zeta} |\lambda^{\nu\mu}_{\zeta_0\zeta_0+\zeta}|^2 \int_{-\infty}^{+\infty} \frac{\mathrm{d}\hbar\omega}{\pi} \frac{\left[n_B(\omega) + n_F(\epsilon_{\mu\zeta_0+\zeta})\right] \mathrm{Im} w(\zeta,\omega)}{\hbar\omega - (\epsilon_{\mu\zeta_0+\zeta} - E) + i\eta}. \tag{169}$$

This is our most general result[2]. It can be computed once $w(\zeta,\omega)$ is obtained.

Following [114], we ignore the dynamics and evaluate the static terms. The Matsubara summation in Eq. 167 leads to

$$\Sigma^{\mathrm{X}}_\nu(\zeta_0) + \Sigma^{\mathrm{C(static)}}_\nu(\zeta_0) = \frac{-1}{2\pi L} \sum_{\mu\zeta} |\lambda^{\nu\mu}_{\zeta_0,\zeta_0+\zeta}|^2 n_F(\epsilon_{\mu\zeta_0+\zeta}) w(\zeta). \tag{170}$$

We insert the expression of $|\lambda^{\nu\mu}_{\zeta_0,\zeta_0+\zeta}|^2$ from Eq. 123[3]. The band-gap reads $E_g = E_g^{(0)} + \Delta E_g$ where the TB band gap reads $E_g^{(0)} = 2\hbar v_F/3R$. After some straighforward steps, using Eq. 170 to compute $\Delta E_g = \Sigma_+(\zeta_0) - \Sigma_-(\zeta_0)$ with $\zeta_0 = (0,0)$, leads to

$$\Delta E_g = \sum_{l=-\infty}^{+\infty} \int_{-\infty}^{+\infty} \frac{\mathrm{d}p}{(2\pi)^2} \frac{\sigma\kappa(l) \tanh(\frac{\beta\epsilon_{+\zeta}}{2})}{\sqrt{\kappa(l)^2 + p^2}} w(\zeta). \tag{171}$$

Eq. 171 diverges logarithmically with the cutoff: the width the graphene's Dirac cone. We follow the "trick" in [114]. We choose a radius-dependent cutoff x_0/R so that $E_g/E_g^{(0)}$ does not depend on R, at $T = 0$K. By restricting their range of validity for $R \lesssim 10$nm, the results only slightly depend on x_0[4].

7.2 SCREENED COULOMB POTENTIAL

7.2.1 *Isolating the electronic contribution*

To obtain the screened static potential w, we can use Eq.149. However, and this is a crucial advantage of our approach, there are 2 compact ways of

[2] n_B and n_F are the Bose-Einstein and Fermi-Dirac distributions, respectively.

[3] Adapted to the cylindrical, it reads $|\lambda^{\nu\mu}_{\zeta_0,\zeta_0+\zeta}|^2 = (1 + \nu\mu \frac{\zeta_0\cdot(\zeta_0+\zeta)}{|\zeta||\zeta+\zeta_0|})/2$.

[4] The idea is to be in the flat region of the logarithm while still keeping a physically relevant cutoff. We use the cutoff function $h_\alpha(x) = \frac{x_0^\alpha}{x_0^\alpha + x^\alpha}$ with $x_0 = 5$ and $\alpha = 4$ and compute

$$\Delta E_g = \frac{1}{2\pi} \sum_l \sigma\kappa(l) \int_0^{+\infty} \frac{\mathrm{d}x}{\pi} \frac{w(l, x|\kappa(l)|)}{\sqrt{1+x^2}} h_\alpha(|\kappa(l)|R\sqrt{1+x^2}). \tag{172}$$

in log-log space, $x = e^y$, $y \in [-10, \log(8x_0)]$ and $N_y = 50$.

expressing w. In contrast to Eq. 149, we now highlight the electronic part (recall the expression of w_e from Eq. 31). It gives

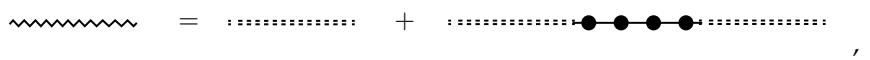

(173)

where the liquid response function renormalized by the presence of the metal $\chi_w^{(e)}$ reads

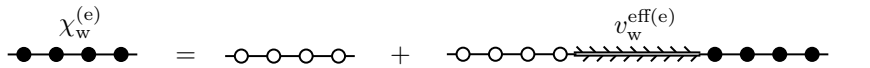

(174)

so that water molecules effectively interact with $v_w^{eff(e)}$

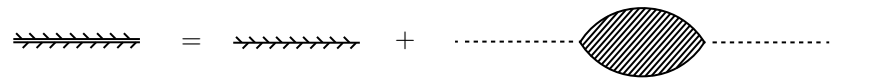

(175)

7.2.2 *A CNT in aa vacuum*

We consider a CNT in a vacuum — i.e., $w = w_e$. In cylindrical coordinates, the Coulomb potential reads[33]

$$v(\rho, \rho', \zeta) = \frac{1}{\epsilon_0} I_l(|p|\rho_<) K_l(|p|\rho_<), \tag{176}$$

where I_l and K_l are modified Bessel function of the first and second kind respectively (of order l). Also $\rho_< = \min(\rho, \rho')$ and $\rho_> = \max(\rho, \rho')$. For a given CNT of radius R, we note $v(\zeta) = I_l(|p|R)K_l(|p|R)/\epsilon_0$. Writing down Eq. 31 using the small spatial extent of the p_z carbon orbitals reads $w_e(\zeta) = v(\zeta) + v(\zeta)\chi_e(\zeta)v(\zeta)$[5]. We recover the relations between the response functions in the 2D planar case:

$$w_e(\zeta) = \frac{v(\zeta)}{\varepsilon_e(\zeta)}; \quad \frac{1}{\varepsilon_e(\zeta)} = 1 + v(\zeta)\chi_e(\zeta); \quad g_e(\zeta) = 1 - \frac{1}{\varepsilon_e(\zeta)}. \tag{178}$$

Within the RPA, $\varepsilon_e(\zeta) = 1 - v(\zeta)\chi_e^{(0)}(\zeta)$ where $\chi_e^{(0)}(\zeta)$ is defined like in Eq. 177. We do not resort to the zone-folding approximation for the response

[5] We have used $\chi_e(\rho, \rho', \zeta) \simeq \frac{1}{\rho\rho'}\delta(\rho - R)\delta(\rho' - R)\chi_e(\zeta)$ and

$$\chi_e(\zeta) = \iint \mathrm{d}\rho_1 \mathrm{d}\rho_2 \rho_1 \rho_2 \chi_e(\rho_1, \rho_2, \zeta). \tag{177}$$

function $\chi_e^{(0)}(\zeta)$, because it makes all CNTs semi-metallic[6]. We compute $\chi_e^{(0)}(\zeta)$ following chapter 5. Adapting Eq. 113 to the static and cylindrical case, we obtain

$$\chi_e^{(0)}(l,p) = -\frac{g_s}{2\pi}\sum_{\sigma}\sum_{\nu\mu}\sum_{m}\int_{-\infty}^{+\infty}\frac{dk}{2\pi}|\lambda^{\mu\nu}_{\zeta_0+\zeta,\zeta_0}|^2\frac{n_F(\epsilon_{\mu(m+l,k+p)}) - n_F(\epsilon_{\nu(m,k)})}{\epsilon_{\mu(m+l,k+p)} - \epsilon_{\nu(m,k)}}. \tag{180}$$

The sum over the $\sigma = \pm 1$ symbol stems from the **K** and **K**′ contributions.

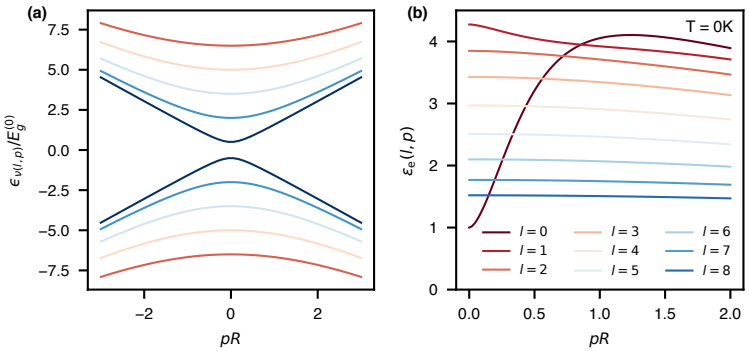

Figure 25: Eigenenergies and static dielectric function of CNTs. **(a)** Eigenenergies of a semiconducing CNT ($\sigma = +1$) normalized by the band gap $E_g^{(0)}$. **(b)** Evolution of $\varepsilon_e(l,p)$ with angular momentum l at $T = 0$ K (no radius dependency).

Fig. 25b shows the dielectric function $\varepsilon_e(\zeta)$, at $T = 0$K. It only depends on pR and l. For $l \neq 0$, $\varepsilon_e(l,p) \simeq \varepsilon_e(l, p \to 0)$. Acccordingly, a CNT responds like a dielectric for an excitation along its circumference. The $l = 0$ term quantifies intraband and interband (between bands depicted with the same color in Fig. 25a) transitions. For $pR > 1$, the finite band mass[7] near the **K** point is not seen and we recover the results of graphene. Using the zone-folding approximation (see Eq. 179), we find $\varepsilon_e(l = 0, p \to \infty) = \varepsilon_e$, for $R \to \infty$. For $pR < 1$, at $T = 0$ K, intraband transitions are suppressed

[6] Even if we *do not* resort to this approximation, it is instructive to link $\varepsilon_e(\zeta)$ with the planar dielectric function $\varepsilon_e(\mathbf{q})$. In the available orthonormal basis, we can decompose an "in-plane" wavevector $\mathbf{q}_\zeta = \frac{l}{R}\frac{\mathbf{C}}{|\mathbf{C}|} + p\frac{\mathbf{T}}{|\mathbf{T}|}$ for the CNT. Comparing the planar and cylindrical expression for the linear response (Eq. 1) we obtain that $\rho'\chi_e(\rho,\rho',\zeta) = \chi_e(\mathbf{q}_\zeta, \rho - R, \rho' - R)$ equating both equations. Further, making the 2D approximation or its cylindrical equivalent, we obtain $\chi_e^{(0)}(\zeta) = R\chi_e^{(0)}(\mathbf{q}_\zeta)$. The zone-folding approximation for the response functions therefore links the dielectric function of the CNT with the response function of graphene as follows:

$$\varepsilon_e(\zeta) = 1 - Rv(\zeta)\chi_e^{(0)}(\mathbf{q}_\zeta) \tag{179}$$

In the limit $R \to \infty$, we should recover the response function of graphene. In fact, writing $\rho = R + z_1$, $\rho' = R + z_2$ and taking the limit $R \to \infty$ gives

$$v(\rho,\rho',\zeta) \xrightarrow[R\to\infty]{} \delta_l \frac{2\pi}{|p|R} e^{-|p||z_1 - z_2|}.$$

Therefore, we recover the graphene dielectric function for $R \to \infty$, with only the $l = 0$ terms remaining. More details can be found here [122].

[7] what makes the band parabolic.

because the Fermi level is in the band gap — i.e., $\varepsilon_e(l=0, p\to 0)=1$. Eq. 172 using $w_e(\zeta)=v(\zeta)/\varepsilon_e(\zeta)$ gives

$$\frac{E_g}{E_g^{(0)}}=2.3\,, \tag{181}$$

in agreement with [114, 123].

At $T=300$ K (see Fig. 42 in appendix G.2), the $l=0$ component is radius-dependent. For large gap CNTs (i.e., small R), thermal smearing puts some holes/electrons in the valence/conduction band. Departure from the $T=0$ K case is limited for $pR>1$. However, the long-wavelength limit changes to $\varepsilon_e(l=0,p)\xrightarrow[p\to 0]{}\infty$, which confers a metallic character to the CNT. The evaluation of Eq. 172 gives $E_g/E_g^{(0)}=2$ for $R=1.5$ nm and $E_g/E_g^{(0)}=1.16$ for $R=6.4$ nm.

The band bap is temperature-dependent, and a systematic investigation is required to account for the results properly. We focus on obtaining w in the presence of a liquid with varying dielectric constant. To restrict the parameter space, we use $T=0$ K for electros and eliminate the radius dependency.

7.2.3 *A liquid outside or inside a CNT*

We insert a liquid inside *or* outside a CNT. Adapting Eq. 14 to the cylindrical geometry, we write the equivalent of Eq. 35 for the liquid[8]. As in the planar case ($\zeta \rightleftarrows q$), we obtain

$$w_w^{\text{in/out}}(\zeta)=v(\zeta)\left[1-g_w^{\text{in/out}}(\zeta)\right], \tag{182}$$

but where the SRFs now read

$$g_w^{\text{out}}(\zeta)=\frac{-I_l(|p|R)}{\epsilon_0 K_l(|p|R)}\iint_R^{+\infty}\mathrm{d}\rho_1\mathrm{d}\rho_2\rho_1\rho_2\chi_w(\zeta,\rho_1,\rho_2)K_l(|p|\rho_1)K_l(|p|\rho_2); \tag{183}$$

$$g_w^{\text{in}}(\zeta)=\frac{-K_l(|p|R)}{\epsilon_0 I_l(|p|R)}\iint_0^{R}\mathrm{d}\rho_1\mathrm{d}\rho_2\rho_1\rho_2\chi_w(\zeta,\rho_1,\rho_2)I_l(|p|\rho_1)I_l(|p|\rho_2). \tag{184}$$

Following this direction, one could express Eq. 149 in terms of SRFs. However, the contributions of electrons and liquid molecules are not sepa-

[8] It reads $w_w^{\text{out}}(\rho,\rho',\zeta)=v(\rho,\rho',\zeta)-\frac{1}{\epsilon_0}g_w^{\text{out}}(\zeta)K_l(|p|\rho)I_l(|p|\rho')$ for $\rho,\rho'\le R$ and $w_w^{\text{in}}(\rho,\rho',\zeta)=v(\rho,\rho',\zeta)-\frac{1}{\epsilon_0}g_w^{\text{in}}(\zeta)I_l(|p|\rho)K_l(|p|\rho')$ for $\rho,\rho'\ge R$.

rated. To identify the band gap variation when inserting a liquid, we use Eq. 173 and obtain

$$w(\zeta) = w_e(\zeta)\left(1 - \frac{g_w^{\text{in/out(e)}}(\zeta)}{\varepsilon_e(\zeta)}\right), \tag{185}$$

where $g_w^{\text{in/out(e)}}(\zeta) = g_w^{\text{in/out}}(\zeta)/\left[1 - g_e(\zeta)g_w^{\text{in/out}}(\zeta)\right]$, as discussed in Eq. 162[9]. Using Eq. 185 and Eq. 178, we look for the total dielectric function — i.e., $w(\zeta) = v(\zeta)/\varepsilon(\zeta)$ — and obtain[10]

$$\varepsilon(\zeta) = \varepsilon_e(\zeta) + \frac{g_w^{\text{in/out}}(\zeta)}{1 - g_w^{\text{in/out}}(\zeta)}. \tag{187}$$

Eq. 187 can be understood as the capacitance of two parallel capacitors (electrons and liquid), in contrast to Eq. 99. Using Eq. 187 and Eq. 183-184, one can therefore compute the band gap of a partially solvated CNT.

7.2.4 *A CNT immersed in a liquid*

For an immersed CNT, the continuum electrostatic limit [115] merely considers a CNT placed in a background dielectric constant of ε_w. From our microscopic perspective, the liquids on both sides of the CNT are not the same because of the non-zero volume of the CNT in which liquid molecules cannot penetrate. We consider two independent interfaces. The SRF of each

[9] In fact, whereas the renormalization of g_e in $g_e^{(w)}$ can be easily understood for the 2D case of graphene (Eq. 162), it is not evident for the 3D case. Using the matrix notation, we can however show that the renormalizations process can be permuted (first electron interaction, second water molecules or vice versa). It reads

$$\begin{aligned} X_w^{(e)} &= \left[I - X_w^{(0)}\left(V_w^{\text{eff}} + \Delta W_e\right)\right]^{-1} X_w^{(0)} \\ &= \left[\left(I - X_w^{(0)} V_w^{\text{eff}}\right)\left(I - \left(I - X_w^{(0)} V_w^{\text{eff}}\right)^{-1} X_w^{(0)} \Delta W_e\right)\right]^{-1} X_w^{(0)} \\ &= \left[I - \left(I - X_w^{(0)} V_w^{\text{eff}}\right)^{-1} X_w^{(0)} \Delta W_e\right]^{-1} \left(I - X_w^{(0)} V_w^{\text{eff}}\right)^{-1} X_w^{(0)} \\ &= (I - X_w \Delta W_e)^{-1} X_w \end{aligned} \tag{186}$$

The integration of Eq. 36 applied to $X_w^{(e)}$ then leads to $g_w^{(e)} = g_w/(1 - g_e g_w)$.

[10] Obviously, it does not matter if one starts from Eq. 149 or Eq. 173 to obtain Eq. 187.

one needs to be renormalized by the presence of the other. Conceptually, it has been done in 6.2.2[11]. Adapting those results, we find[12]

$$w(\zeta) = w_{\mathrm{e}}(\zeta)\left(1 - \frac{g_{\mathrm{w|e|w}}(\zeta)}{\varepsilon_{\mathrm{e}}(\zeta)}\right), \tag{188}$$

where $g_{\mathrm{w|e|w}}(\zeta)$ reads

$$g_{\mathrm{w|e|w}}(\zeta) = \frac{g_{\mathrm{w}}^{\mathrm{in(e)}}(\zeta) + g_{\mathrm{w}}^{\mathrm{out(e)}}(\zeta) - 2g_{\mathrm{w}}^{\mathrm{in(e)}}(\zeta)g_{\mathrm{w}}^{\mathrm{out(e)}}(\zeta)/\varepsilon_{\mathrm{e}}(\zeta)}{1 - g_{\mathrm{w}}^{\mathrm{in(e)}}(\zeta)g_{\mathrm{w}}^{\mathrm{out(e)}}(\zeta)/\varepsilon_{\mathrm{e}}^{2}(\zeta)}. \tag{189}$$

Making some rearrangements and generalizing to the dynamical case, we obtain

$$\varepsilon(\zeta,\omega) = \varepsilon_{\mathrm{e}}(\zeta,\omega) + \frac{g_{\mathrm{w}}^{\mathrm{in}}(\zeta,\omega)}{1 - g_{\mathrm{w}}^{\mathrm{in}}(\zeta,\omega)} + \frac{g_{\mathrm{w}}^{\mathrm{out}}(\zeta,\omega)}{1 - g_{\mathrm{w}}^{\mathrm{out}}(\zeta,\omega)} \tag{190}$$

Eq. 188 and Eq. 183-184 constitute the central result of this chapter.

Eq. 188 shows the contribution of three parallel capacitors and is also valid in the planar geometry ($\zeta \rightleftarrows q$). It deals with all cases (inside, outside, inside and outside) at once. Most importantly, it conferes to the liquid a non-local and dynamical response and one can therefore tackle Eq. 169. It relies on a microscopic computation of SRFs (Eq. 183 and Eq 184).

We leave for future work the construction of a specific microscopic model to obtain $g_{\mathrm{w}}^{\mathrm{in}}(\zeta)$ and $g_{\mathrm{w}}^{\mathrm{out}}(\zeta)$, or the conduction of MM simulations in order to calculate them. We have shown in part ii how to do so. However, we check that we recover known results in the continuum electrostatic limit.

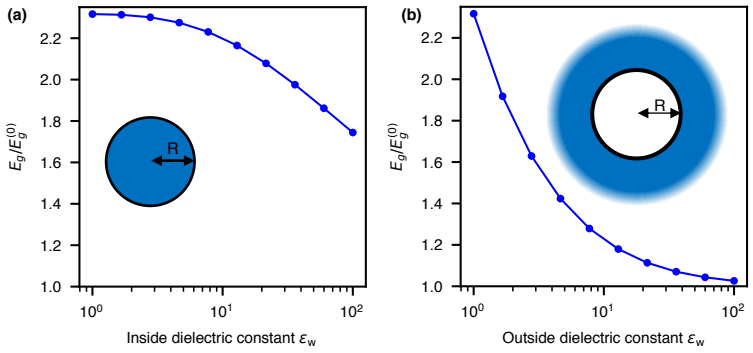

Figure 26: Electronic band gap of a CNT with a dielectric material (ε_w) inside **(a)** and outside **(b)**, at $T = 0K$ (electronic temperature). Note the $E_g^{(0)} = \frac{2\hbar v_F}{3R}$ is the tight-binding band gap. As mentioned in the text, this is valid for $R \lesssim 20a$.

7.3 RESULTS

In appendix G.3, we solve the continuum electrostatic problem to find $g_w^{in/out}(\zeta \to 0)$, assuming an homogeneous, isotropic dielectric medium with dielectric constant ε_w. We find

$$g_w^{in}(\zeta \to 0) = \frac{\varepsilon_w - 1}{\varepsilon_w + 1/\alpha_l(|p|R)} \qquad g_w^{in/out}(\zeta \to 0) = \frac{\varepsilon_w - 1}{\varepsilon_w + \alpha_l(|p|R)}, \quad (191)$$

with

$$\alpha_l(|p|R) = -\frac{K_l(|p|R)}{K_l'(|p|R)} \frac{I_l'(|p|R)}{I_l(|p|R)}. \quad (192)$$

Using Eq. 191, Eq. 187 and Eq. 172, we evaluate the electronic band gap for a liquid inside or outside the CNT in Fig. 26. For large dielectric constants, $E_g \simeq E_g^{(0)}$ because the electron-electron interactions are completely screened. However, a dielectric background outside the CNT has more effect than inside. Those results have been obtained in [115].

For an immersed CNT, using Eq. 190 and Eq. 191, we obtain

$$\varepsilon(\zeta \to 0) = \varepsilon_e(\zeta) + \varepsilon_w - 1, \quad (193)$$

[11] It has been done for the reversed case, a liquid slab delimitated by two metals. We make the substitutiuon e $\rightleftarrows$ w in Eq. 154

[12]

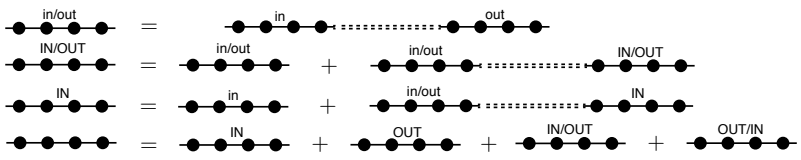

which is explicitly used in [115]. Therefore, our approach recovers the state-of-the-art result in the static and long-wavelength limit.

Conclusion

In this chapter 7, we have built theoretical tools that were called for in the scientific community interested in evaluating electronic band gaps of CNTs. In routine calculations, the liquid is merely described by its dielectric constant ε_w. A pioneering researcher pointed out the limit of this method in one of his articles [115]. Our framework, which uses Hedin's approach for constructing the screened potential, expresses the dielectric function on the tube in terms of SRFs. It confers non-local and dynamical properties to the liquid. We provide the microscopic correlations functions to compute in order to evaluate them. Beyond the particular case of CNTs, we hope that our work, enriching the description of the surrounding liquid in solid-state calculations, will interest researchers in solid-state physics.

Future work

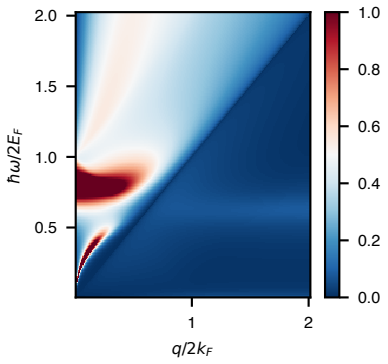

Figure 27: Loss function $-\mathrm{Im}\,[1/\varepsilon(q,\omega)]$ of solvated graphene. The electronic temparature is $T = 0$K and Fermi energy $E_F = 70$ meV. We used the model of Eq. 88 for $g_w(q,\omega)$ with $d = 1.52$Å.

To show the practical advantages of our approach for some solid-state physics applications, we conclude this chapter with an example in the field of graphene plasmonics [124]. We argue that the plasmon dispersion can be evaluated precisely with Eq. 190. One usually solves Eq. 193 to find plasmon modes of solvated graphene [74]. Let us use Eq. 190 instead. For a graphene sheet immersed in water, it reads

$$\varepsilon(q,\omega) = \varepsilon_e(q,\omega) + \frac{2g_w(q,\omega)}{1 - g_w(q,\omega)} \tag{194}$$

where $g_{\mathrm{w}}(q,\omega)$ is the SRF of water (Eq. 88) and $\varepsilon_{\mathrm{e}}(q,\omega)$ is the dielectric function of graphene (at $T = 0$ K, see Eq. 127 and Eq. 178).

Fig. 27 shows the loss function $\mathrm{Im}\left[-1/\varepsilon(q,\omega)\right]$ of solvated graphene. The libration peak of water (large red area) acts as a damped surface optical phonon that modifies graphene's intrinsic plasmon (thin bright red spot in the lower-left part) and creates satellites for $\hbar\omega > 2E_F$ (light red area). Those insights are absent in the literature for liquids (for solid dielectric substrate see, e.g., [125] for graphene). It paves the way toward a more refined plasmon dispersion evaluation thanks to a microscopic description of dielectrics at metal surfaces.

INTERMEZZO: METAL/LIQUID VAN DER WAALS ENERGY

THEORY

We evaluate the vdW energy between a metal and a liquid in this interlude. We recover, in our framework, the well-known Lifshitz formula. Computing solid/liquid vdW energies is tedious because it requires the knowledge of the excitation spectra of the liquid and the solid in the entire range of energies. It is a common issue for MM or AIMD simulations that resort to ansatz in computing such types of interactions. Therefore, this interlude links our description and the use of LJ parameters in MM.

First, we find the mean interfacial electrostatic energy between the metal and the liquid. It can be written $\langle \hat{U}_{\rm ew} \rangle = \langle \delta\hat{U}_{\rm ew} \rangle + U^0_{\rm ew}$. In 3.2.2, we obtained $U^0_{\rm ew} = 0$ for a neutral liquid and a metal. We now assume $n^0_{\rm m} = 0$ and $n^0_{\rm w} = 0$. Using Eq. 42, we find

$$\begin{aligned} \langle \hat{U}_{\rm ew}(t_1) \rangle &= \int \mathrm{d}\mathbf{x}_1 \int \mathrm{d}2 v(12) \langle \delta\hat{n}_{\rm e}(1) \delta\hat{n}_{\rm w}(2) \rangle \\ &= \frac{i\hbar}{2} \int \mathrm{d}\mathbf{x}_1 \int \mathrm{d}2 v(12) \chi^{\rm K}_{\rm ew}(12). \end{aligned} \tag{195}$$

Using $v(12) \propto \delta(t_1 - t_2)$ and making the Fourier transform in the plane, we obtain

$$\langle \hat{U}_{\rm ew}(t_1) \rangle = \frac{i\hbar}{2} \sum_{\mathbf{q}} \iint \mathrm{d}z_1 \mathrm{d}z_2 v(q, z_1, z_2) \chi^{\rm K}_{\rm ew}(q, z_1, z_2, t_1). \tag{196}$$

At equilibrium, $\langle \hat{U}_{\rm ij}(t_1) \rangle$ does not depend on t_1 and we fix $t_1 = 0$. $\chi^{\rm K}_{\rm ew}$ is linked to $\chi^{\rm R}_{\rm ew}$ by virtue of the FDT in Eq. 71. It reads

$$\langle \hat{U}_{\rm ew} \rangle = -\sum_{\mathbf{q}} \int \frac{\mathrm{d}\hbar\omega}{2\pi} f(\omega) \iint \mathrm{d}z_1 \mathrm{d}z_2 v(q, z_1, z_2) \mathrm{Im}\chi_{\rm ew}(q, z_1, z_2, \omega), \tag{197}$$

where $f(\omega) = \coth(\beta\hbar\omega/2)$. The integration over z_2 is restricted to $z_2 > 0$ because it runs over liquid molecules and the one of z_1 for $z_1 < 0$ because it runs over the electron positions. We define a new SRF that reads

$$g_{\rm ew}(q, \omega) = +\frac{1}{2q\epsilon_0} \iint \mathrm{d}z_1 \mathrm{d}z_2 e^{qz_1} e^{-qz_2} \chi_{\rm ew}(q, z_1, z_2, \omega). \tag{198}$$

Using Eq.197 and Eq. 198, we find

$$\langle \hat{U}_{\text{ew}} \rangle = -\sum_{\mathbf{q}} \int \frac{\mathrm{d}\hbar\omega}{2\pi} f(\omega) \mathrm{Im} g_{\text{ew}}(q,\omega). \tag{199}$$

The vdW energy is due to charge fluctuations in both media. A type of thermodynamical integration must therefore be computed for $\langle \hat{U}_{\text{ew}} \rangle$. We use the adiabatic connection to slowly drive the Hamiltonian $\hat{H}_0$ to $\hat{H}$ while remaining in the ground state [126]. We introduce the parameter λ such that $\hat{H}_\lambda$ represents the Hamiltonian in which electron-liquid interactions are reduced by a factor $0 \leq \lambda \leq 1$. We write $\hat{U}_{\text{ew}} = U_\lambda [\hat{n}_{\text{e}}, \hat{n}_{\text{w}}]$,where U_λ means that a factor λ attenuates the Coulomb interactions in Eq. 42: $v \to \lambda v$. The energy $E_\lambda = \langle \hat{H}_\lambda \rangle_\lambda$ is evaluated for a fixed λ. We write

$$E_{\text{ew}}^{\text{vdW}} = E_1 - E_0 = \int_0^1 \mathrm{d}\lambda \frac{\mathrm{d}E_\lambda}{\mathrm{d}\lambda}, \tag{200}$$

and use the Hellman-Feynman [127] theorem, $\frac{\mathrm{d}E(\lambda)}{\mathrm{d}\lambda} = \langle \frac{\mathrm{d}\hat{H}_\lambda}{\mathrm{d}\lambda} \rangle_\lambda$, to obtain

$$E_{\text{ew}}^{\text{vdW}} = \int_0^1 \frac{\mathrm{d}\lambda}{\lambda} \langle \hat{U}_{\text{ew}} \rangle_\lambda. \tag{201}$$

Inserting Eq. 199 in Eq. 201, we define g_{ew}^λ as the SRF with $v \to \lambda v$. We find

$$E_{\text{ew}}^{\text{vdW}} = -\sum_{\mathbf{q}} \int \frac{\mathrm{d}\hbar\omega}{2\pi} f(\omega) \int_0^1 \frac{\mathrm{d}\lambda}{\lambda} \mathrm{Im} g_{\text{ew}}^\lambda(q,\omega). \tag{202}$$

To obtain g_{ew}^λ, we look for χ_{ew}. We use the rules of 2.3.3 and write down all linked diagrams that start with δn_{e} and end with δn_{w}. We obtain

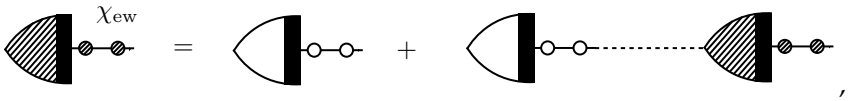

, (203)

with

. (204)

In Eq. 203, the Coulomb potential is always separable $v(q,z,z') = e^{\mp qz} e^{\pm qz'} 1/2q\epsilon_0$ — see also the remark below Eq. 198. Moreover, the double integration in Eq. 197 can actually be interpreted as a trace in the (z,z') basis: $g_{\text{ew}} = \mathrm{Tr}\,[V X_{\text{ew}}]$. Therefore, using $V = SS^T$ and the cyclic property of the

trace we get $g_{\rm ew} = \mathrm{Tr}\left[S^T X_{\rm ew} S\right] = S^T X_{\rm ew} S$. This greatly simplifies our work. Using Eq. 204, we obtain

$$g_{\rm ew}^{(0)} = \mathrm{Tr}\left[V X_{\rm ew}\right] = \mathrm{Tr}\left[S S^T X_{\rm e} S S^T X_{\rm w}\right] = \mathrm{Tr}\left[S^T X_{\rm e} S S^T X_{\rm w} S\right] = g_{\rm e} g_{\rm w}. \quad (205)$$

We solve Eq. 203 using Eq. 205. It reads

$$g_{\rm ew} = \frac{g_{\rm e} g_{\rm w}}{1 - g_{\rm e} g_{\rm w}}. \quad (206)$$

Obtaining $g_{\rm ew}^{\lambda}$ is straighforward from Eq. 206. Making the integration of Eq. 202, we obtain

$$\int_0^1 \frac{\mathrm{d}\lambda}{\lambda} g_{\rm ew}^{\lambda}(q,\omega) = \int_0^1 \mathrm{d}\lambda \frac{g_{\rm e} g_{\rm w}}{1 - \lambda g_{\rm e} g_{\rm w}} = -\log\left(1 - g_{\rm e} g_{\rm w}\right). \quad (207)$$

Inserting Eq. 207 in Eq. 202, we find

$$\frac{E_{\rm ew}^{\rm vdW}(d)}{\mathcal{A}} = \int \frac{\mathrm{d}^2\mathbf{q}}{(2\pi)^2} \int \frac{\mathrm{d}\hbar\omega}{2\pi} f(\omega) \mathrm{Im}\left[\log\left(1 - g_{\rm e}(q,\omega) g_{\rm w}(q,\omega) e^{-2qh}\right)\right]. \quad (208)$$

where we have separated both media by a distance h[13]. Eq. 208 generalizes Lifshitz's formula for vdW interactions between solids [128], as recently obtained in [129]. Our result does not distinguish quantum solids or classical liquids and uses well-defined microscopic SRFs. Using Matsubara's summation[14], we find

$$\frac{\beta E_{\rm ew}^{\rm vdW}(h)}{\mathcal{A}} = \sum_{i\Omega_n} \int_0^{+\infty} \frac{\mathrm{d}q}{2\pi} q \log\left(1 - g_{\rm e}(q, i\Omega_n) g_{\rm w}(q, i\Omega_n) e^{-2qh}\right). \quad (210)$$

where $\Omega_n = 2\pi n k_B T$.

The summation in Eq. 210 extends to large frequencies (see also the $\coth(\beta\hbar\omega/2)$ factor in Eq. 208). In practice, atomic electronic excitations of $\Omega_n \simeq 100\mathrm{eV}$ are required to reach $\varepsilon(i\Omega_n) = 1$ [130]! The study of the SRF in the high-frequency limit is beyond the scope of this work. The work in part ii allows for evaluation of the zeroth-order ($i\Omega_n = 0$) term only. It reads $E_{\rm ew}^{\rm vdWo}(h)$, with

$$\frac{\beta E_{\rm ew}^{\rm vdWo}(h)}{\mathcal{A}} = \int_0^{+\infty} \frac{\mathrm{d}q}{2\pi} q \log\left(1 - g_{\rm e}(q) g_{\rm w}(q) e^{-2qh}\right). \quad (211)$$

[13] It has nothing to do with the incompressible size of the vacuum gap d that exists for $h = 0$.

[14] We use

$$\int \frac{\mathrm{d}\hbar\omega}{2\pi} f(\omega) \mathrm{Im} H(\omega) \to k_B T \sum_{i\Omega_n} H(i\Omega_n) \quad (209)$$

where $H(i\Omega_n)$ is express with $\mathrm{Im} H(\omega)$ as in Eq. 168.

We argue that $E_{\rm ew}^{\rm vdWo}(h)$ and $E_{\rm ew}^{\rm vdW}(h)$ are approximately linked by an unknown prefactor. Slow charge fluctuations can occur on all length scales, fast oscillations are relatively located in space. Therefore, the shape of $E_{\rm ew}^{\rm vdW}(h)$ should be contained in $E_{\rm ew}^{\rm vdWo}(h)$. We proceed in two steps. First, we introduce

$$A(i\Omega_n) = \frac{g_{\rm e}(q,i\Omega_n)g_{\rm w}(q,i\Omega_n)}{g_{\rm e}(q)g_{\rm w}(q)}, \tag{212}$$

and assume that it does not depend on q.[15] Note that $A(0) = 1$. Second, from [130] we obtain $\varepsilon_{\rm w}(i\Omega_n) \lesssim 2$ for $|\Omega_n| > 0$. Therefore, for $|\Omega_n| > 0$, $g_{\rm w}(q,i\Omega_n)/g_{\rm w}(q) \lesssim 1/2$ so that $A(i\Omega_n) \lesssim 1/2$. Inserting in Eq. 210, we use $\log(1-x) \simeq -x$ for $x \lesssim 1/2$, which gives

$$E_{\rm ew}^{\rm vdW}(h) \simeq \left(1 + \sum_{i\Omega_n} A(i\Omega_n)\right) E_{\rm ew}^{\rm vdWo}(h) = A_\infty E_{\rm ew}^{\rm vdWo}(h), \tag{213}$$

which supports our initial statement, with unknown prefactor A_∞.

RESULTS

We tackle the graphene/water interface and first construct a reference. In MM, the interfacial vdW energy is the sum of carbon-water pairwise LJ potentials:

$$E_{\rm ew}^{\rm LJ} = \sum_{{\rm e}_i}\sum_{{\rm w}_j} V^{\rm LJ}(|\mathbf{x}_{{\rm e}_i} - \mathbf{x}_{{\rm w}_j}|); \qquad V^{\rm LJ}(\mathbf{x}) = 4\epsilon_{\rm LJ}\left(\frac{\sigma_{\rm LJ}^{12}}{|\mathbf{x}|^{12}} - \frac{\sigma_{\rm LJ}^{6}}{|\mathbf{x}|^{6}}\right), \tag{214}$$

where $\sigma_{\rm LJ}$ and $\epsilon_{\rm LJ}$ are the carbon-oxygen LJ parameters. we can compute $E_{\rm ew}^{\rm LJ}$ analytically for a single rigid graphene sheet in $z = 0$, interacting with a semi-infinite water medium. To do so, we use the most straightforward molecular profile $n_0(z) = n_0\Theta(z - (h + d^{\rm LJ}))$, where n_0 is the bulk molecular density, and $d^{\rm LJ}$ the vacuum gap due to the repulsive LJ term in Eq. 214 that avoids overlapping. We obtain[16]:

$$\frac{E_{\rm ew}^{\rm LJ}(h)}{\mathcal{A}} = -\frac{4\pi\epsilon_{\rm LJ}\sigma_{\rm LJ}^3 n_0 N_{\rm u}^{\rm e}}{3\mathcal{A}_{\rm u}}\left[\frac{1}{2}\left(\frac{\sigma_{\rm LJ}}{h + d^{\rm LJ}}\right)^3 - \frac{1}{15}\left(\frac{\sigma_{\rm LJ}}{h + d^{\rm LJ}}\right)^9\right], \tag{215}$$

where $\mathcal{A}_{\rm u} = \sqrt{3}a^2/2$ is the graphene unit cell area that contains $N_{\rm u}^{\rm e} = 2$ carbon atoms. For a given force field, we find $d^{\rm LJ} = (2/5)^{1/6}\sigma_{\rm LJ}$ by imposing $\min E_{\rm ew}^{\rm LJ}(h) = E_{\rm ew}^{\rm LJ}(h = 0)$ — we suppose that the vacuum gap thickness

[15] In practice, dividing by the zero-frequency component removes spatial dependencies such as the exponential e^{2qd} that plays a significant role in the dispersion of $g_{\rm w}(q,i\Omega_n)$ (see e.g. Fig. 8).

[16] It starts by $\frac{E_{\rm ew}^{\rm LJ}}{\mathcal{A}} = n_0\frac{N_{\rm u}^{\rm e}}{\mathcal{A}_{\rm u}}\int_{h+d0}^{+\infty}{\rm d}z\int{\rm d}^2\mathbf{r}V^{\rm LJ}(|\mathbf{x}|)$.

minimizes the LJ vdW energy. Using Table 2, we find $d^{\mathrm{LJ}}_{\mathrm{Werder}} = 2.74\text{Å}$ and $d^{\mathrm{LJ}}_{\mathrm{Aluru}} = 2.95\text{Å}$.

We compare the attractive part of the model in Eq. 215 to the field-theoretic results (Eq. 213 and Eq. 211), by fitting the unknown parameter A_∞. We compute Eq. 211 using the raw simulation data of $g_{\mathrm{w}}^{\mathrm{Werder}}(q)$ and $g_{\mathrm{w}}^{\mathrm{Aluru}}(q)$ (see Fig. 7) to avoid the introduction of a vacuum gap thickness. Computing Eq. 211 only requires graphene's SRF (see Eq. 127)[17]. The results are shown in Fig. 28.

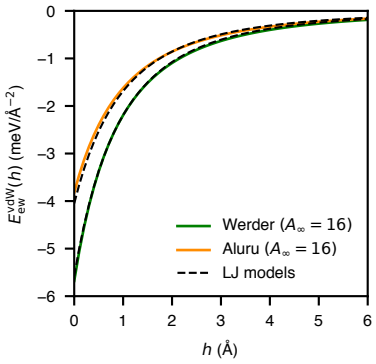

Figure 28: Interfacial vdW energies. We use Eq. 211 and 213 with the raw SRFs for the Werder and Aluru force fields (see Fig. 8). The corresponding LJ models are obtained using the attractive part of Eq. 215 with the force field parameters taken in Table 2. We use only the carbon-oxygen interaction for the Aluru force field.

The field-theoretic and LJ models are in excellent agreement for both force fields. Not only does this validate our approximation, but it also seems versatile because they both use the same prefactor $A_\infty = 16$[18]. It also shows the physical relevance of using a vacuum gap in our modelings.

We have expressed the surface vdW energy between a metal and a solid. We recovered Lifshitz's formula with our familiar tools, the SRFs. Arguing that the unknown high-frequency contribution can be encompassed in a prefactor A_∞, we compared the adapted results to the relevant LJ modeling (used in MM simulations). By fitting a single and shared prefactor, our field-theoretic results match the LJ modeling for both force fields. It bridges the gap between our pure electrostatic approach to the interface and the ad hoc models used in MM simulations.

[17] We use $E_F = k_B T$ and find no significant variations of $E_{\mathrm{ew}}^{\mathrm{vdW}}(h)$ for E_F

[18] The agreement with the Aluru force field may be slightly less accurate because it contains hydrogen-carbon interactions.

8

NON-ADIABATIC METAL/LIQUID FRICTION

The following results exist thanks to a collaboration with Nikita Kavokine, Marie-Laure Bocquet, and Lydéric Bocquet. However, these authors cannot be held liable for the content of this section.

In nanometric channels, the estimation of the water permeability becomes subtle because the surface/volume ratio of the liquid medium increases. In textbooks, the effect of the surface is usually described by a no-slip boundary condition at the interface with the , that is, an infinite solid/liquid friction. More refined descriptions are also considered by quantifying the friction coefficients using diverse experimental or simulation techniques. However, the study of the water-carbon couple has led to a puzzling observation [131, 1].

Water exhibit low friction in CNTs, with friction coefficient (λ) decreasing with decreasing tube radius (R), as shown in Fig. 29. For $R \to \infty$, experiments [132] on flat graphite provide a friction coefficient of $\lambda_{\text{exp}}^{\text{Graphite}} \simeq 1.2 \times 10^5$ N.s.m^{-3} in relatively good well agreement with simulation results $\simeq 4.5 \times 10^4$ N.s.m^{-3}. However, there is a large discrepancy between the experimental and simulations data for decreasing radius, be they quantum (AIMD) or classical (MM).

In those simulations, the curvature effect disappears for $R \geq 2.5$nm, and the flat limit is reached. This radius effect can be understood by a surface curvature effect on the scale of a typical water molecule [133]. However, the experimental data of [6] in Fig. 29 show a different behavior regarding the radius dependency. The friction coefficient nearly exponentially depends on the radius, and the limit $R \to \infty$ is not reached for $R = 60$ nm$\gg d_{\text{OH}}$. These data challenge the current theories of solid/liquid friction that are based on a roughness-based picture in which the solid acts as a static external potential for the liquid molecules [134].

Whereas AIMD constitutes an expensive but highly accurate simulation method, it does resort to the BOA that we now put into question. The breakdown of the BOA has already been observed in graphene [16]. Its peculiar conical band structure intersection at the Fermi level (see part ii) prevents (to some extent that needs to be determined) the decoupling of the electronic and nuclear wavefunctions. For instance, the highest optical phonon energy

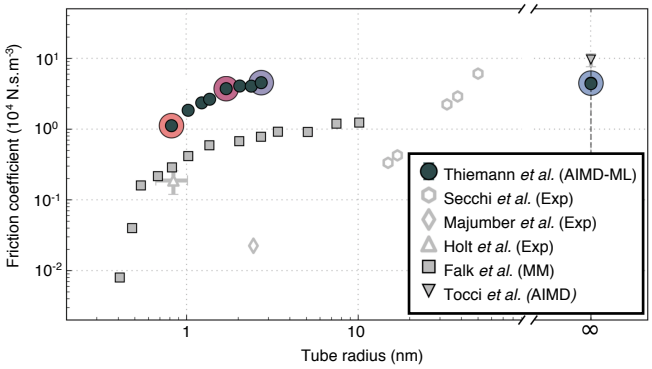

Figure 29: Friction coefficient evolution of water inside CNTs with varyig radii as obtained from different experiments and simulations. The gathering of the data from this figure was made by the authors of [13]. We freely adapted their figure — the colour-circled data are meaningless in our context. The reported data can be found (in the same order) in [13], [6], [2], [3], [133], and [12]. "Exp" indicates experimental measurements, "MM" indicates force fields molecular mechanics, "AIMD" refers to BO quantum simulations and "AIMD-ML" refers to the same kind of simualtions assisted with a machine learning framwork.

$\sim$ 200meV can oscillate several periods before the electrons fully relax to the adiabatic ground state. Water has some high-frequency components (we have seen dynamical peaks in water's SRF around $\sim$ 100meV in part ii, Fig 4) so we may investigate this aspect.

Moreover, we have seen in chapter 7 that electronic properties of CNTs change on length scales large compared to molecular water size. The TB band gap of a semiconduting CNT is $E_g^{(0)} = \frac{2\hbar v_F}{3R} \simeq k_B T$ for $R = 15$nm. The charge carrier density in the conduction band $n_e \propto e^{-\beta E_g^{(0)}}$ could, for instance, be the source of the exponential scaling of the friction coefficient with the radius.

Our approach is the following. Assuming that simulations obtain results in agreement with experimental measurements for $R \to \infty$ by an error compensation effect, we investigate if a non-adiabatic (nBO) contribution can be responsible for the observed friction on graphene/graphite: $\lambda_{\text{exp}}^{\text{Graphite}} \simeq 1.2 \times 10^5 \text{N.s.m}^{-3}$. If so, we will investigate if a transition from a metal-like to a insulating-like behavior of CNTs when R decreases could explain the observed trend of the experimental data reported in Fig. 29.

Whereas numerical applications for the water/graphene couple will be critical, we dwell on the physical insights revealed by identifying a new mechanism of solid/liquid friction. We derive friction coefficients by progressively reducing the number of assumptions we use, to keep track of the role of non-adiabaticity. The friction coefficient is defined as follows: for a solid and a liquid in a relative velocity $\mathbf{v}$, the liquid experiences a

force of $\mathbf{F}_{\text{ew}} = -\mathcal{A}\lambda\mathbf{v}$, where $\mathcal{A}$ is the surface area. The solid experiences $\mathbf{F}_{\text{we}} = -\mathbf{F}_{\text{ew}}$. We extract λ with the normalized dissipated power:

$$\lambda = -\frac{\mathbf{F}_{\text{ew}} \cdot \mathbf{v}}{\mathcal{A}|\mathbf{v}|^2} \quad \left[\text{N.s.m}^{-3}\right] \tag{216}$$

8.1 TYPES OF FRICTION

8.1.1 *Classical friction*

Here we derive the surface roughness-based friction coefficient. We start from a classical Kubo formula [134]. At equilibrium, the friction coefficient is linked to the correlation function of solid/liquid force and reads

$$\lambda_{\text{BO}} = \frac{1}{\mathcal{A}k_B T}\int_0^{+\infty} \mathrm{d}t \langle \mathbf{F}_{\text{ew}}(t)\mathbf{F}_{\text{ew}}(0)\rangle. \tag{217}$$

We consider that the charge density of the solid does not fluctuate $\delta\hat{n}_{\text{m}} = 0$. The Hamiltonian (Eq. 74) points to the remaining operator $\hat{U}_{\text{w}}^{\langle \text{m}\rangle}$ that includes $\delta\hat{n}_{\text{w}}$ and n_{m}^0 — or equivalently, the static external potential of the metal: $\phi_{\text{m}}^0 = \int \mathrm{d}2v(12)n_{\text{m}}^0(2)$. There is no reason to keep the quantum formalism in this particular case so we replace $\delta\hat{n}_{\text{w}}$ by δn_{w} and write the force experienced by the liquid at a time t:

$$\mathbf{F}_{\text{ew}}(t) = -\int \mathrm{d}\mathbf{x}\nabla_{\parallel}\phi_{\text{m}}^0(\mathbf{x})\delta n_{\text{w}}(\mathbf{x},t). \tag{218}$$

where $\nabla_{\parallel}$ is the derivative in the direction parallel to the surface. Inserting Eq. 218 in Eq. 217 leads to

$$\lambda_{\text{BO}} = \frac{1}{\mathcal{A}k_B T}\int \mathrm{d}\mathbf{x}\int \mathrm{d}\mathbf{x}'\nabla_{\parallel}\phi_{\text{e}}^0(\mathbf{x}')\nabla_{\parallel}\phi_{\text{e}}^0(\mathbf{x})\int_0^{+\infty}\mathrm{d}t\langle\delta n_{\text{w}}(\mathbf{x},t)\delta n_{\text{w}}(\mathbf{x}')\rangle, \tag{219}$$

from which we recognize the structure factor of water's charge density after Fourier transformation[1]. We obtain

$$\lambda_{\text{BO}} = \frac{1}{\mathcal{A}k_B T}\frac{1}{2}\int\frac{\mathrm{d}\mathbf{q}}{(2\pi)^2}q^2\int \mathrm{d}z\mathrm{d}z'\phi_{\text{m}}^0(\mathbf{q},z)\phi_{\text{m}}^0(-\mathbf{q},z')S_{\text{w}}(\mathbf{q},z,z',\omega=0). \tag{220}$$

We specify the absolute value in the Coulomb potential

$$\phi_{\text{m}}^0(\mathbf{q},z) = \frac{e^{-qz}}{2q\epsilon_0}\int e^{qz}n_{\text{m}}^0(\mathbf{q},z) = \frac{e^{-qz}}{2q\epsilon_0}n_{\text{m}}^{\text{s}0}(\mathbf{q}). \tag{221}$$

[1] We use $\int_0^{+\infty}\mathrm{d}t\langle n_{\text{w}}(\mathbf{x},t)n_{\text{w}}(\mathbf{x}')\rangle = \frac{1}{2}\int\frac{\mathrm{d}^2\mathbf{q}}{(2\pi)^2}S_{\text{w}}(\mathbf{q},z,z',\omega=0)e^{i\mathbf{q}(\mathbf{x}-\mathbf{x}')}$.

We introduce a *static* surface structure factor for the metal that contains its "charge roughness":

$$S_{\mathrm{m}}^{\mathrm{s0}}(\mathbf{q}) = \frac{1}{\mathcal{A}}\langle n_{\mathrm{m}}^{\mathrm{s0}}(\mathbf{q}) n_{\mathrm{m}}^{\mathrm{s0}}(-\mathbf{q})\rangle. \tag{222}$$

We neglected this term ($S_{\mathrm{e}}^{\mathrm{s0}}(\mathbf{q}) = 0$) in previous applications because we considered flat and locally neutral surfaces. Inserting in Eq. 220, we obtain

$$\lambda_{\mathrm{BO}} = \frac{1}{2k_B T}\int \mathrm{d}\mathbf{q}\left(\frac{\hat{\mathbf{v}}\cdot\hat{\mathbf{q}}}{4\pi\epsilon_0}\right)^2 S_{\mathrm{m}}^{\mathrm{s0}}(\mathbf{q}) S_{\mathrm{w}}^{\mathrm{s}}(\mathbf{q}, \omega = 0), \tag{223}$$

where we have chosen the origin for the angular integration as the direction of the velocity $\hat{\mathbf{v}} = \mathbf{v}/|\mathbf{v}|$[2]. Eq. 223 can be found in [135] and can be refined to include non-Coulombic forces. Eq. 223 can be understood as an overlap between two *surface* structure factors. If the typical length scale of charge corrugation in the metal matches the slowest charge fluctuation in water, friction will be high. The friction coefficient, therefore, quantifies a *matching* of correlation lengths.

8.1.2 *Electronic friction*

Here, we look for the first-order correction to the BOA, assuming a flat interface and $S_{\mathrm{m}}^{\mathrm{s0}}(\mathbf{q}) = 0$. This breakdown has been studied under various names in the literature, but the one of electronic friction [136] seems to be adequate in our case. We are not dealing with a breakdown of the BOA from a chemical perspective [137]: liquid molecules remain rigid, and the metal nuclei are frozen. Electronic friction can be defined as follows:

> "Electronic friction is a correction to the Born-Oppenheimer approximation, whereby nuclei in motion experience a drag in the presence of a manifold of electronic states."[136]

Let us simplify our system to understand the underlying mechanism better. We consider the friction experienced by a charge density above a metallic surface (see Fig. 30). At rest ($\mathbf{v} = 0$), electrons accumulate (or deplete) to screen the charge density. We schematically represent the charge image in the metal in Fig. 30 (left panel). When a constant velocity ($\mathbf{v} \neq 0$) is given to the charge density, its image charge in the metal must follow. For a perfect metal, the image charge instantaneously follows that charge density (like an image in a mirror). However, if the metal is not perfect, the image charge "lags behind". Electrons move in the crystal lattice, and the mechanisms for energy loss are therefore the same as those governing

[2] It is for comparison with future formulas of the friction coefficient.

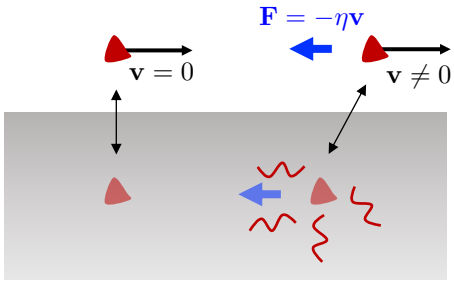

Figure 30: Schematic illustration of the electronic friction exerted on a charge density (red) above a metal — see text for description. The introduced friction coefficient $\eta = \mathcal{A}\lambda$ is not surfacic in this case.

Ohmic dissipation. The dissipated energy comes from the velocity $\mathbf{v}$ of the charge density in the first place. Therefore, it experiences a friction force in the direction opposite to its trajectory.

We express this friction force with the metal's SRF [138]. Consider the moving external (to the metal) charge density $n_{\text{ext}}(\mathbf{x}, t) = n_{\text{ext0}}(\mathbf{x} + \mathbf{v}t)$ where $\mathbf{v}$ is parallel to the metal surface. The friction force is constant in time and we can evaluate it at $t = 0$, that is

$$\mathbf{F}_{\text{e}\to\text{ext}} = -\int \mathrm{d}\mathbf{x} \nabla_{\parallel} \phi_{\text{ind}}(\mathbf{x}, t = 0) n_{\text{ext0}}(\mathbf{x}). \tag{224}$$

After Fourier transformation, we obtain

$$\mathbf{F}_{\text{e}\to\text{ext}} = -\int \mathrm{d}z \int \frac{\mathrm{d}\mathbf{q}}{(2\pi)^2} (i\mathbf{q}) \phi_{\text{ind}}(\mathbf{q}, z, t = 0) n_{\text{ext0}}(-\mathbf{q}, z), \tag{225}$$

and using $\phi_{\text{ind}}(1) = \int \mathrm{d}2 \Delta w_{\text{e}}(12) n_{\text{ext}}(2)$ (see Eq. 2 with $w = w_{\text{e}}$), we obtain

$$\phi_{\text{ind}}(\mathbf{q}, z, t = 0) = \int \frac{\mathrm{d}\omega}{2\pi} \int \mathrm{d}z' \Delta w_{\text{e}}(\mathbf{q}, z, z', \omega) n_{\text{ext}}(\mathbf{q}, z', \omega). \tag{226}$$

Eq. 226 involves the Fourier transform of two quantities n_{ext} and Δw_{e}. First,

$$\begin{aligned} n_{\text{ext}}(\mathbf{q}, z, \omega) &= \int \mathrm{d}\mathbf{x} \int \mathrm{d}t n_{\text{ext}}(\mathbf{x}, z, t) e^{-i(\mathbf{q}\mathbf{x} + \omega t)} \\ &= 2\pi\delta(\omega - \mathbf{v}\mathbf{q}) n_{\text{ext0}}(\mathbf{q}, z), \end{aligned} \tag{227}$$

means that a constant velocity in space-time gives a Doppler shift of $\mathbf{v} \cdot \mathbf{q}$ in Fourier space. Then, from Eq. 35,

$$\Delta w_{\text{e}}(\mathbf{q}, z, z', \omega) = -\frac{1}{2q\epsilon_0} g_{\text{e}}(\mathbf{q}, \omega) e^{-qz} e^{-qz'}, \tag{228}$$

because the external charge density is outside the medium $z, z' \geq 0$. Inserting Eq. 228 and Eq. 227 in Eq. 226, and then in Eq. 225, we obtain

$$\mathbf{F}_{e\to ext} = \frac{i}{2\epsilon_0}\int \frac{d\mathbf{q}}{(2\pi)^2}\hat{\mathbf{q}} g_e(\mathbf{q}, \omega = \mathbf{v}\mathbf{q}) \left|n^s_{ext0}(\mathbf{q})\right|^2, \tag{229}$$

where $\hat{\mathbf{q}} = \mathbf{q}/q$. However, the imaginary part of the SRF is an odd function of frequency whereas the real part is even — i.e., $g_e(-\mathbf{q}, -\omega) = g_e^*(\mathbf{q}, \omega)$. In integrating Eq. 229, the real part disappears. Specializing to the case of point charge at altitude z_0 — e.g. $\left|n^s_{ext0}(\mathbf{q})\right|^2 = e^{-2qz_0}$—, we obtain

$$\eta = \frac{1}{4\pi\epsilon_0}\int \frac{d\mathbf{q}}{(2\pi)^2}\frac{(\hat{\mathbf{v}}\cdot\hat{\mathbf{q}})}{|\mathbf{v}|}\mathrm{Im} g_e(\mathbf{q}, \mathbf{v}\cdot\mathbf{q}) e^{-2qz_0}, \tag{230}$$

where $\eta = \mathcal{A}\lambda$ is the relevant friction coefficient for a single point-like charge.

Eq. 230 involves the imaginary part of the metallic response function, which indicates that dissipation only occurs in the metal. The velocity of the charged particle is not assumed to be small in Eq. 230 so it can excite some plasmons — collective charge oscillations — in the metal, as probed in Electron-Energy Loss Spectroscopy (EELS), for instance [122]. However, *the particle's velocity does not have to be significant for the friction to exist.* In the linear regime, for small velocities compared to typical charge oscillation frequencies in the metal, we can write

$$\lim_{\mathbf{v}\to 0} \mathrm{Im} g_e(\mathbf{q}, \mathbf{v}\cdot\mathbf{q}) = \mathbf{v}\cdot\mathbf{q}\lim_{\omega\to 0}\frac{\mathrm{Im} g_e(\mathbf{q}, \omega)}{\omega}. \tag{231}$$

Inserting Eq. 231 in Eq. 230, the velocity disappears from the friction coefficient, as expected by the linear regime assumption. We will be interested in typical velocities of $|\mathbf{v}| \sim \mu\mathrm{m.s}^{-1}$ [6], which are ten orders of magnitudes lower than microscopic velocities, so the linear regime is relevant.

We have obtained the friction coefficient of one particle above a metal. To tackle the friction of a liquid, should we sum the friction coefficients of all its constituting particles? Is $\mathbf{v}$ the relative solid/liquid macroscopic velocity or the microscopic ones? The answer to those questions, we refer to Eq. 227 and Eq. 229. *Even if introducing a macroscopic velocity of a medium is equivalent to shifting the velocity of all its constituting particles*[3]*, we cannot simply add the friction coefficients because of the term* $\left|n^s_{ext0}(\mathbf{q})\right|^2$ *in* Eq. 229.

Can we bridge the gap between this single-particle mechanism and the metal/liquid picture? We can first consider that the external charge density is the mean average charge density of the medium — e.g. $n_{ext0} = n^0_w$. The latter is due to the mean charge structuration in the liquid due to the solid lattice.

[3] To better understand this first aspect, we can use the microscopic expression in Eq. 82. It reads $n^s_w(\mathbf{q}, t) = e^{-i\mathbf{q}\mathbf{v}t}\sum_i c_i e^{-i\mathbf{q}\mathbf{r}_i(t)} e^{-qz_i(t)} = \sum_i c_i e^{-\mathbf{q}(\mathbf{r}_i(t)+\mathbf{v}t)} e^{-qz_i(t)}$.

Note that a charge layering in the direction normal to the surface — such as the one in Fig. 12a — is insufficient to generate friction because $n_{\mathrm{w}}^{\mathrm{s}0}(\mathbf{q}) \propto \delta_{\mathbf{q}}$ and the infinite interface is translationally invariant. We are dealing with the same reasoning as in the classical case, and we can introduce $S_{\mathrm{w}}^{\mathrm{s}0}(\mathbf{q})$ in analogy to Eq. 222 and rewrite Eq. 229 as

$$\mathbf{F}_{\mathrm{ew}} \cdot \mathbf{v} = -\mathcal{A} \int \frac{\mathrm{d}\mathbf{q}}{(2\pi)^2} \frac{(\mathbf{v}\cdot\mathbf{q})^2}{2\epsilon_0 q} \lim_{\omega\to 0} \frac{\mathrm{Im} g_{\mathrm{e}}(\mathbf{q},\omega)}{\omega} S_{\mathrm{w}}^{\mathrm{s}0}(\mathbf{q}). \tag{232}$$

We insert the FDT for the SRF,

$$\mathrm{Im} g(\mathbf{q},\omega) = \frac{\tanh(\beta\hbar\omega/2)}{2\epsilon_0 q\hbar} S^{\mathrm{s}}(\mathbf{q},\omega), \tag{233}$$

in Eq. 232 to obtain

$$\lambda_{\mathrm{nBO}}^{0} = \frac{1}{2k_B T} \int \mathrm{d}\mathbf{q} \left(\frac{\hat{\mathbf{v}}\cdot\hat{\mathbf{q}}}{4\pi\epsilon_0} \right)^2 S_{\mathrm{e}}^{\mathrm{s}}(\mathbf{q},\omega=0) S_{\mathrm{w}}^{\mathrm{s}0}(\mathbf{q}). \tag{234}$$

Eq. 234 is very similar to Eq 223 but its meaning is now different. Here dissipation occurs in the metal and not in the liquid. Electrons travel in a static potential exerted by the nuclei and the average one of the liquid. It gives them new channels to scatter and dissipate energy. In this view, it is maybe better to understand this process as the reversed classical one. Liquid molecules have a certain structuration at the interface because they see the metal lattice. They generate a periodic potential for the electrons — same periodicity. Electrons move at a constant velocity in this potential and can scatter on it. This additional energy dissipation mechanism is no longer due to Ohmic loss but solid/liquid friction.

Consequently, we should be able to link solid/liquid friction and metals' differential resistivities, as pointed out in [139]. It echoes the electron/nuclei force-force correlation function to compute — the quantum analog of Kubo formula (Eq. 217) — to calculate conductivities of metals [31]. Interestingly, there is sizeable electrical resistivity enhancement when water adsorbs on graphene [140]. However, we have seen in part ii that $S_{\mathrm{w}}^{\mathrm{s}0}(\mathbf{q}) \ll S_{\mathrm{w}}^{\mathrm{s}}(\mathbf{q})$ (see the remark below Eq. 83). Charge structuration is relatively small at the graphene/water interface [12], and the contribution of Eq. 234 is therefore negligible.

Assuming no mean charge corrugation for the liquid and the solid — e.g. $S_{\mathrm{w}}^{\mathrm{s}0}(\mathbf{q}) = 0$ and $S_{\mathrm{m}}^{\mathrm{s}0}(\mathbf{q}) = 0$ — where could the friction come from? The liquid is neutral on average, but the instantaneous electric fields are pretty large at the interface. We are facing a subtle issue regarding the averaging process. By assuming that the liquid's fastest damped charge oscillation is slower than the slowest one in the metal, we try to use Eq. 229.

In other words, electrons always see static liquid molecules, and we can compute friction coefficients λ for every possible molecular configuration in the liquid[4]. The averaged friction coefficient $\lambda^{(1)}_{\text{nBO}}$ should constitute a first guess for the searched quantity[5].

Replacing $\left|n^{s0}_{w}(\mathbf{q})\right|^2$ by $\langle|\delta n^{s}_{w}(\mathbf{q})|^2\rangle$ in Eq. 232 gives

$$\lambda^{(1)}_{\text{nBO}} = \frac{1}{2k_BT}\int \mathrm{d}\mathbf{q}\left(\frac{\hat{\mathbf{v}}\cdot\hat{\mathbf{q}}}{4\pi\epsilon_0}\right)^2 S^{s}_{e}(\mathbf{q},\omega=0)S^{s}_{w}(\mathbf{q}). \tag{235}$$

Eq. 235 is again an overlap between two structure factors, but this time it quantifies the *matching of the fluctuations wavelengths* in both media. Dissipation still occurs in the metal only. We can include the result of Eq. 234 in Eq. 235 by enlarging the definition of the liquid's surface charge structure factor[6].

8.1.3 *Van der Waals friction*

So far, we have assumed the decoupling of the dynamics of liquid molecules and electrons. We now tackle the theoretical difficulty of assessing the range of validity of Eq. 235 by reintroducing the dynamics. The relative motion of the two bodies now requires using the out-of-equilibrium framework as discussed in 2.2.2.

The first step consists in writing the instantaneous electron/water force as the Keldsyh response function, as in Eq. 195. It reads

$$\begin{aligned}\langle\hat{\mathbf{F}}_{\text{ew}}(t_1)\rangle &= \int \mathrm{d}\mathbf{x}_1\int \mathrm{d}2\nabla_{\parallel}v(12)\langle\delta\hat{n}_e(1)\delta\hat{n}_w(2)\rangle \\ &= \frac{i\hbar}{2}\int \mathrm{d}\mathbf{x}_1\int \mathrm{d}2\nabla_{\parallel}v(12)\chi^{K}_{\text{ew}}(12).\end{aligned} \tag{236}$$

We cannot use the FDT because we are not in an equilibrium situation (the media are moving with a relative velocity $\mathbf{v}$). However, the average force does not depend on time. Using $v(12)\propto\delta(t_1-t_2)$ and looking at $t_1=0$, we find — see also from Eq. 196 to Eq. 199 —

$$\frac{\langle\hat{\mathbf{F}}_{\text{ew}}\rangle}{\mathcal{A}} = -\frac{1}{2}\sum_{\mathbf{q}}\int\frac{\mathrm{d}\hbar\omega}{2\pi}\mathbf{q}\mathrm{Re}g^{K}_{\text{ew}}(q,\omega). \tag{237}$$

[4] It is the Monte-Carlo picture of phase-space averaging that is relevant here.
[5] Of course, we will check it below.
[6] This means by defining $S^{s}_{w}(\mathbf{q}) = \langle|n^{s}_{w}(\mathbf{q})|^2\rangle/\mathcal{A}$ and no longer $S^{s}_{w}(\mathbf{q}) = \langle|\delta n^{s}_{w}(\mathbf{q})|^2\rangle/\mathcal{A}$.

To find $g^{\mathrm{K}}_{\mathrm{ew}}$, we follow the rules in 2.3.3[7]. Using Eq. 205 and Eq. 203, we obtain

$$\begin{cases} g^{\mathrm{R/A}}_{\mathrm{ew}} = & g^{\mathrm{R/A}}_{\mathrm{e}} g^{\mathrm{R/A}}_{\mathrm{w}} + g^{\mathrm{R/A}}_{\mathrm{e}} g^{\mathrm{R/A}}_{\mathrm{w}} g^{\mathrm{R/A}}_{\mathrm{ew}} \\ g^{\mathrm{K}}_{\mathrm{ew}} = & g^{\mathrm{R}}_{\mathrm{e}} g^{\mathrm{K}}_{\mathrm{w}} + g^{\mathrm{K}}_{\mathrm{e}} g^{\mathrm{A}}_{\mathrm{w}} + g^{\mathrm{R}}_{\mathrm{e}} g^{\mathrm{R}}_{\mathrm{w}} g^{\mathrm{K}}_{\mathrm{ew}} + (g^{\mathrm{R}}_{\mathrm{e}} g^{\mathrm{K}}_{\mathrm{w}} + g^{\mathrm{K}}_{\mathrm{e}} g^{\mathrm{A}}_{\mathrm{w}}) g^{\mathrm{A}}_{\mathrm{ew}} \end{cases}, \tag{238}$$

where we omitted the $(\mathbf{q}, \omega)$ index for clarity. The solution for the retarded and advanced component were obtained in Eq. 206. For the Keldysh component, we find

$$g^{\mathrm{K}}_{\mathrm{ew}} = \frac{g^{\mathrm{R}}_{\mathrm{e}} g^{\mathrm{K}}_{\mathrm{w}} + g^{\mathrm{K}}_{\mathrm{e}} g^{\mathrm{A}}_{\mathrm{w}}}{|1 - g_{\mathrm{e}} g_{\mathrm{w}}|^2}, \tag{239}$$

where we have used $g^{\mathrm{R}}_{\mathrm{e}}(\mathbf{q}, \omega) = g^{\mathrm{A}*}_{\mathrm{e}}(\mathbf{q}, \omega)$ in the denominator. Using the reaction force $\langle \hat{\mathbf{F}}_{\mathrm{ew}} \rangle = -\langle \hat{\mathbf{F}}_{\mathrm{we}} \rangle$, we can compute half the difference of Eq. 239 and its alternative (w $\rightleftarrows$ e),

$$\frac{1}{2}(g^{\mathrm{K}}_{\mathrm{ew}} - g^{\mathrm{K}}_{\mathrm{we}}) = i \frac{g^{\mathrm{K}}_{\mathrm{w}} \mathrm{Im} g_{\mathrm{e}} - g^{\mathrm{K}}_{\mathrm{e}} \mathrm{Im} g_{\mathrm{w}}}{|1 - g_{\mathrm{e}} g_{\mathrm{w}}|^2}. \tag{240}$$

How do we find the Keldysh response function of both media? Considering the extremely slow relative velocity between the two media, a reasonable assumption is that they both verify the FDT (Eq. 71). Nevertheless, we shall not forget that the Doppler shift of $\pm \frac{\mathbf{vq}}{2}$[8] they both acquire (see Eq. 227). Therefore,

$$g^{\mathrm{K}}_{\mathrm{e/w}}(\mathbf{q}, \omega \mp \frac{\mathbf{vq}}{2}) = 2i f(\omega \mp \frac{\mathbf{vq}}{2}) \mathrm{Im} g_{\mathrm{e/w}}(\mathbf{q}, \omega \mp \frac{\mathbf{vq}}{2}), \tag{241}$$

where we recall that $f(\omega) = \coth(\frac{\beta\hbar\omega}{2})$. Inserting Eq. 241 in Eq. 240 and taking the limit $\mathbf{v} \to 0$, gives

$$\frac{1}{2}(g^{\mathrm{K}}_{\mathrm{ew}} - g^{\mathrm{K}}_{\mathrm{we}}) = 2\mathbf{vq} \left| \frac{\mathrm{d} f(\omega)}{\mathrm{d}\omega} \right| \frac{\mathrm{Im} g_{\mathrm{e}} \mathrm{Im} g_{\mathrm{w}}}{|1 - g_{\mathrm{e}} g_{\mathrm{w}}|^2}. \tag{242}$$

Inserting Eq. 242 in Eq. 237 — using $\langle \hat{\mathbf{F}}_{\mathrm{ew}} \rangle = \frac{1}{2}\left(\langle \hat{\mathbf{F}}_{\mathrm{ew}} \rangle - \langle \hat{\mathbf{F}}_{\mathrm{we}} \rangle\right)$, gives

$$\lambda_{\mathrm{nBO}} = \sum_{\mathbf{q}} \int \frac{\mathrm{d}\hbar\omega}{2\pi} (\hat{\mathbf{v}} \cdot \mathbf{q})^2 \left| \frac{\mathrm{d} f(\omega)}{\mathrm{d}\omega} \right| \frac{\mathrm{Im} g_{\mathrm{e}} \mathrm{Im} g_{\mathrm{w}}}{|1 - g_{\mathrm{e}} g_{\mathrm{w}}|^2}. \tag{243}$$

Using Eq. 233, Eq. 243 can be expressed as

$$\lambda_{\mathrm{nBO}} = \frac{1}{2k_B T} \int \mathrm{d}\mathbf{q} \left(\frac{\hat{\mathbf{v}} \cdot \hat{\mathbf{q}}}{4\pi\epsilon_0} \right)^2 \int \frac{\mathrm{d}\omega}{2\pi} \frac{S^{\mathrm{s}}_{\mathrm{e}}(\mathbf{q}, \omega) S^{\mathrm{s}}_{\mathrm{w}}(\mathbf{q}, \omega) \mathrm{sech}^2(\beta\hbar\omega/2)}{|1 - g_{\mathrm{e}}(q, \omega) g_{\mathrm{w}}(q, \omega)|^2}. \tag{244}$$

[7] Using the equilibrium framework leads to $\langle \hat{\mathbf{F}}_{\mathrm{ew}} \rangle = 0$ because $g^{\mathrm{K}}_{\mathrm{ew}}$ is purely imaginary according to the FDT (Eq. 71)

[8] We find convenient to symmetrize the velocities.

Eq. 243 can be found in the works of Persson and Volokitin [141, 142, 143]. However, it has been rigorously derived only in the local case. Eq. 244, like Eq. 223 and Eq. 235, is a (weighted) overlap between two surface charge structure factor, now resolved in the frequency domain. *The non-adiabatic friction coefficient quantifies the wavelength and frequency matching of the charge fluctuations in both media.* How to understand the underlying microscopic mechanism? In practice, for all metal/liquid interfaces we deal with in this work, Eq. 244 reduces to a form similar to Eq. 235 and can thus be understood semi-classically, as in the electronic friction picture. However, written as in Eq. 244, quantum arguments are needed to understand the microscopic friction force.

We picture two solids — say (1) and (2) — with collectives modes $\omega_{\mathbf{q}}^{(1)}$ and $\omega_{\mathbf{q}}^{(2)}$ of charge oscillations — describing quasiparticles such as phonons or plasmons — that carry a momentum $\hbar\mathbf{q}$. At room temperature, the population of one mode follows the Bose-Einstein distribution $n_B(\omega_{\mathbf{q}}^{(1/2)})$. The population of one mode can vary if another quasiparticle mode exists with the same energy. More precisely, the exchange rate of a quanta from mode (1) to mode (2) is given by Fermi golden rule $\tau_{\mathbf{q}}^{-1}(1 \to 2) \propto n_B(\omega_{\mathbf{q}}^{(1)})\delta(\omega_{\mathbf{q}}^{(1)} - \omega_{\mathbf{q}}^{(2)})$. The exchanged momentum $\hbar\mathbf{q}$ is a consequence of this quasiparticle transfer. At an interface between two solids, the population of the modes in the two media fluctuates if $\omega_{\mathbf{q}}^{(1)} = \omega_{\mathbf{q}}^{(2)}$, but they are, on average, the same at equilibrium because $n_B(\omega_{\mathbf{q}}^{(1)}) = n_B(\omega_{\mathbf{q}}^{(2)})$. More precisely, $\tau_{\mathbf{q}}^{-1}(1 \to 2) = \tau_{\mathbf{q}}^{-1}(2 \to 1)$ or $\Delta\tau_{\mathbf{q}}^{-1} = 0$. Accordingly, the net momentum transfer between the two solids is, on average, zero.

What happens if $\mathbf{v} \neq 0$? The frequency modes of one medium are Doppler shifted by $\pm\mathbf{vq}$. It is, indeed, how the macroscopic velocity is translated in the microscopic picture: the modes carrying momentum along the velocity direction are more populated than the one in the opposite direction — i.e., $n_B(\omega_{\mathbf{q}} - \mathbf{vq}) > n_B(\omega_{\mathbf{q}})$ for $\mathbf{v} \cdot \mathbf{q} > 0$. In turn, at the interface between the two media, we obtain $\Delta\tau_{\mathbf{q}}^{-1} \sim \pm\mathbf{v} \cdot \mathbf{q}(\mathrm{d}n_B(\omega_{\mathbf{q}}^{(1/2)})/\mathrm{d}\omega)\delta(\omega_{\mathbf{q}}^1 - \omega_{\mathbf{q}}^2)$ for $\mathbf{v} \to 0$. Summing over existing modes in both media requires the introduction of spectral functions. In the quantum framework, these are the structure factors. Therefore, we have accounted for the main ingredients of Eq. 244.

What is the role of the $\mathrm{sech}^2(\beta\hbar\omega/2)$ term? It acts like a cutoff for frequencies larger than $2k_BT/\hbar$. It is the equivalent of the factor $\mathrm{d}n_B(\omega_{\mathbf{q}}^{(1/2)})/\mathrm{d}\omega$ that rapidly converges to zero for $\omega_{\mathbf{q}}^{(1/2)} \gtrsim 2k_BT/\hbar$. What is the denominator about? It comes from the infinite resummation of the reflecting electric field at the interface. It is our framework's signature: by putting both media on an equal footing, it allows recursive and mutual screening (the coupled interactions in 6.3.4). It has played a role in evaluating the vdW energy in 7.3.

However, the fluctuations frequencies involved here are not the relevant ones to compute the vdW energy. It appears that vdW friction and vdW energy are quite decoupled.

8.1.4 *Three practical formulas*

This section discusses the wavelength and frequency matching of the charge fluctuations in a metal and a liquid. Eq. 244 can generally be simplified at a solid/liquid interface. First, we cut off the frequency integral of Eq. 244 at $2k_BT/\hbar$, roughening the filter's edges. Making the angular integration in Eq. 244, we introduce formula I for the non-adiabatic contribution to the solid/liquid friction:

$$\lambda_{\mathrm{nBO}}^{(\mathrm{I})} \simeq \frac{\pi}{k_BT}\int_0^{+\infty}\frac{\mathrm{d}qq}{(4\pi\epsilon_0)^2}\int_0^{2k_BT/\hbar}\frac{\mathrm{d}\omega}{2\pi}\frac{S_{\mathrm{e}}^{\mathrm{s}}(q,\omega)S_{\mathrm{w}}^{\mathrm{s}}(q,\omega)}{|1-g_{\mathrm{e}}(q,\omega)g_{\mathrm{w}}(q,\omega)|^2}. \tag{245}$$

How accurate is our first guess for the friction coefficient in Eq. 235? We ignore the denominator that cannot be rigorously obtained without resorting to our hybrid framework[9]. We assume the decoupling of the dynamics — i.e., $S_{\mathrm{e}}^{\mathrm{s}}(\mathbf{q},2k_BT/\hbar)\simeq S_{\mathrm{e}}^{\mathrm{s}}(\mathbf{q},\omega=0)$ and $S_{\mathrm{w}}^{\mathrm{s}}(\mathbf{q},\omega)\simeq 0$ for $\omega > 2k_BT/\hbar$. Therefore, we can pull out $S_{\mathrm{e}}^{\mathrm{s}}(\mathbf{q},\omega=0)$ from the integral and perform the integration to recover Eq. 235. Our first guess is recovered from the general formula Eq. 244 (or Eq. 245), and the criteria for its validity are now obtained.

The spectral functions of typical metals and liquids at room temperature give the range of typical charge oscillation frequencies. Typical excitations in metals have energies around $E_F/\hbar \gg 2k_BT/\hbar$. Debye collective relaxation modes in liquids usually satisfy $\tau_{\mathrm{D}}^{-1} \ll 2k_BT/\hbar$. Therefore, decoupling the dynamics is relevant in the general case. However, our first guess (Eq. 235) misses to account for the recursive and mutual screening (the denominator of Eq. 245). Considering the small imaginary part of $g_{\mathrm{e}}(q,\omega)$ and $g_{\mathrm{w}}(q,\omega)$ for $\omega < 2k_BT/\hbar$ (see part ii), we only keep the real parts. We suggest formula II for the non-adiabatic contribution of the solid/liquid friction when $\tau_{\mathrm{D}}^{-1} \ll k_BT/\hbar \ll E_F/\hbar$[10]:

$$\lambda_{\mathrm{nBO}}^{(\mathrm{II})} \simeq \frac{\pi}{2k_BT}\int_0^{+\infty}\frac{\mathrm{d}qq}{(4\pi\epsilon_0)^2}\frac{S_{\mathrm{e}}^{\mathrm{s}}(q,\omega=0)S_{\mathrm{w}}^{\mathrm{s}}(q)}{\left(1-g_{\mathrm{e}}(q)g_{\mathrm{w}}(q)\right)^2}. \tag{246}$$

[9] Of course, other approaches with the same results might be constructed differently.

[10] The more specific criteria $S_{\mathrm{e}}^{\mathrm{s}}(\mathbf{q},2k_BT/\hbar)\simeq S_{\mathrm{e}}^{\mathrm{s}}(\mathbf{q},\omega=0)$ and $S_{\mathrm{w}}^{\mathrm{s}}(\mathbf{q},\omega)\simeq 0$ for $\omega > 2k_BT/\hbar$ are of course the most relevant ones that should be satisfied. However, those two conditions are usually linked.

This assumption localizes dissipation in the metal. The quantum picture vanishes and the relevant (semi-classical) microscopic mechanism is electronic friction, as detailed above.

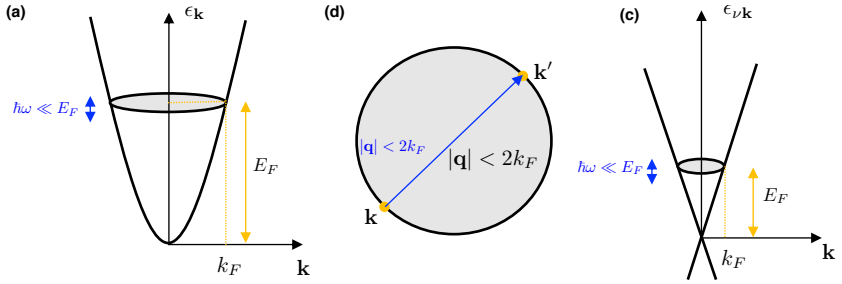

Figure 31: Band structure of **(a)** a 2D jellium **(c)** graphene. **(b)** Details of the scattering event on the Fermi surface given an energy $\hbar\omega \ll k_B T$. Here $\mathbf{k}$ is a 2D wavevector. .

We now discuss the wavelength matching of the charge fluctuations. Fig. 31a and Fig. 31c show a schematic band structure for a 2D electron gas (2DEG)[11] and graphene, respectively. As seen in chapter 1 or chapter 5, the energy dispersion is $\epsilon_{\mathbf{k}} = \hbar^2 k^2/2m$[12] and $\epsilon_{\nu\mathbf{k}} = \nu\hbar v_F k$, respectively. The advantage of using the (surface) charge structure factor of the metal $S_e^s(q,\omega)$ is that we can restrict the integration of Eq. 246. $S_e^s(q,\omega)$ quantifies the number of electron-hole pairs that can be created with a momentum of $\mathbf{q}$ and an energy $\hbar\omega$. A look at a metallic band structure (see Fig. 31) gives us an upper bound for the norm of the maximum scattering wavevector $\mathbf{q} = |\mathbf{k} - \mathbf{k}'|$, at low energy $\hbar\omega = |\epsilon_{\mathbf{k}} - \epsilon_{\mathbf{k}'}| \ll E_F$. We look for possible "horizontal" transitions between two states in the band structure. Zooming on the electronic Fermi surface (Fig. 31b), we find a common criterion — $|\mathbf{q}| < 2k_F$ — for graphene and 2DEG. For a 3D material, one needs to project all electronic bands along the 2D wavevector plane, like in Fig. 15. For a 3D jellium, the convexity of the band structure implies that the same criteria is still valid. This reasoning is exact at $T = 0$K. Thermal smearing alters this argument, but as long as $k_B T \ll E_F$, the criteria $|\mathbf{q}| \lesssim 2k_F$ is still valid.

We compute $S_e^s(q, \omega = 0)$ in Fig. 32 for graphene and for a 3D jellium to ensure we are not missing some important considerations when the metal has some thickness. We use the RPA+SRA level for the jellium — details are given in appendix H.1. We use analytical formulas at $T = 0K$ in all cases. As discussed, the results only depend on $q/2k_F$. For the 3D jellium, the variation with k_F is captured by solely looking at the value in $q = k_F$.

[11] $\mathbf{k}$ is a 2Dwavevector here.
[12] We use $m^* = m$, the mass of an electron.

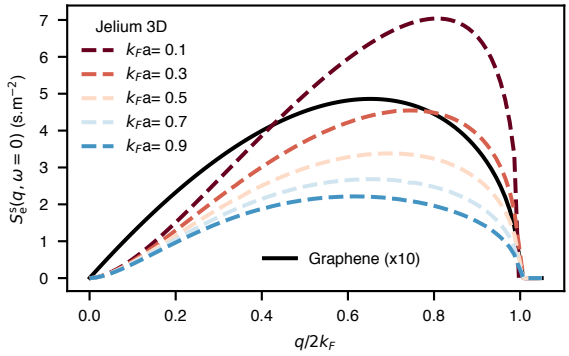

Figure 32: Surface charge structure factor for a 3D jellium and graphene, for various k_F, at $T = 0$K. There is no variation of $S^s_e(q, \omega = 0)$ with k_F for graphene.

The static surface charge structure factor $S^s_w(q)$ for the liquid is linked to the static SRF by the FDT (see e.g. 299 and Eq. 233). We use

$$S^s_w(q) = 2k_B T \epsilon_0 q g_w(q). \tag{247}$$

Using $g_w(q \ll 1/2d) = \frac{\varepsilon_w - 1}{\varepsilon_w + 1}$ (see Eq. 86) and restricting the integration of Eq. 246 to $q < 2k_F$, we suggest formula III for the friction coefficent. It is valid in the case of frequency $\tau_D^{-1} \ll k_B T/\hbar \ll E_F \hbar$ *and* wavelength $4k_F d \ll 1$ decoupling. It reads

$$\lambda^{(III)}_{nBO} \simeq \frac{\varepsilon_w - 1}{\varepsilon_w + 1} \frac{2}{3} \frac{k_F^3}{4\pi\epsilon_0} S^s_e(k_F, \omega = 0) H(\frac{q_{TF}}{2k_F}, \varepsilon_w), \tag{248}$$

where the analytical expression of H is given and discussed in Appendix H.2. We have used $g_e(q) = \frac{q_{TF}}{q + q_{TF}}$, that is valid for $q < 2k_F$ for a wide variety of materials such as graphene, FLG, and 2DEG (see chapter 5). The evaluation of Eq. 248 for typical metals and complementary discussions can be found in appendix H.2. In the following, we focus on carbon materials.

8.2 RESULTS

8.2.1 *Case of graphene and FLG*

For graphene, $q_{TF}/2k_F = 2\alpha_e$ where $\alpha_e = 1/4\pi\epsilon_0\hbar v_F = 2.2$ is the fine structure constant of the material. Using the limit $\varepsilon_w \gg 2\alpha_e$ in $H(2\alpha_e, \varepsilon_w)$ and $\frac{\varepsilon_w - 1}{\varepsilon_w + 1} \simeq 1$, we obtain

$$\lambda^{(Graphene)}_{nBO} \simeq \frac{k_F^3 \alpha_e (1 + 2\alpha_e)}{\pi\epsilon_0} S^s_e(k_F, \omega = 0) \simeq \frac{(k_F a)^3}{3} \times 10^1 \text{ (N.s.m}^{-3}) \tag{249}$$

with $a = \sqrt{3}d_{cc} = 2.46$Å and $k_F a \ll 1$ for typical doping.

For FLG, we use $q_{TF} = q_s$ (Eq. 130 and Eq. 131) to evaluate $\lambda_{nBO}^{(III)}$ in Eq. 248. We replace $S_e^s(k_F, \omega = 0)$ by $S_e^s(k_F, \omega = 0)/2$ to consider FLG instead of graphene[13]. Using $\varepsilon_w = 71$, we obtain

$$\lambda_{nBO}^{(FLG)} \simeq 0.17(\frac{2k_F}{q_s})^3 H(\frac{q_s}{2k_F}, \varepsilon_w) \simeq 6 \times 10^{-2} \text{ (N.s.m}^{-3}\text{)}. \tag{250}$$

with $k_F = q_s/4\alpha_e$ (a doping of $E_F = 0.27$ eV) for the numerical application.

We have assumed $k_B T \ll E_F$ to obtain Eq. 249 and Eq. 250, but they are upper bounds for the case $E_F \to 0$. From those results, we conclude that non-adiabatic contributions to the friction coefficient for graphene or FLG, at the RPA level, are many orders of magnitude smaller than the experimental value on graphite $\lambda_{exp}^{Graphite} \simeq 1.2 \times 10^5$ N.s.m^{-3}.

8.2.2 *Case of graphite*

Although our first-principle calculations at the RPA level show convergence of $g_e(q, \omega)$ with the number of layers N for FLG (see Fig. 18), they miss to reproduce an experimentally seen low-energy plasmon [144, 145, 146, 147, 148, 149, 150, 151] near $\omega_P \simeq 50$meV, at $T = 300$K, in graphite[14]. This is not the case of other theoretical studies [152, 153] that predict some of its characteristics. This plasmon puts into question the use of $\lambda_{nBO}^{(II)}$, that is the decoupling of the dynamics. We need to study it in detail and answer several questions.

Why don't we see this plasmon in our study? The abovementionned theoretical studies look for low-energy plasmons in bulk graphite (at the RPA level), meaning that they have an infinite number of graphene layers. They deal with a continuous q_z index instead of discrete band indices ν (like us), which reveals our finite number of layers N. We can therefore suppose that we did not converge exactly our results for graphite ($N \to \infty$) in the $N = 12$ case, in the low-energy region. In [152], the plasmon exists with a wavevector $q_z \leq 0.03$Å^{-1}. It corresponds to oscillation wavelength of about $N = 1/(q_z c/2) \simeq 20$ layers, larger than our maximum number of layers. Note that we have chosen not to follow the computation of the bulk graphite

[13] It can be refined depending on the exact number of graphene layers if $N \leq 5$. This change is motivated by two arguments. First, the slope of $\text{Im}g_e(q, \omega)$ for $\omega \to 0$ in Fig. 18b that converges to the one of graphene divided by a factor of 2. This is observed at the RPA level for $T = 300$K, by solving the Schrödinger equation for FLG. The second argument comes from a simple model we build in appendix H.3, in which we express $S_e^s(q, \omega = 0)$ with the analytical graphene's response function $\chi_e^{(0)}(q, \omega)$, by coupling independent graphene layers. We also obtain the factor of 2, or less (i.e. there is a slight variation with k_F).

[14] Those Electron Energy-Loss Spectroscopy (EELS) experiments that we choose not to detail here measure signals that are proportional to $\text{Im}g_m(q, \omega)$.

dielectric function because it is numerically too demanding. The authors of [152] only study the case $\mathbf{q} = 0$, which is not of great interest to us.

What is the history of this low-energy plasmon? It has been ignored in the first studies of the electronic properties of graphite — e.g. [154]. We find two reasons for that. First, condensed-matter experimentalists seem to be more interested in different range of energies (i.e. $\sim$ 1eV at $T = 0$K and not really $\sim k_B T \simeq 25$meV at room temperature). Therefore, it has been overlooked in most studies. The second reason is the experimental difficulties in measuring such low-energy excitations [148]. In the latter studies [144, 145, 146, 147], it seems that it may have been confused with phonons contributions because of their similar energies [148]. The study [148] is the first (and only) one that tries to reconcile experimental data regarding the dispersion of this plasmon with the most resolved apparatus. This plasmon was observed later in several experiments [149, 150, 151, 155], but its dispersion has never been studied since then. Finally, the last study ([156], cited more than two hundred times but for different reasons) attributes a peak to this plasmon for graphene on SiC(0001). We choose to restrict the discussion of this plasmon to graphite.

What is the physical origin of this low-energy plasmon? Experimentally, this plasmon is seen to be polarized in the direction normal to the graphene sheet, along $\mathbf{e}_z$ (in our case). It corresponds to a collective charge oscillation of electrons traveling between graphene layers. It is possible because the electronic states on different layers are coupled (see, e.g., the Hamiltonian matrix in Eq. 124). Accordingly, this plasmon could not be found with the simpler model we build in Appendix H.3 in which graphene layers are only electrostatically coupled.

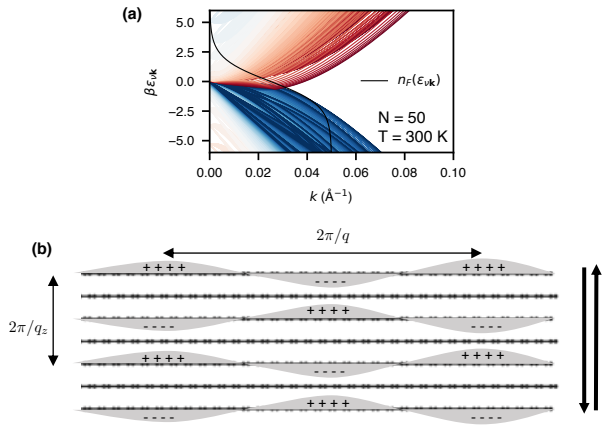

Figure 33: **(a)** Zoom on the band structure of FLG ($N = 50$) near the Fermi level showing the overlap between valence and conductions bands in graphite. A color corresponds to a electronic band ($2N$ bands in total). Multiple lines with the same color represent different angles in the BZ. Note that $\mathbf{k}$ is a two-dimensional vector here. **(b)** Schematic illustration of the low-energy intersheet plasmon mode.

Between which states those electronic transitions occur? In graphite, electronic states that are spatially localized on graphene layers that are far apart actually have similar energies. It can be seen by looking at the band structure of graphite, projected in the 2D plane (see Fig. 33a for $N = 50$. See also Fig. 15d for $N = 16$). At the Fermi level (assuming $E_F = 0$), many electronic bands overlap. Electrons can travel between graphene sheets at negligible energy cost ($\hbar\omega = |\epsilon_{\nu\mathbf{k}} - \epsilon_{\mu\mathbf{k}'}| \simeq k_B T$) and small parallel momentum $q = |\mathbf{k} - \mathbf{k}'|$. One can picture waves of electrons tunneling between sheets at $T = 300$K, as shown in Fig. 33b. Letting aside the q_z dispersion that is not the most relevant to us, we look at the topmost layer of the slab (assuming a large number of layers for the reasons abovementioned).

What is the momentum dispersion in the plane? Looking for horizontal transitions ($\hbar\omega \simeq 0$) in Fig. 33a, and considering the thermal smearing, we find them limited to wavevectors $q \leq |\mathbf{k} - \mathbf{k}'| \simeq 0.12\text{Å}^{-1}$. In the most resolved experiment [148], the plasmon cannot be traced for $q \geq q_{\max}$ with $q_{\max} = 0.18\text{Å}^{-1}$, which agrees with our estimation. The slight underestimation can be explained *(i)* because we look at horizontal transitions instead of one involving having a vertical component of $\hbar\omega \simeq \hbar\omega_P$ *(ii)* of the limitation of the model (and the TB parameters fitted on another experiment) *(iii)* of the limits of this "by-hand" estimation that (at least) do not weight the contribution of larger wavevectors properly. In a study [147] prior to [148], values reaching $q_{\max} = 0.4\text{Å}^{-1}$ were find at $T = 300$K and $q_{\max} = 0.6\text{Å}^{-1}$ at $T = 600$K. The authors of [148] argue that we cannot experimentally distinguish this plasmon from the LA phonon mode for $q \geq 0.18\text{Å}^{-1}$.

How can this plasmon play a role in non-adiabatic friction? Fig. 33b shows how this plasmon can act as charge corrugation on the top graphene layer of graphite. The value of $q_{\max}$ is crucial because it gives the wavelength of this corrugation. Also, the use of the BOA is put into question because $\omega_P \simeq 2k_B T/\hbar$. We need to evaluate $\lambda^{(\mathrm{I})}_{\mathrm{nBO}}$ in this case.

To evaluate the contribution of this plasmon, we choose a simple model for $g_e(q,\omega)$ to focus on the relevant low-frequency region. We write

$$\frac{g_e(q,\omega)}{g_e(q)} = \frac{\omega_P^2}{\omega_P^2 - \omega^2 - 2i\gamma\omega}\Theta(q_{\max} - q), \tag{251}$$

where $\gamma = 25$meV [148] is the plasmon width and $g_e(q)$ is the SRF of graphite (or FLG for $N > 4$). Eq. 251 ensures the correct limit for $g_e(q, \omega = 0)$ and the FDT. From Eq. 251 and the FDT (Eq. 233), we obtain $S^{\mathrm{s}}_e(q,\omega)$. We show in appendix (see Fig. 46) $S^{\mathrm{s}}_e(q,\omega)$ alongside with $S^{\mathrm{s}}_w(q,\omega)$. Again, we find very accurate to evaluate $\lambda^{(\mathrm{I})}_{\mathrm{nBO}}$ by pulling out $S^{\mathrm{s}}_e(q,\omega = 0)$ out of the integral. It is

actually due to the larger frequency that can be traced back to $\varepsilon_w \ll \omega_P \tau_D$[15]. Using the static FDT (Eq. 247), we obtain

$$\lambda_{\rm nBO}^{\rm (Graphite)} \simeq \frac{k_B T \gamma}{\omega_P^2} \int_0^{+\infty} \frac{{\rm d}q}{2\pi} \frac{q^3 g_e(q) g_w(q)}{\left(1 - g_e(q) g_w(q)\right)^2}. \tag{252}$$

We compute Eq. 252 using $k_B T \gamma / \omega_P^2 = 1/4$, Eq. 127 with $q_{\rm TF} = q_s$ ($E_F^{\rm eff} \simeq 0.27$ eV) for $g_e(q)$ (see chapter 5), and $g_w(q)$ (in Eq. 86). The results are shown Fig. 34, with respect to $d/d_{\rm OH}$ (with $d_{\rm OH} = 1$Å), for several $q_{\rm max}$.

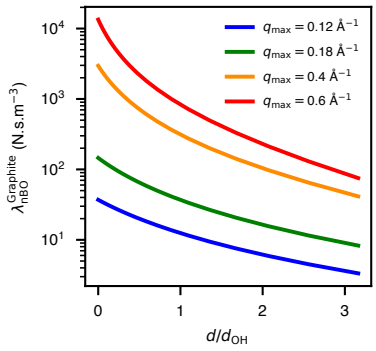

Figure 34: Graphite/water non-adiabatic contribution to the friction coefficient as a function of $d/d_{\rm OH}$.

Our reference values are $d = (d_{\rm Aluru} + d_{\rm Werder})/2 = 1.52$Å (see MM simulations in chapter 3) and $q_{\rm max} = 0.18$Å^{-1} (see [148]), from which we find $\lambda_{\rm nBO}^{\rm (Graphite)} \simeq 30$ N.s.m^{-3}. However, for $d = d_{\rm OH}$ and $q_{\rm max} = 0.4$Å^{-1}, we find $\lambda_{\rm nBO}^{\rm (Graphite)} \simeq 300$ N.s.m^{-3}. Using larger values for $q_{\rm max}$, keeping in mind the plasmon picture, is quite unrealistic according to Fig. 33a. Using smaller values for $d < d_{\rm OH}$ is not in the spirit of our microscopic approach and would deteriorate the results obtained for the vdW energy in Fig. 28. It would nevertheless lead to results closer to the graphite experimental values $\lambda_{\rm exp}^{\rm Graphite} \simeq 1.2 \times 10^5$N.s.m^{-3} or simulation data $\simeq 4.5 \times 10^4$N.s.m^{-3}.

Conclusion

In this chapter 8, we estimated the role of non-adiabatic effects in understanding friction at the metal/liquid interface. In the absence of a static corrugation, the roughness-based picture no longers hold, but the friction can still be understood as an overlap between two dynamical surface charge structure factors. The friction coefficient quantifies the overlap between charge fluctuations wavelength and frequency in both media. The general friction formula that we derive could be simplified in all cases we dealt

[15] The libration peak of water $\omega_L \simeq 100$ meV puts the BOA into perspective, but it is irrelevant here because $\omega_L > 2k_B T/\hbar$.

with for metal/liquid friction, leading to a semi-classical result that can be understood with the electronic friction picture, as defined in [136]. In the case of wavelength decoupling, we have given analytical formulas with typical parameters of metals — k_F and q_{TF} — and polar liquids — ε_{w}.

We conclude that, within the limits of our formalism, the non-adiabatic contribution to the solid/liquid friction seems to be three orders of magnitude lower than the experimentally measured value on graphite — and way lower for graphene. However, considering the sensibility to the inherent parameter of our microscopic framework, the vacuum gap thickness d, we advocate for further interest in this question.

GENERAL CONCLUSION

In a nutshell, we summarize the main results of this work by distinguishing the theoretical results from the ones specific to the graphene/water interface. We then discuss the limits of our approach and future perspectives.

From the theoretical point of view, our first contribution is the microscopic formulation of the electrostatic problem at interfaces (part i). We consider materials infinite in only two directions. In the third, they are closed by an impenetrable plane so that the charge density profile vanishes at this altitude (chapter 2). We use the linear response framework to obtain the electrostatic potential but displace the problem in resolving an integral equation for the response function. The latter involves a non-interacting response function $\chi^{(0)}$ and the mean-field potential between particles v_{inter} (chapter 1). In practice, it is solved by a mere matrix inversion (part ii). For instance, the effect of microscopic parameters on the screening of an applied constant electric field can be studied (chapter 4). We no longer have to resort to a phenomenological approximation to solve the interfacial electrostatic problem. The framework provides a way to deal with ions at water interfaces without reducing the liquid to its bulk dielectric function (chapter 6).

Our second contribution comes from the hybrid quantum/classical coupling. We encompassed a liquid's fluctuations and dielectric response in a quantum field by introducing a fictitious quantum operator (chapter 2). It allowed us to formulate the interfacial self-consistent electrostatic problem by hijacking the electron-phonon problem in solid-state physics. As a result, we can benefit from decades-long development in this field. For instance, physical observables can be linked to screened potentials (chapter 6), self-energies (chapter 7) or specific response functions (chapter 8), expressed in terms of Feynman diagrams. The framework ensures the self-consistency of the electrostatic problem — electrons see the liquid molecules that see the electrons. Those coupled interactions make the physical observables non-longer linearly dependent on the response of the two media at the interface.

On the other hand, the results — that exist thanks to the elaboration of the previous framework — regarding the graphene/water interface can be summarized as follows. First, we have seen that coupled dipole/electron and electron/electron interactions were crucial to understanding the PMF of an ion at the interface (chapter 6). Our results reproduced a reference PMF

obtained using expensive AIMD free energy perturbation calculations[16]. Unlike typical TF metals, the interface's microscopic details change graphene's screening properties. In return, we find that graphene could not be modeled by a TF model that is valid both in vacuum and in water because of its peculiar semi-metallic band structure.

Regarding the electronic band gap of a solvated CNT (chapter 7), we obtain an analytical expression of the non-local and dynamical dielectric function on the tube's surface. It is expressed with the inside/outside liquid's SRFs, which are defined by microscopic correlation functions. It is now possible to infer the non-local and dynamical properties of a metal's liquid environment, and we prompt physicists in the specific domains to evaluate environmental effects with this refined microscopic description. We show how water's libration peak alters graphene's loss spectra as an example of overlooked contributions.

Finally, we estimated the non-adiabatic contributions to the metal/liquid friction phenomenon (chapter 8). We have seen that friction can always be formulated as an overlap between two surface charge structure factors. For the non-adiabatic contribution, the friction coefficient quantifies the matching between frequency and wavelength charge fluctuations in both media. The relative frequency decoupling allows evaluating the first-order correction to the BOA in all cases under scrutiny. Therefore, the semi-classical mechanism of electronic friction in which dissipation is localized in the metal is relevant. Our estimation of the contribution of this process to experimentally measured values does not allow us to call the BOA into question in AIMD — at least, not for computing friction. Nevertheless, our approach provides the tools to enrich our understanding of solid/liquid friction.

What are the limits of our approach? The main limit is most probably about the lack of chemistry. We consider closed media so that charge transfer is forbidden. The argument relying on the overall neutrality of both media can be challenged. If it is accepted that there is no charge transfer on average or for a single adsorbed (say water) molecule, it says nothing about the dynamical fluctuations of charge transfer. The second apparent limit of our framework is the validity of our description for wavevectors comparable to the inverse lattice $q \sim 1/a$. This limit is linked to the first because chemical effects predominate (exchange-correlation interaction, hydrogen-bond, charge transfer) on the atomic size. Metal/liquid electrostatic interactions are cut off by a factor $e^{-2z/a}$, and only adsorbed molecules play a role.

Future directions for the friction? It could be interesting to evaluate the link between metal/liquid friction and charge transfer fluctuations. Both media

[16] We have written an article [157] on this subject. It is currently in the submission process.

could exchange (fraction of) electrons; the question would be to determine the specific surface area or time scale. There is some experimental evidence for such a triboelectrification effect [158]. This would be a red wire to include chemical effects in the present formalism.

What is left to do regarding the framework? One could rederive the main equations of this work, including local-field effects. It would "complete" the purely physical description. For completeness, it would be beneficial to include phonons in one wants to tackle dynamical properties. The diagrams equations in this thesis can all be expressed in terms of the matrices of the elementary blocks. Numerically, it is a real advantage, and one can quickly think of a code that computes $W = W_\mathrm{w} + W_\mathrm{w} X_\mathrm{e} W_\mathrm{w}$ for large systems, in seconds.

Machine learning approaches may revolutionize molecular simulations and enrich the insights they bring into metal/liquid interfaces [13]. I believe making them talk with cheaper analytical models is crucial so that new ideas can emerge from a scientist's head. We tried to twine our approach with simulation results (see chapter 3, 4, 6, 8 and Intermezzo) because we think they can benefit from each other[17]. We hope this versatile approach, which can be generalized for any metal/liquid couple, will be appreciated by some researchers in the liquid and metal community.

[17] That is all the more the case with our microscopic approach that allows the tuning of, for instance, an hydrogen partial charge, tight-binding parameters, etc..

ABSTRACT EN FRANÇAIS

Un cadre théorique est introduit pour aborder les interactions électrostatiques aux interfaces métal/liquide. En adoptant une perspective microscopique, nous déplaçons le problème électrostatique dans la résolution d'une équation intégrale pour la fonction de réponse linéaire du système interfacial. En décrivant les fluctuations et la réponse diélectrique du liquide dans le formalisme de la théorie quantique des champs, nous héritons de nouveaux concepts pour aborder les interactions collectives en champ moyen. La précision et la versatilité de notre approche nous permettent de décrire des interfaces carbonées en considérant la spécificité de leurs structures de bandes électroniques. Cette méthode est ensuite mise en pratique pour étudier le potentiel de force moyenne d'un ion solvaté près d'une surface de graphène, la largeur de la bande électronique interdite d'un nanotube solvaté, l'interaction de van der Waals entre du graphène et de l'eau, et des coefficients de friction solide/liquide. La validité des hypothèses classiques concernant le découplage des temps et longueurs caractéristiques aux interfaces métal/liquide, peut être systématiquement évaluée.

RÉSUMÉ EN FRANÇAIS

Cette thèse est motivée par un enthousiasme nouveau pour la nanofluidique [1]. Cette discipline étudie les liquides dans des canaux de quelques milliardièmes de mètres. Cette étude est permise grâce aux progrès techniques titanesques concernant la fabrication de ces canaux ou la détection de ce qui en sort. À cette échelle nanométrique on observe plutôt une "foule" de molécules sortant d'un canal (voir, par exemple, Fig. 1a) et non un jet d'eau comme celui du robinet de la cuisine. Les expériences qui permettent ces mesures ne seront pas abordés dans ce travail, mais nous devons commencer par dire notre émerveillement pour de telles prouesses qui sont la condition nécessaire à notre travail théorique (voir Fig. 1b). Pour citer quelques travaux majeurs, on peut se réferer par exemple à [2, 3, 4, 5, 6].

Pourquoi travailler dans la nanofluidique ? La nécessité d'utiliser des énergies propres et renouvelables pour traverser les crises écologiques actuelles et futures a motivé beaucoup de recherche scientifique dans des domaines divers. La nanofluidique soutient l'espoir de pouvoir exploiter des phénomènes osmotiques aux embouchures de mers et rivières. En effet, à cette échelle, apparaissent des phénomènes exotiques qui permettent de générer des courants électriques comme celui de diffusio-osmose[18]. Des processus similaires proposent des solutions aux enjeux concernant l'approvisionnement en eau par sa désalinisation. Ces applications sont détaillées ici [8].

Pourquoi des liquides comme l'eau ont un comportement étrange dans ces canaux ? La réduction d'échelle (de macro à micro, puis nano) change les interactions physiques dominantes. En nanofluidique, de nouveaux phénomènes apparaissent grâce à l'augmentation du ratio surface/volume pour le liquide. Pour le comprendre, on peut regarder la matrice de transport qui relie quelques forces appliquées à leurs observables ad hoc (voir Fig. 1c). Quand seuls les termes diagonaux subsistent, on peut indépendamment relier les forces appliquées (respectivement une différence de pression, de potentiels chimiques ou un champ électrique) aux observables (flux du solvant, flux d'excès du soluté, courant ionique). Cependant, les effets de surfaces produisent des termes non-diagonaux importants, de sorte que de

[18] Processus dans lequel une différence de concentration en sel entre deux réservoirs reliés par un canal nanométrique induit un courant ionique grâce à une interaction différente des cations et anions avec la surface du canal. Voir [7] pour plus de détails.

nouvelles options s'offrent à nous pour, par exemple, générer un courant ionique avec une différence de concentration en sel. Pour identifier ces termes croisés, une description physique/chimique précise de l'interface canal/liquide est alors nécessaire. C'est ici que l'intervention de chimistes théoriciens devient pertinente.

Il faut remarquer que l'émergence des nanocanaux permettant la mesure de flux arrive avec l'apparition du graphène en 2004 et l'intérêt nouveau pour les nanomatériaux à base de carbone [11]. L'enthousiasme de la communauté de la physique du solide pour le développement d'instruments capables de manipuler des nanomatériaux 1D ou 2D est maintenant apprécié de la communauté nanofluidique. Parmi ces matériaux van de Waals (vdW) et leurs assemblages [10], le graphène à un rôle emblématique. Cependant, isoler une feuille de graphène est compliqué et il s'avère plus simple d'utiliser des formes allotropiques du graphène pour la construction de canaux : des nanotubes de carbone (CNTs), plusieurs feuilles de graphène (FLG), du graphite.

Il existe cependant un matériau qui a la même maille cristalline que le graphène — le nitrure de bore hexagonal (hBN) — et qui est aussi souvent utilisé. La différence entre un CNT et un BNNT (nanotube de nitrure de bore) en nanofluidique illustre l'importance de la spécificité de l'interaction canal/liquide ou canal/ion [4, 6, 159], au-delà des considérations géométriques. Cependant, en dynamique moléculaire classique, ou mécanique moléculaire (MM), le graphène et l'hBN sont très semblables. Leur différence réside seulement dans la valeur des paramètres d'interaction vdW avec l'eau, c'est-à-dire avec les paramètres du potentiel de Lennard-Jones entre atomes [12]. L'apparente sursimplification qui est faite dans ces simulations est maintenant contestée avec des approches théoriques plus sophistiquées [25].

Le graphène et l'hBN diffèrent plus fondamentalement si l'on compare leurs réponses à un champ électromagnétique. Le graphène est un semimétal alors que l'hBN est un isolant. Pour les isolants, les méthodes de simulations et notamment leurs formes les plus précises, les dynamiques moléculaires ab initio (AIMD), sont fiables. Grâce à cette approche, l'interface hBN/eau a déjà dévoilé quelques-uns de ses secrets [14] et ne sera pas étudié dans ce travail. À l'inverse, il y a des raisons de remettre en question la fiabilité des simulations AIMD pour l'interface graphène/eau. D'abord, leurs coûts ne permettent pas d'utiliser des boîtes de simulations plus grandes que la longueur de corrélation typique des électrons. Pour la même raison, l'étude de sels à ces interfaces ne peut se faire qu'à des concentrations élevées. Mis

à part la fonctionnelle d'échange-corrélation ad hoc pour le calcul quantique effectué grâce à la théorie de la fonctionnelle de la densité éléctronique (DFT), la dyamique repose sur l'approximation Born-Oppheinmer (BOA). Celle-ci peut ne pas être respectée pour des molécules aux interfaces métalliques à cause du continuum de niveaux d'énergie près du niveau de Fermi. En fait, sans considérer le liquide, elle ne tient théoriquement et expérimentalement pas dans le cas du graphène [16].

Cette thèse se concentre sur l'interface graphène/eau et essaye de trouver quelques éléments qui nous indiquent la spécificité de ce couple. Le but n'est bien sûr pas d'obtenir des résultats quantitatifs, mais plutôt d'estimer des contributions "d'ordre deux", ignorées jusque-là. Pour ce faire, nous aurons besoin d'une approche robuste et élastique qui permet de considérer les interactions électrostatiques entre les électrons de la surface et les dipôles du liquide. De manière surprenante, nous n'avons trouvé qu'une seule façon de traiter cette interface analytiquement dans la littérature. C'est l'approche électrostatique continue qui décrit l'eau seulement par sa constante diélectrique bulk[19]. Cela nous a incités à proposer une approche microscopique de l'électrostatique. L'élaboration de cette nouvelle méthode et l'obtention de formules concernant d'importantes observables physiques constituent peut-être la partie la plus importante de ce travail en vue de cette béance dans la littérature.

À la fin des années 70, beaucoup d'efforts ont été dédiés à la compréhension de ces interfaces métal/diélectrique en présence d'ions par des méthodes analytiques. Ce travail a été fait en grande partie par A.A. Kornyshev et M.A. Vorotynsev et se cristallise dans [17] et [18]. Beaucoup de remarques cruciales étaient déjà présentes comme l'importance de la réponse non-local du diélectrique à ces interfaces. Cette méthode est toujours utilisée aujourd'hui [19, 20]. Cependant, l'intérêt relativement faible pour les approches analytiques dans le traitement de ces systèmes compliqués[20] peut être compris avec l'essor de la chimie computationelle et son large développement depuis les années 2000. Les simulations quantiques ont été et sont toujours d'inégalables outils d'étude des interfaces graphène/eau (voir par exemple [12, 22, 23, 24, 13]). Cependant, comme on l'a dit, la plus grande et la plus lente oscillation de dipôles/charges dans le système est limitée.

[19] On montrera dans ce travail que l'approche plus sophistiquée [17] qui permet aux diélectriques d'avoir une réponse non-locale — celle mentionnée au prochain paragraphe— ne fonctionne par pour l'eau : elle n'est tout simplement pas applicable ! Bien sûr, d'autres méthodes peuvent exister, mais nous ne les connaissons pas.

[20] "God made the bulk; surfaces were invented by the devil." — Wolfang Pauli, cité dans Growth, Dissolution, and Pattern Formation in Geosystems (1999) by Bjørn Jamtveit and Paul Meakin, p. 291

Pour tenter de résoudre ces problèmes, la dynamique moléculaire classique propose des modèles semi-classiques. Conscient que leur manque intrinsèque de métallicité demande l'introduction de paramètres décrivant le métal, beaucoup d'efforts ont été dédiés à la compréhension du rôle de sa polarisation en surface — voir par exemple [25] pour le graphène. Une approche générale est prometteuse [26]. Elle consiste à conférer aux atomes du métal une charge fluctuante qui est imposée à chaque pas de temps de la simulation, pour maintenir un potentiel constant à l'électrode[21]. Dépassant le modèle du conducteur parfait, elle permet même de conférer un écrantage de type Thomas-Fermi (TF) au métal [30].

Cependant, la spécificité d'un métal réside dans sa structure de bande. Le graphène est un semi-métal qui se comporte comme un métal sur de grandes distances, mais comme un isolant sur les petites. Ce comportement semble a priori difficile à inférer dans un Hamiltonien, au-delà du modèle TF. En outre, la procédure d'optimisation des charges atomiques dans le métal joue le rôle d'une BOA en AIMD. Dès lors, malgré les récents progrès considérables, il reste des questions ouvertes concernant cette interface auxquelles nous pouvons essayer de répondre. Il est inutile de dire que notre rôle ne peut que se limiter à un support analytique qualitatif. Nous allons donc questionner les hypothèses réalisées dans la construction des modèles mentionnés et peut-être suggérer de nouvelles directions pour améliorer de futures simulations.

On remarque finalement qu'en physique des solides, les communautés s'intéressant au graphène semblent ignorer le rôle de l'environnement diélectrique d'un métal, au-delà de la description électrostatique continue. Celle-ci ignore la réponse dynamique et non-locale du liquide. Il y aussi donc aussi ici des observables comme des conductivités électroniques, des dispersions de plasmons ou des bandes interdites électroniques de semi-conducteurs solvatés, à raffiner avec une meilleure une description de l'interface métal/liquide.

On peut conclure de cette introduction que notre travail réside premièrement dans l'élaboration d'une approche pratique de l'électrodynamique aux interfaces métal/liquide (partie i). Celle-ci doit être assez générale pour traiter un éventail de questions ouvertes concernant des effets "d'ordre deux" qui sont généralement ignorés à l'interface graphène/eau. Ainsi, dans la partie iii, nous obtiendrons les expressions de plusieurs observables physiques et étudierons :

- le potentiel de force moyenne d'un ion solvaté à l'interface métal/liquide,

[21] Pour une description détaillée des simulations semi-classiques, l'on renvoit à [27] et à [28, 29] pour les détails concernant la méthode du potentiel constant.

- la taille de la bande interdite électronique d'un CNT solvaté,
- la friction métal/liquide et sa contribution non-adiabatique à l'interface graphène/eau

Dans une moindre mesure, nous rencontrerons aussi la dispersion du plasmon du graphène solvaté, la réponse d'un slab d'eau à un champ électrique, l'énergie interfaciale de vdW. Nous verrons le rôle central de certaines fonctions de réponse que nous devrons donc construire en partie ii, avant les évaluations numériques qui se situent sous les formules, en partie iii.

PARTIE I La difficulté de la formulation de l'électrodynamique à une interface métal/liquide réside dans le fait de devoir faire dialoguer des domaines distincts de la physique : solide/liquide et quantique/classique. Dans les approches existantes, il y a toujours une préférence, car il y a certains points de vue. Il est intéressant de noter que la méthode encore aujourd'hui utilisée [17] — mais qu'on essayera de dépasser — a justement su placer le solide et le liquide sur un pied d'égalité. Malgré la réduction grossière, fixons les idées et schématisons ces deux domaines avec deux livres emblématiques [31, 32].

Cherchons les similitudes entre ces deux domaines en ce qui concerne l'électrodynamique. Dans les deux cas, on trouve un usage de la théorie de la réponse linéaire dynamique et non-locale. Notre premier point d'entrée sera donc de définir une fonction de réponse pour le métal χ_e et pour le diélectrique χ_w, tel que si un potentiel électrostatique extérieur ϕ_{ext} est appliqué à l'un d'entre eux, il répondra linéairement en induisant une densité de charge n_{ind} qui, en moyenne s'écrit :

$$\langle n_{ind}(1)\rangle = \int d2\chi(1,2)\phi_{ext}(2). \tag{253}$$

On a utilisé et utiliserons une notation regroupant espace et temps — i.e., $1 \equiv (\mathbf{x}_1, t_1)$ — pour la lisibilité. Dès lors, dans un système qui ne comporte que le métal ou que le diélectrique, on pourra trouver le potentiel total en considérant la somme de deux potentiels : celui appliqué ϕ_{ext} et celui généré par la nouvelle densité de charge induite ϕ_{ind}.

Nous pouvons donc exprimer le potentiel (total) ϕ_{tot} grâce à χ dans n'importe quel système fermé. On a donc déplacé le problème dans l'obtention de χ qui nous permet d'apporter des détails microscopiques. Nous allons construire χ avec une fonction plus simple $\chi^{(0)}$ qui considère que les particules[22] du système sont indépendantes, i.e. comme dans le gaz parfait, elles n'interagissent

[22] Ce sont les électrons pour le métal et les molécules polaires pour le liquide.

pas. À cette fonction de réponse $\chi^{(0)}$ nous devons ajouter un potentiel de force moyen entre particules v_{inter}. On construira χ en faisant une *renormalisation en champ moyen* de $\chi^{(0)}$. Il s'agit d'écrire qu'une particule répond au potentiel extérieur appliqué ainsi qu'au potentiel moyen induit par toutes les autres particules similaires. Ainsi, on obtient une équation intégrale de χ en fonction de $\chi^{(0)}$ et v_{inter}:

$$\chi(11') = \chi^{(0)}(11') + \iint \mathrm{d}2\mathrm{d}3\chi^{(0)}(12)v_{\text{inter}}(23)\chi(31'). \tag{254}$$

Ainsi, nous avons réduit le problème central de l'obtention du potentiel électrodynamique dans un métal ou un liquide à l'obtention de $\chi^{(0)}$ et v_{inter} et à la résolution d'une équation intégrale. A fortiori, à une interface, nous aurons besoin de $\chi_{\text{e}}^{(0)}$, $\chi_{\text{w}}^{(0)}$ et v_{inter} ("w" pour le liquide et "e" pour les électrons). Ce sont les briques élémentaires de notre approches. Dans ces travail, toutes les observables physiques pourront être exprimées grâce à elles seules. Cependant, leur définition est générale (nous n'avons toujours pas précisé de géométrie) et elles comportent *a priori* 8 indices ! Dans la suite de ce premier chapitre, nous donnons quelques exemples classiques pour exprimer des résultats connus sous cette forme dans le cas de systèmes homogènes, infinis et isotropes. Nous proposons aussi un d'expliciter certaines formules pour le cas d'un milieu semi-infini isolé. Ainsi, nous rencontrons pour la première fois une quantité qui s'avérera centrale dans notre travail. Il s'agit de la fonction de réponse de surface g (SRF) qui s'exprime grâce à χ comme ceci :

$$g(q,\omega) = \frac{-1}{2\epsilon_0 q} \iint \mathrm{d}z_1\mathrm{d}z_2 e^{-q(z_1+z_2)}\chi(q,z_1,z_2,\omega). \tag{255}$$

Nous avons utilisé le fait que pour une interface infinie (ici encore avec le vide) et à l'équilibre, la transformée de Fourier était pertinente dans le temps et le plan — $\mathbf{x} = (\mathbf{r}, z)$ en coordonnées cylindriques et $\mathbf{k} = (\mathbf{q}, q_z)$ dans l'espace réciproque. On comprend aussi que la connexion avec l'électrostatique continue se fait dans la limite des grandes longueurs d'ondes des fonctions de réponse manipulée. Par exemple, nous retrouvons le coefficient de réflexion du milieu semi-infini comme ceci :

$$g(q,\omega) \xrightarrow[q\to 0]{} \frac{\varepsilon(\omega)-1}{\varepsilon(\omega)+1}, \tag{256}$$

où $\varepsilon(\omega) = \varepsilon(k \to 0, \omega)$ est la fonction diélectrique du milieu homogène, isotropique et infini correspondant.

Le deuxième chapitre de cette partie pose les fondations de notre approche. On y décrit l'interface graphène/eau pour en conclure que les interactions

chimiques y sont a priori négligeables (pas d'échange d'électrons). Dès lors, on peut procéder à la fermeture des deux sous-systèmes métallique et liquide à l'interface. En effet, l'introduction abstraite d'une paroi imperméable entre les deux milieux permettra de construire un modèle microscopique de l'interface. Les Hamiltoniens du liquide et du métal sont d'abord construits séparément. Du côté du métal, c'est une pratique courante et l'on découple surtout les électrons des noyaux de la maille pour préparer l'ajout rigoureux du liquide. Du côté du liquide polaire, nous construisons un Hamiltonien qui peut s'écrire en fonction de $\chi^{(0)}$ et v_{inter}. Des comparaisons sont faites avec les fonctionelles de polarisation dans l'objectif de clarifier ce en quoi notre approche s'en démarque.

L'étape suivante consiste à résoudre les incompatibilités fondamentales qui subsistent encore pour le couplage classique/quantique en exprimant la densité de charge du liquide polaire avec un opérateur bosonique quantique. On montre comment obtenir, à partir de l'Hamiltonien classique du liquide et en imposant une dynamique ad hoc, une action qui peut s'insérer dans la théorie quantique des champs. On exploite à notre avantage des parallèles connus entre celle-ci [160] et la dynamique des champs statistiques formulée par Martin, Siggia et Rose [36]. Dès lors, une fois le liquide polaire transposé — seulement formellement — dans cet univers, nous bénéficions d'outils issus de théorie perturbation comme les diagrammes de Feynman. Ils permettent de combiner de manière systèmatique les fonctions de réponse du liquide et du métal (à travers $\chi^{(0)}$et v_{inter}) en fonction du cadre donné. Nous les adaptons et simplifions à nos besoins à la fin de cette partie.

PARTIE II Cette deuxième partie est dédiée à l'obtention des briques élémentaires de notre approche $(\chi^{(0)}, v_{\text{inter}})$ et des SRFs (g) pour l'eau et le graphène (ou plusieurs feuillets de graphène — FLG). On introduit à travers trois chapitres, trois méthodes originales pour obtenir ces quantités. Pour l'eau, nous procédons d'abord à des simulations moléculaires classiques dans plusieurs géométries pour obtenir des informations dynamiques. Ensuite, nous résolvons l'équation intégrale Eq. 254 pour un slab d'eau et procédons à diverses études concernant l'eau interfaciale. Enfin, nous résolvons Eq. 254 pour un système comportant plusieurs couches de graphène (FLG) grâce à l'utilisation de fonctions de Wannier et un modèle "tight-binding".

Des simulations MM sont réalisées pour de l'eau bulk, à l'interface avec du graphène et confinée dans deux feuilles de graphène, pour deux champs de force différents. Elles nous permettent d'abord de nous intéresser aux fonctions de réponse dynamiques du milieu homogène, isotrope et infini.

Nous repérons le pic de Debye et de libration dans le spectre de l'eau et nous construisons des modèles analytiques pour les modéliser. Nous nous faisons une idée de la SRF dans la limite de l'électrostatique continue grâce à l'Eq. 256. Les simulations interfaciales nous apportent tout d'abord des éléments complémentaires sur les Hamiltoniens statiques de référence qui seront considérés pour la théorie de perturbation. Un protocole est proposé pour obtenir g grâce au théorème de fluctuation–dissipation (FDT) qui s'écrit :

$$\mathrm{Im}g(q,\omega) = \frac{\tanh(\hbar\omega/2k_BT)}{2\epsilon_0 q\hbar} S^{\mathrm{s}}(q,\omega). \tag{257}$$

On a ici introduit une nouvelle fonction de corrélation importante que l'on nomme le facteur de structure de charge de surface. L'analyse des simulations consiste donc à obtenir $S^{\mathrm{s}}(q,\omega)$. Grâce à l'Eq. 257 et à des propriétés d'analyse complexe de fonctions de réponse, nous construisons une méthode d'obtention, des références et des modèles pour $g_{\mathrm{w}}(q,\omega)$.

Dans un second temps, en partant d'un modèle géométrique d'une molécule d'eau (modèle SPC/E, aussi utilisé pour le MM) nous dérivons une expression analytique pour $\chi^{(0)}$ dans le cas d'un slab d'eau. Nous inférons ensuite un potentiel d'interaction moyen entre molécules d'eau v_{inter} qui est construit grâce à des résultats expérimentaux ou de simulations. Les éléments de l'Eq. 254 étant réunis, nous montrons comment celle-ci peut-être résolue pour $\chi_{\mathrm{w}}(q,z,z')$ grâce à une simple inversion matricielle. Nous comparons nos résultats avec ceux de la littérature pour finalement prolonger notre étude de la réponse diélectrique de l'eau à une interface. L'effet d'un champ électrique extérieur est étudié et la pertinence de l'introduction d'une constante diélectrique effective dans notre approche microscopique est discutée.

En dernier lieu, nous procédons à la même démarche du côté graphène et FLG. Cette fois-ci, le formalisme quantique est nécessaire. Pour se placer à température ambiante, nous utilisons l'approche de Matsubara pour obtenir $\chi_{\mathrm{e}}^{(0)}$. Les interactions d'échange-corrélation ne sont pas considérées dans v_{inter} et nous nous plaçons donc au niveau "random phase approximation" (RPA)[23]. Une solution originale pour le FLG est proposée pour la résolution de l'Eq. 254 en réhabilitant des idées proposées lors de l'apparition des fonctions de Wannier [69]. Un modèle bien connu de "tight-binding" pour le graphène et FLG est adopté et les SRFs $g_{\mathrm{e}}(q,\omega)$ sont calculées, comparées et discutées.

[23] Leur ajout n'est cependant pas problèmatique.

PARTIE III La dernière partie de ce travail consiste à obtenir des expressions pour des observables physiques pertinentes aux interfaces métal/liquide avec des applications pour le graphène et l'eau. La première qui nous intéressera est le potentiel de force moyenne d'ion solvaté, s'approchant de l'interface. Elle nécessite l'obtention du potentiel électrostatique à l'interface considérée. Nous établissons d'abord les limites conceptuelles et pratiques (pour l'eau) de l'approche existante. Ensuite, nous utilisons notre approche et organisons nos briques élémentaires ($\chi_e^{(0)}, \chi_w^{(0)}, v_{inter}$) pour obtenir l'expression du potentiel total dû à une densité de charge externe à cette interface. Notre résultat théorique est similaire à celui d'Hedin [95] et son traitement du problème électron-phonon. En utilisant les résultats de la partie II, le PMF du potassium (K^+) à l'interface graphène/eau est calculé. La comparaison avec des résultats longs et couteux de calculs d'énergie libre effectué en AIMD démontre la pertinence de notre approche. Nous procédons à l'analyse des différentes contributions du PMF, toujours en lien avec un regard critique sur les hypothèses effectuées en simulation (métallicité, "fit" de paramètres dans le vide, importance des interactions électroniques). Finalement, nous concluons sur la particuliarité du graphène et sa structure de bande semi-métallique. L'insuffisance du modèle de TF pour décrire la réponse diélectrique du graphène de manière cohérente dans le vide et dans l'eau (en même temps) est relevée.

Dans un deuxième temps, nous nous intéressons à l'évaluation de la bande interdite électronique (ou "gap") d'un CNT. Cette étude est motivée par l'appel explicite d'un chercheur pour une description microscopique du liquide aux interfaces CNT/eau. Nous la construisons en ayant recours à des calculs GW pour obtenir l'expression du "gap". Elle prend en entrée l'expression de la fonction de Green du système sur le CNT que nous pouvons exprimer analytiquement grâce aux SRFs g_e et g_w. Nous exprimons les fonctions de corrélations microscopiques à calculer dans une étude future. Les résultats obtenus dans ce chapitre — en donnant une description microscopique et dynamique de l'environnement des électrons à la surface solvatée d'un métal — permettent aussi de mieux décrire les excitations du système. À titre d'exemple, et pour inciter à la réévaluation de ces subtilités ignorées, nous montrons que le pic de libration de l'eau altère le spectre d'excitation du graphène solvaté.

Le dernier chapitre de ce travail examine l'hypothèse d'une contribution non-adiabatique au phénomène de friction aux interfaces graphène/eau. Après l'exposition des motivations d'un tel questionnement et un rappel de la description classique de la friction — une image basée sur une idée de

corrugation statique — nous partons à la recherche de corrections à BOA. Nous trouvons que le coefficient de friction à une interface peut toujours s'exprimer comme un recouvrement entre deux facteurs de structure de charge de surface S^s_w et S^s_e. La contribution non-adiabatique quantifie les similitudes entre les fluctuations temporelles et spatiales de charge dans les deux millieux. La formule générale pour la friction entre deux solides[24] se simplifie dans le cas d'une interface métal/eau grâce au découplage des temps et longueurs de corrélation dans les deux matériaux. Le processus de friction électronique est évalué pour l'interface graphène/eau et FLG/eau. En outre, des données spectroscopiques expérimentales nous enjoignent à étudier de plus près le cas du graphite et de son plasmon de basse énergie. Trois ordres de grandeurs séparent notre estimation des contributions non-adiabatiques à la friction expérimentalement mesurée.

En conclusion, nous discutons brièvement des limites et perspectives de notre cadre théorique. Notre approche de l'électrostatique surmonte des obstacles théoriques non négligeables. Elle permet d'étudier les interfaces métal/liquide rigoureusement à partir de modèles microscopiques et à un prix computationnel négligeable. Elle pourrait constituer un outil complémentaire aux simulations moléculaires avec lesquelles un dialogue a été amorcé dans ce travail. Nous espérons qu'elle sera appréciée par quelques chercheurs de disciplines différentes.

[24] introduite par Persson et al. [143], et que nous généralisons.

Part IV

APPENDICES

A

APPENDICES OF CHAPTER 1

A.1 STANDARD APPROACH TO ELECTROSTATICS

Herein, we summarize the standard approach to electrostatics. Gauss's law relates the electric field $\mathbf{E}$ in the vacuum to the electric charge density ρ it stems from:

$$\nabla \cdot \mathbf{E} = \frac{\rho}{\epsilon_0}. \tag{258}$$

The vector fields we introduce — e.g., $\mathbf{E}$ — are expectation values of operators for quantum systems. Helmholtz allows us to decompose the electric field into a divergence-free field (or "transverse") and an irrotational one (or "longitudinal"). Introducing the electrostatic potential ϕ and the vector potential $\mathbf{A}$, it reads [33]:

$$\mathbf{E} = -\nabla\phi - \partial_t \mathbf{A}. \tag{259}$$

Using the Coulomb gauge — i.e., $\nabla \cdot \mathbf{A} = 0$ —, and inserting in Eq. 259 in Eq. 258, we obtain Poisson's equation:

$$\nabla^2\phi = -\frac{\rho}{\epsilon_0}. \tag{260}$$

Assuming that a charge labeling is possible, the linearity of Eq. 260 prompts us to separate charges. Some are external to the medium under consideration ρ_{ext}, some are present without the external perturbation ρ^0, and others ρ_{ind} (also noted $\delta\rho$) are induced by the presence of the external ones. It means that we can write $\phi = \phi_{\text{ext}} + \phi^0 + \phi_{\text{ind}}$, each potential solving independently Eq. 260.

POLARIZATION AND DISPLACEMENT FIELD It is usual to make yet another distinction regarding the nature of the charges. When the system is probed with wavelengths λ *extremely large* compared to typical atomic separation distance a, averages can be made on large volumes $\mathcal{V}$ compared to a. Therefore, if we can find a volume $\mathcal{V}$ such that $a \ll \mathcal{V}^{\frac{1}{3}} \ll \lambda$, we can separate charges that are bound (ρ_{b}) to a position (move on scale of a) and others that are free (ρ_{f}, that can move on large scales $\mathcal{V}^{\frac{1}{3}}$). For instance, polar molecules in a dielectric can be considered bound charges, whereas electrons

in a metal are free. With this distinction — e.g. $\rho = \rho_{\text{ext}} + \rho_{\text{b}} + \rho_{\text{f}}$ — we rewrite Eq. 258 as

$$\nabla \cdot \langle \mathbf{D} \rangle_{\mathcal{V}} = \rho_{\text{f}} + \rho_{\text{ext}}. \tag{261}$$

where we have introduced the volume averaged displacement field $\langle \mathbf{D} \rangle_{\mathcal{V}} = \epsilon_0 \langle \mathbf{E} \rangle_{\mathcal{V}} + \langle \mathbf{P} \rangle_{\mathcal{V}}$. The polarization is expressed in terms of the bound charge density as follows $\rho_{\text{b}} = -\nabla \cdot \langle \mathbf{P} \rangle_{\mathcal{V}}$. To what end this charge separation is practical? Because for $\lambda \ggg a$, the constitutive relation for a local dielectric media can be written in its long-wavelength limit. Therefore, it takes an elementary form: $\langle \mathbf{P} \rangle_{\mathcal{V}} = \epsilon_0 \chi_{\text{T}} \langle \mathbf{E} \rangle_{\mathcal{V}}$. The local transverse susceptiblity reads $\chi_{\text{T}} = \varepsilon_{\text{w}} - 1$ where ε_{w} is the dielectric constant of the medium. Inserting in Eq. 261, we find that

$$\nabla \cdot \langle \mathbf{E} \rangle_{\mathcal{V}} = \frac{\rho_{\text{f}} + \rho_{\text{ext}}}{\epsilon_0 \varepsilon_{\text{w}}}, \tag{262}$$

which is Gauss's law in a dielectric material. This formulation of Maxwell's equations is called "in matter" or "macroscopic". Note that this formulation implies that the distinction between bound and free charges is possible and that $\lambda \ggg a$.

GENERALIZATION OF THE BOUND AND FREE CHARGE SEPARATION The polarization and displacement field can still be introduced without assuming the volume averaging. However, to which charge density can we attribute the polarization? In the literature regarding dielectrics and where free charges are absent, it is ubiquitous to identify the bound charge to the induced charge density in the system. The following set of equations is therefore obtained:

$$\rho_{\text{ind}} = -\nabla \cdot \mathbf{P} \; ; \quad \nabla \cdot \mathbf{D} = \rho_{\text{ext}} \; ; \quad \mathbf{D} = \epsilon_0 \mathbf{E} + \mathbf{P}. \tag{263}$$

We call it the standard approach of electrostatics. What happens if free charges are present? What is, in this case, the physical meaning of the polarization if it contains a contribution from free charges? It appears that the introduction of $\mathbf{D}$ and $\mathbf{P}$ is no longer relevant if we do not make the long-wavelength limit assumption for the dielectric.

CONSTITUTIVE EQUATION In this thesis, we will consider a dielectric/metal interface at the microscopic scale, and we do not resort to the bound/free charge distinction (nor the introduction of $\mathbf{D}$ and $\mathbf{P}$). However, in the literature, this distinction is implicitly made, assuming the ambiguity in the definition of the polarization $\mathbf{P}$ when free charges are present (see Eq.

263). It is most probably why the polarization is ignored and the constitutive equation links **E** and **D**, using

$$\mathbf{D}(1) = \epsilon_0 \iint \mathrm{d}1\mathrm{d}2\underline{\varepsilon}(1,2)\mathbf{E}(2) \tag{264}$$

where $\underline{\varepsilon}$ is the dielectric tensor and where we use $1 = (\mathbf{x}_1, t_1)$.

A.2 TRANSLATIONAL INVARIANCE

The Fourier transform is defined as follows:

$$f(\mathbf{k}) = \int \mathrm{d}\mathbf{r} f(\mathbf{r}) e^{-i\mathbf{k}\mathbf{x}} \quad f(\mathbf{r}) = \frac{1}{\mathcal{V}} \sum_{\mathbf{k}} f(\mathbf{k}) e^{+i\mathbf{k}\mathbf{x}}, \tag{265}$$

with $\frac{1}{\mathcal{V}} \sum_{\mathbf{k}} \xrightarrow[\mathcal{V}\to+\infty]{} \int \frac{\mathrm{d}\mathbf{k}}{(2\pi)^3}$. We express

$$n(\mathbf{x}) = \int \mathrm{d}\mathbf{x}' \chi(\mathbf{x}, \mathbf{x}') \phi(\mathbf{x}'), \tag{266}$$

when $\chi(\mathbf{x}, \mathbf{x}')$ only depends on $\mathbf{x} - \mathbf{x}'$. We insert the inverse Fourier transform of ϕ in Eq. 266. It gives, after Fourier transformation,

$$n(\mathbf{k}) = \frac{1}{\mathcal{V}} \sum_{\mathbf{k}'} \chi(\mathbf{k}, -\mathbf{k}') \phi(\mathbf{k}'). \tag{267}$$

In Fourier space, $\chi(\mathbf{k}, -\mathbf{k}')$ reads

$$\chi(\mathbf{k}, -\mathbf{k}') = \iint \mathrm{d}\mathbf{x}\mathrm{d}\mathbf{x}' \chi(\mathbf{x}, \mathbf{x}') e^{-i\mathbf{k}\mathbf{x}} e^{+i\mathbf{k}'\mathbf{x}'} \tag{268}$$

Using $\mathbf{x}' = \mathbf{x} - \mathbf{x}''$ and the invariance by translation, we compute the integral over $\mathbf{x}$. Therefore,

$$\chi(\mathbf{k}, -\mathbf{k}') = \mathcal{V}\delta_{\mathbf{k}-\mathbf{k}'} \chi(\mathbf{k}') \xrightarrow[\mathcal{V}\to\infty]{} (2\pi)^3 \delta(\mathbf{k} - \mathbf{k}') \chi(\mathbf{k}') \tag{269}$$

where $\chi(\mathbf{k}') = \int \mathrm{d}\mathbf{x}'' \chi(\mathbf{x}, \mathbf{x} - \mathbf{x}'') e^{-i\mathbf{k}'\mathbf{x}''}$. Eq. 269 shows that $\chi(\mathbf{x}, \mathbf{x}')$ has a diagonal representation in the Fourier basis. Inserting Eq. 269 in Eq. 267 gives $n(\mathbf{k}) = \chi(\mathbf{k})\phi(\mathbf{k})$. We will extensively use this property at an translationally invariant interface (see Fig. 35). We recap those results in a mathematical "toolbox" (Table 5).

Fig. 35	Planar (cylindrical coordinates)
$\mathbf{x}$	$(\mathbf{r}, z)$
$\mathrm{d}\mathbf{x}$	$\mathrm{d}\mathbf{r}\mathrm{d}z$
$\delta(\mathbf{x})$	$\delta(\mathbf{r})\delta(z)$
$\mathbf{k}$	$(\mathbf{q}, q_z)$
Fourier transfom	$f(\mathbf{q}) = \int \mathrm{d}\mathbf{r} f(\mathbf{r}) e^{-i\mathbf{q}\mathbf{r}}$
inverse Fourier transform	$f(\mathbf{r}) = \mathcal{A}^{-1} \sum_{\mathbf{q}} f(\mathbf{q}) e^{+i\mathbf{q}\mathbf{r}}$
limit sum-integral	$\mathcal{A}^{-1} \sum_{\mathbf{q}} \xrightarrow[\mathcal{A}\to\infty]{} \int \frac{\mathrm{d}^2\mathbf{q}}{(2\pi)^2}$ $\mathcal{A}\delta_{\mathbf{q}} \xrightarrow[\mathcal{A}\to\infty]{} (2\pi)^2 \delta(\mathbf{q})$
$f * g$	$\int_{-\infty}^{+\infty} \mathrm{d}z f(q, z, z') g(q, z')$
linear response	$n(\mathbf{q}, z) = \int \mathrm{d}z' \chi(\mathbf{q}, z, z') \phi(\mathbf{q}, z')$
plane invariance	$\chi(\mathbf{q}, -\mathbf{q}') = (2\pi)^2 \delta(\mathbf{q} - \mathbf{q}') \chi(\mathbf{q}')$

Table 5: Mathematical toolbox for the infinite, homogeneous, and isotropic in the plane interface.

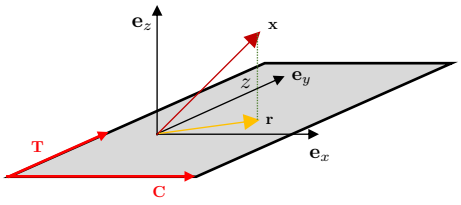

Figure 35: Planar geometry with cylindrical coordinates. The vectors **T** and **C** are relevant for chapter 7 only.

B

APPENDICES OF CHAPTER 2

B.1 DFT CALCULATIONS

We carried out an ab-initio molecular dynamics (AIMD) simulation of a graphene-water interface of area 12.83 Å $\times$ 12.35 Å using the CP2K software. The simulation is identical to the one described in [22] with the difference that the hydroxide ion is replaced by a water molecule. A VASP calculation was performed on a single configuration extracted from the dynamics, again following [22]. We used the Perdew, Burke and Ernzerhof functional [161] with the D3 dispersion correction scheme [162], which has been shown to provide a good description of the water/graphene interface [23]. Plane waves with kinetic energy larger than 600 eV were cut off and convergence was reached when the difference between total energy and eigenvalue energies was smaller than 10^{-6} eV. The resulting electronic density, once averaged in the direction parallel to the interface, is shown in Fig. 1b of the main text.

B.2 LINK WITH POLARIZATION FUNCTIONALS

Felderhof [163, 164] showed that we could write a functional of the polarization field in a dielectric medium whose minimization leads to the completion of Maxwell's equations. The Hamiltonian of the system, using the polarization field $\mathbf{P}$ instead of δn_w — with $\delta n_w = -\nabla \cdot \mathbf{P}$ —, reads

$$H_w^{pol} = \frac{1}{2\epsilon_0} \iint d\mathbf{x}_1 d\mathbf{x}_2 \mathbf{P}(\mathbf{x}_1) \underline{\bar{\chi}}_w^{-1}(\mathbf{x}_1, \mathbf{x}_2) \mathbf{P}(\mathbf{x}_2) - \frac{1}{\epsilon_0} \int d\mathbf{x}_1 \mathbf{D}(\mathbf{x}_1) \cdot \mathbf{P}(\mathbf{x}_1). \tag{270}$$

By differentiating with respect to $\mathbf{P}$, we find the constitutive equation in the static case:

$$\frac{\delta H_w^{pol}[\mathbf{P}]}{\delta \mathbf{P}} = 0 : \ \mathbf{P}(\mathbf{x}_1) = \int d\mathbf{x}_2 \underline{\bar{\chi}}_w(\mathbf{x}_1, \mathbf{x}_2) \mathbf{D}(\mathbf{x}_2). \tag{271}$$

We have used $\int d\mathbf{x}_1 \underline{\bar{\chi}}_w^{-1}(\mathbf{x}, \mathbf{x}_1) \cdot \underline{\bar{\chi}}_w(\mathbf{x}_1, \mathbf{x}') = \underline{I}\delta(\mathbf{x} - \mathbf{x}')$. Therefore, using Eq. 263 and Eq. 264, we obtain

$$\underline{\varepsilon}_w^{-1}(12) = 1 - \underline{\bar{\chi}}_w(12). \tag{272}$$

We split the displacement field into a longitudinal and transverse component $\mathbf{D} = \mathbf{D}^{\mathrm{L}} + \mathbf{D}^{\mathrm{T}}$ (Helmholtz decomposition). An external electrostatic potential only appears in the longitudinal term: $\mathbf{D}^{\mathrm{L}} = -\epsilon_0 \nabla \phi_{\mathrm{ext}} = \epsilon_0 \mathbf{E}_{\mathrm{ext}}$. An excitation stemming from a charge density only produces a longitudinal excitation. Inserting in Eq. 270, it reads

$$\begin{aligned}\int \mathrm{d}\mathbf{x}_1 \mathbf{E}_{\mathrm{ext}}(\mathbf{x}_1) \cdot \mathbf{P}(\mathbf{x}_1) &= -\int \mathrm{d}\mathbf{x}_1 \nabla_1 \phi_{\mathrm{ext}}(\mathbf{x}_1) \cdot \mathbf{P}(\mathbf{x}_1) \\ &= \int \mathrm{d}1 \nabla_1 \cdot \mathbf{P}(\mathbf{x}_1) \phi_{\mathrm{ext}}(\mathbf{x}_1) - \int \mathrm{d}\mathbf{x}_1 \nabla_1 \cdot [\phi_{\mathrm{ext}}(\mathbf{x}_1) \mathbf{P}(\mathbf{x}_1)] \\ &= -\int \mathrm{d}1 \delta n_{\mathrm{w}}(\mathbf{x}_1) \phi_{\mathrm{ext}}(\mathbf{x}_1) - \oiint \phi_{\mathrm{ext}}(\mathbf{x}_1) \mathbf{P}(\mathbf{x}_1) \cdot \mathrm{d}\mathbf{S}_1.\end{aligned} \tag{273}$$

We have used an identity of operators and the divergence theorem to introduce the surface charge density $\sigma(\mathbf{x}_1) = \mathbf{P}(\mathbf{x}_1) \cdot \mathrm{d}\mathbf{S}_1$. For a constant external potential (or no potential), we obtain that

$$\int \mathrm{d}\mathbf{x}_1 \delta n_{\mathrm{w}}(\mathbf{x}_1) = -\oiint_{\mathbf{S}_1} \sigma(\mathbf{x}_1). \tag{274}$$

Eq. 274 says that if you cut a dielectric medium, net charges will appear on the surface because some molecules will be cut in two. The overall neutrality condition requires to include charges on the surface.

Charges on the surface also react to the external electric field, hence the second term in Eq. 273. For an infinite slab, there is no surface polarization in the direction parallel to the interface because it is never cut. However, the symmetry breaking in the direction normal to the interface can lead to a net surface charge. The latter integrates to 0 on the infinite surface,

$$\oiint_{\mathbf{S}_1} \sigma(\mathbf{x}_1) = 0 \tag{275}$$

Therefore, if ϕ_{ext} is constant on the boundaries, then the second term in Eq. 273 integrates to 0 along the infinite surface. For instance, this is valid for a constant electric field D_z/ϵ_0 applied in the direction normal to the surface.

Without any assumption regarding ϕ_{ext}, Eq. 273 shows that the excitation will couple the surface charges to the charges in the volume. It points out the crucial role of the volume boundaries. In a macroscopic formalism, media are cut with sharp boundaries (e.g., one-side being the medium and the other vacuum). However, from a microscopic point of view, the medium does not terminate abruptly but smoothly on average. The surface boundary is no longer clearly defined. At a plane interface, we can therefore use a volume encompassing all molecules so that none of them can be cut in two. It adds up to closing the medium with an impenetrable plane. To remove

the surface charge due to the dielectric media's abrupt termination, we introduce a smooth molecular profile that vanishes on the volume boundaries. The response function of the dielectric medium will also smoothly decay near the boundary. This assumption will come in 2.3.1. Our framework therefore comes with the assumption $\sigma(\mathbf{x}) = 0$ on the volume boundaries (impenetrable plane).

To link the dielectric response tensor to the susceptiblity of Eq. 1, we insert Eq. 273 in Eq. 270 (without the surface charge term) and obtain

$$H_{\mathrm{w}}^{\mathrm{pol}/\sigma=0} = \frac{1}{2\epsilon_0} \iint \mathrm{d}\mathbf{x}_1 \mathrm{d}\mathbf{x}_2 \mathbf{P}(\mathbf{x}_1) \underline{\bar{\chi}}_{\mathrm{w}}^{-1}(\mathbf{x}_1, \mathbf{x}_2) \mathbf{P}(\mathbf{x}_2) + \int \mathrm{d}\mathbf{x}_1 \delta n_{\mathrm{w}}(\mathbf{x}_1) \phi_{\mathrm{ext}}(\mathbf{x}_1). \tag{276}$$

ϕ_{ext} generates the moments of δn_{w}. In the expression of the response function $\chi_{\mathrm{w}}(\mathbf{x}_1, \mathbf{x}_2) = \frac{\delta \langle \delta n_{\mathrm{w}}(\mathbf{x}_1) \rangle}{\delta \phi_{\mathrm{ext}}(\mathbf{x}_2)}$, only quadratic terms will participate. Using $\mathbf{P} = \mathbf{P}^{\mathrm{L}} + \mathbf{P}^{\mathrm{T}}$ and the Helmholtz decomposition for the longitudinal field:

$$\mathbf{P}^{\mathrm{L}}(\mathbf{x}_1) = \nabla_1 \int \frac{\delta n_{\mathrm{w}}(\mathbf{x}_2)}{4\pi |\mathbf{x}_1 - \mathbf{x}_2|} \mathrm{d}\mathbf{x}_2, \tag{277}$$

we can express χ_{w}^{-1} with the tensor $\underline{\chi}_{\mathrm{w}}^{-1}$:

$$\chi_{\mathrm{w}}^{-1}(\mathbf{x}_1, \mathbf{x}_2) = - \iint \frac{\mathrm{d}\mathbf{x}_{3\&4}}{\epsilon_0 (4\pi)^2} \nabla_3 \left(\frac{1}{|\mathbf{x}_3 - \mathbf{x}_1|} \right) \cdot \underline{\bar{\chi}}_{\mathrm{w}}^{-1}(\mathbf{x}_3, \mathbf{x}_4) \cdot \nabla_4 \left(\frac{1}{|\mathbf{x}_4 - \mathbf{x}_2|} \right) \tag{278}$$

In Fourier space, for the case of an homogeneous, isotropic, infinite dielectric, Eq. 278 reads

$$\chi_{\mathrm{w}}^{-1}(\mathbf{k}) = -\frac{1}{k^2 \epsilon_0} \hat{\mathbf{k}} \cdot \underline{\bar{\chi}}_{\mathrm{w}}^{-1}(\mathbf{k}) \cdot \hat{\mathbf{k}}.$$

The longitudinal response $\bar{\chi}_{\mathrm{w}}(\mathbf{k}) = \hat{\mathbf{k}} \cdot \underline{\bar{\chi}}_{\mathrm{w}}^{-1}(\mathbf{k}) \cdot \hat{\mathbf{k}}$ is therefore linked to $\chi_{\mathrm{w}}(\mathbf{k})$ as follows (see also Eq. 16):

$$\chi_{\mathrm{w}}(\mathbf{k}) = -k^2 \epsilon_0 \bar{\chi}_{\mathrm{w}}(\mathbf{k}).$$

B.3 A LIQUID IN A QUANTUM FRAMEWORK

The liquid Hamiltonian (see Eq. 62) written at an arbitrary time t_1, reads

$$H_{\mathrm{w}}(t_1) = -\frac{1}{2} \iint \mathrm{d}\mathbf{x}_1 \mathrm{d}\mathbf{x}_2 n(1) \chi^{-1}(\mathbf{x}_1, \mathbf{x}_2) n(\mathbf{x}_2, t_1) + \int \mathrm{d}\mathbf{x}_1 n(1) \phi(1), \tag{279}$$

where we simplified the notations ($\delta n_{\mathrm{w}} \to n$, $\chi_{\mathrm{w}} \to \chi$) for the sake of clarity. We included the external potential ($\phi_{\mathrm{ext}} \to \phi$). The dynamics of liquids are a combination of Gaussian processes, be them harmonic oscillators or diffusive processes. For simplicity, we impose the simplest dynamic by using

the Langevin equation. For instance, the same treatment can be refined by incorporating an acceleration term. The charge density is a non-conservative order parameter, so we use the simplest model for stochastic systems – type A in the nomenclature of Hohenberg and Halperin [165]. The Langevin equation reads

$$\frac{\partial n(1)}{\partial t_1} = F(1) + \xi(1) \tag{280}$$

where $\langle \xi(1)\xi(2)\rangle = \langle \xi\xi\rangle \delta(1-2)$ and where $\langle \xi\xi\rangle = 2k_BT$ would indicate equilibrium[1]. The "force" $F(1)$ is the functional derivative of H_w (Eq. 279):

$$F(1) = -\frac{\delta H_w}{\delta n(1)} = -\phi(1) + \int \mathrm{d}\mathbf{x}_2 \chi^{-1}(\mathbf{x}_1, \mathbf{x}_2) n(\mathbf{x}_2, t_1) \tag{281}$$

The dynamic is markovian, and the susceptibility χ^{-1} has no time argument. Once $\xi(1)$ is known, the Langevin equation is entirely deterministic, and the average of a quantity can be understood as an average over multiple realizations of the random force. Therefore, we introduce functional probability $\mathcal{P}[n, \xi]$ of a trajectory $n(1)$ to occur, given the random noise $\xi(1)$. Its expression requires the Dirac functional, and is obtained from Eq. 280:

$$\mathcal{P}[n, \xi] = \delta[\dot{n}(1) - F(1) - \xi(1)] = \int \mathcal{D}\tilde{n} e^{-i\int \mathrm{d}1 \tilde{n}(1)[\dot{n}(1) - F(1) - \xi(1)]} \tag{282}$$

We have used the functional Fourier transform for the last equality. It introduces an auxiliary field $\tilde{n}$. The noise averaging is a (weighted) integration over the different realizations of the random force. Using the notation $\int \mathrm{d}1 f(1)g(1) = fg$ in the exponent, we obtain[2]

$$\langle \mathcal{P}[n, \xi]\rangle_{\text{noise}} = \int \mathcal{D}\xi e^{-\frac{\xi^2}{2\langle \xi\xi\rangle}} \mathcal{P}[n, \xi] = \int \mathcal{D}\tilde{n} e^{-i\tilde{n}[\dot{n} - F] - \frac{1}{2}\langle \xi\xi\rangle \tilde{n}^2}. \tag{283}$$

The partition function, $\mathcal{Z}[\phi] = \int \mathcal{D}[n] \langle \mathcal{P}[n, \xi]\rangle_{\text{noise}}$, reads

$$\mathcal{Z}[\phi] = \int \mathcal{D}[n, \tilde{n}] e^{-i\tilde{n}[\dot{n} - F] - \frac{1}{2}\langle \xi\xi\rangle \tilde{n}^2}. \tag{284}$$

We extract from F the external potential ϕ that acts like a source to generate the moments of the auxiliary field $\tilde{n}$. Accordingly, we introduce the auxiliary external potential $\tilde{\phi}$ that generates the moments of n. We impose the normal-

[1] For clarity, we remove the prefactors that ensure homogeneity. We do believe we benefit from this non-orthodox choice.

[2] We do not report the Jacobian in the denominator and we may be missing some subtelties that are beyond our mathematical skills. However, we will be interested in response functions that are obtained by Gaussian integration of the partition function. We miss now the correct prefactor and will miss its inverse later.

ization $\mathcal{Z}[\phi, \tilde{\phi} = 0] = 1$. The response of the mean field due to an external perturbation reads:

$$\left.\frac{\delta\langle n(1)\rangle}{\delta\phi(2)}\right|_{\tilde{\phi}=0} = i\left.\frac{\delta^2\mathcal{Z}}{\delta\tilde{\phi}(1)\delta\phi(2)}\right|_{\tilde{\phi}=0} = -i\langle n(1)\tilde{n}(2)\rangle. \tag{285}$$

By rewriting the exponent in Eq. 284, we express it as Keldysh action [40, 42]. We use $fDg = \int \mathrm{d}1 \int \mathrm{d}2 f(1)D(12)g(2)$ in the exponent. We find that we can write

$$\mathcal{Z}[\phi, \tilde{\phi}] = \int \mathcal{D}[n, \tilde{n}]\, e^{+\frac{i}{2}\left(\tilde{n}\chi_{\mathrm{R}}^{-1}n + n\chi_{\mathrm{A}}^{-1}\tilde{n} + \tilde{n}\chi_{\mathrm{K}}^{-1}\tilde{n}\right) - i(\tilde{n}\phi + n\tilde{\phi})}, \tag{286}$$

with the following definitions of the inverse propagators:

$$\chi_{\mathrm{R}}^{-1}(12) = -\left[\delta(1-2)\partial_{t_2} - \delta(t_1 - t_2)\chi^{-1}(\mathbf{x}_1\mathbf{x}_2)\right]; \tag{287}$$

$$\chi_{\mathrm{A}}^{-1}(12) = \chi_{\mathrm{R}}^{-1}(21)\,; \quad \chi_{\mathrm{K}}^{-1}(12) = +i\langle\xi\xi\rangle\delta(1-2). \tag{288}$$

We have split in two Eq. 281 two build, with redundancy, χ_{A}^{-1} and χ_{R}^{-1}. The matrix form of the action appears once the vectors fields $\mathcal{N}(1) = [\tilde{n}(1), n(1)]$ and $\Phi(1) = [\phi(1), \tilde{\phi}(1)]$ are introduced. The susceptibility matrix reads

$$\mathcal{X}_{-\pi/4}^{-1}(12) = \begin{pmatrix} \chi_{\mathrm{K}}^{-1}(12) & \chi_{\mathrm{R}}^{-1}(12) \\ \chi_{\mathrm{A}}^{-1}(12) & 0 \end{pmatrix} \quad \mathcal{X}_{-\pi/4}(12) = \begin{pmatrix} 0 & \chi_{\mathrm{A}}(12) \\ \chi_{\mathrm{R}}(12) & \chi_{\mathrm{K}}(12) \end{pmatrix}, \tag{289}$$

the action reads $S[\mathcal{N}] = \frac{1}{2}\mathcal{N}\mathcal{X}_{-\pi/4}^{-1}\mathcal{N}$, and the partition function reduces to

$$\mathcal{Z}[\Phi] = \int \mathcal{D}[\mathcal{N}]\, e^{iS[\mathcal{N}] - i\mathcal{N}\Phi}. \tag{290}$$

By gaussian integration, we obtain

$$i\left.\frac{\delta^2\mathcal{Z}}{\delta\Phi(1)\delta\Phi(2)}\right|_{\Phi=0} = -i\int \mathcal{D}[\mathcal{N}]\,\mathcal{N}(1)\mathcal{N}(2)e^{+\frac{i}{2}\mathcal{N}\mathcal{X}_{-\pi/4}^{-1}\mathcal{N}} \tag{291}$$

$$= -i\begin{pmatrix} \langle\tilde{n}(1)\tilde{n}(2)\rangle_0 & \langle\tilde{n}(1)n(2)\rangle_0 \\ \langle n(1)\tilde{n}(2)\rangle_0 & \langle n(1)n(2)\rangle_0 \end{pmatrix} \overset{\text{Gauss.}}{=} \mathcal{X}_{-\pi/4} \tag{292}$$

Using Eq. 285, we find that the *retarted* response fuction, χ_{R}, is the response function to an external potential: $\chi_{\mathrm{R}} = \chi$.

Let us fully characterize $\mathcal{X}_{-\pi/4}$ for the most straightforward dissipative dynamics, imposed by the Langevin equation. We use

$$\int d2\chi_{\mathrm{R/A/K}}^{-1}(12)\chi_{\mathrm{R/A/K}}(21') = \delta(11'). \tag{293}$$

For the homogeneous, isotropic, infinite case, we use Eq. 287 and Eq. 293 in Fourier space. It reads $\chi^{-1}_{\mathrm{R/A}}(k,\omega) = -\left[\pm i\omega - \chi^{-1}(k)\right]$, or

$$\frac{\chi_{\mathrm{R/A}}(k,\omega)}{\chi(k)} = \frac{1}{1 \mp i\omega\tau(k)} \qquad \frac{\chi_{\mathrm{K}}(k,\omega)}{\chi(k)} = -i\frac{\langle\xi\xi\rangle}{2}\frac{2\tau(k)}{1+\omega^2\tau^2(k)} \tag{294}$$

with $\tau(k) = \chi(k)$ (recall that the prefactors are ignored), and we recover $\chi_{\mathrm{R/A}}(k,\omega=0) = \chi(k)$. For the off-diagonal Keldysh term, we used $\chi_{\mathrm{K}} = -\chi_{\mathrm{R}}\chi_{\mathrm{K}}^{-1}\chi_{\mathrm{A}}$. Eq. 294 are familiar equations for classical relaxation dynamics[3]. Finally, we check that $\langle\xi\xi\rangle = 2k_BT$ does ensure the classical FDT. First, using Eq. 291 we find $\chi_{\mathrm{K}}(12) = -iS(12)$ where the *dynamical structure factor* or correlation function, reads $S(12) = \langle\delta n(1)\delta n(2)\rangle$. Second, $i\mathrm{Im}\chi_{\mathrm{R}}(k,\omega) = \frac{\omega}{\langle\xi\xi\rangle}\chi_{\mathrm{K}}(k,\omega)$. Using both equations and $\langle\xi\xi\rangle = 2k_BT$, gives

$$\mathrm{Im}\chi_{\mathrm{R}}(k,\omega) = -\frac{\omega}{2k_BT}S(k,\omega) \qquad S(k,t=0) = -\beta\chi(k). \tag{296}$$

Eq. 296 is the classical FDT (right) [35] and its static consequence (right) due to Kramers-Kronig (KK) relations (see appendix B.4 or Eq. 299).

B.4 KRAMERS-KRONIG RELATIONS

Response functions respect specific properties such as causality: $\chi(t_1 - t_2) = 0$ for $t_1 < t_2$. It implies that the complex function $\chi(z)$ is analytic in the upper-half plane (Titchmarsh's theorem). Moreover, when the system is excited at very high frequencies, it no longer responds to the perturbation: $\chi(\omega \to \infty) \to 0$. It goes to zero faster than $|\omega|^{-1}$ because the dissipated power $\hbar\omega\mathrm{Im}\chi(\omega)$ should also converge to zero. On a semi-circle contour $\mathcal{C}$ that avoids the real pole at ω of the function $z \to \frac{\chi(z)}{z-\omega}$, the residue theorem gives

$$\oint_{\mathcal{C}} \frac{\chi(z)}{z-\omega}\mathrm{d}z = 2\pi i\sum \mathrm{Res}_{\mathcal{C}}\chi = 0 = \mathcal{P}\int_{-\infty}^{+\infty}\mathrm{d}\omega'\frac{\chi(\omega')}{\omega'-\omega} - i\pi\chi(\omega). \tag{297}$$

Here, $\mathcal{P}$ is the Cauchy principal value. Equating the real and imaginary part of Eq. 297, we find:

$$\mathrm{Re}\chi(\omega) = \mathcal{P}\int_{-\infty}^{+\infty}\frac{\mathrm{d}\omega'}{\pi}\frac{\mathrm{Im}\chi(\omega')}{\omega'-\omega}. \tag{298}$$

[3] In the time domain, we find

$$\frac{\chi_{\mathrm{R/A}}(k,t)}{\chi(k)} = \frac{\theta(\pm t)}{\tau(k)}e^{\mp t/\tau(k)} \qquad \frac{\chi_{\mathrm{K}}(k,t)}{\chi(k)} = -i\frac{\langle\xi\xi\rangle}{2}e^{-|t|/\tau(k)} \tag{295}$$

The response function χ can be obtained with the sole knowledge of the structure factor, at equilibrium. Note that $\mathrm{Im}\chi(\omega)$ is an odd function, while $\mathrm{Re}\chi(\omega)$ is even[4].

[4] It may be clearer written as $\mathrm{Im}\chi(\omega) = -\frac{i}{2}\int_{-\infty}^{+\infty} \mathrm{d}t e^{-i\omega t}\left[\chi(t) - \chi(-t)\right]$).

C

APPENDIX OF CHAPTER 3

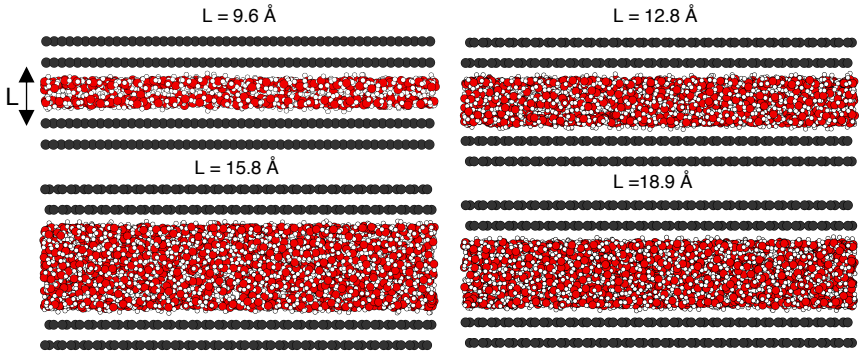

Figure 36: Snapshots of the slab simulations with varying L. The surface area is 64.158×61.745 Å^2.

In conducting slab simulations, we merely want to check if the surface response function changes with confinement effects. The slab simulations contained $N = 800, 1200, 1600$, or 2000 water molecules depending on the slab thickness – resp. $L = 9.6, 12.8, 15.8$ and 18.9 Å . The two solid surfaces each consisted of two staggered graphene layers, with a surface area 64.158×61.745 Å^2. The positions of the carbon atoms were frozen relative to each other. The distance between the surfaces is first equilibrated during 400 ps, then it is fixed, and the subsequent 6 ns are used for analysis. Werder parameters are used for the water-carbon interaction. The results for the static surface response function are shown in Fig.37, using $d_{\text{Werder}} = 1.3$Å as in the bulk case. We find no variation of $g_{\text{w}}(q)$ for $L > 1$nm. The same conclusions are obtained regarding the dynamics (not shown). We also do not find any differences in the SRF using two or three graphene layers in the MM simulations.

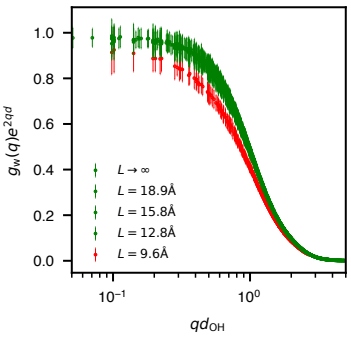

Figure 37: Static surface response function of water confined in slabs of length L. We use the Werder force field and d_{Werder}.

D

APPENDICES OF CHAPTER 4

D.1 BULK NON-INTERACTING SUSCEPTIBILITY $\chi_w^{(0)}(k)$

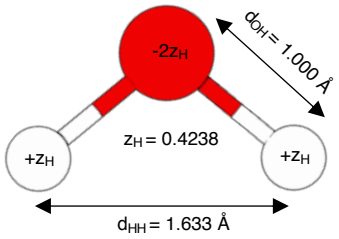

Figure 38: SPC/E water molecule [48].

In this paragraph we detail our model for bulk water. First, we precise that we will consider static external perturbations only. The time integration in Eq.1 gives that the mean induced charge density does not depend on time (as expected) and that the relevant response quantity is the zero-frequency component of the response function - e.g. $\chi_w(\mathbf{k}) = \chi_w(\mathbf{k}, \omega = 0)$ in the homogeneous and isotropic system. We briefly recall how to obtain it using Kramers-Kronig relations and the FDT [35] :

$$\chi_w(\mathbf{k}) = \mathrm{Re}\chi_w(\mathbf{k}, \omega = 0) \tag{299}$$

$$\overset{\text{Eq. 298}}{=} \int_{-\infty}^{+\infty} \frac{d\omega'}{\pi} \frac{\mathrm{Im}\chi_w(\mathbf{k}, \omega')}{\omega'} \tag{300}$$

$$\overset{\text{Eq. 296}}{=} \int_{-\infty}^{+\infty} \frac{d\omega'}{\pi} \frac{-\frac{\omega'}{2k_B T} S_w(\mathbf{k}, \omega')}{\omega'} \tag{301}$$

$$= -\beta S_w(\mathbf{k}, t = 0) = -\beta S_w(\mathbf{k}) \tag{302}$$

$$= -\frac{\beta}{\mathcal{V}} \langle n_w(\mathbf{k}) n_w(-\mathbf{k}) \rangle \tag{303}$$

The charge density of the water molecules $n_w(\mathbf{x})$ — that must be replaced by $\delta n_w(\mathbf{x}) = n_w(\mathbf{x}) - \langle n_w(\mathbf{x}) \rangle$ if the mean is not zero — is composed of point-like charges. In a field formulation, we can write the charge density as a convolution between the fixed charge density $\sigma(\mathbf{x}, \Omega)$ of one rigid water molecule oriented with an angle Ω, and the molecular number density $N_w(\mathbf{x}, \Omega)$ – i.e. $\int_{\mathcal{V}} \int_{\Omega} N_w = N = n_0 \mathcal{V}$ so that n_0 is the molecular density

$$N_w(\mathbf{x}, \Omega) = \sum_i \delta(\mathbf{x} - \mathbf{x}_i) \delta(\Omega - \Omega_i) \; ; \quad \sigma(\mathbf{x}, \Omega) = \sum_\alpha c_\alpha \delta(\mathbf{x} - \mathbf{s}_\alpha(\Omega)), \tag{304}$$

They both depend on the molecule's orientation Ω that we do not need to explicit here, but details can be found in e.g. [166]. The index i runs on different molecules and α on different atoms in the molecule with the partial charges c_α. $\mathbf{s}_\alpha(\Omega)$ is the position of the atom α positions given the orientation Ω of the molecule. Those quantities for the SPC/E model [48] can be found in Fig. 38. It gives

$$n_{\mathrm{w}}(\mathbf{x}) = \int \mathrm{d}\Omega \int \mathrm{d}\mathbf{x}' \sigma(\mathbf{x}-\mathbf{x}', \Omega) N_{\mathrm{w}}(\mathbf{x}', \Omega) \tag{305}$$

With those definitions, the structure factor reads

$$S_{\mathrm{w}}(\mathbf{k}) = \frac{1}{\mathcal{V}} \iint \mathrm{d}\Omega_1 \mathrm{d}\Omega_2 \sigma(\mathbf{k}, \Omega_1)\sigma(-\mathbf{k}, \Omega_2) \left\langle N_{\mathrm{w}}(\mathbf{k}, \Omega_1) N_{\mathrm{w}}(-\mathbf{k}, \Omega_2)\right\rangle \tag{306}$$

The molecular number density field can be split into two parts that highlight intramolecular and intermolecular correlations

$$\langle N_{\mathrm{w}}(\mathbf{k}, \Omega_1) N_{\mathrm{w}}(-\mathbf{k}, \Omega_2)\rangle = \langle \sum_i \delta(\Omega_1 - \Omega_i)\delta(\Omega_2 - \Omega_i)\rangle + \sum_{i, j\neq i} \ldots \tag{307}$$

Therefore, we can write $S_{\mathrm{w}}(\mathbf{k}) = S_{\mathrm{w}}^{(0)}(\mathbf{k}) + S_{\mathrm{w}}^{(\mathrm{inter})}(\mathbf{k})$ with

$$S_{\mathrm{w}}^{(0)}(\mathbf{k}) = \frac{1}{\mathcal{V}} \int \mathrm{d}\Omega_1 \sigma(\mathbf{k}, \Omega_1)\sigma(-\mathbf{k}, \Omega_1)\langle N_{\mathrm{w}}(\Omega_1)\rangle \tag{308}$$

and the orientational density $N_{\mathrm{w}}(\Omega_1) = \sum_i \delta(\Omega - \Omega_i)$. In the bulk $\langle N_{\mathrm{w}}(\Omega_1)\rangle = 1/8\pi^2$ is homogeneous and

$$S_{\mathrm{w}}^{(0)}(\mathbf{k}) = n_0 \sum_{\alpha,\beta} c_\alpha c_\beta \int \frac{\mathrm{d}\Omega_1}{8\pi^2} e^{-i\mathbf{k}(\mathbf{s}_\alpha(\Omega_1) - \mathbf{s}_\beta(\Omega_1))} = n_0 \sum_{\alpha,\beta} c_\alpha c_\beta j_0(k d_{\alpha\beta}) \tag{309}$$

where j_0 is the zeroth order spherical Bessel function, the interatomic distances read $d_{\alpha\beta} = |\mathbf{s}_\alpha - \mathbf{s}_\beta|$ and n_0 is the molecular bulk density. For SPC/E water, we have

$$S_{\mathrm{w}}^{(0)}(k) = n_0 z_{\mathrm{H}}^2 \left[6 - 8\mathrm{sinc}(k d_{\mathrm{OH}}) + 2\mathrm{sinc}(k d_{\mathrm{HH}})\right] \tag{310}$$

where z_{H} is the partial charge on the hydrogen atom, d_{OH} and d_{HH} are the bond distances of the SPC/E molecule Berendsen *et al.* [48] and $n_0 = 0.03298$ Å^{-3}. This gives the response function of the independent - or non-interacting - molecules that reads

$$\chi_{\mathrm{w}}^{(\mathrm{o})}(k) = -\beta S_{\mathrm{w}}^{(0)}(k) \tag{311}$$

D.2 THE MEAN-FIELD WATER POTENTIAL $v_{\mathrm{w}}^{\mathrm{EFF}}$

To find an expression for $v_{\mathrm{w}}^{\mathrm{eff}}$, we rearrange Eq. 89 to make an effective dielectric function $\varepsilon_{\mathrm{w}}^{\mathrm{eff}}(k)$ appear:

$$\frac{v_{\mathrm{w}}^{\mathrm{eff}}(k)}{v(k)} = \frac{1}{\varepsilon_{\mathrm{w}}^{\mathrm{eff}}(k)} = \frac{1}{\bar{\chi}_{\mathrm{w}}(k)} - \frac{1}{\bar{\chi}_{\mathrm{w}}^{(0)}(k)}. \tag{312}$$

$\varepsilon_{\mathrm{w}}^{\mathrm{eff}}(k)$ is known in the long-wavelenght limit because

$$S_{\mathrm{w}}^{(0)}(k) \xrightarrow[k\to 0]{} n_0 \frac{4}{3} k^2 z_{\mathrm{H}}^2 d_{\mathrm{OH}}^2 \cos^2\left(\frac{\theta_{\mathrm{HOH}}}{2}\right) = n_0 \frac{k^2 \mu^2}{3} = k_B T n_0 \alpha k^2. \tag{313}$$

We notice the Debye-Langevin polarizability $\alpha = \frac{\mu^2}{3k_B T}$ with μ the dipole moment of the SPC/E water molecule (see SPC/E water molecule in Fig. 38 for z_{H}, d_{OH}, θ_{OHO}). Using the dimensionless susceptibilities $\bar{\chi}_{\mathrm{w}}(k) = -\chi_{\mathrm{w}}(k)/\epsilon_0 k^2$, and he limit $\bar{\chi}_{\mathrm{w}}(k) \xrightarrow[k\to 0]{} 1 - \frac{1}{\varepsilon_{\mathrm{w}}}$, we obtain

$$\frac{1}{\varepsilon_{\mathrm{w}}^{\mathrm{eff}}(k=0)} = \frac{1}{\varepsilon_{\mathrm{w}}^{\mathrm{eff}}} = \frac{\varepsilon_{\mathrm{w}}}{\varepsilon_{\mathrm{w}} - 1} - \frac{\epsilon_0}{n_0 \alpha}. \tag{314}$$

As expected, the intermolecular potential is zero — or $\varepsilon_{\mathrm{w}}^{\mathrm{eff}} \to \infty$ – if water molecules behave independently i.e. $\bar{\chi}_{\mathrm{w}} = \bar{\chi}_{\mathrm{w}}^{(0)}$. For water, $\varepsilon_{\mathrm{w}}^{\mathrm{eff}} \simeq 1.04$ so that the description of interacting molecular form factors with a bare Coulomb potential is accurate in the long-wavelength limit. The effective charge-charge potential in real space for water is given by the Fourier transform of Eq. 90. It read

$$v_{\mathrm{w}}^{\mathrm{eff}}(x) = \frac{1 - e^{-\kappa x} - x\gamma \frac{\kappa}{\pi} e^{-\kappa^2 x^2/2}}{4\pi\epsilon_0 \varepsilon_{\mathrm{w}}^{\mathrm{eff}} x}. \tag{315}$$

Using Eq. 315, we find

$$v_{\mathrm{w}}^{\mathrm{eff}}(x) \simeq \frac{v(x)}{\varepsilon_{\mathrm{w}}^{\mathrm{eff}}} \qquad \kappa x \gg 1. \tag{316}$$

The partial Fourier transformation that is used to fill the $V_{\mathrm{w}}^{\mathrm{eff}}$ matrix reads

$$v_{\mathrm{w}}^{\mathrm{eff}}(q, |z - z'|) = \frac{1}{4\pi\epsilon_0 \varepsilon_{\mathrm{w}}^{\mathrm{eff}}} \ldots \tag{317}$$

$$\ldots \left(\frac{2\pi}{q} e^{-q|z-z'|} - \frac{2\pi}{Q} e^{-Q|z-z'|} - \gamma \frac{2\pi}{\kappa} e^{-q^2/2\kappa^2} \frac{e^{-\kappa^2 (z-z')^2}}{\pi} \right) \tag{318}$$

where $Q^2 = q^2 + \kappa^2$.

D.3 NON-INTERACTING SUSCEPTIBILITY $\chi_{\mathrm{w}}^{(\mathrm{o})}(q,z,z')$

Looking for the response function $\chi_{\mathrm{w}}(q,z,z')$ at interfaces, we can proceed from Eq. 299 to Eq. 303 to find a relation between the susceptibility and the corresponing structure factor. Equally, we dwell on the non-interacting part and find

$$\chi_{\mathrm{w}}^{(0)}(q,z,z') = -\beta S_{\mathrm{w}}^{(0)}(q,z,z') \tag{319}$$

We proceed like in the bulk and after some straighforward steps, we obtain

$$S_{\mathrm{w}}^{(0)}(\mathbf{q},z,z') = \frac{1}{\mathcal{A}} \iint \mathrm{d}\Omega_1 \mathrm{d}z_1 \sigma(\mathbf{q},z-z_1,\Omega_1)\sigma(-\mathbf{q},z'-z_1,\Omega_1)\langle N_{\mathrm{w}}(z_1,\Omega_1)\rangle, \tag{320}$$

with

$$\sigma(\mathbf{q},z,\Omega) = \sum_{\alpha} c_\alpha e^{-i\mathbf{q}\mathbf{s}_\alpha(\Omega)}\delta(z-z_\alpha(\Omega))\,;\;\; N_{\mathrm{w}}(z_1,\Omega) = \sum_i \delta(\Omega_1-\Omega_i)\delta(z_1-z_i). \tag{321}$$

Looking at the structure of the product $\sigma(\mathbf{q},z,\Omega_1)\sigma(-\mathbf{q},z',\Omega_1)$, we can express it with the sum and differences of z and z' as follows

$$\begin{aligned}
\sigma(\mathbf{q},z,\Omega_1)\sigma(-\mathbf{q},z',\Omega_1) &= \sum_{\alpha\beta} c_\alpha c_\beta e^{-i\mathbf{q}(\mathbf{s}_\alpha(\Omega)-\mathbf{s}_\beta(\Omega))}\delta\left(z-z_\alpha(\Omega)\right)\delta\left(z'-z_\beta(\Omega)\right) \\
&= \sum_{\alpha\beta} c_\alpha c_\beta e^{-i\mathbf{q}(\mathbf{s}_\alpha(\Omega)-\mathbf{s}_\beta(\Omega))} && (322)\\
&\times \delta\left(z-z'-\left[z_\alpha(\Omega)-z_\beta(\Omega)\right]\right) && (323)\\
&\times \delta(z+z'-\left[z_\alpha(\Omega)+z_\beta(\Omega)\right]) && (324)
\end{aligned}$$

This makes the convolution of Eq. 320 with $N_{\mathrm{w}}(z_1,\Omega_1)$ possible. It reads

$$\begin{aligned}
S_{\mathrm{w}}^{(0)}(\mathbf{q},z,z') = \frac{1}{\mathcal{A}}\int \mathrm{d}\Omega \sum_{\alpha\beta} c_\alpha c_\beta e^{-i\mathbf{q}(\mathbf{s}_\alpha(\Omega)-\mathbf{s}_\beta(\Omega))}\delta\left(z-z'-\left[z_\alpha(\Omega)-z_\beta(\Omega)\right]\right) && (325)\\
\times N_{\mathrm{w}}\left(\frac{z+z'-\left[z_\alpha(\Omega)+z_\beta(\Omega)\right]}{2},\Omega\right) && (326)
\end{aligned}$$

For an homogeneous density, we would be able to get the term involving N_{w} out of the summation. Assuming equiprobable orientation of molecules in

the entire slab, we would recover the inverse fourier transform of the bulk structure factor, i.e.

$$S_{\mathrm{w}}^{(0)}(\mathbf{q}, |z-z'|) = \int \frac{\mathrm{d}q_z}{2\pi} e^{iq_z|z-z'|} S_{\mathrm{w}}^{(0)}(\mathbf{k}) \tag{327}$$

$$= n_0 z_H^2 \left[6\delta(z-z') - 8I(q, d_{\mathrm{OH}}, |z-z'|) + 2I(q, d_{\mathrm{HH}}, |z-z'|)\right] \tag{328}$$

with $I(q,d,z) = J_0(q\sqrt{d^2-z^2})\Theta(d-|z|)/2d$ and J_0 is the zeroth order Bessel function. We work in this direction and try to express $S_{\mathrm{w}}^{(0)}(\mathbf{q}, z, z')$ with $S_{\mathrm{w}}^{(0)}(\mathbf{q}, |z-z'|)$. Using the condition enforced by the first Dirac delta function in Eq. 325 — $z = z' + \left[z_\alpha(\Omega) - z_\beta(\Omega)\right]$ — we can replace the term involving N_{w} by either $N_{\mathrm{w}}\left(z' - z_\beta(\Omega), \Omega\right)$, or $N_{\mathrm{w}}\left(z - z_\alpha(\Omega), \Omega\right)$, but also by $\sqrt{N_{\mathrm{w}}\left(z - z_\alpha(\Omega), \Omega\right) N_{\mathrm{w}}\left(z' - z_\beta(\Omega), \Omega\right)}$, without any approximation. Making now the approximation $N_{\mathrm{w}}\left(z - z_\alpha, \Omega\right) \simeq N_{\mathrm{w}}\left(z, \Omega\right)$ and assuming equiprobable orientation of molecules in the entire slab we can write

$$S_{\mathrm{w}}^{(0)}(q, z, z') \simeq \frac{\sqrt{n_0(z) n_0(z')}}{n_0} S_{\mathrm{w}}^{(0)}(q, |z-z'|), \tag{329}$$

which is the main result of this paragraph. This approximation is valid if the molecular profile typically varies on a scale larger than the size of a water molecule. Note however that the Taylor expansion of N_{w} near the interface give rises to terms linear in $z_\alpha(\Omega)$ that can most probably gives a zero contribution when the angular integration is carried out (under the approximation of equiprobable orientation). Combining Eq. 319 and Eq. 329 gives Eq. 91.

D.4 COMPARISON WITH MD RESULTS

The smoothed step function molecular density profile $n_0(z)$ is chosen because:

- the use of $v_{\mathrm{w}}^{\mathrm{eff}}$ that implies that molecules interact as is they were in the bulk, that is with an homogeneous molecular density n_0.
- it gives the same $\bar{\chi}_{\mathrm{w}}(z)$ we obtain by using the real hydrogen density of the MD simulation. We use the hydrogens because they can go at altitudes at which oxygens cannot.

The MM results of [65] for $\bar{\chi}_{\mathrm{w}}(z)$ are shown in Fig. 39. The use of $\sigma_0 = 0.3$Å gives the correct amplitude for the first peak. The oscillation period, amplitude and decay length are also in good agreement. By tuning the molecular density profile, we can fit exactly the MM results, but our goal is

not to reproduce the local dielectric of an MM simulation that uses effective LJ potentials or effective interactions between the surface and the water molecules — graphene is absent when we build χ_w.

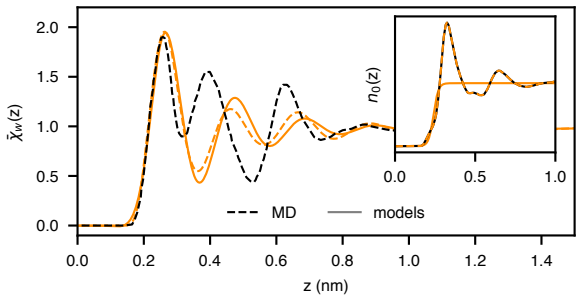

Figure 39: The results in Fig. 10, compared with the MM simulation results in [65].

E

APPENDICES OF CHAPTER 5

E.1 COULOMB VERTEX

Inserting the Bloch expansion Eq. 104 in $\hat{n}_e = \Psi^\dagger\Psi$ and Fourier-transforming in the plane gives

$$\langle\psi_{\mu\mathbf{p}}(z)|e^{-i\mathbf{qr}}|\psi_{\nu\mathbf{k}}(z)\rangle = \frac{1}{N_p}\sum_{\kappa p}\sum_{\kappa' p'} e^{i\mathbf{p}\mathbf{R}_{p'}} e^{-i\mathbf{k}\mathbf{R}_p} (d^{\kappa'}_{\mu\mathbf{p}})^* d^{\kappa}_{\nu\mathbf{k}} \dots \tag{330}$$

$$\dots \int \mathrm{d}\mathbf{r} e^{-i\mathbf{qr}} \phi^*(\mathbf{r} - \boldsymbol{\tau}_{\kappa' p'}, z - z_{\kappa'}) \phi(\mathbf{r} - \boldsymbol{\tau}_{\kappa p}, z - z_\kappa). \tag{331}$$

Making the change of variable $\mathbf{r}' = \mathbf{r} - \mathbf{R}_{p'}$ in the integral and $\mathbf{R}_{p'} = \mathbf{R}_p + \mathbf{R}_{p''}$ in the summation leads to

$$\langle\psi_{\mu\mathbf{p}}(z)|e^{-i\mathbf{qr}}|\psi_{\nu\mathbf{k}}(z)\rangle = \sum_{\kappa p}\sum_{\kappa' p''} e^{i(\mathbf{p}-\mathbf{q})\mathbf{R}_{p''}} e^{i(\mathbf{p}-\mathbf{k}-\mathbf{q}))\mathbf{R}_p} d^{\kappa}_{\nu\mathbf{k}} (d^{\kappa'}_{\mu\mathbf{p}})^* \dots \tag{332}$$

$$\dots \int \mathrm{d}\mathbf{r} e^{-i\mathbf{qr}} \phi^*(\mathbf{r} - \boldsymbol{\tau}_\kappa, z - z_\kappa) \phi(\mathbf{r} - \boldsymbol{\tau}_{\kappa' p''}, z - z_{\kappa'}) \tag{333}$$

The sum over the lattice sites $\mathbf{R}_p$ gives the conservation of momentum $\mathbf{p} = \mathbf{k} + \mathbf{q}$ so

$$U(s,z) = \int \mathrm{d}\mathbf{r} e^{-i\mathbf{qr}} \phi^*(\mathbf{r} - \boldsymbol{\tau}_\kappa, z - z_\kappa) \phi(\mathbf{r} - \boldsymbol{\tau}_{\kappa'} - \mathbf{R}_p, z - z_{\kappa'}), \tag{334}$$

with $s = \{\kappa, \kappa', p\}$. Therefore, we get

$$\lambda^{\mu\nu}_{\mathbf{k}+\mathbf{q}\mathbf{k}}(z) = \sum_s e^{i\mathbf{k}\mathbf{R}_p} (d^{\kappa'}_{\mu\mathbf{k}+\mathbf{q}})^* d^{\kappa}_{\nu\mathbf{k}} U(s,z). \tag{335}$$

Eq. 107 with Eq. 335, assuming $U(s,z) = 0$ if $p \neq 0$ and $\kappa \neq \kappa'$.

E.2 COMPUTATION $\chi_{\mathrm{E}}^{(0)}(q,z,z',\omega)$

We note $\mathrm{T}_\tau\left[\!\left[.\right]\!\right]$ the imaginary time-ordering operator with $\tau \in [-\beta,\beta]$ and $\beta = 1/k_B T$. The response function, as given by linear response theory in the imaginary time formulation [31], reads

$$\chi_{\mathrm{e}}(\mathbf{q},z,z',\tau) = -\frac{1}{\mathcal{A}}\left\langle \mathrm{T}_\tau\left[\!\left[\hat{n}_{\mathrm{e}}(\mathbf{q},z,\tau)\hat{n}_{\mathrm{e}}(-\mathbf{q},z')\right]\!\right]\right\rangle. \tag{336}$$

$\chi_{\mathrm{e}}(\mathbf{q},z,z',\tau)$ is related to $\chi_{\mathrm{e}}(\mathbf{q},z,z',t)$ in the frequency domain, by analytic continuation on the real axis, that is $\chi_{\mathrm{e}}(\mathbf{q},z,z',\omega) = \chi_{\mathrm{e}}(\mathbf{q},z,z',i\Omega_m \to \omega + i\eta)$, where $\Omega_m = 2\pi m k_B T$ is a Matsubara bosonic frequency. We do not distinguish them in the notations, apart from the type of argument (real or complex). Inserting Eq.105 in Eq. 336, gives rise correlators' expectation values $\langle C\rangle$. They have the following form:

$$\langle C\rangle = \left\langle \mathrm{T}_\tau\left[\!\left[\hat{c}^\dagger_{\mu\mathbf{k}+\mathbf{q}}(\tau)\hat{c}_{\nu\mathbf{k}}(\tau)\hat{c}^\dagger_{\delta\mathbf{p}-\mathbf{q}}\hat{c}_{\gamma\mathbf{p}}\right]\!\right]\right\rangle \tag{337}$$

Inserting $\langle . \rangle = \mathrm{Tr}(e^{-\beta\hat{H}}.)$, Eq. 337 gives [31]:

$$\langle C\rangle = -\frac{\left\langle \mathrm{T}_\tau\left[\!\left[\hat{S}(\beta,0)\hat{c}^\dagger_{\mu\mathbf{k}+\mathbf{q}}(\tau)\hat{c}_{\nu\mathbf{k}}(\tau)\hat{c}^\dagger_{\delta\mathbf{p}-\mathbf{q}}\hat{c}_{\gamma\mathbf{p}}\right]\!\right]\right\rangle_0}{\left\langle \hat{S}(\beta,0)\right\rangle_0} \tag{338}$$

Greek letters represent band index and $\hat{S}(\beta,0) = \mathrm{T}_\tau\left[\!\left[\exp(-\int_0^\beta \mathrm{d}\tau \hat{H}_{\mathrm{int}}(\tau))\right]\!\right]$ is the propagator in the imaginary time interaction representation – e.g. $\hat{H}_{\mathrm{int}}(\tau) = e^{\tau\hat{H}_0}H_{\mathrm{int}}e^{-\tau\hat{H}_0}$ where H_{int} is given by Eq. 75. Eq 338 shows that the complex expectation value $\langle . \rangle = \mathrm{Tr}(e^{-\beta\hat{H}})$ can be expressed pertubatively with respect to the quadratic Hamiltonian: $\langle . \rangle_0 = \mathrm{Tr}(e^{-\beta\hat{H}^{(0)}})$. It follows from Wick's theorem that we can express Eq. 338 in terms of all possible products of single-particle Matsubara Green's functions.

The non-interacting response function $\chi_{\mathrm{e}}^{(0)}$ is obtained by ignoring the interaction of the electrons between themselves or with their environment. Therefore, computing Eq. 336 adds up to developping the propagator $\hat{S}$ to zeroth order, that is $\hat{S}(\beta,0) = 1$. This gives

$$\begin{aligned}\langle C\rangle_0 &= -\left\langle \mathrm{T}_\tau\left[\!\left[\hat{c}_{\delta\mathbf{p}-\mathbf{q}}\hat{c}^\dagger_{\nu\mathbf{k}}(\tau)\right]\!\right]\right\rangle_0\left\langle \mathrm{T}_\tau\left[\!\left[\hat{c}_{\mu\mathbf{k}+\mathbf{q}}(\tau)\hat{c}^\dagger_{\gamma\mathbf{p}}\right]\!\right]\right\rangle_0 \\ &\quad + \left\langle \mathrm{T}_\tau\left[\!\left[\hat{c}_{\mu\mathbf{k}+\mathbf{q}}(\tau)\hat{c}^\dagger_{\nu\mathbf{k}}(\tau)\right]\!\right]\right\rangle_0\left\langle \mathrm{T}_\tau\left[\!\left[\hat{c}_{\delta\mathbf{p}-\mathbf{q}}\hat{c}^\dagger_{\gamma\mathbf{p}}\right]\!\right]\right\rangle_0 \qquad (339)\\ &= -\mathcal{G}^{(0)}_\nu(\mathbf{k},\tau)\mathcal{G}^{(0)}_\mu(\mathbf{k}+\mathbf{q},-\tau)\delta_{\gamma\mu}\delta_{\nu\delta}\delta_{\mathbf{p},\mathbf{k}+\mathbf{q}} \qquad (340)\end{aligned}$$

where we have used in Eq. 339 that $\left\langle \mathrm{T}_\tau \left[\!\left[\hat{c}_{\mu \mathbf{k}+\mathbf{q}}(\tau) \hat{c}^\dagger_{\nu \mathbf{k}}(\tau) \right]\!\right] \right\rangle_0 = 0$ for $\mathbf{q} \neq 0$ and that for $\mathbf{q} = 0$, charge electroneutrality (considering the frozen lattice of nuclei) gives that it is also equal to zero. Finally, the properties of the creation and anhiliation operators leads to the conditions $\delta_{\gamma\mu}\delta_{\nu\delta}\delta_{\mathbf{p},\mathbf{k}+\mathbf{q}}$ that stems from the orthogonality of the eigenstates. We have introduced the non-interacting Matsubara's single-particle Green's function $\mathcal{G}_\nu^{(0)}(\mathbf{k},\tau) = -\left\langle \mathrm{T}_\tau \left[\!\left[c_{\nu\mathbf{k}\delta} c^\dagger_{\nu\mathbf{k}}(\tau) \right]\!\right] \right\rangle_0$, whose expression in Matsubara fermionic space is given by

$$\mathcal{G}_\nu^{(0)}(\mathbf{k}, ik_n) = \int_0^\beta \mathrm{d}\tau e^{-ik_n\tau} \mathcal{G}_\nu^{(0)}(\mathbf{k},\tau) = \frac{1}{ik_n - \epsilon_{\nu\mathbf{k}}} \tag{341}$$

where $k_n = \pi(2n+1)k_B T$. Note that the inverse transform reads $\mathcal{G}_\nu^{(0)}(\mathbf{k},\tau) = \frac{1}{\beta}\sum_n e^{ik_n\tau}\mathcal{G}_\nu^{(0)}(\mathbf{k}, ik_n)$. Finally, combining Eq. 105, Eq. 336, Eq. 341, and Eq. 339, we obtain

$$\chi_{\mathrm{e}}^{(0)}(\mathbf{q}, z, z', \tau) = \frac{1}{\mathcal{A}} \sum_{\nu\mu\mathbf{k}} \lambda^{\mu\nu}_{\mathbf{k}+\mathbf{q}\mathbf{k}}(z) \mathcal{G}_\nu^{(0)}(\mathbf{k},\tau) \mathcal{G}_\mu^{(0)}(\mathbf{k}+\mathbf{q}, -\tau) \lambda^{\nu\mu}_{\mathbf{k}\mathbf{k}+\mathbf{q}}(z'), \tag{342}$$

where $\lambda^{\nu\mu}_{\mathbf{k}\mathbf{k}+\mathbf{q}}(z') = \sum_\kappa d^\kappa_{\mu\mathbf{k}+\mathbf{q}} (d^\kappa_{\nu\mathbf{k}})^* u^*_{\mathbf{q}}(z,\kappa)$ that is obtained similarly as Eq. 107. Fourier transforming with $\chi_{\mathrm{e}}^{(0)}(\mathbf{q}, z, z', i\Omega_m) = \int_0^\beta d\tau e^{-i\Omega_m\tau} \chi_{\mathrm{e}}^{(0)}(\mathbf{q}, z, z', \tau)$, we recover

$$\chi_{\mathrm{e}}^{(0)}(\mathbf{q}, z, z', i\Omega_m) = \frac{k_B T}{\mathcal{A}} \sum_{\nu\mu\mathbf{k}} \sum_{ik_n} \lambda^{\mu\nu}_{\mathbf{k}+\mathbf{q}\mathbf{k}}(z) \mathcal{G}_\nu^{(0)}(\mathbf{k}, ik_n) \ldots \tag{343}$$

$$\ldots \mathcal{G}_\mu^{(0)}(\mathbf{k}+\mathbf{q}, ik_n + i\Omega_m) \lambda^{\nu\mu}_{\mathbf{k}\mathbf{k}+\mathbf{q}}(z'). \tag{344}$$

where we have used the convolution theorem. Making the substitution $i\Omega_m \to \omega + i\eta$ gives Eq. 113.

E.3 $\chi_{\mathrm{E}}^{(0)}(q)$ FOR GRAPHENE

The analytical expression of $\chi_{\mathrm{e}}^{(0)}(q,\omega)$ for graphene can be found in [74]. In the static case, it reads:

$$\chi_{\mathrm{e}}^{(0)}(q) = -\frac{2k_F}{\hbar v_F \pi}\left[1 + \Theta\left(\frac{q}{2k_F} - 1\right) \ldots \right. \tag{345}$$

$$\left. \ldots \left(\frac{q}{2k_F}\left[\frac{\pi}{4} - \arcsin\left(\frac{2k_F}{q}\right)\right] - \frac{1}{2}\sqrt{1 - \left(\frac{2k_F}{q}\right)^2} \right) \right] \tag{346}$$

F

APPENDICES OF CHAPTER 6

F.1 ANALYTICAL EXPRESSION OF $\bar{\chi}_{\mathrm{w}}^{\infty}$

Computing Eq. 141 using Eq. 145 is a non-trivial complex analysis exercise. Briefly, we express the integral as

$$\bar{\chi}_{\mathrm{w}}^{\infty}(q,z) = \frac{2}{\pi}\mathrm{Re}\int_{1}^{+\infty} \mathrm{d}x \frac{\bar{\chi}_{\mathrm{w}}(qx)}{x\sqrt{x^2-1}} e^{iqz\sqrt{x^2-1}} \tag{347}$$

and use the residue theorem on a contour that avoids the real branches $]-\infty,-1[$ and $]+1,+\infty[$. We have fives poles in the contour, four from χ and one in zero. Be careful with the definition of the complex square root. This allows to obtain an analytical expression for $\bar{\chi}^{\infty}(q,z)$ in general. We report the result for $z=0$:

$$\begin{aligned}\frac{\bar{\chi}_{\mathrm{w}}^{\infty}(q)}{\bar{\chi}_{\mathrm{w}}^{\infty}(0)} = 1 + \frac{\lambda q}{\sqrt{2}}\left(\frac{\bar{\chi}_{\mathrm{w}}(q)}{\bar{\chi}_{\mathrm{w}}(0)}\right)^{1/4} \\ \times\left(\frac{\alpha^2}{\sqrt{1-\alpha^4}}\sqrt{1+\left(\frac{\bar{\chi}_{\mathrm{w}}(q)}{\bar{\chi}_{\mathrm{w}}(0)}\right)^{1/2}(\alpha^2-\lambda^2q^2)}\right. \\ \left. -\sqrt{1-\left(\frac{\bar{\chi}_{\mathrm{w}}(q)}{\bar{\chi}_{\mathrm{w}}(0)}\right)^{1/2}(\alpha^2-\lambda^2q^2)}\right).\end{aligned} \tag{348}$$

F.2 GRAPHENE LAYER-LAYER CORRECTIONS

For two confining plates centered in $z=0$ and $z=L$, the expression of the electronic response function is obtained by following the steps from Eq. 150 to Eq. 154. It gives

$$\chi_{\mathrm{e}}^{(\mathrm{w})}(q,z,z') = \chi_{\mathrm{e}\uparrow}^{(\mathrm{w})}(q)\delta(z)\delta(z') + \chi_{\mathrm{e}\downarrow}^{(\mathrm{w})}(q)\delta(L-z)\delta(L-z') \tag{349}$$

$$+\chi_{\mathrm{e}\uparrow\downarrow}^{(\mathrm{w})}(q)\delta(z-L)\delta(z') + \chi_{\mathrm{e}\downarrow\uparrow}^{(\mathrm{w})}(q)\delta(z)\delta(L-z') \tag{350}$$

with

$$\chi^{(w)}_{e\uparrow}(q) = \frac{\chi^{(w)}_{e/Gr}(q)}{1 - \left[w_w(q,0,L)\chi^{(w)}_{e/Gr}(q)\right]^2} \qquad \chi^{(w)}_{e\downarrow}(q) = \chi^{(w)}_{e\uparrow}(q) \tag{351}$$

$$\chi^{(w)}_{e\uparrow\downarrow}(q) = \frac{\chi^{(w)}_{e/Gr}(q) w_w(q,0,L)\chi^{(w)}_{e/Gr}(q)}{1 - \left[w_w(q,0,L)\chi^{(w)}_{e/Gr}(q)\right]^2} \qquad \chi^{(w)}_{e\downarrow\uparrow}(q) = \chi^{(w)}_{e\uparrow\downarrow}(q) \tag{352}$$

and where

$$\chi^{(w)}_{e/Gr}(q) = \frac{\chi^{(0)}_{e}(q)}{1 - w_w(q,0,0)\chi^{(0)}_{e}(q)} \tag{353}$$

The uncoupled and semi-coupled curves are obtained by replacing $w_w(q,0,0)$ with $v(q,0,0) = 1/2q\epsilon_0$ in Eq. 353.

F.3 OTHER COMPARISON

Extracting the electronic contribution F_e, we compare our results with the one of [85] in Fig. 40. They decompose the wall-ion contribution for the adsorption site of SCN^-, which is an ion too large and anisotropic to be quantitatively compared with isotropic ion in presence of water. Nevertheless, the good agreement with our results regarding metal-ion potential attenuation validates our description of the system.

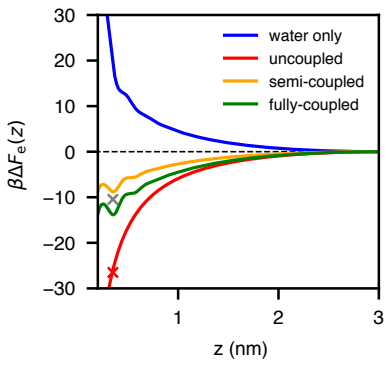

Figure 40: Electronic contribution to the PMF shown in Fig 23a. The crosses are results extracted from Ref. [85].

G

APPENDICES OF CHAPTER 7

G.1 G_0W IN GRAPHENE

The single-particle Green's function G follows the Dyson equation:

$$G(1,1') = G^{(0)}(1,1') + \iint \mathrm{d}2\mathrm{d}3 G^{(0}(1,2)\Sigma(2,3)G(3,1'), \tag{354}$$

where $G^{(0)}$ is the non-interacting Green's function that is build in the eigenstates basis of the quadratic TB hamiltonian. To calculate the self-energy $\Sigma(1,2)$, Hedin [119] suggested the GW approximation:

$$\Sigma(1,2) = iG(1,2)w(1^+,2). \tag{355}$$

Here w is the screened potential and where the " $+$ " indicates a forward infinitesimal time shift. The retarted Green's function of the electronic system can be decomposed on the electronic energy levels

$$G(\mathbf{x}_2,\mathbf{x}_3,t_1,t_2) = \sum_{\alpha\gamma\mathbf{k}_\alpha\mathbf{k}_\gamma} \psi_{\alpha\mathbf{k}_\alpha}(\mathbf{x}_2)\psi^*_{\gamma\mathbf{k}_\gamma}(\mathbf{x}_3)G_{\alpha\gamma}(\mathbf{k}_\alpha,\mathbf{k}_\gamma,t_2,t_3). \tag{356}$$

We underline that in this section, that $\mathbf{k}$'s are two-dimensional wavevectors. At equilibrium, for a translationally invariant interface, G only depends on time and space coordinate difference. Going into frequency space in time, we find using Eq. 356, Eq. 355 and Eq. 354, that

$$\begin{aligned}\Sigma_{\nu\mu}(\mathbf{k}_\nu,\mathbf{k}_\mu,E) = i\sum_{\alpha\gamma}\int\frac{\mathrm{d}(\hbar\omega)}{2\pi}\iint \mathrm{d}\mathbf{x}_2\mathrm{d}\mathbf{x}_3\psi^*_{\nu\mathbf{k}_\nu}(\mathbf{x}_2)\psi_{\alpha\mathbf{k}_\alpha}(\mathbf{x}_2)... \\ ...G_{\alpha\gamma}(\mathbf{k}_\alpha,\mathbf{k}_\gamma,E+\hbar\omega)e^{i\delta\omega}w(\mathbf{x}_2,\mathbf{x}_3,\omega)\psi^*_{\gamma\mathbf{k}_\gamma}(\mathbf{x}_3)\psi_{\mu\mathbf{k}_\mu}(\mathbf{x}_3)\end{aligned} \tag{357}$$

The screened potential w is expressed in terms of its inverse Fourier transform and reads $w(\mathbf{x}_2,\mathbf{x}_3,\omega) = \mathcal{A}^{-1}\sum_{\mathbf{q}} e^{-i\mathbf{q}(\mathbf{r}_2-\mathbf{r}_3)}w(\mathbf{q},\omega,z_2,z_3)$. To conserve the crystal momentum (i.e. $\lambda^{\nu\alpha}_{\mathbf{k}_\nu\mathbf{k}_\alpha}(-\mathbf{q}) \neq 0$ or $\lambda^{\gamma\mu}_{\mathbf{k}_\alpha\mathbf{k}_\mu}(\mathbf{q}) \neq 0$ see chapter 5) we need that $\mathbf{k}_\nu - \mathbf{q} = \mathbf{k}_\alpha$ (resp. $\mathbf{k}_\gamma + \mathbf{q} = \mathbf{k}_\mu$). Also, the starting point is $G_{\alpha\gamma} = G^{(0)}_{\alpha\gamma} \propto \delta_{\alpha\gamma}\delta_{\mathbf{k}_\nu\mathbf{k}_\mu}$ that has diagonal entries at equilibrium so that introducing

$$W^{\alpha}_{\nu\mu\mathbf{k}}(\mathbf{q},\omega) = \iint \mathrm{d}z_2\mathrm{d}z_3 \lambda^{\nu\alpha}_{\mathbf{k}\mathbf{k}-\mathbf{q}}(z_2) w(\mathbf{q},\omega,z_2,z_3) \lambda^{\alpha\mu}_{\mathbf{k}-\mathbf{q}\mathbf{k}}(z_3), \tag{358}$$

we can rewrite

$$\Sigma_{\nu\mu}(\mathbf{k},E) = \frac{i}{\mathcal{A}} \sum_{\alpha\mathbf{q}} \int \frac{\mathrm{d}(\hbar\omega)}{2\pi} G_{\alpha}(\mathbf{k}-\mathbf{q},E+\hbar\omega) e^{i\delta\omega} W^{\alpha}_{\nu\mu\mathbf{k}}(\mathbf{q},\omega). \tag{359}$$

We can also check that non-diagonal terms are zero because we only consider classical — Coulomb type of interactions so that eigenstates are not mixed ($\Sigma_{\nu\mu} \propto \delta_{\nu\mu}$). Finally, considering the small spatial extent of the carbon p_z orbital, we make the 2D approximation, that is $w(\mathbf{q},\omega,z_2,z_3) \simeq w(\mathbf{q},\omega,0,0) = w(\mathbf{q},\omega)$ in Eq.358. It gives

$$\Sigma_{\nu}(\mathbf{k},E) = \frac{i}{\mathcal{A}} \sum_{\mu\mathbf{q}} \int \frac{\mathrm{d}(\hbar\omega)}{2\pi} |\lambda^{\nu\mu}_{\mathbf{k}\mathbf{k}-\mathbf{q}}|^2 G_{\mu}(\mathbf{k}-\mathbf{q},E+\hbar\omega) w(\mathbf{q},\omega) e^{i\delta\omega}. \tag{360}$$

This can be expressed in the Matsubara formalism [31] as long as we consider a thermal equilibrium state at temperature T. The Matsubara bosonic frequencies $\Omega_m = 2\pi m k_B T$ are introduced and we read

$$\Sigma_{\nu}(\mathbf{k},E) = \frac{-1}{\beta\mathcal{A}} \sum_{\mu\mathbf{q}} \sum_{i\Omega_m} |\lambda^{\nu\mu}_{\mathbf{k}\mathbf{k}-\mathbf{q}}|^2 \mathcal{G}_{\mu}(\mathbf{k}-\mathbf{q},ik_n+i\Omega_m) w(\mathbf{q},i\Omega_m). \tag{361}$$

G.2 CARBON NANOTUBES (CNTS)

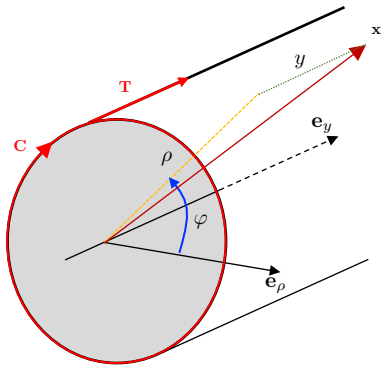

Figure 41: A CNT as rolled graphene ribbon. To be compared with Fig. 35.

Fig. 41	Cylinder (cylindrical coordinates)
$\mathbf{x}$	(ρ, φ, y)
$\mathrm{d}\mathbf{x}$	$\rho \mathrm{d}\rho \mathrm{d}\varphi \mathrm{d}y$
$\delta(\mathbf{x})$	$\frac{1}{\rho}\delta(\rho)\delta(\varphi)\delta(y)$
$\mathbf{k}$	$(q_\rho, l, p) = (q_\rho, \zeta)$
Fourier transform	$f(\zeta) = \int_0^{2\pi} \mathrm{d}\varphi \int_0^{L_y} \mathrm{d}y f(\varphi, y) e^{-i(\varphi l/R + py)}$
inverse Fourier transform	$f(\varphi, y) = (2\pi L_y)^{-1} \sum_\zeta f(\zeta) e^{+i(\varphi l/R + py)}$
limit sum-integral	$L_y^{-1} \sum_p \xrightarrow[L_y \to \infty]{} \int_{-\infty}^{+\infty} \frac{\mathrm{d}p}{2\pi}$ $L_y \delta_p \xrightarrow[L_y \to \infty]{} 2\pi\delta(p)$
$f * g$	$\int_0^{+\infty} \mathrm{d}\rho' \rho' f(\rho, \rho') g(\rho')$
linear response	$n(\rho, \zeta) = \int \mathrm{d}\rho' \rho' \chi(\rho, \rho', \zeta) \phi(\rho', \zeta)$

Table 6: Mathematical toolbox for the infinite, homogeneous, and isotropic on its surface tube.

A CNT is a rolled graphene ribbon. The chiral vector uniquely defines the CNT because it links two overlapping carbon atoms in the ribbon. Given the lattice vectors $\mathbf{a}_1$,$\mathbf{a}_2$ of the graphene lattice, it reads $\mathbf{C} = n\mathbf{a}_1 + m\mathbf{a}_2$. The circumference of the CNT is $|\mathbf{C}| = 2\pi R$ with R the radius of the CNT. Along the nanotube axis, we can introduce another vector that gives the minimal translation before repetition along with the axis of the tube [71]:

$$\mathbf{T} = \frac{2m+n}{d_R}\mathbf{a}_1 - \frac{m+2n}{d_R}\mathbf{a}_2 \qquad d_R = \gcd(2m+n, m+2n). \tag{362}$$

This vector is orthogonal to $\mathbf{C}$ as shown Fig. 41 that shows the CNT and its corresponding unrolled ribbon. We choose $\mathbf{e}_y = \frac{\mathbf{T}}{|\mathbf{T}|}$ to be aligned with the tube axis of length L_y and $\mathbf{e}_{x'} = \frac{\mathbf{C}}{|\mathbf{C}|}$. In our coordinate system, it gives $x'/|\mathbf{C}| = \varphi/2\pi$ or $x' = \varphi R$. Note that locally, considering the small spatial extension of the p_z orbital, when can assimilate the vertical direction of the planar system to the distance from the cylinder, that is $z \simeq \rho - R$. In cartesian space that links the planar and cylindrical coordinates, we can therefore write

$$\mathbf{x} = \varphi R \mathbf{e}_{x'} + y\mathbf{e}_y + (\rho - R)\mathbf{e}_z. \tag{363}$$

In the so-called zone folding approximation, we obtain the eigenstates of the graphene ribbon with a periodic boundary condition in the $\mathbf{e}_x$ direction. This means that the wavefunction should be periodic. Using Eq. 121, we must therefore imposes that $\psi_{\nu\mathbf{k}}(\mathbf{r} + \mathbf{C}) = e^{-i\mathbf{k}\mathbf{C}}\psi_{\nu\mathbf{k}}(\mathbf{r}) = \psi_{\nu\mathbf{k}}(\mathbf{r})$. This is

equivalent to discretizing the reciprocal space in one direction such that the Brilioun zone is now a set of parallel lines. We are interested of the condition $e^{-i\mathbf{k}\mathbf{C}} = 1$ for $\mathbf{k}$ near $\mathbf{K}$ or $\mathbf{K}'$. Using $\mathbf{K}\cdot\mathbf{C} = (n-m)/3$, we find convenient to distinguish cases and write $n+m \in 3\mathbb{N} - \sigma$ with $\sigma = 0, \pm 1$. The periodic boundary condition reads $\mathbf{ffik}\cdot\mathbf{C} = 2\pi(l + \sigma/3)$. Turning to the eigenenergies (see Eq. 122), we find that

$$\epsilon_{\nu\zeta} = \nu\hbar v_F \sqrt{(l+\sigma/3)^2/R^2 + p^2}, \tag{364}$$

where the symbol $\zeta = (l, p)$ for the wavevector in the CNT has replaced the $\mathbf{k} - \mathbf{K}$ symbol for the planar surface. Note that near $\mathbf{K}'$, we replace σ by $-\sigma$. The consequence of such a dispersion relation is that some tubes ($\sigma = 0$) are semimetallic like graphene, and others ($\sigma = \pm 1$) are semiconducting.

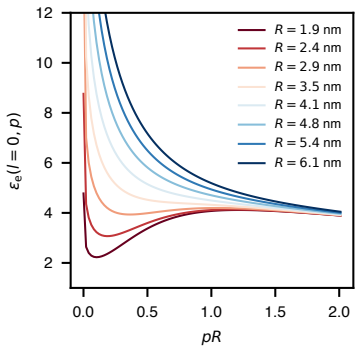

Figure 42: Static dielectric constant $\varepsilon_e(l=0,p)$ of a CNT a $T = 300$ K.

G.3 CYLINDRICAL SRF OF A DIELECTRIC

In this paragraph, we derive the SRF of a liquid inside or outside a CNT in the continuum electrostatic limit (see Fig. 43). This means that we can use standard electrostatics — Eq. 262 and the constitutive Eq. 264. We use the following tensor for the dielectric

$$\underline{\varepsilon}_w = \begin{pmatrix} \varepsilon_w^\rho & 0 & 0 \\ 0 & \varepsilon_w^\varphi & 0 \\ 0 & 0 & \varepsilon_w^y \end{pmatrix}, \tag{365}$$

to show the first steps of the derivation in one considers of an anisotropic material. We detail the electrostatic problem for the outside case in Fig. 43a. We consider the space entirely filled wih a liquid outside a hollow cylinder of radius R. This region is denoted (2) (see Fig. 43a). The zone (0) contains an external charge that polarizes the dielectric medium which induces a

potenial back on it. There is no charge in region (1). *There is no CNT in this section, no electrons. Only a cylindrical steric constraint*. The external charge only help in expressing the SRF. At the end of the computation, we will use $\mathcal{V}_1 \to 0$.

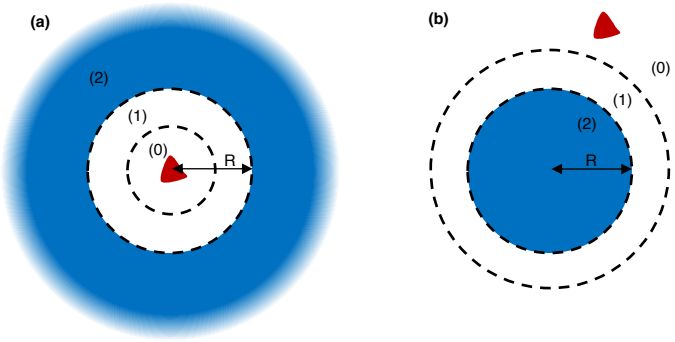

Figure 43: Geometry for a dielectric outside **(a)** or inside **(b)** a CNT of radius R.

Denoting $\phi^{(i)}$ the electrostatic potential in region (i), we use Eq. 262 for region (1) and (2), and get

$$\nabla \cdot \left[\underline{\varepsilon}_{\mathrm{w}}^{(i)} \nabla \phi^{(i)}(\mathbf{x}) \right] = 0 \quad i \in 1,2 \tag{366}$$

with $\underline{\varepsilon} = 1 \quad \underline{\varepsilon}_{\mathrm{w}}^{(2)} = \underline{\varepsilon}_{\mathrm{w}}$. The boundary conditions — continuity of potential of vertical component of displacement field — in $\rho = R$ read

$$\begin{cases} \phi^{(1)}(\rho = R^-) = \phi^{(2)}(\rho = R^+) \\ \partial_\rho \phi^{(1)}|_{\rho=R^-} = \varepsilon_{\mathrm{w}}^{\rho} \partial_\rho \phi^{(2)}|_{\rho=R^+} \end{cases} \tag{367}$$

Expressing 366 in both region (1) and (2), we get

$$\begin{aligned} \rho^2 \partial_\rho^2 \phi^{(1)} + \rho \partial_\rho \phi^{(1)} + \left[\rho^2 \partial_y^2 + \partial_\varphi^2 \right] \phi^{(1)} = 0 \\ \rho^2 \partial_\rho^2 \phi^{(2)} + \rho \partial_\rho \phi^{(2)} + \left[\rho^2 \mu_y^2 \partial_y^2 + \mu_\varphi^2 \partial_\varphi^2 \right] \phi^{(2)} = 0 \end{aligned} \tag{368}$$

where $\mu_y = \varepsilon_{\mathrm{w}}^{\rho} / \varepsilon_{\mathrm{w}}^{y}$ and $\mu_\varphi = \varepsilon_{\mathrm{w}}^{\rho} / \varepsilon_{\mathrm{w}}^{\varphi}$ quantify the anisotropy. Expanding the potential in its Fourier components

$$\phi^{(i)}(\rho, \varphi, y) = \frac{1}{2\pi L_y} \sum_{\zeta} \phi^{(i)}(\rho, \zeta) e^{+i(\varphi l / R + p y)}, \tag{369}$$

we insert back in Eq. 368 and obtain two equations of the type

$$x^2 \frac{d^2 y}{dx^2} + x \frac{dy}{dx} - \left(x^2 + \alpha^2 \right) y = 0. \tag{370}$$

Two independent solutions are $I_\alpha(x)$ and $K_\alpha(x)$ such that we can express the solutions as follows:

$$\begin{cases} \phi^{(1)}(\rho,\zeta) = F_\zeta^{(1)} I_l(|p|\rho) + G_\zeta^{(1)} K_l(|p|\rho) \\ \phi^{(2)}(\rho,\zeta) = F_\zeta^{(2)} I_{l\mu_\varphi}(\mu_y|p|\rho) + G_\zeta^{(2)} K_{l\mu_\varphi}(\mu_y|p|\rho). \end{cases} \tag{371}$$

When the dielectric is outside the CNT, the potential must vanish for $\rho \to \infty$ so that $F_\zeta^{(2)} = 0$. Similarly to Eq. 38, we define the SRF as follows

$$g_{\mathrm{w}}^{\mathrm{out}}(\zeta) = -\frac{\phi_{\mathrm{ind}}(\zeta, \rho = R)}{\phi_{\mathrm{ext}}(\zeta, \rho = R)} = -\frac{F_\zeta^{(1)} I_l(|p|R)}{G_\zeta^{(1)} K_l(|p|\rho)}. \tag{372}$$

The last equality of Eq. 372 stems from the fact that the contribution with $I_l(|p|\rho)$ in $\phi^{(1)}$ in Eq. 371 cannot be the one of the external charge because $\phi_{\mathrm{ext}}(\zeta, \rho \to \infty) \to 0$. Using the boundary condition and specializing to the isotropic case, i.e. ,$\varepsilon_{\mathrm{w}}^{\rho} = \varepsilon_{\mathrm{w}}^{y} = \varepsilon_{\mathrm{w}}^{\varphi}$, we get from Eq. 367 that

$$\begin{aligned} F_\zeta^{(1)} I_l(|p|R) + G_\zeta^{(1)} K_l(|p|R) &= G_\zeta^{(2)} K_l(|p|R) \\ F_\zeta^{(1)} I_l'(|p|R) + G_\zeta^{(1)} K_l'(|p|R) &= \varepsilon_{\mathrm{w}} G_\zeta^{(2)} K_l'(|p|R). \end{aligned} \tag{373}$$

Finally, using Eq. 372 and Eq. 373, we get

$$g_{\mathrm{w}}^{\mathrm{out}}(\zeta) = \frac{\varepsilon_{\mathrm{w}} - 1}{\varepsilon_{\mathrm{w}} + \alpha_l(|p|R)} \qquad \alpha_l(|p|R) = -\frac{K_l(|p|R)}{K_l'(|p|\rho)} \frac{I_l'(|p|R)}{I_l(|p|R)}. \tag{374}$$

For the inside case (see Fig. 43b), Eq. 371 is still valid but now $G_\zeta^{(2)} = 0$ because the potential cannot diverge at the center of the dielectric in the absence of exteral charge. This time we have $g_{\mathrm{w}}^{\mathrm{in}}(\zeta) = -\frac{\phi_{\mathrm{ind}}(\zeta,\rho=R)}{\phi_{\mathrm{ext}}(\zeta,\rho=R)} = -\frac{G_\zeta^{(1)} K_l(|p|R)}{F_\zeta^{(1)} I_l(|p|R)}$ and

$$g_{\mathrm{w}}^{\mathrm{in}}(\zeta) = \frac{\varepsilon_{\mathrm{w}} - 1}{\varepsilon_{\mathrm{w}} + 1/\alpha_l(|p|R)} \tag{375}$$

H

APPENDICES OF CHAPTER 9

H.1 $S_e^s(q,\omega)$ FOR A 3D JELLIUM (RPA+SRA)

Computing $S_e^s(q,\omega)$ adds up in computing $g_e(q,\omega)$ using the FDT (see Eq. 233). To compute $g_e(q,\omega)$ we resort to the SRA in Eq. 142. To compute $\bar{\chi}_e^\infty$, we use Eq. 141. To find the bulk response function of the medium $\bar{\chi}_e$ we resort to the RPA in Eq. 27. Finally, we need the non-interacting response function $\chi_e^{(0)}(k,\omega)$. We obtain it by computing analytically at $T = 0$K a formula of the type Eq. 110 for the bulk case. This well-known result can be find in textbooks [31]. It reads, using $\tilde{k} = \frac{k}{2k_F}$ and $\tilde{\omega} = \frac{\hbar\omega}{E_F}$,

$$\mathrm{Re}\chi_e^{(0)}(k,\omega) = -\epsilon_0 k_{TF}^2 \left(\frac{1}{2} + f\left(\tilde{k},\tilde{\omega}\right) + f\left(\tilde{k},-\tilde{\omega}\right)\right); \tag{376}$$

$$\begin{aligned}\mathrm{Im}\chi_e^{(0)}(k,\omega) = -\epsilon_0 k_{TF}^2 \Bigg[& \pi h(\tilde{k},\tilde{\omega})\Theta(\tilde{\omega} - |\tilde{k} - \tilde{k}^2|)... \\ & ... \times \Theta(\tilde{k} + \tilde{k}^2 - \tilde{\omega}) + \frac{\pi\tilde{\omega}}{2\tilde{k}}\Theta(\tilde{\omega})\Theta(\tilde{k} - \tilde{k}^2 - \tilde{\omega})\Bigg].\end{aligned} \tag{377}$$

We have introduced

$$f(\tilde{k},\tilde{\omega}) = h(\tilde{k},\tilde{\omega})\log\left|\frac{\tilde{k} + \tilde{k}^2 - \tilde{\omega}}{\tilde{k} - \tilde{k}^2 + \tilde{\omega}}\right| \qquad h(\tilde{k},\tilde{\omega}) = \frac{1 - \left[\tilde{\omega}/\tilde{k} - \tilde{k}\right]^2}{8\tilde{k}} \tag{378}$$

and we recall for completness the dispersion relation $\epsilon_{\mathbf{k}} = \frac{\hbar k^2}{2m}$, the TF wavevector $k_{TF} = \left(\frac{4k_F}{\pi a_0}\right)^{1/2}$, Fermi energy $E_F = \frac{\hbar k_F^2}{2m}$ and charge carrier density $n_e^0 = \frac{k_F^3}{3\pi^2}$.

H.2 NON-ADIABATIC FRICTION ON TYPICAL METALS

The expression of H reads

$$H(\frac{q_{TF}}{2k_F},\varepsilon_w) = 3\int_0^1 \mathrm{d}x x^2 \left(\frac{x+\alpha}{x+\alpha/\kappa}\right)^2 \tag{379}$$

and can be computed to give

$$H(\alpha,\varepsilon_{\rm w}) = 1+3\frac{(\kappa-1)}{\kappa}\left[\alpha+(\kappa-3)\frac{\alpha^2}{\kappa+\alpha}\right. \tag{380}$$

$$\left.+2\frac{(\kappa-2)}{\kappa^2}\alpha^3\left(\frac{\kappa}{\kappa+\alpha}-\log(1+\frac{\kappa}{\alpha})\right)\right] \tag{381}$$

where we have introduced $\kappa=(\varepsilon_{\rm w}+1)/2$ and $\alpha=q_{\rm TF}/2k_F$. Fig. 44 shows $H(\frac{q_{\rm TF}}{2k_F},\varepsilon_{\rm w})$ that distinguishes metals ($\frac{q_{\rm TF}}{2k_F}$), and liquids ($\varepsilon_{\rm w}$).

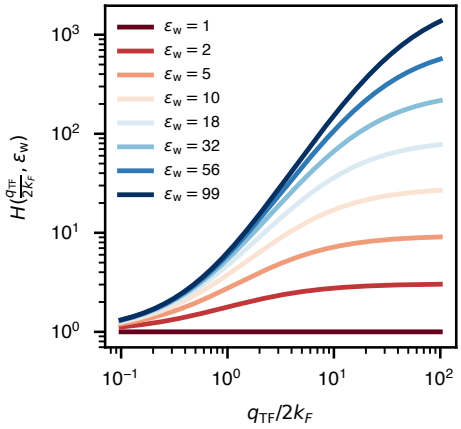

Figure 44: $H(\frac{q_{\rm TF}}{2k_F},\varepsilon_{\rm w})$ computed from Eq. 380.

Herein, we try to evaluate the maximum friction coefficient that can be obtained assuming frequency and wavelength decoupling for a 3D jellium—using $\lambda^{\rm (III)}_{\rm nBO}$. Using $k_F=1/4d$, we find an upperbound for metal with $k_{\rm TF}<(\pi a_0 d)^{-1/2}$. Inserting Eq. 247 in Eq. 246 and we can pull $g_{\rm w}(q<1/2d)\simeq\frac{\varepsilon_{\rm w}-1}{\varepsilon_{\rm w}+1}$ out of the integral. The charge structure factor for the jellium $S^{\rm s}_{\rm e}(k_F=1/4d,\omega=0)$ can be read in Fig. 32 is also pulled out of the integral[1]. We find that using $q_{\rm TF}=k_F$ approximately reproduces the calculated SRF $g_{\rm e}(q)$ and we use this value to quantify H. Therefore the $d-$dependant maximum value for $\lambda^{\rm (III\text{-}max)}_{\rm nBO}$ reads

$$\lambda^{\rm (III\text{-}max)}_{\rm nBO}\simeq\frac{\varepsilon_{\rm w}-1}{\varepsilon_{\rm w}+1}\frac{S^{\rm s}_{\rm e}(\frac{1}{4d},\omega=0)}{128\pi\epsilon_0 d^3}\frac{H(1/2,\varepsilon_{\rm w})}{3}. \tag{382}$$

In fact, Eq. 382, can be obtained by considering an assembly of independent dipoles. Inserting $S^{\rm s}_{\rm w}(q)=\int_0^{+\infty}n_0(z)\mu^2q^2e^{-2qz}{\rm d}z$ with the dipole density $n_0(z)=\Theta(z-d)$ in Eq. 235, gives after some algebra $\lambda^{(1)}_{\rm nBO}=\frac{g^{(0)}_{\rm w}(0)}{3}\frac{S^{\rm s}_{\rm e}(\frac{1}{4d},\omega=0)}{128\pi\epsilon_0 d^3}$. It is similar to Eq. 382 by replacing $g_{\rm w}(0)$ with the non-interacting SRF $g^{(0)}_{\rm w}(0)=3\pi n_0\alpha$, where the Langevin-Debye polarisability reads $\alpha=\mu^2/3k_BT$. The corrective factor $H(1/2,\varepsilon_{\rm w})$ is find to be very close

[1] a small overestimation can be anticipated here. In any case, we look for an upper bound.

to $g_{\rm w}^{(0)}(0)/g_{\rm w}(0)$, for SPC/E water, which makes the independent dipole model relevant for the upper bound $\lambda_{\rm nBO}^{\rm (III\text{-}max)}$. The numerical application gives

$$\lambda_{\rm nBO}^{\rm (III\text{-}max)} = \frac{S_{\rm e}^{\rm s}(\frac{1}{4d},\omega=0)}{128\pi\epsilon_0 d^3}\pi\alpha n_0 \simeq 20\times\left(\frac{d_{\rm OH}}{d}\right)^3. \quad ({\rm N.s.m^{-3}}) \tag{383}$$

which is valid for 3D metals with $k_{\rm TF}\leq 0.77\left(\frac{d_{\rm OH}}{d}\right)^{1/2}$ Å^{-1}. Here $d_{\rm OH}=1$Å is the oxygen-hydrogen distance in the SPC/E water molecule. For $d=(d_{\rm Aluru}+d_{\rm Werder})/2=1.52$Å, given by our MD simulations for graphene (see Fig. 7), we find $\lambda_{\rm nBO}^{\rm (III\text{-}max)}\simeq 5.7$ N.s.m^{-3} for 3D metals with $k_{\rm TF}\leq 0.63$Å^{-1}.

What if the charge fluctuation wavelengths cannot be decoupled ? For metals with large Fermi wavevector $k_F>1/4d$, we must compute $\lambda_{\rm nBO}^{\rm (II)}$ in Eq. 246. We restrict the integration from $1/2d<q<2k_F$ because we have already evaluated the part $q<1/2d$ in Eq.383[2]. The denominator in Eq. 246 no longer plays an important role due to the e^{-2qd} factor and we ignore it. For increasing k_F, we find that the friction increases and converge for $k_F d\gtrsim 1$ to

$$\lambda_{\rm nBO}^{\rm (II)}-\lambda_{\rm nBO}^{\rm (III\text{-}max)}\simeq\frac{\varepsilon_{\rm w}-1}{\varepsilon_{\rm w}+1}\frac{S_{\rm e}^{\rm s}(k_F,\omega=0)}{128\pi\epsilon_0 d^3}\frac{10}{e}\simeq 20\times\left(\frac{d_{\rm OH}}{d}\right)^3({\rm N.s.m^{-3}}). \tag{384}$$

By considering larger Fermi wavevector $k_F>1/4d$, we find that we need to multiply our previous estimate in Eq. 383 by a factor of 2 because $10/e\simeq\pi\alpha n_0\simeq H(1/2,\varepsilon_{\rm w})/3$. In other words, the same contribution to the friction can be find for $q<1/2d$ and $q>1/2d$.

We can summarize our results as follows. If charge fluctuations wavelength and frequencies between the liquid and the solid are decoupled as it is usually the case, one should resort to Eq. 248 and the evaluation of $\lambda_{\rm nBO}^{\rm (III)}$. For a generic jellium model, we can estimate an upper bound for the friction and we find it adds up in summing up the friction coefficients of independent dipoles — see $\lambda_{\rm nBO}^{\rm (III\text{-}max)}$in Eq. 383. The result is limited by the closest dipole distance to the surface d and converge for increasing until $k_F\simeq 1/d$. For the non-local properties of the liquid to play a role, it needs to contain wavelength fluctuations at length scales $q_{\rm w}<1/2d$. For dense metals, with $d=d_{\rm OH}$, we obtain the upper bound $\lambda_{\rm nBO}^{\rm (II)}\simeq 40$ N.s.m^{-3}.

[2] To be more precise, we should multiply are results by $S_{\rm e}^{\rm s}(k_F,\omega=0)/S_{\rm e}^{\rm s}(1/2d,\omega=0)<1$.

H.3 $S^{s}_{E}(q,\omega)$ OF FLG AND GRAPHITE

To quantify the surface charge structure factor $S^{s}_{e}(q,\omega)$ of graphite at $T = 0K$, we build a small model using the single layer non-interacting response function of grpaphene $\chi^{(0)}_{e}(q,\omega)$. To renormalize electron-electron interactions at the RPA level, we solve Eq. 115. However, we cut off all non-diagonal inter-layer interactions in Eq. 124. Therefore, we solve N independant Schrödinger equations to get N times $\chi^{(0)}_{e}(q,\omega)$. We then couple the graphene layers as follows. We write

$$X_0[z,z'] = \sum_i \chi^{(0)}_{e}(q,\omega)\delta(z-z_i)\delta(z'-z_i). \tag{385}$$

We operate in the layer-layer (i,j) basis in which $\tilde{X}_0$ is diagonal and solve Eq. 117. Here $\tilde{V}[i,j] = e^{-q\frac{c}{2}|i-j|}/2q\epsilon_0$ and

$$\tilde{X} = (I - \chi^{(0)}_{e}(q,\omega)\tilde{V})^{-1}\chi^{(0)}_{e}(q,\omega). \tag{386}$$

Finally, we compute the SRF as

$$g_e(q,\omega) = -\frac{1}{2q\epsilon_0}\sum_{i,j}\tilde{X}[i,j]e^{-q\frac{c}{2}(i+j)}. \tag{387}$$

Taking the imaginary part and using the FDT, we compute Fig. 45 that supports the argument of the main text.

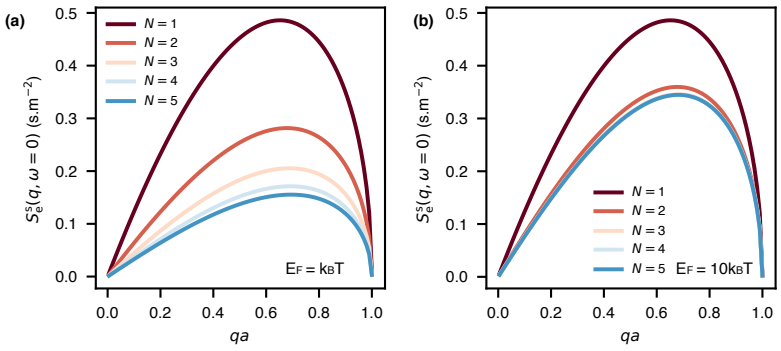

Figure 45: Surface charge structure factor of FLG for increasing number of layers N and **(a)** $E_F = k_BT$ and **(b)** $E_F = 10k_BT$

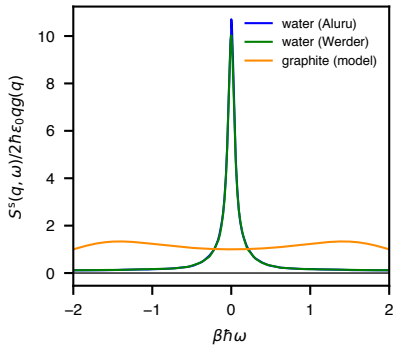

Figure 46: Surface structure factor of water from MD simulation (Aluru and Werder) and graphite from the model for $g_e(q,\omega)$ in Eq. 251. The range of validity for the wavevector is $q < 1/2d$ and $q < q_{max}$ respectively.

BIBLIOGRAPHY

[1] L. Bocquet, Nature Materials **19**, 254 (2020).

[2] M. Majumder, N. Chopra, R. Andrews, and B. J. Hinds, Nature **438**, 44 (2005).

[3] J. K. Holt, H. G. Park, Y. Wang, M. Stadermann, A. B. Artyukhin, C. P. Grigoropoulos, A. Noy, and O. Bakajin, Science **312**, 1034 (2006).

[4] A. Siria, P. Poncharal, A.-L. Biance, R. Fulcrand, X. Blase, S. T. Purcell, and L. Bocquet, Nature **494**, 455 (2013).

[5] B. Radha, A. Esfandiar, F. C. Wang, A. P. Rooney, K. Gopinadhan, A. Keerthi, A. Mishchenko, A. Janardanan, P. Blake, L. Fumagalli, M. Lozada-Hidalgo, S. Garaj, S. J. Haigh, I. V. Grigorieva, H. A. Wu, and A. K. Geim, Nature **538**, 222 (2016).

[6] E. Secchi, S. Marbach, A. Niguès, D. Stein, A. Siria, and L. Bocquet, Nature **537**, 210 (2016).

[7] S. Marbach and L. Bocquet, Chemical Society Reviews **48**, 3102 (2019).

[8] A. Siria, M.-L. Bocquet, and L. Bocquet, Nature Reviews Chemistry **1**, 0091 (2017).

[9] S. Gravelle, "Nanofluidics: a pedagogical introduction," (2016).

[10] A. K. Geim and I. V. Grigorieva, Nature **499**, 419 (2013).

[11] A. K. Geim and K. S. Novoselov, Nature Materials **6**, 183 (2007).

[12] G. Tocci, L. Joly, and A. Michaelides, Nano Letters **14**, 6872 (2014).

[13] F. L. Thiemann, C. Schran, P. Rowe, E. A. Müller, and A. Michaelides, ACS Nano (2022), publisher: American Chemical Society.

[14] B. Grosjean, *Reactivity of Boron Nitride and Carbon Based Nanomaterials with Water : a study from first principles*, Ph.D. thesis, Sorbonne Université (2019).

[15] W. Dou and J. E. Subotnik, The Journal of Physical Chemistry A **124**, 757 (2020).

[16] S. Pisana, M. Lazzeri, C. Casiraghi, K. S. Novoselov, A. K. Geim, A. C. Ferrari, and F. Mauri, Nature Materials **6**, 198 (2007).

[17] M. Vorotyntsev and A. A. Kornyshev, Zh. Eksp. Teor. Fiz. **78**, 1008 (1980).

[18] A. A. Kornyshev and M. A. Vorotyntsev, Surface Science **101**, 23 (1980).

[19] A. M. Gabovich, M. S. Li, H. Szymczak, and A. I. Voitenko, Surface Science **606**, 510 (2012).

[20] V. Kaiser, J. Comtet, A. Niguès, A. Siria, B. Coasne, and L. Bocquet, Faraday Discussions **199**, 129 (2017).

[21] D. Frenkel and B. Smit, *Understanding molecular simulation: from algorithms to applications*, 2nd ed., Computational science series No. 1 (Academic Press, San Diego, 2002).

[22] B. Grosjean, M.-L. Bocquet, and R. Vuilleumier, Nature Communications **10**, 1656 (2019).

[23] J. G. Brandenburg, A. Zen, M. Fitzner, B. Ramberger, G. Kresse, T. Tsatsoulis, A. Grüneis, A. Michaelides, and D. Alfè, The Journal of Physical Chemistry Letters **10 (3)**, 358 (2019).

[24] L. Joly, R. H. Meißner, M. Iannuzzi, and G. Tocci, ACS Nano **15**, 15249 (2021), publisher: American Chemical Society.

[25] R. P. Misra and D. Blankschtein, The Journal of Physical Chemistry C **121**, 28166 (2017).

[26] J. I. Siepmann and M. Sprik, The Journal of Chemical Physics **102**, 511 (1995).

[27] L. Scalfi, M. Salanne, and B. Rotenberg, Annual Review of Physical Chemistry **72**, 189 (2021).

[28] D. T. Limmer, C. Merlet, M. Salanne, D. Chandler, P. A. Madden, R. van Roij, and B. Rotenberg, Physical Review Letters **111**, 106102 (2013).

[29] T. Dufils, G. Jeanmairet, B. Rotenberg, M. Sprik, and M. Salanne, Physical Review Letters **123**, 195501 (2019).

[30] L. Scalfi, T. Dufils, K. G. Reeves, B. Rotenberg, and M. Salanne, The Journal of Chemical Physics **153**, 174704 (2020).

[31] G. D. Mahan, *Many-Particle Physics* (Springer US, 1990).

[32] J.-P. Hansen and I. R. McDonald, *Theory of simple liquids* (Academic Press, 2013).

[33] J. Schwinger, L. Deraad, K. Milton, and W.-y. Tsai, *Classical Electrodynamics* (CRC Press, 2019).

[34] R. Starke and G. A. H. Schober, arXiv:1606.00012 [cond-mat] (2020).

[35] R. Kubo, Reports on Progress in Physics **29**, 255 (1966).

[36] P. C. Martin, E. D. Siggia, and H. A. Rose, Physical Review A **8**, 423 (1973).

[37] R. Phythian, Journal of Physics A: Mathematical and General **8**, 1423 (1975).

[38] H.-K. Janssen, Zeitschrift for Physik B Condensed Matter and Quanta **23**, 377 (1976).

[39] C. De Dominicis, Physical Review B **18**, 4913 (1978), publisher: American Physical Society.

[40] L. V. Keldysh, Sov. Phys. JETP **20**, 1018 (1965).

[41] J. Rammer and H. Smith, Reviews of Modern Physics **58**, 323 (1986).

[42] J. Rammer, *Quantum Field Theory of Non-equilibrium States* (Cambridge University Press, Cambridge, 2007).

[43] R. Zwanzig, *Nonequilibrium statistical mechanics* (Oxford University Press, Oxford ; New York, 2001).

[44] A. I. Larkin and Y. N. Ovchinnikov, Soviet Journal of Experimental and Theoretical Physics **41**, 960 (1975).

[45] X. Li, J. Feng, E. Wang, S. Meng, J. Klimeš, and A. Michaelides, Physical Review B **85**, 085425 (2012).

[46] W. R. Hanke, Physical Review B **8**, 4585 (1973).

[47] S. Plimpton, Journal of Computational Physics **117**, 1 (1995).

[48] H. J. C. Berendsen, J. R. Grigera, and T. P. Straatsma, The Journal of Physical Chemistry **91**, 6269 (1987).

[49] J.-P. Ryckaert, G. Ciccotti, and H. J. C. Berendsen, Journal of Computational Physics **23**, 327 (1977).

[50] H. C. Andersen, Journal of Computational Physics **52**, 24 (1983).

[51] G. Bussi, D. Donadio, and M. Parrinello, The Journal of Chemical Physics **126**, 014101 (2007).

[52] P. A. Bopp, A. A. Kornyshev, and G. Sutmann, The Journal of Chemical Physics **109**, 1939 (1998).

[53] D. C. Elton, *Understanding the dielectric properties of water*, PhD Thesis, The Graduate School, Stony Brook University: Stony Brook, NY. (2016).

[54] D. C. Elton and M. Ferněndez-Serra, Nature Communications **7**, 10193 (2016).

[55] A. S. Barker, Physical Review B **12**, 4071 (1975).

[56] T. Werder, J. H. Walther, R. L. Jaffe, T. Halicioglu, and P. Koumoutsakos, The Journal of Physical Chemistry B **107**, 1345 (2003).

[57] Y. Wu and N. R. Aluru, The Journal of Physical Chemistry B **117**, 8802 (2013).

[58] J. Moser, A. Verdaguer, D. Jiménez, A. Barreiro, and A. Bachtold, Applied Physics Letters **92**, 123507 (2008).

[59] M. Hernéndez, A. Cabo Montes de Oca, M. Oliva-Leyva, and G. G. Naumis, Physics Letters A **383**, 125904 (2019).

[60] P. Loche, C. Ayaz, A. Schlaich, D. J. Bonthuis, and R. R. Netz, The Journal of Physical Chemistry Letters **9**, 6463 (2018).

[61] G. Jeanmairet, N. Levy, M. Levesque, and D. Borgis, Journal of Physics: Condensed Matter **28**, 244005 (2016).

[62] D. A. Kirzhnits, Soviet Physics Uspekhi **30**, 575 (1987).

[63] P. A. Bopp, A. A. Kornyshev, and G. Sutmann, Physical Review Letters **76**, 1280 (1996).

[64] D. J. Bonthuis, S. Gekle, and R. R. Netz, Langmuir **28**, 7679 (2012).

[65] G. Monet, F. Bresme, A. Kornyshev, and H. Berthoumieux, Physical Review Letters **126**, 216001 (2021).

[66] L. Fumagalli, A. Esfandiar, R. Fabregas, S. Hu, P. Ares, A. Janardanan, Q. Yang, B. Radha, T. Taniguchi, K. Watanabe, G. Gomila, K. S. Novoselov, and A. K. Geim, Science **360**, 1339 (2018).

[67] N. Kavokine, R. R. Netz, and L. Bocquet, Annual Review of Fluid Mechanics **53**, 377 (2021).

[68] D. Bohm and D. Pines, Physical Review **92**, 609 (1953).

[69] C. Wu and W. Hanke, Solid State Communications **23**, 829 (1977).

[70] A. Grüneis, C. Attaccalite, L. Wirtz, H. Shiozawa, R. Saito, T. Pichler, and A. Rubio, Physical Review B **78**, 205425 (2008).

[71] J.-C. Charlier, X. Blase, and S. Roche, Reviews of Modern Physics **79**, 677 (2007).

[72] C. Zener, Physical Review **36**, 51 (1930).

[73] T. Zhu, M. Antezza, and J.-S. Wang, Physical Review B **103**, 125421 (2021).

[74] E. H. Hwang and S. Das Sarma, Physical Review B **75**, 205418 (2007).

[75] E. H. Hwang and S. Das Sarma, Physical Review Letters **101**, 156802 (2008).

[76] T. Ando, A. B. Fowler, and F. Stern, Reviews of Modern Physics **54**, 437 (1982).

[77] C. Y. Son and Z.-G. Wang, Proceedings of the National Academy of Sciences **118**, e2020615118 (2021).

[78] E. H. Hwang, B. Y.-K. Hu, and S. Das Sarma, Physica E: Low-dimensional Systems and Nanostructures **40**, 1653 (2008).

[79] A. Esfandiar, B. Radha, F. C. Wang, Q. Yang, S. Hu, S. Garaj, R. R. Nair, A. K. Geim, and K. Gopinadhan, Science **358**, 511 (2017).

[80] J. Comtet, A. Niguès, V. Kaiser, B. Coasne, L. Bocquet, and A. Siria, Nature Materials **16**, 634 (2017).

[81] T. Mouterde, A. Keerthi, A. R. Poggioli, S. A. Dar, A. Siria, A. K. Geim, L. Bocquet, and B. Radha, Nature **567**, 87 (2019).

[82] M. Salanne, B. Rotenberg, K. Naoi, K. Kaneko, P.-L. Taberna, C. P. Grey, B. Dunn, and P. Simon, Nature Energy **1**, 16070 (2016).

[83] D. L. McCaffrey, S. C. Nguyen, S. J. Cox, H. Weller, A. P. Alivisatos, P. L. Geissler, and R. J. Saykally, Proceedings of the National Academy of Sciences **114**, 13369 (2017).

[84] P. Iamprasertkun, W. Hirunpinyopas, A. Keerthi, B. Wang, B. Radha, M. A. Bissett, and R. A. W. Dryfe, The Journal of Physical Chemistry Letters **10**, 617 (2019).

[85] R. P. Misra and D. Blankschtein, The Journal of Physical Chemistry C **125**, 2666 (2021).

[86] C. D. Williams, J. Dix, A. Troisi, and P. Carbone, The Journal of Physical Chemistry Letters **8**, 703 (2017).

[87] C. Zhan, M. R. Ceron, S. A. Hawks, M. Otani, B. C. Wood, T. A. Pham, M. Stadermann, and P. G. Campbell, Nature Communications **10**, 4858 (2019).

[88] M. Ruggeri, K. Reeves, T.-Y. Hsu, G. Jeanmairet, M. Salanne, and C. Pierleoni, The Journal of Chemical Physics **156**, 094709 (2022).

[89] A. Schlaich, D. Jin, L. Bocquet, and B. Coasne, Nature Materials **21**, 237 (2022).

[90] R. P. Misra and D. Blankschtein, Langmuir **37**, 722 (2021).

[91] A. A. Kornyshev, A. I. Rubinshtein, and M. A. Vorotyntsev, Journal of Physics C: Solid State Physics **11**, 3307 (1978).

[92] G. E. H. Reuter and E. H. Sondheimer, Proceedings of the Royal Society of London. Series A. Mathematical and Physical Sciences **195**, 336 (1948).

[93] A. Griffin and J. Harris, Canadian Journal of Physics **54**, 1396 (1976).

[94] M. Kardar, *Statistical Physics of Fields* (Cambridge University Press, Cambridge, 2007).

[95] L. Hedin and S. Lundqvist, in *Solid State Physics*, Vol. 23 (Elsevier, 1970) pp. 1–181.

[96] F. Giustino, Reviews of Modern Physics **89**, 015003 (2017).

[97] D. Horinek, A. Herz, L. Vrbka, F. Sedlmeier, S. I. Mamatkulov, and R. R. Netz, Chemical Physics Letters **479**, 173 (2009).

[98] L. Scalfi and B. Rotenberg, Proceedings of the National Academy of Sciences **118**, e2108769118 (2021).

[99] Y. Marcus, Chemical Reviews **109**, 1346 (2009).

[100] Q. Cao, S.-J. Han, J. Tersoff, A. D. Franklin, Y. Zhu, Z. Zhang, G. S. Tulevski, J. Tang, and W. Haensch, Science **350**, 68 (2015).

[101] M. M. Shulaker, G. Hills, N. Patil, H. Wei, H.-Y. Chen, H.-S. P. Wong, and S. Mitra, Nature **501**, 526 (2013).

[102] P. W. Barone, S. Baik, D. A. Heller, and M. S. Strano, Nature Materials **4**, 86 (2004).

[103] D. M. Guldi, G. M. A. Rahman, M. Prato, N. Jux, S. Qin, and W. Ford, Angewandte Chemie International Edition **44**, 2015 (2005).

[104] T. Ando, Journal of the Physical Society of Japan **66**, 1066 (1997).

[105] P. T. Araujo, A. Jorio, M. S. Dresselhaus, K. Sato, and R. Saito, Physical Review Letters **103**, 146802 (2009).

[106] M. S. Dresselhaus, G. Dresselhaus, R. Saito, and A. Jorio, Annual Review of Physical Chemistry **58**, 719 (2007).

[107] M. J. O'Connell, S. M. Bachilo, C. B. Huffman, V. C. Moore, M. S. Strano, E. H. Haroz, K. L. Rialon, P. J. Boul, W. H. Noon, C. Kittrell, J. Ma, R. H. Hauge, R. B. Weisman, and R. E. Smalley, Science **297**, 593 (2002).

[108] M. Dresselhaus, G. Dresselhaus, R. Saito, and A. Jorio, Physics Reports **409**, 47 (2005).

[109] G. Dukovic, F. Wang, D. Song, M. Y. Sfeir, T. F. Heinz, and L. E. Brus, Nano Letters **5**, 2314 (2005).

[110] R. B. Weisman and S. M. Bachilo, Nano Letters **3**, 1235 (2003).

[111] Y. Miyauchi, R. Saito, K. Sato, Y. Ohno, S. Iwasaki, T. Mizutani, J. Jiang, and S. Maruyama, Chemical Physics Letters **442**, 394 (2007).

[112] S. Berger, F. Iglesias, P. Bonnet, C. Voisin, G. Cassabois, J.-S. Lauret, C. Delalande, and P. Roussignol, Journal of Applied Physics **105**, 094323 (2009).

[113] Y. Hirana, Y. Tanaka, Y. Niidome, and N. Nakashima, Journal of the American Chemical Society **132**, 13072 (2010).

[114] H. Sakai, H. Suzuura, and T. Ando, Journal of the Physical Society of Japan **72**, 1698 (2003).

[115] T. Ando, Journal of the Physical Society of Japan **79**, 024706 (2010).

[116] T. Ando, Physica E: Low-dimensional Systems and Nanostructures **43**, 798 (2011).

[117] A. R. T. Nugraha, R. Saito, K. Sato, P. T. Araujo, A. Jorio, and M. S. Dresselhaus, Applied Physics Letters **97**, 091905 (2010).

[118] S. Cambré, S. M. Santos, W. Wenseleers, A. R. T. Nugraha, R. Saito, L. Cognet, and B. Lounis, ACS Nano **6**, 2649 (2012).

[119] L. Hedin, Physical Review **139**, A796 (1965).

[120] D. F. DuBois, Annals of Physics **8**, 24 (1959).

[121] T. M. Rice, Annals of Physics **31**, 100 (1965).

[122] R. Hambach, *Theory and ab-initio calculations of collective excitations in nanostructures: towards spatially-resolved EELS*, Ph.D. thesis, Ecole Polytechnique X (2010).

[123] L. Aspitarte, D. R. McCulley, A. Bertoni, J. O. Island, M. Ostermann, M. Rontani, G. A. Steele, and E. D. Minot, Scientific Reports **7**, 8828 (2017).

[124] A. Politano and G. Chiarello, Nanoscale **6**, 10927 (2014).

[125] I. J. Luxmoore, C. H. Gan, P. Q. Liu, F. Valmorra, P. Li, J. Faist, and G. R. Nash, ACS Photonics **1**, 1151 (2014).

[126] D. C. Langreth and J. P. Perdew, Physical Review B **15**, 2884 (1977).

[127] R. P. Feynman, Physical Review **56**, 340 (1939).

[128] E. M. Lifshitz, Journal of Experimental Theoretical Physics USSR **29**, 94 (1954).

[129] V. Despoja, M. Šunjić, and L. Marušić, Physical Review B **75**, 045422 (2007).

[130] J. M. Fernández-Varea and R. Garcia-Molina, Journal of Colloid and Interface Science **231**, 394 (2000).

[131] S. Faucher, N. Aluru, M. Z. Bazant, D. Blankschtein, A. H. Brozena, J. Cumings, J. Pedro de Souza, M. Elimelech, R. Epsztein, J. T. Fourkas, A. G. Rajan, H. J. Kulik, A. Levy, A. Majumdar, C. Martin, M. McEldrew, R. P. Misra, A. Noy, T. A. Pham, M. Reed, E. Schwegler, Z. Siwy, Y. Wang, and M. Strano, The Journal of Physical Chemistry C **123**, 21309 (2019).

[132] A. Maali, T. Cohen-Bouhacina, and H. Kellay, Applied Physics Letters **92**, 053101 (2008).

[133] K. Falk, F. Sedlmeier, L. Joly, R. R. Netz, and L. Bocquet, Nano Letters **10**, 4067 (2010).

[134] L. Bocquet and J.-L. Barrat, Physical Review E **49**, 3079 (1994).

[135] J.-L. Barrat and L. Bocquet, Faraday Discussions **112**, 119 (1999).

[136] W. Dou and J. E. Subotnik, The Journal of Chemical Physics **148**, 230901 (2018).

[137] A. M. Wodtke, J. C. Tully, and D. J. Auerbach, International Reviews in Physical Chemistry **23**, 513 (2004).

[138] B. N. J. Persson and S. Andersson, Physical Review B **29**, 4382 (1984).

[139] B. Persson, D. Schumacher, and A. Otto, Chemical Physics Letters **178**, 204 (1991).

[140] F. Yavari, C. Kritzinger, C. Gaire, L. Song, H. Gulapalli, T. Borca-Tasciuc, P. M. Ajayan, and N. Koratkar, Small **6**, 2535 (2010).

[141] B. N. J. Persson and Z. Zhang, Physical Review B **57**, 7327 (1998).

[142] A. I. Volokitin and B. N. J. Persson, Journal of Physics: Condensed Matter **11**, 345 (1999).

[143] A. I. Volokitin and B. N. J. Persson, Physical Review B **74**, 205413 (2006).

[144] R. E. Palmer, J. F. Annett, and R. F. Willis, Physical Review Letters **58**, 2490 (1987).

[145] J. F. Annett, R. E. Palmer, and R. F. Willis, Physical Review B **37**, 2408 (1988).

[146] E. Jensen, R. Palmer, W. Allison, and J. Annett, Physical Review Letters **66**, 492 (1991).

[147] P. Laitenberger and R. E. Palmer, Physical Review Letters **76**, 1952 (1996).

[148] M. Portail, M. Carrere, and J. M. Layet, Surface Science **433-435**, 863 (1999).

[149] M. Portail, I. Forbeaux, N. Papageorgiou, M. CarrÃšre, D. Roy, and J.-M. Layet, Surface Science **454-456**, 384 (2000).

[150] T. Angot, M. Portail, I. Forbeaux, and J. Layet, Surface Science **502-503**, 81 (2002).

[151] M. Gleeson, B. Kasemo, and D. Chakarov, Surface Science **524**, L77 (2003).

[152] F.-L. Shyu and M.-F. Lin, Journal of the Physical Society of Japan **69**, 3781 (2000).

[153] F. L. Shyu and M. F. Lin, Journal of the Physical Society of Japan **70**, 897 (2001).

[154] E. A. Taft and H. R. Philipp, Physical Review **138**, A197 (1965).

[155] L. Vitali, M. A. Schneider, K. Kern, L. Wirtz, and A. Rubio, Physical Review B **69**, 121414 (2004).

[156] Y. Liu, R. F. Willis, K. V. Emtsev, and T. Seyller, Physical Review B **78**, 201403 (2008).

[157] A. Robert, H. Berthoumieux, and M.-L. Bocquet, (2022), arXiv:2204.08779 [cond-mat].

[158] T. A. L. Burgo and A. Erdemir, Angewandte Chemie **126**, 12297 (2014).

[159] A. Keerthi, S. Goutham, Y. You, P. Iamprasertkun, R. A. W. Dryfe, A. K. Geim, and B. Radha, Nature Communications **12**, 3092 (2021).

[160] P. C. Martin and J. Schwinger, Physical Review **115**, 1342 (1959).

[161] J. P. Perdew, K. Burke, and M. Ernzerhof, Physical Review Letters **77**, 3865 (1996).

[162] S. Grimme, J. Antony, S. Ehrlich, and H. Krieg, The Journal of Chemical Physics **132**, 154104 (2010).

[163] B. U. Felderhof, The Journal of Chemical Physics **67**, 493 (1977).

[164] M. Dinpajooh, M. D. Newton, and D. V. Matyushov, The Journal of Chemical Physics **146**, 064504 (2017).

[165] P. C. Hohenberg and B. I. Halperin, Reviews of Modern Physics **49**, 435 (1977).

[166] G. Jeanmairet, M. Levesque, R. Vuilleumier, and D. Borgis, The Journal of Physical Chemistry Letters **4**, 619 (2013), publisher: American Chemical Society.

RÉSUMÉ

Un cadre théorique est introduit pour aborder les interactions électrostatiques aux interfaces métal/liquide. En adoptant une perspective microscopique, nous déplaçons le problème électrostatique dans la résolution d'une équation intégrale pour la fonction de réponse linéaire du système interfacial. En décrivant les fluctuations et la réponse diélectrique du liquide dans le formalisme de la théorie quantique des champs, nous héritons de nouveaux concepts pour aborder les interactions collectives en champ moyen. La précision et la versatilité de notre approche nous permettent de décrire des interfaces carbonées en considérant la spécificité de leurs structures de bandes électroniques.

Cette méthode est ensuite mise en pratique pour étudier le potentiel de force moyenne d'un ion solvaté près d'une surface de graphène, la largeur de la bande électronique interdite d'un nanotube solvaté, l'interaction de van der Waals entre du graphène et de l'eau, et des coefficients de friction solide/liquide. La validité des hypothèses classiques concernant le découplage des temps et longueurs caractéristiques aux interfaces métal/liquide, peut être systématiquement évaluée.

MOTS CLÉS

Métal, liquide, électrostatique, interface, graphène, eau, théorie quantique des champs, champ moyen, fonction de réponse, renormalisation, équation intégrale.

ABSTRACT

A theoretical framework is introduced to tackle electrostatics interactions at metal/liquid interfaces. By adopting a microscopic perspective, we displace the electrostatic problem in resolving an integral equation for the linear response function of the interfacial system. By describing the liquid's fluctuations and dielectric response in the framework of quantum field theory, we inherit new concepts to deal with collective interactions at the mean-field level. The precision and versatility of our approach allow us to scrutinize carbon interfaces, taking into account the specificity of their electronic band structures.

This method then is used to study the mean force potential of an aqueous ion at the graphene interface, the electronic band gap of a solvated carbon nanotube, the van der Waals interactions between a metal and a liquid, and solid/liquid friction coefficient. The validity of mainstream hypothesis regarding time and length scales decoupling at metal/liquid interfaces can be systematically challenged.

KEYWORDS

Metal, liquid, electrostatics, interface, graphene, water, quantum field theory, mean-field, response function, renormalization, integral equation.